

Generation of Radical Cations and Carbocations by Tris(bipyridyl)ruthenium Photosensitization

by

Felix S. Lee

Submitted in partial fulfillment of the requirements
for the degree of Doctor of Philosophy

at

Dalhousie University

Halifax, Nova Scotia

August 2004

© Copyright by Felix S. Lee, 2004



National Library
of Canada

Bibliothèque nationale
du Canada

Acquisitions and
Bibliographic Services

Acquisitions et
services bibliographiques

395 Wellington Street
Ottawa ON K1A 0N4
Canada

395, rue Wellington
Ottawa ON K1A 0N4
Canada

Your file Votre référence

ISBN: 0-612-94054-3

Our file Notre référence

ISBN: 0-612-94054-3

The author has granted a non-exclusive licence allowing the National Library of Canada to reproduce, loan, distribute or sell copies of this thesis in microform, paper or electronic formats.

L'auteur a accordé une licence non exclusive permettant à la Bibliothèque nationale du Canada de reproduire, prêter, distribuer ou vendre des copies de cette thèse sous la forme de microfiche/film, de reproduction sur papier ou sur format électronique.

The author retains ownership of the copyright in this thesis. Neither the thesis nor substantial extracts from it may be printed or otherwise reproduced without the author's permission.

L'auteur conserve la propriété du droit d'auteur qui protège cette thèse. Ni la thèse ni des extraits substantiels de celle-ci ne doivent être imprimés ou autrement reproduits sans son autorisation.

In compliance with the Canadian Privacy Act some supporting forms may have been removed from this dissertation.

Conformément à la loi canadienne sur la protection de la vie privée, quelques formulaires secondaires ont été enlevés de ce manuscrit.

While these forms may be included in the document page count, their removal does not represent any loss of content from the dissertation.

Bien que ces formulaires aient inclus dans la pagination, il n'y aura aucun contenu manquant.

Canada

DALHOUSIE UNIVERSITY

To comply with the Canadian Privacy Act the National Library of Canada has requested that the following pages be removed from this copy of the thesis:

Preliminary Pages

Examiners Signature Page (pii)

Dalhousie Library Copyright Agreement (piii)

Appendices

Copyright Releases (if applicable)

Table of Contents

List of Figures	viii
List of Tables	xv
Abstract	xvii
List of Abbreviations and Symbols Used	xviii
Acknowledgements	xx
Chapter One: Introduction	1
1.1 Introduction	1
1.2 Enzymatic stabilization of reactive intermediates	3
1.2.1 π -Cation interactions	5
1.2.1.1 Gas-phase studies	6
1.2.1.2 Solution-phase studies	8
1.2.1.3 π -Cation interactions in biological systems	11
1.2.1.3.1 Oxidosqualene cyclase	13
1.3 Studying and generating reactive intermediates in biology	15
1.3.1 Direct irradiation	19
1.3.2 Photosensitization	21
1.4 Tris(bipyridyl)ruthenium photosensitizers	24
1.4.1 Amphoteric nature of the $^3\text{MLCT}$ state	29
1.5 Biological applications of tris(bipyridyl)ruthenium complexes	31
1.6 Scope of thesis	33
Chapter Two: Intermolecular Substrate Oxidation	36
2.1 Introduction	36
2.1.1 Dependence of reduction potentials on ligand substitution	38
2.1.2 Tris(bipyridyl)ruthenium complexes as oxidants	41
2.1.3 Organic substrates	43

2.2	Results	46
2.2.1	Ru(II)* excited state as an oxidant	46
2.2.2	Oxidation of Ru(II)* excited states to Ru(III)	49
2.2.3	Substrate oxidation by Ru(III)	56
2.3	Discussion	66
2.3.1	Relationship between thermodynamics and kinetics	66
2.3.2	Reactivity of Ru(II)* excited states	70
2.3.2.1	Reactivity with organic substrates	70
2.3.2.2	Reactivity with electron acceptor	71
2.3.3	Reactivity of Ru(III) states with organic substrates	73
2.3.4	Selective oxidation of organic substrates	75
2.4	Conclusion	75
Chapter Three:	Oxidation of <i>N,N</i>-Dimethyl-<i>p</i>-toluidine	77
3.1	Introduction	77
3.2	Results	80
3.2.1	Intermolecular oxidation	80
3.2.1.1	Intermolecular oxidation by Ru(II)*	81
3.2.1.2	Intermolecular oxidation by Ru(III)	85
3.2.2	Intramolecular oxidation	95
3.2.2.1	Intramolecular oxidation by Ru(II)*	98
3.2.2.2	Intramolecular oxidation by Ru(III)	104
3.2.2.2.1	Irradiation of the slowest complex: Ru(dmb) ₂ (C ₇ -NT)	106
3.2.2.2.2	Irradiation of the fastest complex: Ru(bpy) ₂ (C ₃ OC ₂ -NT)	109
3.2.2.2.3	Irradiation of other complexes	116
3.3	Discussion	125
3.3.1	Electron acceptor as an Ru(I) oxidant	125
3.3.2	Effect of linker	127
3.4	Conclusion	131
Chapter Four:	Intramolecular Oxidation of Diphenylalkanes	133

4.1	Introduction	133
4.2	Results	139
4.2.1	Excited-state lifetime measurements	139
4.2.2	Laser-flash irradiation with an electron acceptor	141
4.2.2.1	Generation of radical cations	142
4.2.2.2	Fragmentation of radical cations	152
4.3	Discussion	163
4.3.1	Radical cation generation	163
4.3.2	Radical cation fragmentation	165
4.4	Conclusion and future work	169
Chapter Five:	Picosecond Dynamics of Ru(II)* Excited States	172
5.1	Introduction	172
5.2	Results	176
5.3	Discussion	180
5.4	Conclusion	184
Chapter Six:	Experimental	186
6.1	General procedures	186
6.2	Synthesis of unlinked tris(bipyridyl)ruthenium complexes	187
6.2.1	Bipyridyl ligands	189
6.2.2	Bis(bipyridyl)ruthenium complexes	191
6.2.3	Tris(bipyridyl)ruthenium complexes	193
6.3	Synthesis of substrate-linked tris(bipyridyl)ruthenium complexes	200
6.3.1	Functionalized bipyridines	200
6.3.2	Diphenylalkane substrates	205
6.3.2.1	Amino-substituted 2,3-dimethyl-2,3-diphenylbutane	206
6.3.2.2	Amino-substituted 3,4-diethyl-3,4-diphenylhexane	208
6.3.2.3	Amino-substituted 3,4-dimethyl-3,4-diphenylhexane	212
6.3.2.4	Amino-substituted 4,5-dimethyl-4,5-diphenyloctane	215
6.3.2.5	Amino- and oxygen-substituted 2,3-dimethyl-2,3-diphenylbutane	218

6.3.2.6	Oxygen-substituted 2,3-dimethyl-2,3-diphenylbutane	220
6.3.3	Bipyridine-linked substrates	222
6.3.4	Substrate-linked tris(bipyridyl)ruthenium complexes	236
6.4	Synthesis of other compounds	241
6.5	Laser-flash photolysis	242
6.5.1	Nanosecond laser-flash photolysis	242
6.5.1.1	Sample preparation	244
6.5.1.2	Acquisition and processing of absorption kinetic traces	245
6.5.1.3	Acquisition and processing of emission kinetic traces	249
6.5.1.4	Acquisition of transient absorption spectra	249
6.5.2	Femtosecond laser-flash photolysis (emission)	251
6.5.2.1	Sample preparation	254
6.5.2.2	Processing of kinetic traces	255
6.6	Product studies	255
References		256

List of Figures

Figure 1-1. Comparison of uncatalyzed (solid line) and catalyzed (dashed line) routes for the conversion of a substrate (S) to a product (P) by an enzyme (E). TS denotes the transition state; ES, E-TS, and EP, the enzyme-bound substrate, transition state, and product, respectively.....	4
Figure 1-2. Schematic representation of a π -cation interaction.	6
Figure 1-3. Binding of a charged organic host into a hydrophobic cyclophane host.....	9
Figure 1-4. Examples tris(bipyridyl)ruthenium complexes in their homoleptic and heteroleptic forms. Substituents are denoted by X and Y, where $X \neq Y$	25
Figure 1-5. (a) Ground-state absorption spectrum of Ru(bpy) ₃ acquired in water and (b) a schematic molecular-orbital representation of the MLCT (metal-to-ligand charge transfer), MC (metal-centered), and LC (ligand-centered) transitions.....	26
Figure 1-6. Transient absorption spectra obtained (●) 0.024 μ s, (○) 0.72 μ s, and (■) 1.2 μ s following 355-nm laser irradiation of Ru(bpy) ₃ in water.....	28
Figure 2-1. Kinetic trace acquired at 620 nm following the 355-nm laser irradiation of Ru(dfmb) ₃ in nitrogen-purged water with (●) 0.0 mM, and (○) 4 mM <i>trans</i> -anethole.....	48
Figure 2-2. Kinetic trace acquired at 620 nm following the 355-nm laser irradiation of Ru(dmeb) ₃ in nitrogen-purged, aqueous 250 mM NaCl in the presence of (●) 0.0 mM, (○) 0.4 mM, and (■) 1.0 mM [Ru(NH ₃) ₆]Cl ₃	50
Figure 2-3. Observed rate constants for the decay of Ru(II)* of (a) Ru(dmeob) ₃ , (b) Ru(dmb) ₃ , (c) Ru(bpy) ₂ (dmb), (d) Ru(bpy) ₃ , (e) Ru(dmeb) ₂ (dmb), (f) Ru(dmeb) ₃ , (g) Ru(dfmb) ₂ (dmb), and (h) Ru(dfmb) ₃ as a function of [Ru(NH ₃) ₆]Cl ₃ , measured from kinetic traces monitored at 370 nm or 620 nm following 355-nm laser irradiation of nitrogen-saturated samples containing 250 mM NaCl. Slope (m) in units of 10 ⁹ M ⁻¹ s ⁻¹	52
Figure 2-4. Kinetic trace acquired at 450 nm following the 355-nm laser irradiation of Ru(dmeob) ₃ in nitrogen-purged, aqueous solutions in the (a) absence or (b) presence of 100 mM [Ru(NH ₃) ₆]Cl ₃ . Figure (b) indicates an Ru(II)*-to-Ru(III) conversion efficiency of approximately 60%.	55

Figure 2-5. Kinetic trace acquired at 450 nm following the 355-nm laser irradiation of Ru(dfmb)₂(dmb) in nitrogen-purged, aqueous 100 mM [Ru(NH₃)₆]Cl₃ in the presence of (●) 0.0 mM, (○) 0.15 mM, and (■) 0.30 mM 4-methoxycumene. 58

Figure 2-6. Observed rate constants for the recovery of Ru(II) of (a) Ru(dmeob)₃, (b) Ru(dmb)₃, (c) Ru(bpy)₂(dmb), (d) Ru(bpy)₃, (e) Ru(dmeb)₂(dmb), (f) Ru(dmeb)₃, (g) Ru(dfmb)₂(dmb), and (h) Ru(dfmb)₃ as a function of *trans*-anethole concentration, measured from kinetic traces monitored at 450 nm following 355-nm laser irradiation of nitrogen-saturated samples in 100 mM [Ru(NH₃)₆]Cl₃. Slope (m) in units of 10⁸ M⁻¹ s⁻¹. 61

Figure 2-7. Observed rate constants for the recovery of Ru(II) of (a) Ru(dmeob)₃, (b) Ru(dmb)₃, (c) Ru(bpy)₂(dmb), (d) Ru(bpy)₃, (e) Ru(dmeb)₂(dmb), (f) Ru(dmeb)₃, (g) Ru(dfmb)₂(dmb), and (h) Ru(dfmb)₃ versus 4-methoxycumene concentration, measured from kinetic traces monitored at 450 nm following 355-nm laser irradiation of nitrogen-saturated samples containing 100 mM [Ru(NH₃)₆]Cl₃. Slope (m) in units of 10⁸ M⁻¹ s⁻¹. 62

Figure 2-8. Observed rate constants for the recovery of Ru(II) of (a) Ru(bpy)₂(dmb), (b) Ru(bpy)₃, (c) Ru(dmeb)₂(dmb), (d) Ru(dmeb)₃, (e) Ru(dfmb)₂(dmb), and (f) Ru(dfmb)₃ as a function of *trans*-stilbene concentration. Rate constants were measured from kinetic traces monitored at 450 nm following 355-nm laser irradiation of nitrogen-saturated samples in 100 mM [Ru(NH₃)₆]Cl₃. Slope (m) in units of 10⁸ M⁻¹ s⁻¹. 63

Figure 2-9. Observed rate constants for the recovery of Ru(II) of (a) Ru(dmeb)₂(dmb), (b) Ru(dmeb)₃, (c) Ru(dfmb)₂(dmb), and (d) Ru(dfmb)₃ as a function of β-methylstyrene concentration. Rate constants were measured from kinetic traces monitored at 450 nm following 355-nm laser irradiation of nitrogen-saturated samples in 100 mM [Ru(NH₃)₆]Cl₃. Slope (m) in units of 10⁸ M⁻¹ s⁻¹. 64

Figure 2-10. Observed rate constants for the recovery of Ru(II) of (a) Ru(dmeb)₂(dmb), (b) Ru(dmeb)₃, (c) Ru(dfmb)₂(dmb), and (d) Ru(dfmb)₃ as a function of 4-methylstyrene, measured from kinetic traces at 450 nm following 355-nm laser irradiation of nitrogen-saturated samples in 100 mM [Ru(NH₃)₆]Cl₃. Slope (m) in units of 10⁸ M⁻¹ s⁻¹. 65

Figure 2-11. Observed rate constants for the recovery of Ru(II) of (a) Ru(dmeb)₃ and (b) Ru(dfmb)₃ as a function of styrene concentration, measured from kinetic traces monitored at 450 nm following 355-nm laser irradiation of nitrogen-saturated samples in 100 mM [Ru(NH₃)₆]Cl₃. Slope (m) in units of 10⁸ M⁻¹ s⁻¹. 65

Figure 2-12. Marcus relationship between the rate (k_{et}) and the free energy (ΔG°) of an electron-transfer reaction.	69
Figure 3-1. Time-resolved kinetic trace of Ru(II)* monitored at 370 nm following 355-nm laser irradiation of Ru(bpy) ₂ (dmb) in nitrogen-saturated 250 mM sodium phosphate pH 6.5 containing (●) 0 mM or (○) 4 mM DMT.	83
Figure 3-2. Observed rate constants for the decay of Ru(II)* of Ru(bpy) ₂ (dmb) as a function of DMT at pH (●) 5.1, (○) 5.6, and (■) 6.5, measured from kinetic traces monitored at 370 nm following 355-nm laser irradiation. Slope (m) in units of $10^9 \text{ M}^{-1} \text{ s}^{-1}$	84
Figure 3-3. Time-resolved kinetic trace monitored at 450 nm following 355-nm laser irradiation of (a) Ru(dmb) ₃ and (b) Ru(bpy) ₂ (dmb) in nitrogen-saturated 250 mM sodium phosphate pH 6.5 containing 60 mM [Ru(NH ₃) ₆]Cl ₃ . Kinetic traces were similar at other pH values investigated.	87
Figure 3-4. (a) Time-resolved kinetic trace of Ru(II) monitored at 450 nm following 355-nm laser irradiation of Ru(dmb) ₃ in nitrogen-saturated 250 mM sodium acetate pH 4.2 with 60 mM [Ru(NH ₃) ₆]Cl ₃ and (●) 0 mM, (○) 1 mM, (■) 2 mM, or (□) 4 mM DMT. (b) Transient absorption spectra collected (●) 0.080 μs , (○) 0.72 μs , (■) 3.6 μs , and (□) 6.0 μs after irradiation of the same compound under similar conditions with 4 mM DMT.	89
Figure 3-5. Observed rate constants for the recovery of Ru(II) of Ru(dmb) ₃ as a function of DMT concentration at pH (a) (●) 3.2, (○) 4.2, (■) 4.7; (b) (●) 5.1, (○) 5.6, (■) 6.5. Rate constants were measured from kinetic traces monitored at 450 nm following 355-nm laser irradiation in the presence of 60 mM [Ru(NH ₃) ₆]Cl ₃ . Slope (m) in units of $10^8 \text{ M}^{-1} \text{ s}^{-1}$	90
Figure 3-6. Observed rate constants for the recovery of Ru(II) of Ru(bpy) ₂ (dmb) as a function of DMT concentration at pH (a) (●) 3.2, (○) 4.2, (■) 4.7; (b) (●) 5.1, (○) 5.6, (■) 6.5. Rate constants were measured from kinetic traces monitored at 450 nm following 355-nm laser irradiation in the presence of 60 mM [Ru(NH ₃) ₆]Cl ₃ . Slope (m) in units of $10^8 \text{ M}^{-1} \text{ s}^{-1}$	91
Figure 3-7. Comparison of the second-order rate constants for the oxidation of DMT by the Ru(III) state of Ru(bpy) ₂ (dmb) to the oxidation by Ru(dmb) ₃ at pH 3.2-6.5.	92
Figure 3-8. Apparent second-order rate constants for the oxidation of DMT by Ru(III) states of (a) Ru(dmb) ₃ and (b) Ru(bpy) ₂ (dmb) in as a function of pH.	94

Figure 3-9. Transient absorption spectra obtained (●) 0.008 μ s, (○) 0.072 μ s, (■) 0.36 μ s, and (□) 0.60 μ s following 355-nm laser irradiation of (a) Ru(bpy) ₂ (dmb) in nitrogen saturated neat water and (b) Ru(bpy) ₂ (C ₃ OC ₂ -NT) in nitrogen-saturated 25 mM sodium phosphate pH 6.5.....	103
Figure 3-10. Determination of the efficiency of radical cation generation by comparing the (a) Ru(II) bleaching at 450 nm to (c) the absorption of the DMT radical cation at 485 nm at longer time scale; (b) depicts the 450 nm recovery at longer time scale.	106
Figure 3-11. Time-resolved kinetic trace collected at (●) 450 nm and (○) 485 nm after 355-nm laser irradiation of Ru(dmb) ₂ (C ₇ -NT) in buffered 60 mM [Ru(NH ₃) ₆]Cl ₃ at pH (a-c) 3.2, (d-f) 4.2, (g-i) 4.7, (j-l) 5.1, (m-o) 5.6, and (p-r) 6.5.....	108
Figure 3-12.. Time-resolved kinetic trace collected at (●) 450 nm and (○) 485 nm after 355-nm laser irradiation of Ru(bpy) ₂ (C ₃ OC ₂ -NT) in buffered 60 mM [Ru(NH ₃) ₆]Cl ₃ at pH (a-c) 3.2, (d-f) 4.2, (g-i) 4.7, (j-l) 5.1, (m-o) 5.6, and (p-r) 6.5.....	111
Figure 3-13. Time-resolved kinetic trace collected at (●) 450 nm and (○) 485 nm after 355-nm laser irradiation of Ru(bpy) ₂ (C ₇ -NT) in buffered 60 mM [Ru(NH ₃) ₆]Cl ₃ at pH (a-c) 3.2, (d-f) 4.2, (g-i) 4.7, (j-l) 5.1, (m-o) 5.6, and (p-r) 6.5.....	118
Figure 3-14. Time-resolved kinetic trace collected at (●) 450 nm and (○) 485 nm after 355-nm laser irradiation of Ru(dmb) ₂ (C ₄ -NT) in buffered 60 mM [Ru(NH ₃) ₆]Cl ₃ at pH (a-c) 3.2, (d-f) 4.2, (g-i) 4.7, (j-l) 5.1, (m-o) 5.6, and (p-r) 6.5.....	122
Figure 3-15. Time-resolved kinetic trace collected at (●) 450 nm and (○) 485 nm after 355-nm laser irradiation of Ru(bpy) ₂ (C ₄ -NT) in buffered 60 mM [Ru(NH ₃) ₆]Cl ₃ at pH (a-c) 3.2, (d-f) 4.2, (g-i) 4.7, (j-l) 5.1, (m-o) 5.6, and (p-r) 6.5.....	123
Figure 3-16. Time-resolved kinetic trace collected at (●) 450 nm and (○) 485 nm after 355-nm laser irradiation of Ru(dmb) ₂ (C ₃ OC ₂ -NT) in buffered 60 mM [Ru(NH ₃) ₆]Cl ₃ at pH (a-c) 3.2, (d-f) 4.2, (g-i) 4.7, (j-l) 5.1, (m-o) 5.6, and (p-r) 6.5.....	124
Figure 4-1. Time-resolved kinetic trace monitored at 450 nm following 355-nm laser irradiation of (a) Ru(bpy) ₂ (C ₇ -O-MPB-O) and (b) Ru(bpy) ₂ (dmb) in nitrogen-saturated 10 mM sodium phosphate pH 7.2 containing 15 mM [Co(NH ₃) ₅ Cl]Cl ₂	143

Figure 4-2. Time-resolved kinetic trace monitored at 490 nm following 355-nm laser irradiation of Ru(bpy) ₂ (C ₄ -O-MPB-N) in nitrogen-saturated 10 mM sodium phosphate pH 7.2 containing 15 mM [Co(NH ₃) ₅ Cl]Cl ₂	146
Figure 4-3. Time-resolved kinetic trace monitored at 490 nm following 355-nm laser irradiation of Ru(bpy) ₂ (C ₄ -N-MPB-H) in nitrogen-saturated 10 mM sodium phosphate pH 7.2 containing 15 mM [Co(NH ₃) ₅ Cl]Cl ₂	146
Figure 4-4. Time-resolved kinetic trace monitored at 490 nm following 355-nm laser irradiation of Ru(bpy) ₂ (C ₄ -N-BZ-N) in nitrogen-saturated 10 mM sodium phosphate pH 7.2 containing 15 mM [Co(NH ₃) ₅ Cl]Cl ₂	147
Figure 4-5. Time-resolved kinetic trace monitored at 490 nm following 355-nm laser irradiation of Ru(bpy) ₂ (C ₄ -N-MPB-N) in nitrogen-saturated 10 mM sodium phosphate pH 7.2 containing 15 mM [Co(NH ₃) ₅ Cl]Cl ₂	147
Figure 4-6. Time-resolved kinetic trace monitored at 490 nm following 355-nm laser irradiation of Ru(bpy) ₂ (C ₇ -N-MPB-N) in nitrogen-saturated 10 mM sodium phosphate pH 7.2 containing 15 mM [Co(NH ₃) ₅ Cl]Cl ₂	148
Figure 4-7. Time-resolved kinetic trace monitored at 490 nm following 355-nm laser irradiation of Ru(bpy) ₂ (C ₄ -N-MPH-N) in nitrogen-saturated 10 mM sodium phosphate pH 7.2 containing 15 mM [Co(NH ₃) ₅ Cl]Cl ₂	148
Figure 4-8. Time-resolved kinetic trace monitored at 490 nm following 355-nm laser irradiation of Ru(bpy) ₂ (C ₄ -N-MPO-N) in nitrogen-saturated 10 mM sodium phosphate pH 7.2 containing 15 mM [Co(NH ₃) ₅ Cl]Cl ₂	149
Figure 4-9. (a) Transient absorption spectra obtained (●) 24 μs, (○) 80 μs, (■) 360 μs, and (□) 600 μs following 355-nm laser irradiation of Ru(bpy) ₂ (C ₄ -N-BZ-N) in nitrogen-saturated 10 mM sodium phosphate pH 7.2 containing 15 mM [Co(NH ₃) ₅ Cl]Cl ₂ . (b) Time-resolved kinetic traces monitored at (●) 490 nm and (○) 380 nm for the same compound under identical conditions.	154
Figure 4-10. (a) Transient absorption spectra obtained (●) 24 μs, (○) 80 μs, (■) 360 μs, and (□) 600 μs following 355-nm laser irradiation of Ru(bpy) ₂ (C ₄ -N-MPB-N) in nitrogen-saturated 10 mM sodium phosphate pH 7.2 containing 15 mM [Co(NH ₃) ₅ Cl]Cl ₂ . (b) Time-resolved kinetic traces monitored at (●) 490 nm and (○) 380 nm for the same compound under identical conditions.	155
Figure 4-11. (a) Transient absorption spectra obtained (●) 44 μs, (○) 96 μs, (■) 360 μs, and (□) 600 μs following 355-nm laser irradiation of Ru(bpy) ₂ (C ₄ -N-MPH-N) in nitrogen-saturated 10 mM sodium phosphate pH 7.2 containing 15	

mM $[\text{Co}(\text{NH}_3)_5\text{Cl}]\text{Cl}_2$. (b) Time-resolved kinetic traces monitored at (●) 490 nm and (○) 380 nm for the same compound under identical conditions. 156

Figure 4-12. (a) Transient absorption spectra obtained (●) 44 μs , (○) 96 μs , (■) 360 μs , and (□) 600 μs following 355-nm laser irradiation of $\text{Ru}(\text{bpy})_2(\text{C}_4\text{-N-MPO-N})$ in nitrogen-saturated 10 mM sodium phosphate pH 7.2 containing 15 mM $[\text{Co}(\text{NH}_3)_5\text{Cl}]\text{Cl}_2$. (b) Time-resolved kinetic traces monitored at (●) 490 nm and (○) 380 nm for the same compound under identical conditions. 157

Figure 4-13. (a) Transient absorption spectra obtained (●) 88 μs , (○) 204 μs , (■) 440 μs , and (□) 664 μs following 355-nm laser irradiation of $\text{Ru}(\text{bpy})_2(\text{C}_4\text{-N-MPB-H})$ in nitrogen-saturated 10 mM sodium phosphate pH 7.2 containing 15 mM $[\text{Co}(\text{NH}_3)_5\text{Cl}]\text{Cl}_2$. (b) Time-resolved kinetic traces monitored at (●) 490 nm and (○) 380 nm for the same compound under identical conditions. 158

Figure 4-14. (a) Transient absorption spectra obtained (●) 24 μs , (○) 80 μs , (■) 360 μs , and (□) 600 μs following 355-nm laser irradiation of $\text{Ru}(\text{bpy})_2(\text{C}_4\text{-O-MPB-N})$ in nitrogen-saturated 10 mM sodium phosphate pH 7.2 containing 15 mM $[\text{Co}(\text{NH}_3)_5\text{Cl}]\text{Cl}_2$. (b) Time-resolved kinetic traces monitored at (●) 490 nm and (○) 380 nm for the same compound under identical conditions. 159

Figure 4-15. (a) Transient absorption spectra obtained (●) 24 μs , (○) 80 μs , (■) 360 μs , and (□) 600 μs following 355-nm laser irradiation of $\text{Ru}(\text{bpy})_2(\text{C}_7\text{-N-MPB-N})$ in nitrogen-saturated 10 mM sodium phosphate pH 7.2 containing 15 mM $[\text{Co}(\text{NH}_3)_5\text{Cl}]\text{Cl}_2$. (b) Time-resolved kinetic traces monitored at (●) 490 nm and (○) 380 nm for the same compound under identical conditions. 160

Figure 5-1. (a) Instrument response function measured using a suspension of corn starch in water. (b and c) Time-resolved kinetic traces monitored at 500 nm following 388-nm laser irradiation of aqueous (b) $\text{Ru}(\text{bpy})_3$ with a single fast component and (c) $\text{Ru}(\text{dmb})_3$ with biexponential kinetics comprised of a fast and slow component. 178

Figure 5-2. Ground-state absorption spectrum of $\text{Ru}(\text{bpy})_3$ 183

Figure 6-1. Transmission nanosecond laser-flash photolysis schematic for the acquisition of kinetic traces and transient absorption spectra..... 243

Figure 6-2. Sample time-resolved kinetic traces illustrating (a) a decay along with the pre-trigger region; (b) the same decay without the pre-trigger and analyzed with a monoexponential equation to calculate $k_{\text{decay}} = 3.0 \times 10^6 \text{ s}^{-1}$; (c) a growth including the pre-trigger; and (d) the same growth without the pre-trigger and analyzed with a monoexponential equation to calculate $k_{\text{growth}} = 3.3 \times 10^3 \text{ s}^{-1}$ 248

Figure 6-3. (a) Sample kinetic trace illustrating a growth at 390 nm, along with four time windows (t_1 - t_4) used for the construction of transient absorption spectra. (b) Spectra illustrating the increase in absorption at 390 nm at the same time windows selected on the kinetic trace. The concomitant decay and growth, with respective maxima near 480 and 370 nm, also result in an isosbestic point near 435 nm.	251
Figure 6-4. Femtosecond laser-flash photolysis schematic for the detection of emission.	252
Figure 6-5. Schematic of streak camera operation for the acquisition of emission. The emitted photon packet is converted to an image equivalent to a kinetic trace.	254

List of Tables

Table 1-1. Reduction potentials (V) for Ru(bpy) ₃ relative to SCE.....	30
Table 2-1. Reduction potentials (V) for tris(bipyridyl)ruthenium complexes relative to SCE in acetonitrile and the electron acceptor [Ru(NH ₃) ₆]Cl ₃ relative to NHE in water.	38
Table 2-2. Reduction potentials (V) for the corresponding radical cations of organic substrates relative to SCE in acetonitrile.	45
Table 2-3. Ru(II)* lifetimes measured at 620 nm after 355-nm irradiation in nitrogen-saturated aqueous solutions. Lifetimes were not affected by 4 mM <i>trans</i> -anethole.	48
Table 2-4. Second-order rate constants and reduction potential differences (ΔE) for the oxidative quenching of Ru(II)* states of tris(bipyridyl)ruthenium complexes by [Ru(NH ₃) ₆]Cl ₃ in 250 mM NaCl.....	51
Table 2-5. Percentages of Ru(II)* oxidized to Ru(III) by 100 mM [Ru(NH ₃) ₆]Cl ₃ for various tris(bipyridyl)ruthenium complexes.	56
Table 2-6. Second-order rate constants ($/10^8 \text{ M}^{-1} \text{ s}^{-1}$) and reduction potential differences ΔE (V) for substrate oxidation by Ru(III) states of tris(bipyridyl)ruthenium complexes.....	60
Table 3-1. Relevant reduction potentials (V) for Ru(dmb) ₃ , Ru(bpy) ₂ (dmb), the substrate <i>N,N</i> -dimethyl- <i>p</i> -toluidine, and the electron acceptor [Ru(NH ₃) ₆]Cl ₃	79
Table 3-2. Second-order rate constants ($/10^7 \text{ M}^{-1} \text{ s}^{-1}$) for the oxidation of DMT by Ru(III) states of Ru(dmb) ₃ and Ru(bpy) ₂ (dmb) as a function of pH.	92
Table 3-3. Excited-state lifetimes of DMT-linked tris(bipyridyl)ruthenium complexes in pH-buffered, nitrogen-purged solutions.	99
Table 3-4. Parameters acquired from the laser-flash irradiation of Ru(dmb) ₂ (C ₇ -NT) in the presence of buffered, nitrogen-purged 60 mM [Ru(NH ₃) ₆]Cl ₃	109
Table 3-5. Parameters acquired from the laser-flash irradiation of Ru(bpy) ₂ (C ₃ OC ₂ -NT) in the presence of buffered, nitrogen-purged 60 mM [Ru(NH ₃) ₆]Cl ₃	112

Table 3-6. Parameters acquired from the laser-flash irradiation of Ru(bpy) ₂ (C ₇ -NT) in the presence of buffered, nitrogen-purged 60 mM [Ru(NH ₃) ₆]Cl ₃ .	117
Table 3-7. Parameters acquired from the laser-flash irradiation of Ru(dmb) ₂ (C ₄ -NT) in the presence of buffered, nitrogen-purged 60 mM [Ru(NH ₃) ₆]Cl ₃ .	120
Table 3-8. Parameters acquired from the laser-flash irradiation of Ru(bpy) ₂ (C ₄ -NT) in the presence of buffered, nitrogen-purged 60 mM [Ru(NH ₃) ₆]Cl ₃ .	120
Table 3-9. Parameters acquired from the laser-flash irradiation of Ru(dmb) ₂ (C ₃ OC ₂ -NT) in the presence of buffered, nitrogen-purged 60 mM [Ru(NH ₃) ₆]Cl ₃ .	121
Table 3-10. Radical cation generation efficiencies for DMT-linked complexes in nitrogen-purged 25 mM sodium phosphate, pH 6.5, with 60 mM [Ru(NH ₃) ₆]Cl ₃ .	121
Table 4-1. Excited-state lifetimes of tris(bipyridyl)ruthenium complexes linked to diphenylalkane substrates in 10 mM sodium phosphate pH 7.2.	139
Table 4-2. Radical cation generation rate constants for tris(bipyridyl)ruthenium complexes linked to diphenylalkane substrates in 10 mM sodium phosphate pH 7.2 containing 15 mM [Co(NH ₃) ₅ Cl]Cl ₂ .	152
Table 4-3. Rate constants for the decay of amino-substituted diphenylalkane radical cations and the growth of corresponding aminobenzyl carbocations in nitrogen-saturated 10 mM sodium phosphate pH 7.2 containing 15 mM [Co(NH ₃) ₅ Cl]Cl ₂ . Literature values are for the fragmentation of the unlinked radical cations of the corresponding substrates.	162
Table 5-1. Spectroscopic properties of tris(bipyridyl)ruthenium complexes in water.	179

Abstract

In enzymatically catalyzed reactions, the stabilization of reactive intermediates *via* amino-acid residues in the active site forms the basis of enzyme catalysis. It is essential then, that we understand the behaviour of enzyme-bound reactive intermediates to thoroughly understand biological catalysis. However, a major obstacle in the study of the behaviour of carbocations in active sites has been the lack of a method for their biocompatible, *in situ* generation.

This thesis therefore investigates methods that could be used to “deliver” reactive intermediates from a organic, precursor substrate to hydrophobic sites, such as an enzyme active site. Specifically, using nanosecond laser-flash photolysis, tris(4,4'-disubstituted-2,2'-bipyridine)ruthenium photosensitizer complexes were used to oxidize substrates to their radical cations, the fragmentation reactions of which can generate carbocations.

Initially, the intermolecular oxidation of a series of organic substrates by various ruthenium complexes in their Ru(II)* and Ru(III) states were studied. The rate constants for oxidation were dependent on both the electron-withdrawing properties of the ligand substituents and the substrate oxidation potentials. These results show that ruthenium complexes are useful for selective substrate oxidation in that their electrochemical properties can be fine-tuned by simple modification of the ligand.

The intramolecular oxidation of an aromatic amine linked to the photosensitizers was also investigated to probe the dual-mechanism nature of oxidation. Herein, the substrate was oxidized by Ru(II)* and Ru(III) states, concomitant with the generation of Ru(I) and Ru(II), respectively. An unconventional use of an electron acceptor for the trapping of Ru(I) is also reported.

Finally, the study culminates in the intramolecular oxidation of a hydrophobic, diphenylalkane substrate that, when oxidized to its radical cation, undergoes fragmentation to generate reactive carbocations. This method could possibly be used to “deliver” carbocations to hydrophobic sites.

List of Abbreviations and Symbols Used

General abbreviations and symbols

δ	chemical shift	k	rate constant
ΔA	change in absorbance	LC	ligand-centered
ΔE	reduction potential difference	lit.	literature value
ΔG°	Gibbs free energy	m	slope of a linear plot
ΔG^\ddagger	free energy of activation	m/z	mass-to-charge ratio
ε	extinction coefficient	MC	metal-centered
λ	wavelength	MLCT	metal-to-ligand charge transfer
λ	reorganization energy	mp	melting point
τ	lifetime	MS	mass spectrometry
aq	aqueous	NHE	normal hydrogen electrode
bp	boiling point	NMR	nuclear magnetic resonance
conc.	concentrated	SGCC	silica gel column chromatography
DNA	deoxyribonucleic acid	SCE	saturated calomel electrode
ESI	electrospray ionization	TEA	triethylamine
GC	gas chromatography	TLC	thin-layer chromatography
ISC	intersystem crossing	UV	ultraviolet

Units of measurement

eV	electron volt	mmol	millimole
fs	femtosecond	mol	mole
g	gram	nm	nanometre
Hz	Hertz	ns	nanosecond
kJ	kilojoule	ppm	parts per million
M	molar	ps	picosecond
mg	milligram	s	second
mJ	millijoule	μ s	microsecond
mL	millilitre	V	volt
mm	millimetre		

Chemicals and compounds

DCM	dichloromethane
DMT	<i>N,N</i> -dimethyl- <i>p</i> -toluidine
EtOAc	ethyl acetate
THF	tetrahydrofuran
bpy	2,2'-bipyridine
dfmb	4,4'-di(trifluoromethyl)-2,2'-bipyridine
dmb	4,4'-dimethyl-2,2'-bipyridine
dmeb	2,2'-bipyridine-4,4-dicarboxylic acid bismethyl ester
dmeob	4,4'-dimethoxy-2,2'-bipyridine
d5fmb	5,5'-di(trifluoromethyl)-2,2'-bipyridine
d5mb	5,5'-dimethyl-2,2'-bipyridine
Arg	arginine
Asn	asparagine
Asp	aspartic acid
Gln	glutamine
Glu	glutamic acid
His	histidine
Lys	lysine
Phe	phenylalanine
Tyr	tyrosine
Trp	tryptophan

Acknowledgements

In chemistry theses, acknowledgement pages are usually written in a relatively uninteresting, generic form. Having written the rest of my thesis and leaving this page until the very end, like what most other students do, I now understand why. The rapid transition from scientific to ordinary, everyday writing, after having written several hundred pages in scientific format, certainly made this the most difficult page to write.

While I am the sole author of this thesis, I am definitely not the only contributor. Numerous persons have played a substantial role throughout my PhD program here at Dalhousie, as teachers, colleagues, and friends. One person, who has been all of these, is none other than my the best supervisor that I could have ever wished for, Dr. Norm Schepp. He has provided not only myself, but all of his students, with an unwavering amount of support, encouragement, dedication, and trust, in addition to playing an active role in their research and keeping their best interests in mind. With my departure as his first PhD student, may he now recover from an unrelenting steady-state flow of questions, each of which frequently exceeded lifetimes of 9×10^{11} ns.

Other Dalhousie members deserving recognition are those of my supervisory committee, Drs. Fran Cozens, Jim Pincock, and Jean Burnell, for their time, effort, interest, and guidance; of course, this includes the respective members' students, who have been willing to offer assistance on countless occasions. As well, acknowledgements are extended to Juergen Mueller, Xiao Feng, and Drs. Don Hooper and Mike Lumsden not only for their technical assistance, but also for their providing of various non-chemistry advice and discussion, including those pertaining to Nortel Networks.

It has also been a pleasure to work some of my friendly and compassionate labmates and comrades, both past and present, including Leah Breen, Matt Clay, Geniece Hallett, Amy Keirstead, Sandy Lancelot, Sherri McFarland, Wendy Monk, and Sara van Rooy, each of which were a great help in their own way. Some have also been members of my "thesis support group" and have allowed me to maintain my sanity, mostly by brightening my life by being able to talk about something else besides chemistry.

Last but not least, acknowledgements are extended to Dalhousie University, the Natural Sciences and Engineering Research Council of Canada, the I. W. Killam Memorial Trusts, the W. C. Sumner Foundation, the Canadian Foundation for Innovation, and Research Corporation for their generous financial support.

Research is what I'm doing when I don't know what I'm doing. – Wernher von Braun

Chapter One: Introduction

1.1 Introduction

Over four billion years have elapsed since the origin of life on Earth. During these years, the continual process of natural selection, guided by unpredictable climate change and natural disasters, has produced over four million different species sharing our planet. Spawning six kingdoms of life, from simple unicellular to complex multicellular organisms, they are linked by several common characteristics; for instance, the use of nucleic acids for the storage of genetic information, adenosine triphosphate for energy, nicotinamide adenine dinucleotides and flavins for electrons, and lipids for membranes.

What is more impressive is that these characteristics are further linked by one common theme, that is the dependence on chemical reactions. Not surprisingly, most of the four million species perform the same fundamental reactions required for life. These reactions do not occur spontaneously, and one reason is that spontaneous reactions can be slow. For example, the spontaneous hydrolysis of a polysaccharide has been estimated to have a half-life of about 4.7×10^6 years.¹ Rather, reactions are performed by a special class of proteins called enzymes, which are biological catalysts in that they increase the rates of chemical reactions. By having a collection of enzymes in any one organism, a balanced regulation of metabolism, and thus the process of life, is achieved.

As biological catalysts, they must satisfy the classic definition of a catalyst in that they are regenerated at the completion of a chemical reaction. How then are these

proteins able to enhance reaction rates over a quintillion-fold?¹ One mechanism by which enzymes can carry out chemical reactions with such phenomenal rate enhancements involves the stabilization of transition states, or reactive intermediates that resemble the transition state, of the rate-determining step.¹⁻³ This concept can also be taken advantage of for the development of synthetic enzymes or catalytic peptides, if methods were available for identifying those capable of stabilizing reactive intermediates. Accordingly, the work presented in this thesis relates to the development of these methods.

In particular, the work involves the design of tris(bipyridyl)ruthenium complexes with linked substrates that are specifically designed to “deliver” reactive intermediates (such as radical cations or carbocations) to remote sites, like those that may be encountered in enzyme active sites. However, the development of these complexes requires a thorough understanding of several fundamental aspects of their chemistry, including their ability to oxidize organic substrates, the effect of substituents on the bipyridyl ligands, the effect of linker size and composition on the intramolecular oxidation of linked substrates, as well as the generation of carbocations using these complexes.

The investigation of these aspects of tris(bipyridyl)ruthenium chemistry is the major focus of this thesis. To place the basic premise of the overall research project into this context, this chapter describes the fundamentals of enzymology with regards to the methods enzymes utilize to stabilize positively charged intermediates. The photochemical generation of reactive intermediates is also presented, as well as a brief introduction to the photophysics of tris(bipyridyl)ruthenium complexes.

1.2 Enzymatic stabilization of reactive intermediates

From a broad perspective, the method by which enzymes catalyze chemical reactions is similar to their classical, non-proteinaceous counterparts in that they provide alternate, faster pathways for the reactions. This principle, otherwise known as the transition state theory of enzyme catalysis,¹⁻³ was originally proposed by Linus Pauling in 1946 in a landmark report describing *molecular architecture and biological reactions*. The theory is based on the fundamental concept that enzymes have a higher affinity for the transition state than the ground state substrate. In other words, the active site of the enzyme is highly complementary to the structure of the transition state, which “fits” in the active site better than the ground state structure.

In fact, the significance of this single concept is two-fold. First, the complementary nature of the active site to the transition state allows for stabilization of the transition state, thus reducing its energy level. Second, because the ground state structure does not “fit” the active site very well, its energy level would be raised upon binding to the enzyme due to significant distortion. The net result is a reduction in activation energy, leading to catalysis. A reaction energy diagram comparing uncatalyzed and enzymatically catalyzed reactions is represented in Figure 1-1.

The theory of enzyme catalysis has indeed been reinforced by transition-state analogues in that they are excellent competitive enzyme inhibitors. In fact, transition-state analogs are frequently used as pharmaceuticals;^{4,5} e.g. antivirals⁶ and antimalarials.⁷ Furthermore, enzymes need to have a greater affinity for the transition state in order to be catalytic; if they only favoured binding of the ground state substrate, they would simply

be substrate-binding proteins as opposed to catalytic enzymes. The ability of an enzyme to have a high affinity for a transition state therefore, lies in the complementary nature of the active site. The active site would, for instance, need to have amino acid side chains that can stabilize, or neutralize, any charged groups (*e.g.* cations) present on the high-energy transition state. Enzymatic reactions may also form high-energy, reactive intermediates that are structurally similar to the transition state of the uncatalyzed route, but interactions between the active site and the transition state would lead to a significant stabilization of the reactive intermediate.

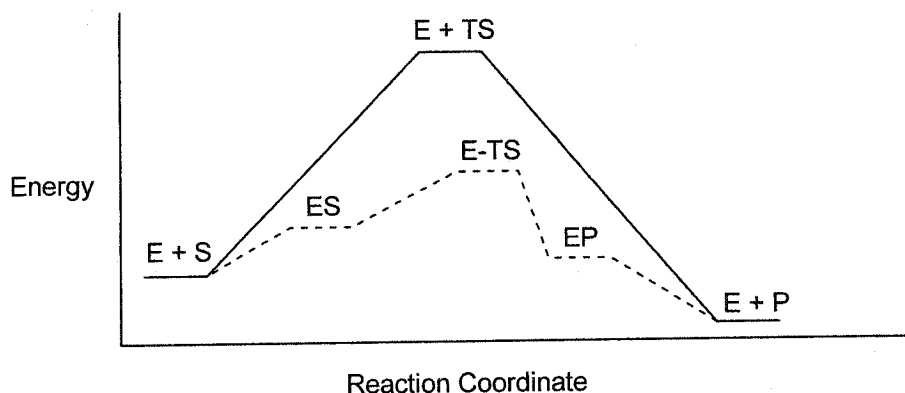


Figure 1-1. Comparison of uncatalyzed (solid line) and catalyzed (dashed line) routes for the conversion of a substrate (S) to a product (P) by an enzyme (E). TS denotes the transition state; ES, E-TS, and EP, the enzyme-bound substrate, transition state, and product, respectively.

Although Pauling's transition-state theory of catalysis at first appears to be fundamentally straightforward, the methods by which enzymes can provide faster reaction pathways, or how they stabilize reactive intermediates, has yet to be fully

understood. Since the study of reactive intermediates is essential in understanding the mechanisms of chemical reactions, including those which are enzyme-catalyzed, it only follows that the study of the behaviour of reactive intermediates in enzyme active sites is important in understanding catalysis as a whole. Three types of reactive intermediates that are frequently encountered in enzymatic catalysis are radicals, such as with coenzyme B₁₂-dependent dehydratases;⁸ radical cations, for instance with ribonucleotide reductase;⁹ and carbocations, for example with the steroid-synthesis enzymes abietadiene synthase¹⁰ and oxidosqualene cyclase.¹¹⁻¹⁴

Of particular relevance to this work is the enzymatic stabilization of carbocations. While it is well-accepted that these positively charged entities can be stabilized by negatively charged amino-acid residues (Asp and Glu) located in the active site, it was only more recently discovered that the side chains of aromatic amino acids (Phe, Tyr, and Trp) also play an important role in positive-charge stabilization.¹⁵ Consequently, this mechanism of stabilization has been termed the *π -cation interaction*. Fundamentals and a brief overview of the development of this interaction, which has yet to be fully understood, are discussed in the subsequent section.

1.2.1 π -Cation interactions

From a fundamental point of view, a π -cation interaction involves the stabilization of any positive charge, whether inorganic or organic in origin, by the electron-rich π -clouds of an aromatic moiety, as represented in Figure 1-2. However, such interactions were not initially applied to, nor accepted in, biological systems featuring reactive

intermediates. Rather, early evidence of the π -cation interaction arose from both gas-phase and solution studies involving stable, instead of reactive, cations.

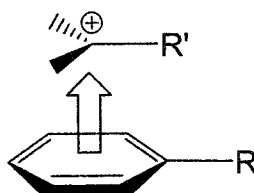


Figure 1-2. Schematic representation of a π -cation interaction.

1.2.1.1 Gas-phase studies

Gas-phase studies initially provided the groundwork required for the fundamental understanding of the π -cation interaction and its significance. In a report over two decades ago, Sunner *et al.*¹⁶ experimentally demonstrated the ability of potassium ions to bind to benzene in the gas phase, with binding energies near 80 kJ/mol. This report sparked numerous experimental and computational studies on the binding of the alkali-metal ions Li^+ , Na^+ , K^+ , and Rb^+ to various aromatic compounds, where for the most part, binding energies with benzene ranged between 60-160 kJ/mol.^{15,17} Interestingly, a trend in binding energy inversely proportional to atomic size was observed, where the binding energy of $\text{Li}^+ > \text{Na}^+ > \text{K}^+ > \text{Rb}^+$. Moreover, these energies are exceedingly high, considering that the binding of K^+ to water is estimated to be 75 kJ/mol;¹⁶ *i.e.* the π -cation effect is a significant interaction that can be stronger than the energy of solvation.

In later studies,^{18,19} Deakyne *et al.* showed that the π -cation interaction was not applicable only to alkali metals, but to polyatomic organic molecules as well. Energies

for the binding of ammonium ions NH_4^+ , CH_3NH_3^+ , and $(\text{CH}_3)_3\text{NH}^+$ to benzene were measured at 81, 79, and 39 kJ/mol, respectively. These observations were groundbreaking in that ions of similar structure are found in biology (e.g. the $\epsilon\text{-NH}_3^+$ group of Lys). However, long before π -cation interactions were even recognized, Burley *et al.*²⁰⁻²² examined the crystal structures of various proteins and noticed that cationic amino-acid residues were strategically placed near the aromatic side chains of Phe, Tyr, and Trp. Moreover, the cationic groups were typically situated perpendicular to the face of the aromatic moieties, a conformation suited to π -cation interaction. Interestingly, the relatively specific term *amino-aromatic interaction* was initially used to describe such interactions.

In order to estimate the ability of the three amino acids Phe, Tyr, and Trp to bind positively charged entities, the binding interaction between benzene, phenol, or indole with Na^+ was determined by computational studies.^{23,24} These simple aromatic compounds model the aromatic side chains of the three amino acids, respectively. Gas-phase binding energies ranged from 105-138 kJ/mol, with the trend indole > phenol > benzene. According to these model studies, it was proposed that Trp can offer the strongest π -cation interaction and hence cation-stabilizing ability, where Trp > Tyr > Phe.

Having established the trend in interaction energy between alkali metals and the three model aromatics, gas-phase studies with the model aromatics and other cations followed.²⁵ The cations of choice were NH_4^+ , CH_3NH_3^+ , and $(\text{CH}_3)_4\text{N}^+$, again ammonium-type structures commonly found in proteins. For each of the three cations, a similar trend was observed, where indole displayed the highest binding energy. As well,

if the energies between any one of the three aromatics and all three cations were compared, the general trend of interaction energy $\text{NH}_4^+ > \text{CH}_3\text{NH}_3^+ > (\text{CH}_3)_4\text{N}^+$ was observed, consistent with the atomic size trend observed with alkali metals.

1.2.1.2 Solution-phase studies

With an understanding of the π -cation interaction in the gas phase, more recent studies²⁶⁻²⁹ in aqueous and organic solutions have demonstrated that π -cation interactions are one of most important non-covalent interactions. Solution studies typically involved the binding of a cationic molecule (guest) to a synthetic, hydrophobic receptor (host). Moreover, studies in solution phase allowed the investigation of one important parameter, that being the difference between π -cation interaction and solvation energies. While gas-phase studies had indicated that the energy of the former is greater than the latter, aqueous studies were required to confirm the computational results. Logically, if the energy of the π -cation interaction were indeed greater than that of solvation, then the entry of the guests into the host molecules would be thermodynamically favourable. The results of such experiments are briefly summarized below.

Fundamental studies initially demonstrated the binding of cationic, organic guests to hydrophobic cyclophane hosts. An example of such binding is illustrated in Figure 1-3, where an adamantyltrimethylammonium ion is located in the interior of the cyclophane host.^{15,28} These hosts were chosen for their excellent solubility in water, while maintaining a hydrophobic interior comprised of aromatic rings. However, given the structure of the host, binding was not immediately attributed to the π -cation interaction.

Other interactions may have also contributed to the binding, including the hydrophobic interaction where the adamantyl moiety interacts with the non-polar regions of the host, and ion-pairing where the carboxylate groups on exterior of the host binds to the ammonium functionality. To address these issues, a systematic approach was taken using a variety of different hosts and guests to demonstrate that the binding is indeed a result of the π -cation interaction.

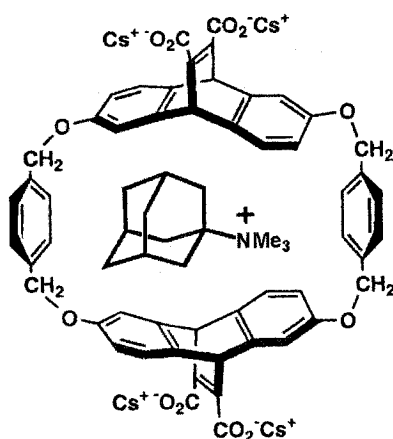


Figure 1-3. Binding of a charged organic host into a hydrophobic cyclophane host.

For instance, the two *para*-substituted phenyl rings on the cyclophane in Figure 1-3 were replaced with cyclohexane moieties.²⁷ This substitution eliminated two aromatic systems, while maintaining an overall hydrophobic interior. Such a substitution, however, resulted in a substantial reduction in the affinity of the host for cationic guests, suggesting that the presence of aromatic moieties, not the carboxylate groups, was a major contributor to guest binding. Similarly, replacement of the phenyl rings in the

cyclophane (Figure 1-3) with furan or thiophene resulted in a lowered affinity for the cationic guests, even though these heterocyclics are electron-rich;³⁰ these observations were rationalized on the basis of electrostatic potential-energy surfaces, where those with more negative surfaces, such as benzene compared to furan or thiophene, showed improved cation binding.

To address the issue of hydrophobic interactions in the guest-host systems, structurally similar naphthalene-type guests were used, with one being cationic and the other neutral.²⁷ Binding interactions in aqueous solution were determined for two similar guests, and surprisingly, binding of the hydrophobic cyclophane to the cationic guest was favoured over the neutral one. Since the cationic guest is also solvated by water molecules, these results also suggest that the energy of the π -cation interaction is indeed greater than solvation.

Interestingly, the binding of cationic guests to cyclophane hosts in organic solutions was also observed.³¹ By using organic solutions, the carboxylate groups on the cyclophane (Figure 1-3) were no longer required for solubility. Not only was the esterified derivative soluble in organic solution, there were no negatively charged groups available to assist in the cation binding. As well, since organic solutions are typically non-polar compared to water, hydrophobic interactions between the guest and the host are minimized. Thus, the binding between the two was directly attributed to the π -cation interaction, not to the carboxylate groups nor hydrophobic interactions.

Where it had been known that the cationic groups of amino acid residues in proteins are preferentially situated near aromatic side chains, later studies focussed on the

binding of cationic biological molecules, for instance acetylcholine, to cyclophane hosts. Surprisingly, it was established that cyclophane has an affinity for acetylcholine comparable to that found in natural acetylcholine receptors.³² Indeed, the crystal structure of acetylcholinesterase revealed several aromatic amino acids in the active site,³³ where the π -cation interaction is thought to assist in acetylcholine binding.^{34,35}

1.2.1.3 π -Cation interactions in biological systems

Long before π -cation interactions were even recognized, an examination of an assortment of protein x-ray structures revealed the close placement of side chain amino groups to aromatic residues.²⁰⁻²² Cationic residues of Arg, Asn, Gln, His, and Lys were typically within van der Waals contact with one or more aromatic rings of Phe, Tyr, and Trp. Of these three amino acids, Trp and Tyr were the most common residues interacting with positively charged amino groups, consistent with gas-phase studies indicating that Phe affords the weakest π -cation, as previously mentioned.

Once the π -cation interactions were recognized in biological systems, many key experiments were performed to evaluate its importance. For example, one study³⁶ evaluated the effect of the π -cation interaction on the pK_a of protonated His (HisH^+) in the enzyme ribonuclease. Normally, the HisH^+ is stabilized by a nearby Trp residue. When Trp was mutated to Tyr, the pK_a of the HisH^+ decreased, while the replacement of Trp with Phe resulted in even more dramatic pK_a decreases. These decreases in pK_a are attributed to changes in the degree of stabilization provided and are in line with the trend

Trp > Tyr > Phe. Similar effects have also been observed in peptides, where NMR studies showed that when Lys residues interacted with Phe, their pK_a values were altered.³⁷

The importance of the π -cation interaction was also noticed when structural changes to a protein were observed when pH changes affected a helix featuring a Phe-His interaction.³⁸ High pH values resulted in His deprotonation and a loss of a crucial interaction that maintained helical structure. This groundbreaking study has led to more recent work illustrating the significance of the π -cation interaction in the maintenance of biological structures, particularly in proteins³⁹⁻⁴² and protein-DNA complexes.⁴³⁻⁴⁵

More recently, the interaction energy between positively charged Arg and the aromatic amino acid Trp in a solvent-exposed model peptide was investigated.⁴² Here, it was found that the *net* stabilization of the positive charge by Trp is in the order of 1.7 kJ/mol, *relative* to the energy of solvation. These results agree with the previously mentioned suggestions that the energy of the π -cation interaction is greater than the energy of solvation.

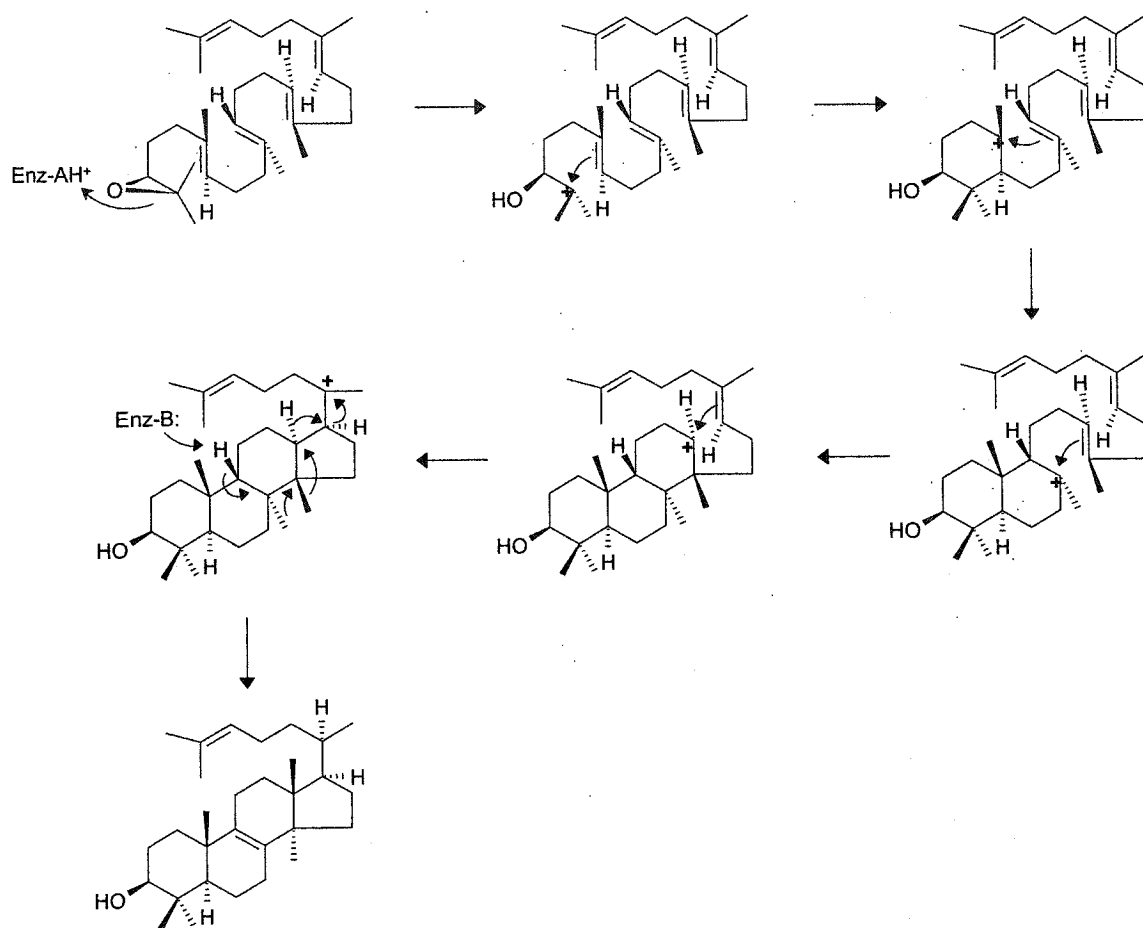
These fundamental studies have led to vast research on π -cation interactions in biological systems. The interaction has been found in acetylcholine receptors, acetylcholine esterase, potassium-ion channels, oxidosqualene cyclase, *S*-adenosyl-methionine-dependent methyl transferases, and many others.¹⁵ Some metalloproteins also use the interaction to bind metal ligands.⁴⁶ From a broad perspective, the π -cation interaction is significant in three biological disciplines: structure, ligand-recognition, and as it pertains to this study, catalysis. The information available on the interaction is now enormous, and it has even found applications in organic synthesis.^{47,48}

1.2.1.3.1 Oxidosqualene cyclase

Of interest to us is oxidosqualene cyclase, an enzyme in the pathway of steroid biosynthesis, as it demonstrates the stabilization of cationic reactive intermediates by aromatic amino acids. The biosynthesis of steroids is a complicated pathway that involves the formation of C_{30} molecules from C_5 isoprene units.⁴⁹ A key reaction in the biosynthetic pathway is the formation of the characteristic tetracyclic structure, a reaction catalyzed by oxidosqualene cyclase. Impressively, this single enzyme orchestrates the cyclization of (3*S*)-2,3-oxidosqualene in a process involving the formation of six carbon-carbon bonds and seven chiral centres (Scheme 1-1).

Amazingly, the substrate oxidosqualene is a stable compound that resists decomposition in glacial acetic acid for over a day.⁵⁰ Yet, the initial opening of the epoxide ring is enzymatically catalyzed by a single Asp residue (Scheme 1-1), leading to the formation of a carbocation. A rapid series of ring closures follows to form a tetracyclic structure in a chair-boat-chair-boat conformation, known as the prosterol cation. Several controlled hydride and methyl shifts on the prosterol cation generates the final product, lanosterol.

Five carbon-centered cationic intermediates may be generated in the reaction pathway. For the reaction to occur with any efficiency, stabilization of the cationic intermediates is critical. In an initial proposal by Johnson *et al.*,⁵¹ it was suggested that the anionic side chains of Asp and Glu performed this task. However, such carboxylate side chains are nucleophilic and may attack the carbocation. Clearly then, anionic side chains would not be suitable, suggesting the presence of another stabilization mechanism.



Scheme 1-1. Proposed literature mechanism of oxidosqualene cyclase. A general base situated on the enzyme is denoted Enz-B, while a general acid is denoted Enz-AH⁺.

When the DNA sequences of bacterial, plant, yeast, and rat oxidosqualene-cyclase genes along with their predicted protein sequences were revealed, it was noticed that the four cyclases contained abnormally high levels of Tyr and Trp.⁵²⁻⁵⁴ In particular, all four predicted structures feature β -strand turn motifs rich in conserved aromatic residues;

these were subsequently named QW motifs. Six repeats of the QW motif were found in the cyclases of the organisms studied, except for seven in the bacteria.

Each QW motif consists of sixteen amino acids with a consensus sequence of Arg/Lys – Gly/Ala – X₂₋₃ – Tyr/Phe/Trp – Leu – X₃ – Gly – X₂₋₅ – Gly – X – Trp, where X denotes the presence of any amino acid. These hydrophobic motifs contain Phe, Tyr, and Trp, the three aromatic amino acids implicated in the stabilization of the intermediate carbocations *via* π -cation interactions. The presence of multiple motifs is rationalized by the presence of several different cationic intermediates generated during the cyclization (Scheme 1-1). Consequently, it was proposed that the aromatic residues stabilize the cationic intermediates *via* the π -cation interaction thus allowing for full control of the regio- and stereochemistry associated with the enzymatic reaction.^{50,55}

The medical-chemistry community has also appreciated the importance of the π -cation interaction in catalysis. Stable, cationic molecules resembling the intermediates found in the oxidosqualene cyclization process (*i.e.* transition-state analogs) have been identified as antimicrobial agents.⁵⁶ These have been shown to be potent inhibitors of oxidosqualene cyclase and show promise as antifungals⁵⁷ and antiprotozoans.^{58,59}

1.3 Studying and generating reactive intermediates in biology

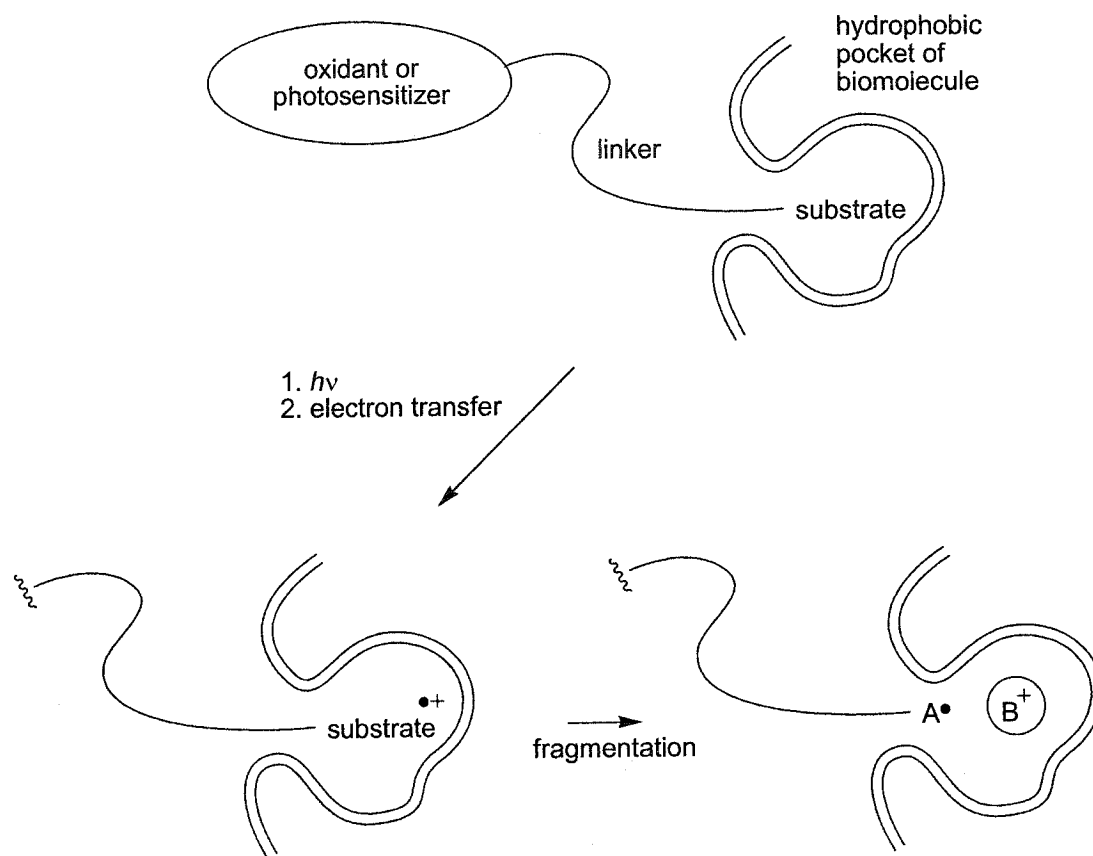
The importance of the π -cation interaction cannot be overemphasized, given the vast amount of multidisciplinary literature illustrating its significance. While energetics data are available concerning the stabilization of non-reactive, cationic entities (*e.g.* side chains of basic amino acids) by the π -cation interaction, no work on the effect of the π -

cation interaction on short-lived, reactive intermediates was found in the literature. For instance, oxidosqualene cyclase provides ample evidence for the stabilization of reactive intermediates by the interaction, but no physical measurements of stability (*e.g.* lifetime enhancements of the reactive intermediates). It is plausible that this deficiency in the literature may be associated with some of the technical challenges involved in the measurement of reactive-intermediate stability, such as that of a carbocation, located in a hydrophobic site, as explained below; proposed methods of overcoming these challenges are also presented.

First of all, it is currently not possible to study the behaviour of an enzyme-bound reactive intermediate that is formed during the progress of an enzymatic reaction. The rapid conversion of the reactive intermediate to another entity forbids “snapshots” of the enzyme-intermediate complex to be spectroscopically obtained. As well, individual enzyme molecules are not necessarily at the same stage of a reaction at any given time, and it is not possible to halt the progress of an enzymatic reaction at a predefined reaction intermediate. Yet, a possible solution to studying the stabilizing effects of the π -cation interaction may be to use synthetic peptides that mimic the hydrophobic sites of the corresponding enzymes. Such peptides would be carbocation-stabilizing peptides rather than being catalytic; the reactive intermediates would therefore not be converted to another entity. The main advantage of this synthetic-peptide strategy lies in the ability to alter the properties of the peptide by making changes to the amino acid sequence; changes to carbocation lifetime due to changes in peptide sequence may provide information on the π -cation interaction.

Another technical challenge lies in the ability to introduce a short-lived, reactive carbocation into a hydrophobic site within the lifetime of the carbocation. While π -cation interactions may favour binding of the carbocation to the site, there is no guarantee that the carbocation will rapidly enter the site over a time frame that is substantially faster than its lifetime. In addition, there is little certainty that the carbocation would even enter the hydrophobic site at all, as the charged intermediate may favour the ionizing, aqueous solvent environment over that of the hydrophobic site. Therefore, a solution for these possible problems may be the *in situ* generation of the reactive intermediate from a hydrophobic, precursor substrate directly within the hydrophobic site, where the hydrophobic nature of both the site and precursor should favour binding of the two. The bound, model precursor can then be converted to its carbocation, as illustrated in Scheme 1-2.

Given the biological significance of enzyme catalysis, it is essential that we thoroughly understand the methods by which enzymes stabilize reactive intermediates. It is well accepted that the study of reactive intermediates is crucial to the overall understanding of chemical reactions, and hence, it is important to understand the catalytic role of the π -cation interaction. Therefore, one of the long-term goals of this ongoing project is to design synthetic peptides capable of stabilizing reactive carbocations so that it is possible to model the reactive intermediate-active site interactions found in natural enzymes.



Scheme 1-2. A proposed method for the introduction of reactive carbocations into remote, hydrophobic sites. The intramolecular oxidation of a substrate to its radical cation induces fragmentation into radical (A) and cation (B) components.

An essential prerequisite to the design of cation-stabilizing peptides is the development of a method that could be used to “deliver” reactive carbocations, originating from a hydrophobic precursor “substrate” already bound to the peptide, in a controlled manner. The experimental technique of choice is nanosecond laser-flash photolysis,⁶⁰ which allows for the rapid generation, observation, and kinetic characterization of short-lived reactive intermediates (e.g. radical cations and

carbocations). In this technique, a short, high-energy laser pulse of ~10 ns either directly or indirectly converts the precursor to a reasonably high concentration of reactive intermediate, which may undergo further reactions. For this technique to be successfully used, the laser-flash photolysis sample must absorb light at the laser wavelength, and the species that absorbs the light needs to undergo a photochemical reaction.

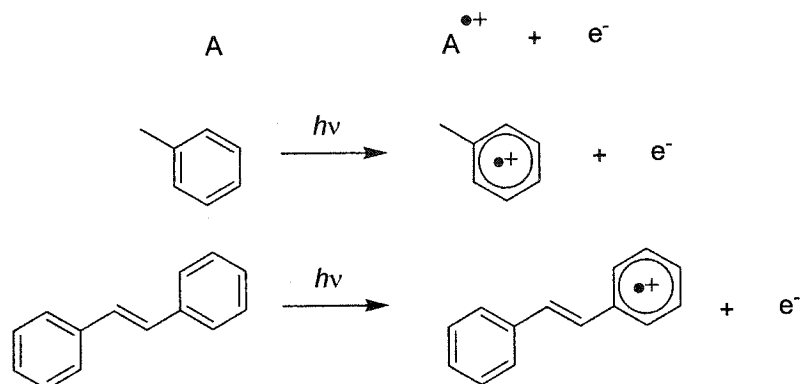
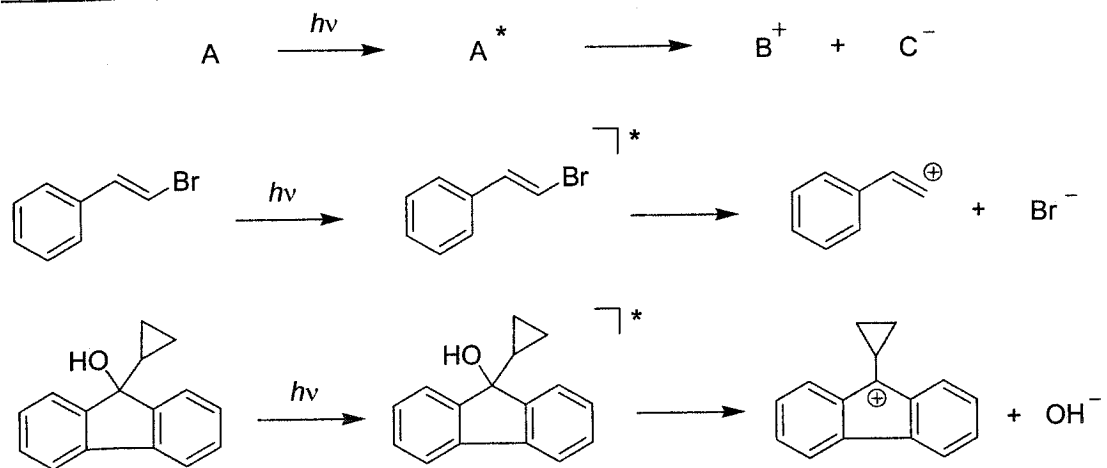
The conversion of a precursor to its radical cation or carbocation is an oxidative procedure that can be accomplished by laser-flash photolysis in a single step or a series of steps triggered by the absorption of light. Two common methods by which laser-flash photolysis can be used for the generation of reactive intermediates are direct irradiation and photosensitization, which are described in greater detail in the following subsections.

1.3.1 Direct irradiation

As the name suggests, direct irradiation involves the absorption of laser light directly by the organic, reactive-intermediate precursor (substrate). This absorption can induce two processes relevant to reactive-intermediate formation, namely photoionization and photoheterolysis. In the former, absorption of light (typically two photons) induces the removal of an electron from the precursor molecule (*i.e.* oxidation) and results in the formation of a radical cation; the resulting radical cation can undergo further reactions, such as fragmentation, though these reactions are not the direct consequence of light absorption.⁶¹ In photoheterolysis, the absorption of light forms an excited precursor that subsequently fragments into cationic and anionic components (Scheme 1-3).

Both direct-irradiation processes have been used extensively for making reactive intermediates, as the simplicity and convenience of direct irradiation cannot be surpassed. Selected recent examples of photoionization are the formation of the radical cations of methylbenzene⁶² and *trans*-stilbene,⁶³ while photoheterolysis has been used to produce styrenyl⁶⁴ and 9-cyclopropyl-9-fluorenyl⁶⁵ carbocations; these are shown in Scheme 1-3.

For any direct irradiation process to be feasible, notwithstanding the structural and chemical requirements for photoheterolysis, it is obvious that the precursor must absorb light at the laser-irradiation wavelength. While at first this may not appear to be an issue since a variety of lasers with different wavelengths are commercially available, there is an inherent problem that undermines the use of direct irradiation in biological studies. The generation of reactive intermediates that are organic in nature no doubt requires the use of organic precursors, and this poses a problem in that most organic compounds absorb in the UV region. Biomolecular structures, such as the side chains of amino acids Phe, Tyr, and Trp are also aromatic in nature and absorb UV light, with Trp contributing to the majority of UV absorption by proteins at 280 nm.⁶⁶ Thus, it is clear that there may be a biocompatibility issue when UV-absorbing precursors are irradiated in the presence of biomolecules, since there is a lack of irradiation selectivity.

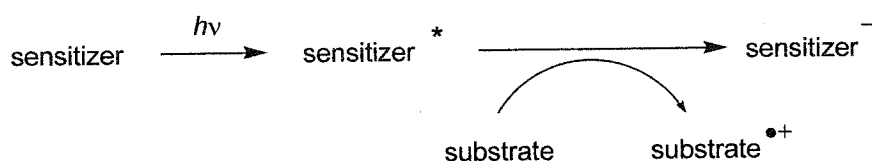
PhotoionizationPhotoheterolysis

Scheme 1-3. Comparison between photoionization and photoheterolysis reactions induced by direct irradiation.

1.3.2 Photosensitization

While direct irradiation relies on the action of light on the precursor molecule, the method of photosensitization is fundamentally different in that it requires the use of a *photosensitizer* (sensitizer), an additional component added to laser-flash photolysis samples to promote *photoinduced electron transfer*.⁶⁰ In this case, a laser-irradiation

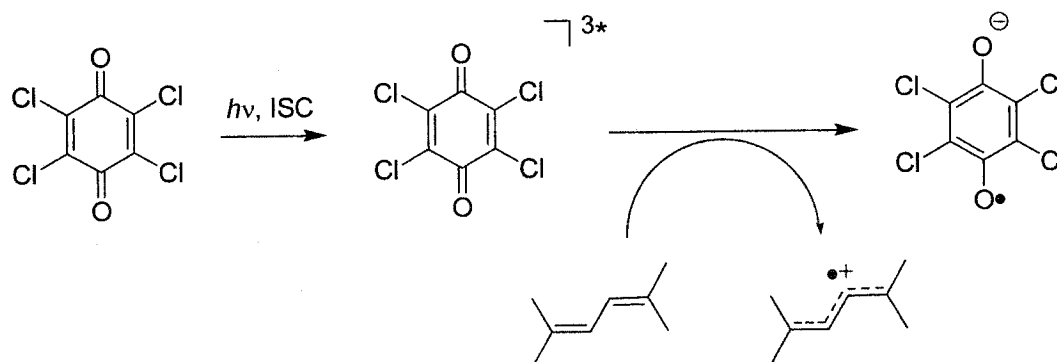
wavelength is chosen to excite only the photosensitizer. Excitation results in changes to the reduction potentials of the photosensitizer, rendering it a better oxidant or reductant than its corresponding ground state. In the case of an oxidant, the excited photosensitizer can accept an electron from a substrate, resulting in a substrate radical cation. The process of photosensitization is illustrated in Scheme 1-4.



Scheme 1-4. Generation of reactive intermediates by photoinduced electron transfer.

One of the main advantages of photosensitization is the predictability and selectivity of electron transfer between the excited photosensitizer and the substrate, since electron transfers are dependent on the differences between the half-cell reduction potentials of the components involved (ΔE).⁶⁰ In other words, the secondary generation of the substrate radical cation is merely an electrochemical process that is activated by light. Like any electrochemical process, an electron transfer that requires the input of energy is usually less favourable than one that is exogonic (positive ΔE , or negative Gibb's free energy ΔG°); theory linking the thermodynamics and kinetics of electron transfer is discussed in the second chapter. Thus, if a photosensitizer were irradiated in the presence of two substrates, one of which leads to a thermodynamically favourable electron transfer and the other unfavourable, only the former is usually oxidized.

Photosensitizers can be divided into two chemical classes, organic and transition-metal. One common organic photosensitizer is chloranil, which becomes an oxidant after excitation and intersystem crossing to the triplet state.⁶⁷ For instance, it has been used for the generation of radical cations of conjugated alkenes,⁶⁷ as shown in Scheme 1-5. In this example, a solution of chloranil was excited at 355 nm (blue light), a wavelength that is typically not absorbed by proteins.⁶⁶ However, the wavelength biocompatibility of chloranil is offset by its poor solubility in water.



Scheme 1-5. Chloranil-sensitized oxidation of conjugated alkenes.

On the other hand, photosensitizers based on transition-metal complexes are usually soluble in water due to their ionic nature and presence as salts. Moreover, as transition-metal complexes, they are usually coloured and absorb light in the visible region (400-700 nm), far above the absorption of biomolecules. Clearly then, the water-soluble nature and absorption properties of these photosensitizers favour their use in

aqueous or biological investigations. One common transition-metal photosensitizer is that based on tris(2,2'-bipyridine)ruthenium dichloride, $\text{Ru}(\text{bpy})_3$.

1.4 Tris(bipyridyl)ruthenium photosensitizers

Tris(bipyridyl)ruthenium photosensitizers are metal-organic dyads, or complexes, that have been the subject of intense research over the last several decades. Being stable, water-soluble, and relatively easy to prepare, they have found a host of applications ranging from charge injection in solar-energy harvesting^{68,69} to studies of charge transport in proteins^{70,71} and DNA.⁷² Most of all, their utility is attributed to their unique photophysical and photochemical properties, some of which are outlined in this section.

Each complex features three, bidentate 2,2-bipyridyl ligands (LL) coordinated to a Ru^{2+} centre in an octahedral geometry (Figure 1-4).^{73,74} Coordination between the metal and ligands is achieved by a mixing of the metal-centre d orbitals and the π and π^* orbitals of the ligand, as well as the lone electron pairs on the nitrogen atoms. Should the three ligands be identical, resulting in a complex of the form $\text{Ru}(\text{LL})_3$, the complex is termed *homoleptic* and corresponds to the D_3 -symmetry point group. However, if a complex contains non-identical ligands, *e.g.* $\text{Ru}(\text{LL})_2(\text{LL}')$, it is termed *heteroleptic* and does not have D_3 symmetry (Figure 1-4).

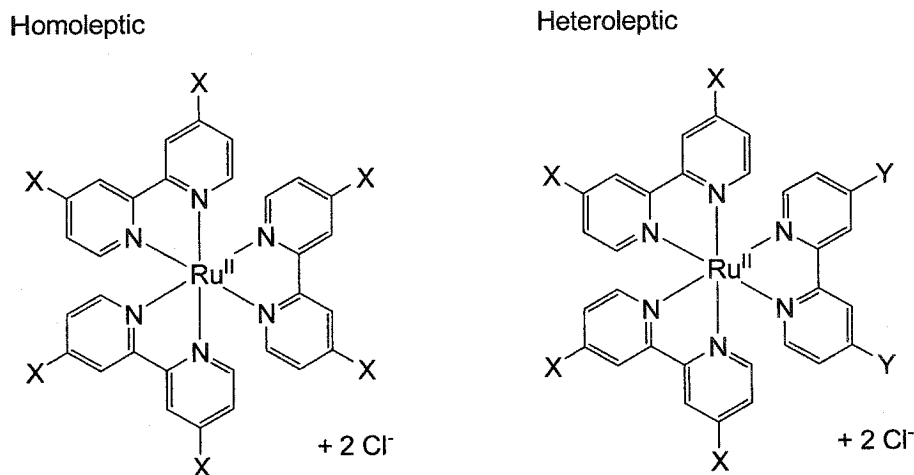


Figure 1-4. Examples tris(bipyridyl)ruthenium complexes in their homoleptic and heteroleptic forms. Substituents are denoted by X and Y, where $X \neq Y$.

Since a complex is comprised of Ru^{2+} and three bipyridyl ligands, it has two net positive charges; *i.e.* an Ru(II) oxidation state on the metal. Thus, the complexes are typically isolated and used in the presence of two chloride or hexafluorophosphate counterions. However, the light absorption properties of these complexes stem from the positively charged photosensitizer core,⁷³ commonly abbreviated as $[\text{Ru}(\text{LL})_3]^{2+}$. In this thesis, all tris(bipyridyl) complexes were isolated as dichloride salts and are simply referred to in the form of $\text{Ru}(\text{LL})_3$ or $\text{Ru}(\text{LL})_2(\text{LL}')$, *e.g.* $\text{Ru}(\text{bpy})_3$ or $\text{Ru}(\text{bpy})_2(\text{dmb})$, where the presence of dichlorides and the Ru(II) oxidation state are implied.

Of significant relevance are the light-absorption properties of these transition-metal complexes. As orange-coloured complexes, they absorb light in the visible range with a characteristic maximum near 450 nm for $\text{Ru}(\text{bpy})_3$, as seen in the ground-state absorption spectrum shown in Figure 1-5 (a). Depending on the wavelength of excitation,

three different excited states have been proposed,⁷³ as seen in Figure 1-5 (b). The lowest-energy excited state corresponds to a metal-to-ligand charge transfer (MLCT), which involves the promotion of an electron from a metal-centered molecular orbital (π_M) that has primarily d character to an empty one on the ligand that has mostly π character (π^*_L). The MLCT transition is best described as a transfer of an electron from the metal centre to the ligand, resulting in a complex resembling a Ru(III) metal centre and a radical anion localized on one of the ligands; *i.e.* MLCT excitation of $[\text{Ru}^{\text{II}}(\text{LL})_3]^{2+}$ leads the formation of $[\text{Ru}^{\text{III}}(\text{LL}^-)(\text{LL})_2]^{2+}$. Since the overall charge of the MLCT state remains the same, this state is simply referred to as the Ru(II)* excited state in the context of this thesis.

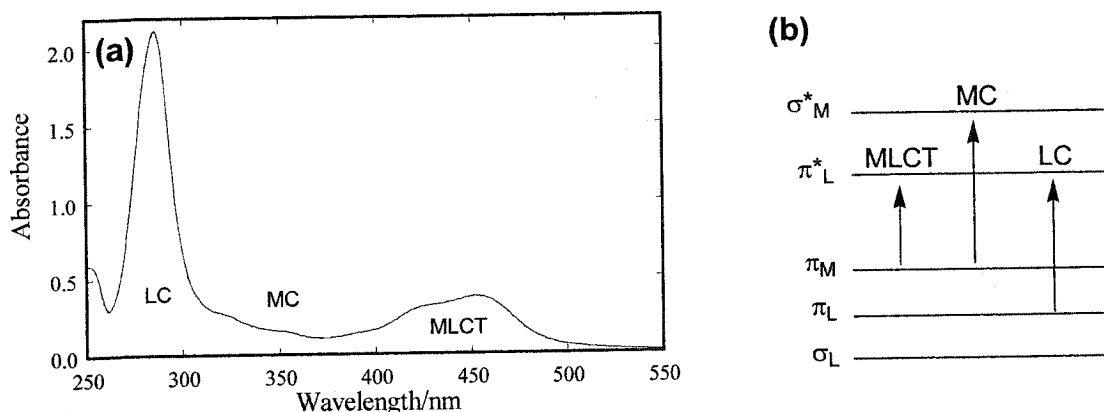


Figure 1-5. (a) Ground-state absorption spectrum of $\text{Ru}(\text{bpy})_3$ acquired in water and (b) a schematic molecular-orbital representation of the MLCT (metal-to-ligand charge transfer), MC (metal-centered), and LC (ligand-centered) transitions.

At moderate excitation energies, Figure 1-5 (a), metal-centered (MC) transitions are also possible. Like the MLCT, this transition involves the promotion of an electron

from the same metal-centered molecular orbital (π_M) that has primarily d character, but instead of promotion to the ligand, it is promoted to another metal-centered molecular orbital (σ^*_M) that also has d character. Thus, the MC state can be described as a $d-d$ transition, which is considered to be symmetry-forbidden for D_3 complexes according to Laporte's rule. These transitions are therefore rather weak, as seen in Figure 1-5 (a), and are assumed to be negligible relative to the MLCT and LC absorptions.

At lower excitation wavelengths (higher energy) in the UV region, ligand-centered (LC) transitions have been proposed. As the name suggests, these involve the promotion of an electron from a π orbital on the ligand (π_L) to another that is also situated on the ligand (π^*_L). The LC transition is therefore analogous to the excitation of a standard organic compound by UV light.

Since upper excited states formed from high-energy excitation rapidly decay (< 1 ns) to the lowest-energy MLCT state,⁷⁵ it is the MLCT state that is responsible for the useful properties of tris(bipyridyl)ruthenium complexes. The lowest-energy MLCT state is in fact a triplet ($^3\text{MLCT}$) derived from the intersystem crossing and thermalization (vibrational cooling) of the non-thermalized (vibrationally hot) singlet ($^1\text{MLCT}$) initially formed upon excitation. The time frame for this process has been estimated at approximately 1 ps.⁷⁶ Thus, in ns laser-flash photolysis studies, where the width of the laser pulse is about 10 ns, it is assumed that after the excitation pulse, only the lowest-energy $^3\text{MLCT}$ state is present. This long-lived state (ca. 500 ns) is herein referred to as Ru(II)^* , and is the basis of chemical reactions involving these complexes.⁷³

Ru(II)^* excited states are also interesting in that they are both luminescent and absorbent, with emission and absorption maxima near 620 nm and 370 nm, respectively, for Ru(bpy)_3 .⁷³ A typical transient absorption spectrum acquired following the ns laser-flash irradiation of Ru(bpy)_3 is shown in Figure 1-6. In addition to the absorption at 370 nm and the emission at 620 nm (observed in the form of negative absorption), there is a negative band centered near 450 nm; this signal corresponds to the bleaching of the initial Ru(II) ground state and, not surprisingly, appears like a mirror image of the MLCT ground-state absorption shown in Figure 1-5 (a). With time, all three bands recover to baseline with kinetics corresponding to the lifetime of Ru(II)^* . Thus, three measurement wavelengths can possibly be used to monitor kinetic processes that may affect the lifetime of Ru(II)^* .

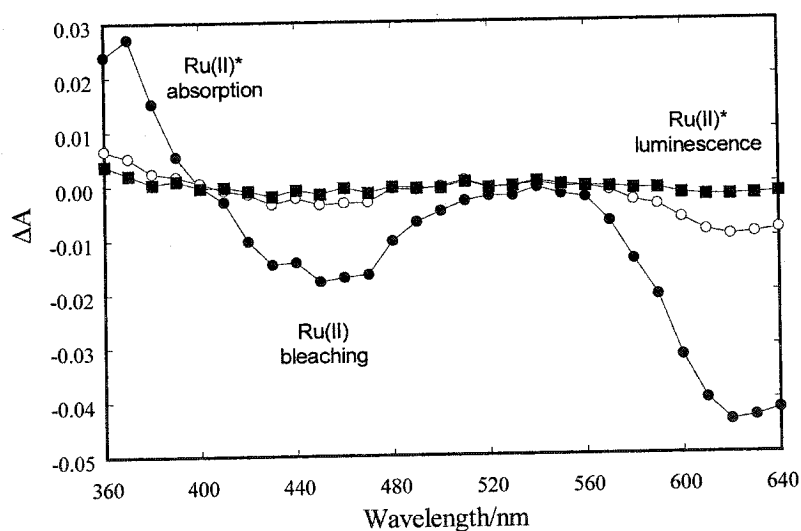
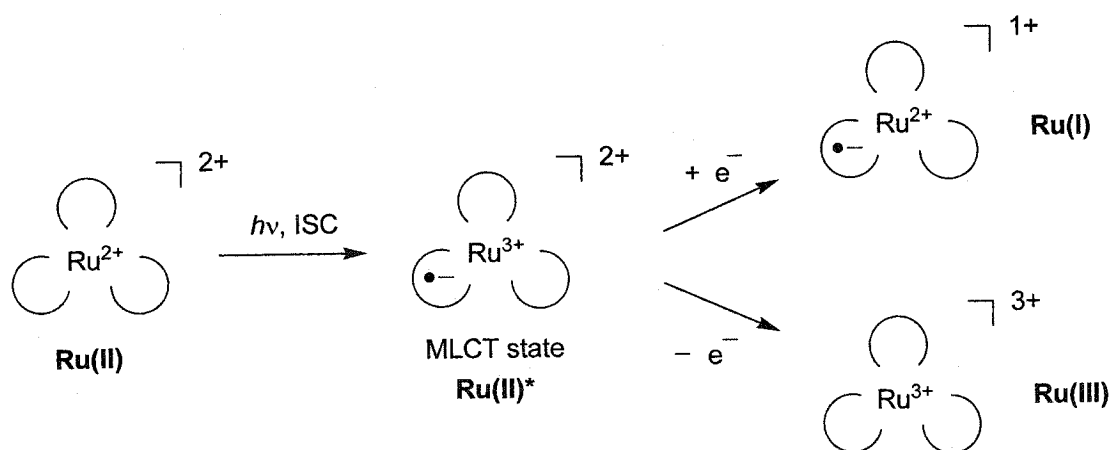


Figure 1-6. Transient absorption spectra obtained (●) 0.024 μs , (○) 0.72 μs , and (■) 1.2 μs following 355-nm laser irradiation of Ru(bpy)_3 in water.

1.4.1 Amphoteric nature of the $^3\text{MLCT}$ state

Besides their luminescent and absorbent behaviour, perhaps the most valuable property of Ru(II)^* excited states ($^3\text{MLCT}$) is their amphoteric nature, in that they are both more easily oxidized and reduced than the initial, stable Ru(II) ground states; *i.e.* the $^3\text{MLCT}$ is suitable for photoinduced electron transfer.⁷³ As shown in Scheme 1-6, reduction takes place at the Ru(III) metal centre, leading to the formation of a complex with a Ru(II) centre and a radical anion localized on one of the ligands. Since the resulting complex has a single net positive charge, it is of the form $[\text{Ru}^{\text{II}}(\text{LL}^-)(\text{LL})_2]^{1+}$ and is herein referred to as Ru(I) for simplicity. On the other hand, oxidation of the $^3\text{MLCT}$ state removes the ligand-localized radical anion, leaving the Ru(III) metal centre; the complex now has three net positive charges and is simply referred to as Ru(III) .



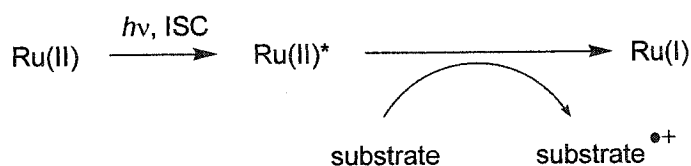
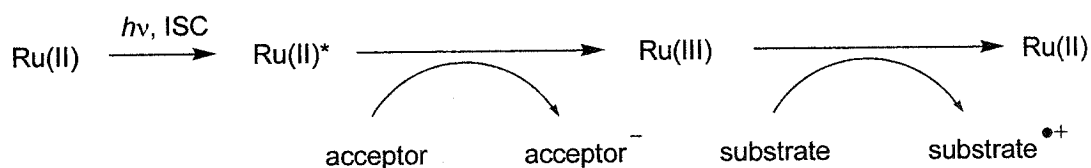
Scheme 1-6. Amphoteric nature of tris(bipyridyl)ruthenium $^3\text{MLCT}$ states. Bipyridyl ligands are schematically represented as loops.

The amphoteric nature of Ru(II)^* excited states infers that Ru(II)^* can be used as an oxidizing or a reducing agent. Relevant reduction potentials for Ru(bpy)_3 are summarized in Table 1-1. If Ru(II)^* is used as an oxidizing agent, such as for the oxidation of a substrate to its radical cation, Ru(I) is formed. Regrettably, Ru(I) is also a powerful reducing agent that may undergo charge-recombination with the radical cation to regenerate starting materials. However, this problem can be circumvented by using Ru(II)^* as a reducing agent and oxidizing it with a *sacrificial electron acceptor* to generate the Ru(III) state. This Ru(III) state can then be used to oxidize the substrate to its radical cation, regenerating the initial Ru(II) state. Moreover, Ru(III) is preferential in that it is a stronger oxidant than Ru(II)^* . These two routes of electron transfer involving Ru(I) and Ru(III) are represented in Scheme 1-7, and are respectively referred to in the thesis as the routes of *initial Ru(II)^* reduction* and *initial Ru(II)^* oxidation*.

Table 1-1. Reduction potentials (V) for Ru(bpy)_3 relative to SCE.

Compound	III/II	II/I	II*/I	III/II*
Ru(bpy)_3	+1.27	-1.31	+0.83	-0.87

Potentials obtained from literature data.⁷¹

Initial Ru(II)* reductionInitial Ru(II)* oxidation

Scheme 1-7. Two possible routes of radical-cation generation by tris(bipyridyl)ruthenium complexes.

1.5 Biological applications of tris(bipyridyl)ruthenium complexes

While Scheme 1-7 depicts substrate oxidation by a tris(bipyridyl)ruthenium complex via intermolecular electron transfer, it is also possible to link the photosensitizer and the substrate together, allowing for intramolecular electron transfer. In this case, the photosensitizer and the substrate are attached by means of a linker, such that electron transfer occurs within the substrate-linked complex. The advantages of a linked substrate are numerous: the effective concentration of the substrate is increased relative to the unlinked form; electron transfer can occur *via* the linker, and a collision between the substrate and sensitizer is not needed; and most of all, a linker allows for electron transfer between the sensitizer and a deeply buried substrate, as in an active site. Moreover, with a linked complex, the water-soluble photosensitizer core can pull a hydrophobic, linked

substrate into solution; this strategy therefore allows the introduction of hydrophobic substrates into a biocompatible, aqueous environment.

Due to the highly biocompatible nature of transition-metal photosensitizers, including $\text{Ru}(\text{bpy})_3$ and its derivatives, they have been used extensively in two relatively modern fields of biochemistry: the study of electron transfer in proteins,⁷⁰ including the oxidation of metalloproteins^{71,77} and the migration of charge in DNA.⁷² In virtually all these cases, electron transfers between the photosensitizer and the biomolecule are intramolecular. With proteins for instance, the photosensitizer has been directly linked to the protein by means of an amino acid side chain, or attached to an unreactive moiety with a high affinity for an enzyme active site. In all these cases, the function of the photosensitizer is to oxidize the biomolecule itself.

Of particular interest is the latter method of Wilker *et al.*,⁷⁷ where an unreactive substrate linked to a tris(bipyridyl)ruthenium photosensitizer is used to “deliver” holes to a metalloprotein. Laser-flash irradiation of the photosensitizer to $\text{Ru}(\text{II})^*$ leads to its conversion to $\text{Ru}(\text{III})$ by an electron acceptor, and the $\text{Ru}(\text{III})$ complex subsequently oxidizes the protein to regenerate the initial $\text{Ru}(\text{II})$ state. The net result is an oxidized state of the protein.

The same principles used in the above example could equally be applied to the generation of reactive intermediates within a hydrophobic site by means of a linked photosensitizer. In this respect, a substrate-linked complex can be used to “deliver” carbocations; as shown in Scheme 1-2, a linked-substrate is oxidized to its radical cation, which can undergo subsequent fragmentation and generate a radical and a carbocation

pair; the photosensitizer is used to oxidize the substrate, *not* the biomolecule itself. Since the hydrophobic precursor is initially bound to the hydrophobic site, it is presumed that carbocation generation would also occur at the same location. This photochemical generation of carbocation is analogous to the enzyme-catalyzed generation of a positively charged intermediate within an active site.

1.6 Scope of thesis

Despite the broad use of tris(bipyridyl)ruthenium complexes in the biochemistry sector, reports on their application for the generation of reactive intermediates, from a physical-organic chemistry point of view, are relatively scarce in the literature. Therefore, the theme of this thesis lies in the biocompatible generation of reactive intermediates, particularly radical cations and carbocations, *via* the oxidation of precursor substrates by tris(4,4'-disubstituted-2,2'-bipyridine)ruthenium photosensitizers in aqueous solutions. While the study concludes in the development of a method that could possibly be used to deliver reactive carbocations to hydrophobic sites, fundamental groundwork was necessary to understand the properties of ruthenium complexes as substrate oxidants. All studies involved the excitation of the normally Ru(II) photosensitizer to its Ru(II)* state using nanosecond laser-flash photolysis, and the transients formed were monitored in real-time by absorption or emission UV-visible spectrophotometry.

The second chapter begins by investigating the effect of ligand 4,4'-disubstitution on the ability of Ru(II)* states to oxidize intermolecularly a variety of organic substrates to their respective radical cations. Ligand substituents ranged from electron-donating

methoxy to electron-withdrawing trifluoromethyl groups, in both homoleptic and heteroleptic configurations. Later on, the conversion of Ru(II)* to Ru(III) by an electron acceptor was evaluated, and the ability of the resulting Ru(III) states to oxidize *intermolecularly* the organic substrates was assessed. Second-order rate constants for both the oxidation of Ru(II)* to Ru(III) by the acceptor, and the oxidation of substrates by Ru(III), were determined. This chapter is, in essence, a determination of the types of organic substrates that could be oxidized by Ru(III) states of complexes containing 4,4'-disubstituted ligands, and, as a corollary, a determination of the type of complex required to oxidize a particular substrate.

Unlike the broad nature of the second chapter, the third chapter concentrates on the oxidation of one basic substrate, *N,N*-dimethyl-*p*-toluidine (DMT), to its radical cation. While some concepts explored in the first chapter are revisited here, this chapter specifically investigates the *intramolecular* oxidation of a DMT moiety that is covalently attached to ruthenium photosensitizers by means of flexible linkers. Substrate oxidation was observed by both Ru(II)* and Ru(III) states. The effect of ligand 4,4'-disubstitution, linker, and pH on the mechanism (initial Ru(II)* reduction or oxidation), rate, and efficiency of DMT oxidation are investigated herein. The unconventional use of a sacrificial electron acceptor as a Ru(I)-trapping agent is also reported in this chapter.

Studies on substrate oxidation culminate in the fourth chapter, which investigates the intramolecular oxidation of sterically hindered, diphenylalkane precursors to their respective radical cations by Ru(II)* and Ru(III). Moreover, the ability of these radical cations to undergo fragmentation reactions, forming distinct radical and carbocation

components, is evaluated. This chapter therefore investigates a rapid method of generating free, unlinked carbocations from a series of hydrophobic substrates in aqueous solution; this method could possibly be used to study of the behaviour of reactive carbocations in the presence of biomolecule stabilization.

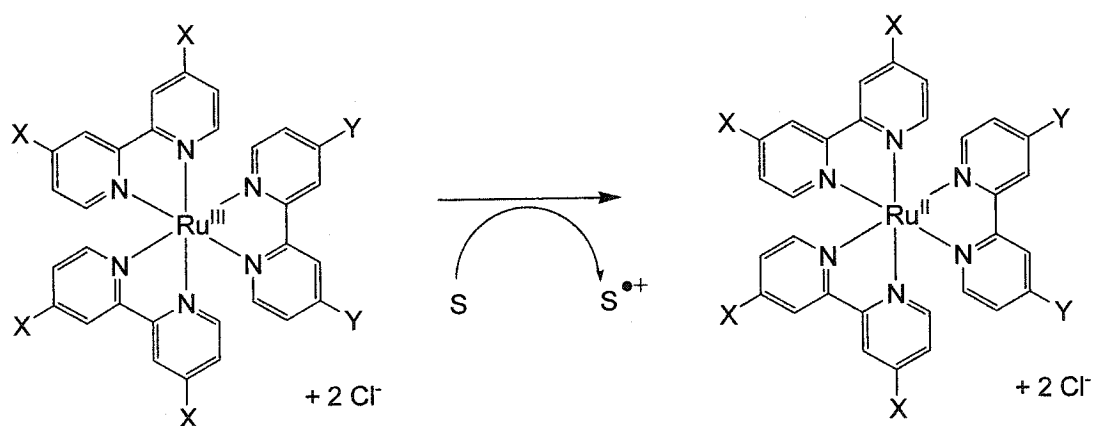
The fifth chapter deviates from the overall theme of the thesis, the use of tris(bipyridyl)ruthenium for reactive-intermediate generation, and offers a preliminary insight on the ultrafast picosecond dynamics of Ru(II)* excited states. Herein, the effects of high-energy excitation and ligand 4,4'-disubstitution on the non-thermalized emission of MLCT states are evaluated by femtosecond laser-flash photolysis. The singlet-or-triplet origins of such emissions are examined and compared to those found in the literature at low-energy excitation.

An extensive amount of time and effort were also invested in the synthesis of tris(bipyridyl)ruthenium complexes, including those featuring intramolecularly linked substrates. Their preparation and characterization, as well as the fundamentals of, and experimental procedures used for, laser-flash photolysis, are detailed in the final chapter.

Chapter Two: Intermolecular Substrate Oxidation

2.1 Introduction

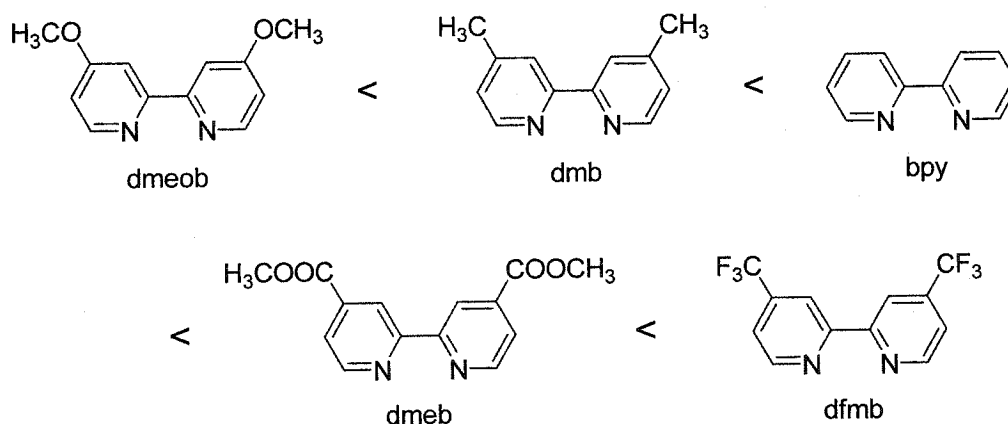
In order to use tris(bipyridyl)ruthenium complexes as oxidants for the generation of reactive intermediates, it is necessary to know which substrates can be oxidized by these complexes. Therefore, this chapter investigates the intermolecular oxidation of six representative organic substrates of different oxidation potential by a series of tris(4,4'-disubstituted-2,2'-bipyridyl)ruthenium complexes in their Ru(III) states. Specifically, the goal of this chapter is to examine the effect of ligand 4,4'-disubstitution on the selectivity of substrate oxidation; *i.e.* an evaluation of the type of substitution required for the oxidation of a particular substrate. These results are obtained in terms of second-order rate constants for the intermolecular-oxidation reaction shown in Scheme 2-1.



Scheme 2-1. Oxidation of a substrate (S) by the Ru(III) state of tris(bipyridyl)ruthenium complexes, where X = Y or X \neq Y, and X or Y = -OCH₃, -CH₃, -H, -COOCH₃, or -CF₃.

As well, this chapter investigates the effect of ligand substitution on the oxidation of Ru(II)* states to Ru(III) by the electron acceptor $[\text{Ru}(\text{NH}_3)_6]\text{Cl}_3$. This electron transfer is a first step of the mechanism involving initial Ru(II)* oxidation and is crucial for the generation of the Ru(III) state used for substrate oxidation.

Five different 4,4'-disubstituted ligands (Scheme 2-2) were chosen for the preparation of eight assorted homoleptic and heteroleptic complexes, and their electrochemical properties, where available in the literature, are summarized in Table 2-1. Reduction potentials are typically reported relative to SCE in acetonitrile, but they have been argued to be equivalent to potentials measured relative to NHE in water.⁷⁸



Scheme 2-2. Bipyridyl ligands in the order of increasing electron-withdrawing ability.

Table 2-1. Reduction potentials (V) for tris(bipyridyl)ruthenium complexes relative to SCE in acetonitrile and the electron acceptor $[\text{Ru}(\text{NH}_3)_6]\text{Cl}_3$ relative to NHE in water.

Compound	III/II	II/I	II*/I	III/II*
$\text{Ru}(\text{dmeob})_3^a$	+0.80	--	--	-1.08 ⁱ
$\text{Ru}(\text{dmb})_3^b$	+1.10	-1.45	+0.64	-0.99
$\text{Ru}(\text{bpy})_2(\text{dmb})^c$	+1.27	-1.36	+0.79	-0.83
$\text{Ru}(\text{bpy})_3^c$	+1.27	-1.31	+0.83	-0.87
$\text{Ru}(\text{dmeb})_2(\text{dmb})^d$	+1.44	-0.96	+0.96 ⁱ	-0.48 ⁱ
$\text{Ru}(\text{dmeb})_3^e$	+1.55	-0.91	+1.06 ⁱ	-0.37 ⁱ
$\text{Ru}(\text{dfmb})_2(\text{dmb})^f$	+1.63	-0.83	+1.08 ⁱ	-0.28 ⁱ
$\text{Ru}(\text{dfmb})_3^g$	+1.75	-0.77	+1.3	-0.35
$[\text{Ru}(\text{NH}_3)_6]\text{Cl}_3^h$	+0.10	--	--	--

^aFrom ref. 78. ^bFrom ref. 79. ^cFrom ref. 71. ^dFrom ref. 80. ^eFrom ref. 80 for ethyl ester derivative. ^fFrom ref. 81 for bpy derivative; potentials for dmb should be more negative. ^gFrom ref. 81. ^hFrom ref. 82. ⁱCalculated from ground-state potentials using emission of 660 nm for $\text{Ru}(\text{dmeob})_3$, 630 nm for $\text{Ru}(\text{dmeb})_3$, 645 nm for $\text{Ru}(\text{dmeb})_2(\text{dmb})$, and 650 nm for $\text{Ru}(\text{dfmb})_2(\text{dmb})$ in nitrogen-purged acetonitrile.

2.1.1 Dependence of reduction potentials on ligand substitution

The electrochemical properties of transition-metal complexes, including tris(bipyridyl)ruthenium derivatives, are strongly dependent on the presence of substituents on the bipyridyl ligands.^{73,74,83-85} From a synthetic point of view, substituents are most easily added to the 4,4'-positions of the ligands. A series of homoleptic complexes with ligands containing 4,4'-disubstituents ranging from electron-donating

dialkylamino to electron-withdrawing trifluoromethyl substituents have been prepared in the literature,^{81,86} and the reduction potentials between these two extremes differ by about one volt for both the Ru(III/II) and Ru(II*/I) couples.

Substituents on the bipyridyl ligands alter the reduction potentials of the complexes by modifying the σ and π properties of the ligands, which influence the amount of charge localized on the ruthenium metal centre.^{73,87} The metal centre of tris(bipyridyl)ruthenium complexes is normally in a relatively low-oxidation Ru(II) state; when it is stabilized by electron-withdrawing ligands, the complex is more difficult to oxidize. Similarly, electron-donating ligands stabilize a Ru(III) metal centre, leading to decreased Ru(III/II) reduction potentials. Likewise, the electrochemical properties of the Ru(II)* excited state, which is an MLCT state featuring a metal centre in the Ru(III) state, are affected by substituents in a similar manner. These are more obvious in Table 2-1, where the reduction potential difference between any half-cell reaction of the same complex remains relatively constant regardless of substituent; *e.g.* the difference between the Ru(III/II) and Ru(III/II*) couples remains at about two volts for all complexes regardless of ligand substituent.

It is not surprising that correlations have been drawn between Ru(III/II) reduction potentials and the Hammett parameters σ_p or σ_m , a measure of the electron-donating or withdrawing properties of substituents in *meta* or *para* positions. Studies by Skarda *et al.*⁸⁴ revealed linear relationships between reduction potentials and the parameters σ_p or σ_m for a series of complexes containing 4,4'- and 5,5'-disubstituted-2,2'-bipyridine ligands, respectively. These observations suggest that the relationship between reduction

potential and substituent lies in the stabilization of the charged ruthenium metal centre. In Skarda's work, all tris(bipyridyl)ruthenium complexes were homoleptic and hence consisted of identical substituents.

In more elaborate work by Slattery *et al.*,^{88,89} linear relationships between Ru(III/II) potentials and Hammett parameters have also been reported for complexes that do not consist entirely of bipyridyl ligands. For instance, 1,3-disubstituted β -diketonate ($R_2\text{Mal}$) ligands were incorporated as heteroleptic complexes $\text{Ru}(\text{bpy})_2(R_2\text{Mal})$ or $\text{Ru}[2,6\text{-bis}(N\text{-pyrazolyl})\text{pyridine}](R_2\text{Mal})(\text{Cl})$, and substituents on the β -diketonate were not necessarily equivalent; *e.g.* one CH_3 and one CF_3 . Here, the Hammett constants of both substituents were summed to provide an overall representation of the electronic effects. Even with the combination of an electron-donating and a withdrawing substituent, a linear relationship between reduction potentials and the summed Hammett values was observed.

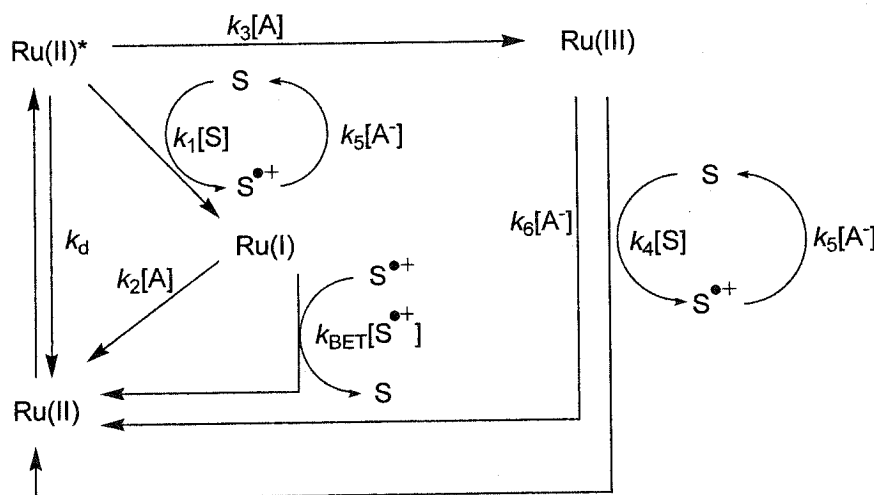
However, no literature has been found on topics related to the relationship between reduction potentials and substituent parameters for complexes containing exclusively bipyridyl ligands, with the same pair of substituents on each ligand, but substituted in a heteroleptic manner. For instance, $\text{Ru}(\text{dfmb})_2(\text{dmb})$, which has not been reported in the literature, features a seemingly counterproductive mixture of CH_3 - and CF_3 -disubstituted ligands. Clearly, an investigation of the electrochemical properties of a large series of tris(bipyridyl)ruthenium complexes with both electron-donating and withdrawing ligands, as well as whether the concept of additive Hammett constants apply to these complexes, would be interesting, but is not the goal of this thesis.

Nonetheless, two of the heteroleptic complexes containing electron-withdrawing ligands, $\text{Ru}(\text{dmeb})_2(\text{dmb})$ and $\text{Ru}(\text{dfmb})_2(\text{dmb})$, were prepared with the methyl derivative dmb instead of the unsubstituted bpy. Although dmb is electron-donating compared to bpy, the methyl groups, or any substitution for that matter, are necessary for the attachment for linked substrates. While the complexes studied here do not have substrates linked, these dmb-containing complexes represent the active photosensitizer cores of complexes that feature linked substrates in subsequent chapters. It is also worth mentioning that the substitution of a single bpy with dmb only results in a marginal reduction of the associated reduction potentials, as shown in Table 2-1; e.g. the potentials for $\text{Ru}(\text{bpy})_2(\text{dmb})$ are no more than 0.04 V towards the negative than $\text{Ru}(\text{bpy})_3$.

2.1.2 Tris(bipyridyl)ruthenium complexes as oxidants

Although tris(bipyridyl)ruthenium complexes are normally found in the $\text{Ru}(\text{II})$ state, they can be readily converted to $\text{Ru}(\text{I})$ and $\text{Ru}(\text{III})$ states, as discussed in the previous chapter. The $\text{Ru}(\text{II})^*$ excited state is both more easily reduced or oxidized than the initial $\text{Ru}(\text{II})$ state (Table 2-1), suggesting that it may be used as an oxidant or reductant. It is clear that $\text{Ru}(\text{II})^*$ may be used to oxidize an organic substrate, along with the associated formation of $\text{Ru}(\text{I})$. However, if a sacrificial electron acceptor is present, $\text{Ru}(\text{II})^*$, as a reductant, can be oxidized to $\text{Ru}(\text{III})$; in turn, $\text{Ru}(\text{III})$ can be used to oxidize the organic substrate. These two strategies, also referred to as routes or pathways, are represented in Scheme 2-3 and herein referred to an *initial $\text{Ru}(\text{II})^*$ reduction* ($k_1[\text{S}]$) or an *initial $\text{Ru}(\text{II})^*$ oxidation* ($k_3[\text{A}]$), respectively.

While the route involving Ru(III), which requires Ru(II)* oxidation, is more elaborate, it has several advantages over that of Ru(II)* reduction. First, the reduction potential (Table 2-1) of Ru(III) is more positive than that of Ru(II)* by about 0.5 V, indicating that it is a more powerful oxidant. Ru(III) is also a stable, ground-state species that is much longer lived than the Ru(II)* transient; *i.e.* Ru(III) does not undergo self-decay and can only return to Ru(II) *via* reduction. Finally, substrate oxidation by Ru(III) would regenerate the initial Ru(II), while oxidation by Ru(II)* would produce the highly reducing Ru(I) that could undergo back-electron transfer with the substrate radical cation, resulting in a futile, energy-wasting pathway. These issues with Ru(II)* as an oxidant clearly indicate that Ru(III) is preferable.



Scheme 2-3. Schematic of the routes of substrate (S) oxidation, characterized by the initial reduction or oxidation of an Ru(II)* excited, amphoteric photosensitizer. An electron acceptor (A) oxidizes the excited state in the initial-oxidation route.

From Scheme 2-3, the two routes of Ru(II)* consumption other than k_d are competitive second-order processes, where both the acceptor and the substrate are competing for Ru(II)*. If the route of Ru(II)* oxidation is desired ($k_3[A]$), then conditions encouraging this route are required. For instance, the concentration of the electron acceptor may need to be substantially higher than the substrate. In addition, the oxidation of Ru(II)* by the acceptor should be more thermodynamically favourable, according to reduction potentials, than reduction by the substrate. Such conditions would ensure that Ru(II)* is preferentially oxidized to Ru(III) much faster than reduction to Ru(I). Thus, in this chapter, the concentration of the electron acceptor $[\text{Ru}(\text{NH}_3)_6]\text{Cl}_3$ was maintained at 100 mM, while that of the organic substrate was significantly lower (≤ 4 mM).

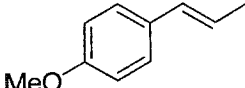
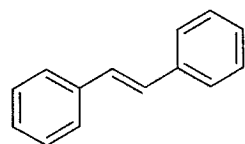
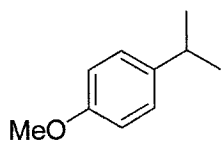
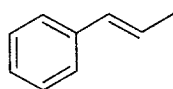
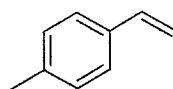
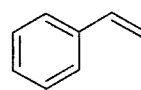
2.1.3 Organic substrates

The ability of tris(bipyridyl)ruthenium complexes to oxidize six non-basic organic substrates to their respective radical cations was investigated in this chapter. These substrates included various styrene derivatives, the radical cations of which are commonly used in the study of reactive intermediates,⁹⁰⁻¹⁰⁰ *trans*-stilbene, an important compound for both photophysical and mechanistic-photochemistry studies,¹⁰¹⁻¹¹¹ and 4-methoxycumene (4-isopropylanisole), a model for a more sophisticated diphenylalkane substrate studied in Chapter 4. The basic substrate *N,N*-dimethyl-*p*-toluidine was also investigated, but is discussed in detail in Chapter 3.

The reduction potentials for the corresponding radical cations of these substrates (Table 2-2) span between 1.3-2.1 V *versus* SCE in acetonitrile, suggesting that the substrates may be oxidized by tris(bipyridyl)ruthenium complexes (Table 2-1). It is apparent from these two tables that Ru(III) would be the ideal oxidant, since the reduction potential of even the strongest Ru(II)* oxidant, Ru(dfmb)₃, is only approximately equal to that of the *trans*-anethole, the most easily oxidized substrate, and would result in an electron transfer that is not thermodynamically favourable.

The abilities of Ru(II)* and Ru(III) states to oxidize the organic substrates were evaluated in the following section to assess the selectivity of substrate oxidation by complexes containing different ligand 4,4'-disubstitution. In both cases, substrate oxidation was deduced from changes to the rate constants of Ru(II)* decay or Ru(III)-to-Ru(II) recovery, rather than the direct monitoring of substrate consumption or radical-cation production. These are explained in greater detail in the next section.

Table 2-2. Reduction potentials (V) for the corresponding radical cations of organic substrates relative to SCE in acetonitrile.

Substrate		(•+)/0
	<i>trans</i> -anethole ^a	+1.33
	<i>trans</i> -stilbene ^b	+1.48
	4-methoxycumene ^c	+1.57
	<i>trans</i> -β-methylstyrene ^d	+1.60
	4-methylstyrene ^d	+1.87
	styrene ^d	+2.05

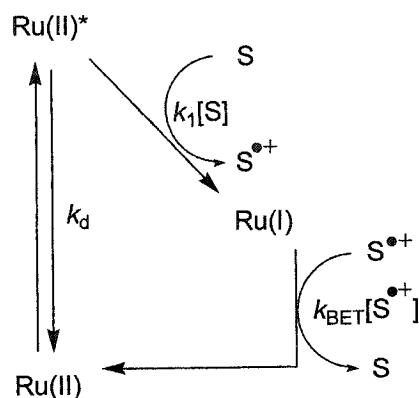
^aFrom ref. 90. ^bFrom ref. 101. ^cFrom ref. 112.

2.2 Results

Laser-flash irradiation experiments were performed in aqueous solutions, and where required, stock acetonitrile solutions of organic substrates were injected into nitrogen-purged samples. In all cases, the amount of acetonitrile solution injected did not exceed 2.5% of the total volume; such small changes to the solvent system and experimental conditions are deemed negligible. As well, the maximum concentration of organic substrate achieved was typically less than 4 mM due to solubility constraints, most often observed in the form of precipitation or cloudiness.

2.2.1 Ru(II)* excited state as an oxidant

The ability of Ru(II)* excited states to oxidize assorted organic substrates was evaluated by monitoring changes to the Ru(II)* decay caused by the addition of organic substrate. Ru(II)* decays were monitored at 370 nm in the form of excited-state absorption, or at 620 nm as emission; both monitoring wavelengths, as expected, afforded virtually identical results. It is important to emphasize that in these experiments, no electron acceptor was present. Under these conditions, as shown in Scheme 2-4, the Ru(II)* excited state can only be depleted by processes k_d and $k_1[S]$, respectively, representing the natural decay of the excited state and the oxidation of the added substrate. The sum of these two rate constants constitutes the total observed rate of Ru(II)* decay, k_{obs} , a pseudo first-order rate ($k_{obs} = k_d + k_1[S]$). Thus, the intermolecular oxidation of a substrate by Ru(II)* was inferred by an increase in the rate of Ru(II)* decay, hence a shorter lifetime, following substrate addition.



Scheme 2-4. Intermolecular oxidation of an organic substrate (S) by Ru(II)* states.

Excited-state lifetimes for the tris(bipyridyl)complexes were measured following the 355-nm laser-flash irradiation of the aqueous samples and are summarized in Table 2-3. When the samples were supplemented with 4 mM *trans*-anethole, the most easily oxidized substrate (Table 2-2), no significant changes to the excited-state lifetimes were observed; a sample kinetic trace is shown in Figure 2-1. This suggests that the Ru(II)* states of all complexes could not oxidize this substrate ($k_1[S]$) at an appreciable rate to impact significantly the observed Ru(II)* decay (k_{obs}). No substrate oxidation was inferred even for the long-lived Ru(II)* state of the strongly oxidizing Ru(dfmb)₃. The remaining substrates were not investigated, since they are even more difficult to oxidize.

Moreover, the inability of Ru(II)* to oxidize the substrates studied is beneficial and indicates that if an electron acceptor were also present in the laser-flash irradiation samples, competition between the substrate and the acceptor would not be an issue (Scheme 2-3). The route of initial Ru(II)* oxidation to Ru(III) would always be favoured, since the route of Ru(II)* reduction by the substrate is negligible.

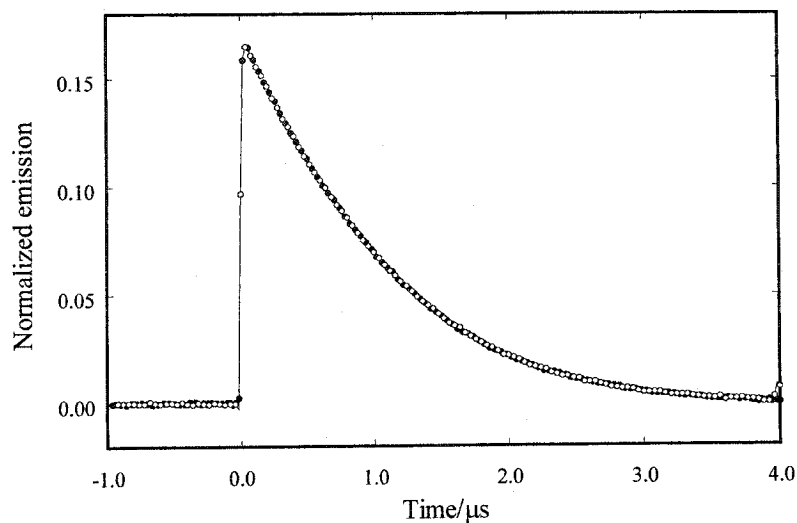


Figure 2-1. Kinetic trace acquired at 620 nm following the 355-nm laser irradiation of Ru(dfmb)_3 in nitrogen-purged water with (●) 0.0 mM, and (○) 4 mM *trans*-anethole.

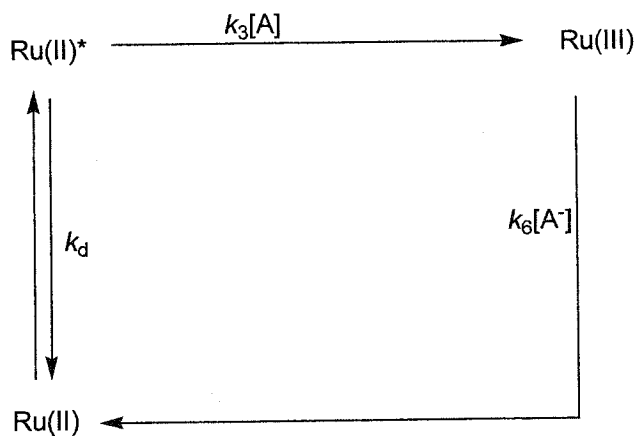
Table 2-3. Ru(II)^* lifetimes measured at 620 nm after 355-nm irradiation in nitrogen-saturated aqueous solutions. Lifetimes were not affected by 4 mM *trans*-anethole.

Compound	Lifetime/ns ^a
Ru(dmeob)_3	60
Ru(dmb)_3	330
$\text{Ru(bpy)}_2(\text{dmb})$	475
Ru(bpy)_3	548
$\text{Ru(dmeb)}_2(\text{dmb})$	516
Ru(dmeb)_3	1320
$\text{Ru(dfmb)}_2(\text{dmb})$	338
Ru(dfmb)_3	1089

^a Lifetimes reproducible within 2%.

2.2.2 Oxidation of Ru(II)* excited states to Ru(III)

In this section, the ability of the electron acceptor $[\text{Ru}(\text{NH}_3)_6]\text{Cl}_3$ to oxidize Ru(II)* excited states was determined by monitoring increases in the rate of Ru(II)* decay caused by the addition of electron acceptor. In this case, as shown in Scheme 2-5, the two processes responsible for the depletion of Ru(II)* are k_d and $k_3[\text{A}]$, with the latter representing the second-order rate of Ru(II)* oxidation by the acceptor. The observed pseudo first-order rate of Ru(II)* decay, k_{obs} , would be a sum of these two processes ($k_{\text{obs}} = k_d + k_3[\text{A}]$). A linear regression analysis of k_{obs} as a function of electron acceptor concentration allows extraction of the second-order rate constant k_3 as the slope.



Scheme 2-5. Intermolecular oxidative quenching of Ru(II)* by an electron acceptor (A).

The second-order rate of Ru(II)^* oxidation by $[\text{Ru(NH}_3)_6]\text{Cl}_3$, k_3 , was evaluated for the various complexes in the absence of any substrate. Briefly, excited-state lifetimes were measured at 370 nm or 620 nm following 355-nm excitation of the samples in nitrogen-purged, 250 mM NaCl; the presence of high ionic strength minimizes the effect of additional changes in ionic strength caused by the addition of electron acceptor.¹¹³⁻¹¹⁶ Concentrated stock solutions of $[\text{Ru(NH}_3)_6]\text{Cl}_3$, also prepared in 250 mM NaCl, were injected and increases in the rate of Ru(II)^* decay were observed. Representative kinetic traces are presented in Figure 2-2, which shows the effect of increasing concentrations of $[\text{Ru(NH}_3)_6]\text{Cl}_3$ on the observed Ru(II)^* decay at 620 nm for the complex Ru(dmeb)_3 .

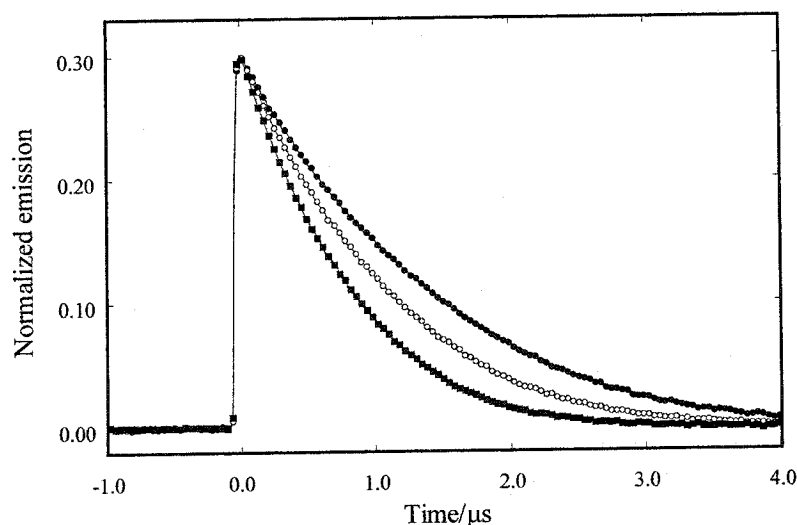


Figure 2-2. Kinetic trace acquired at 620 nm following the 355-nm laser irradiation of Ru(dmeb)_3 in nitrogen-purged, aqueous 250 mM NaCl in the presence of (●) 0.0 mM, (○) 0.4 mM, and (■) 1.0 mM $[\text{Ru(NH}_3)_6]\text{Cl}_3$.

The second-order rate constant k_3 for the oxidation of Ru(II)^* by the electron acceptor for the series of complexes was extracted by plotting the observed rate constants of Ru(II)^* decay as a function of $[\text{Ru(NH}_3)_6]\text{Cl}_3$ concentration, as shown in Figure 2-3. Second-order rate constants are summarized in Table 2-4; the value obtained for Ru(bpy)_3 is in good agreement with literature values¹¹³⁻¹¹⁶ of between $2\text{--}3 \times 10^9 \text{ M}^{-1} \text{ s}^{-1}$. As well, an overall trend to the rate constants of oxidation is noticeable. As the complexes contain more electron-withdrawing groups, making Ru(II)^* more difficult to oxidize (Table 2-1), the rate of oxidation by the acceptor decreases. This dependence between the kinetics and thermodynamics is discussed later on.

Table 2-4. Second-order rate constants and reduction potential differences (ΔE) for the oxidative quenching of Ru(II)^* states of tris(bipyridyl)ruthenium complexes by $[\text{Ru(NH}_3)_6]\text{Cl}_3$ in 250 mM NaCl.

Complex	Rate/ $10^8 \text{ M}^{-1} \text{ s}^{-1}$	$\Delta E/\text{V}$
Ru(dmeob)_3	20	+1.18
Ru(dmb)_3	25	+1.09
$\text{Ru(bpy)}_2(\text{dmb})$	22	+0.93
Ru(bpy)_3	21	+0.97
$\text{Ru(dmeb)}_2(\text{dmb})$	9.6	+0.58
Ru(dmeb)_3	6.1	+0.47
$\text{Ru(dfmb)}_2(\text{dmb})$	1.5	+0.38
Ru(dfmb)_3	0.59	+0.45

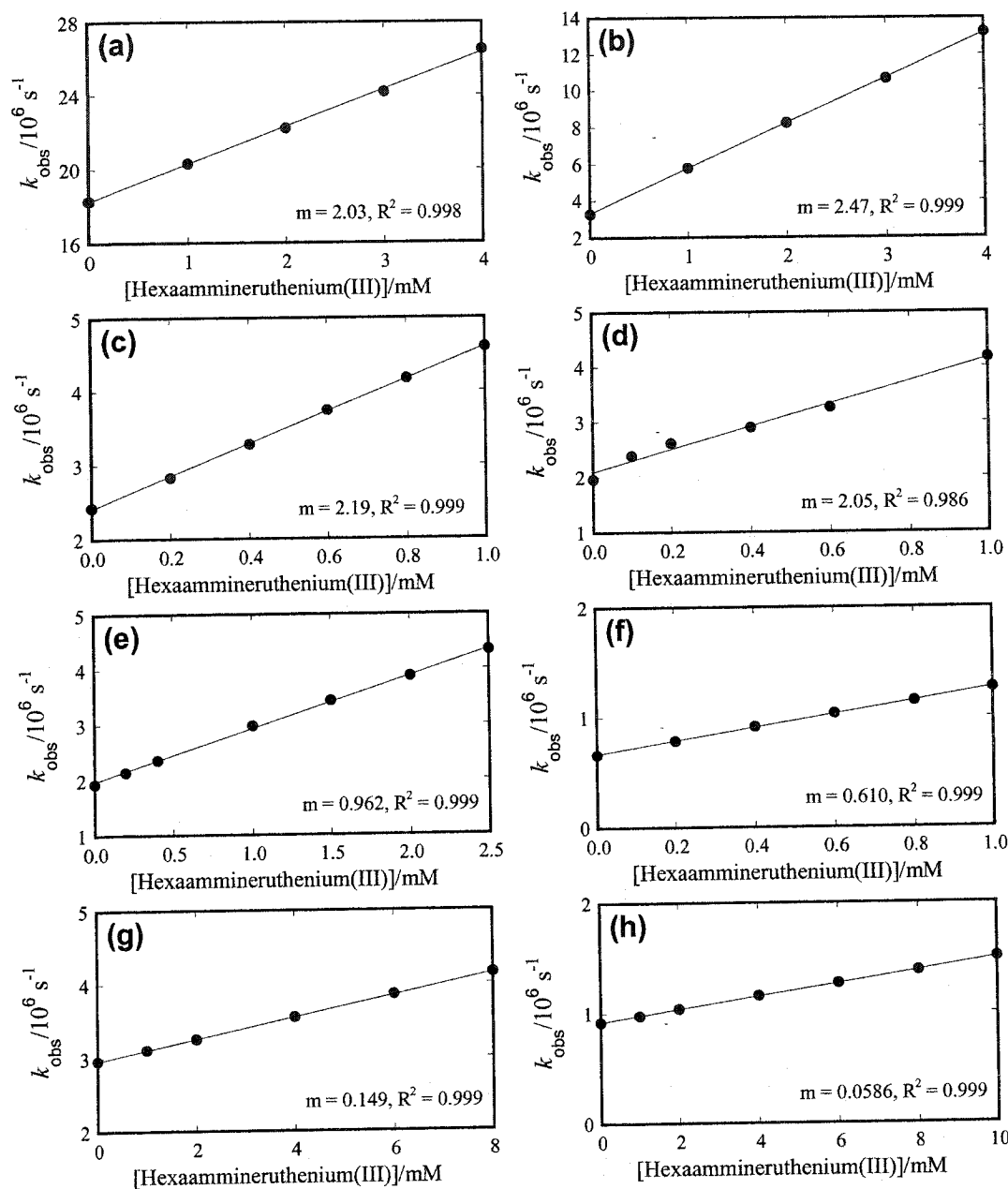


Figure 2-3. Observed rate constants for the decay of Ru(II)^* of (a) Ru(dmeob)_3 , (b) Ru(dmb)_3 , (c) $\text{Ru(bpy)}_2(\text{dmb})$, (d) Ru(bpy)_3 , (e) $\text{Ru(dmeb)}_2(\text{dmb})$, (f) Ru(dmeb)_3 , (g) $\text{Ru(dfmb)}_2(\text{dmb})$, and (h) Ru(dfmb)_3 as a function of $[\text{Ru(NH}_3)_6]\text{Cl}_3$, measured from kinetic traces monitored at 370 nm or 620 nm following 355-nm laser irradiation of nitrogen-saturated samples containing 250 mM NaCl. Slope (m) in units of $10^9 \text{ M}^{-1} \text{ s}^{-1}$.

However, the second-order rate constants alone do not provide an indication of the *efficiency* of the Ru(II)*-to-Ru(III) conversion; *i.e.* the amount of Ru(II)* that is successfully converted to Ru(III). From Scheme 2-5, it is evident that the efficiency of this oxidation by the electron acceptor is not dependent on $k_3[A]$ itself, but rather the relative rate constants of k_d and $k_3[A]$. In other words, a Ru(II)* state that is slowly oxidized, yet very long-lived, may result in a higher fractional conversion to Ru(III) than one that is quickly oxidized but short-lived. Therefore, it is beneficial to have a $k_3[A]$ as high as possible relative to the energy-wasting, deactivation process k_d , and, experimentally, this can be accomplished by using a high concentration of electron acceptor to “trap” the excited state. In this case, a fixed concentration of 100 mM [Ru(NH₃)₆]Cl₃ was arbitrarily chosen for convenience, without NaCl. Higher concentrations could have been used; however, since the electron acceptor also absorbs to a small extent at 355 nm, though it is not photoactive, high concentrations would have reduced the amount of Ru(II) excited to Ru(II)* by competitive light absorption.

The determination of the efficiency of the Ru(II)*-to-Ru(III) conversion was possible by monitoring changes in absorption at 450 nm, near the MLCT absorption maximum of the initial, ground-state Ru(II). Thus, since laser-flash irradiation of the sample consumes Ru(II) *via* excitation to Ru(II)*, the kinetic trace at 450 nm was observed as a negative absorption (bleaching). The most negative value achieved for the signal corresponds to the amount of Ru(II)* formed, based on the extinction coefficient of Ru(II). In the absence of an electron acceptor, the bleaching recovered to baseline with kinetics equivalent to the Ru(II)* lifetime due to the decay of Ru(II)* back to Ru(II), a

scenario represented in Figure 2-4 (a). However, when 100 mM $[\text{Ru}(\text{NH}_3)_6]\text{Cl}_3$ was also present in the laser-flash irradiation mixtures, Figure 2-4 (b), the $\text{Ru}(\text{II})^*$ formed can now decay back to $\text{Ru}(\text{II})$ and be oxidized to $\text{Ru}(\text{III})$. The former process results in a rise of the bleaching signal immediately after the laser pulse due to the regeneration of $\text{Ru}(\text{II})$, while oxidation of $\text{Ru}(\text{II})^*$ to $\text{Ru}(\text{III})$ does not generate a transient that absorbs at 450 nm. Thus, the bleaching recovery at 450 nm appears interrupted and does not recover to baseline levels at short time scales; at longer time scales, $\text{Ru}(\text{III})$ is slowly converted back to $\text{Ru}(\text{II})$ by $k_6[\text{A}^-]$. These characteristics permit the calculation of the amount of $\text{Ru}(\text{II})^*$, which originated from $\text{Ru}(\text{II})$, that is oxidized to $\text{Ru}(\text{III})$ by the acceptor.

Figure 2-4 (b), $\text{Ru}(\text{dmeob})_3$, shows a representative calculation of the efficiency of the $\text{Ru}(\text{II})^*$ to $\text{Ru}(\text{III})$ conversion. The most negative value of the bleaching (-0.0475) corresponds to the amount of $\text{Ru}(\text{II})^*$ made. Immediately after the laser pulse, this negative value recovers by about 0.020 towards the positive (41 %), which represents the amount of $\text{Ru}(\text{II})^*$ that decayed back to $\text{Ru}(\text{II})$. Thus, the balance of 59 % that did not immediately recover corresponds to that oxidized to $\text{Ru}(\text{III})$ by the acceptor.

Data pertaining to the efficiencies of the $\text{Ru}(\text{II})^*$ -to- $\text{Ru}(\text{III})$ conversion for all complexes are summarized in Table 2-5. These results, especially that of $\text{Ru}(\text{dmeob})_3$, clearly show that both $\text{Ru}(\text{II})^*$ lifetime (Table 2-3) and oxidation rate (Table 2-4) influence the conversion efficiencies.

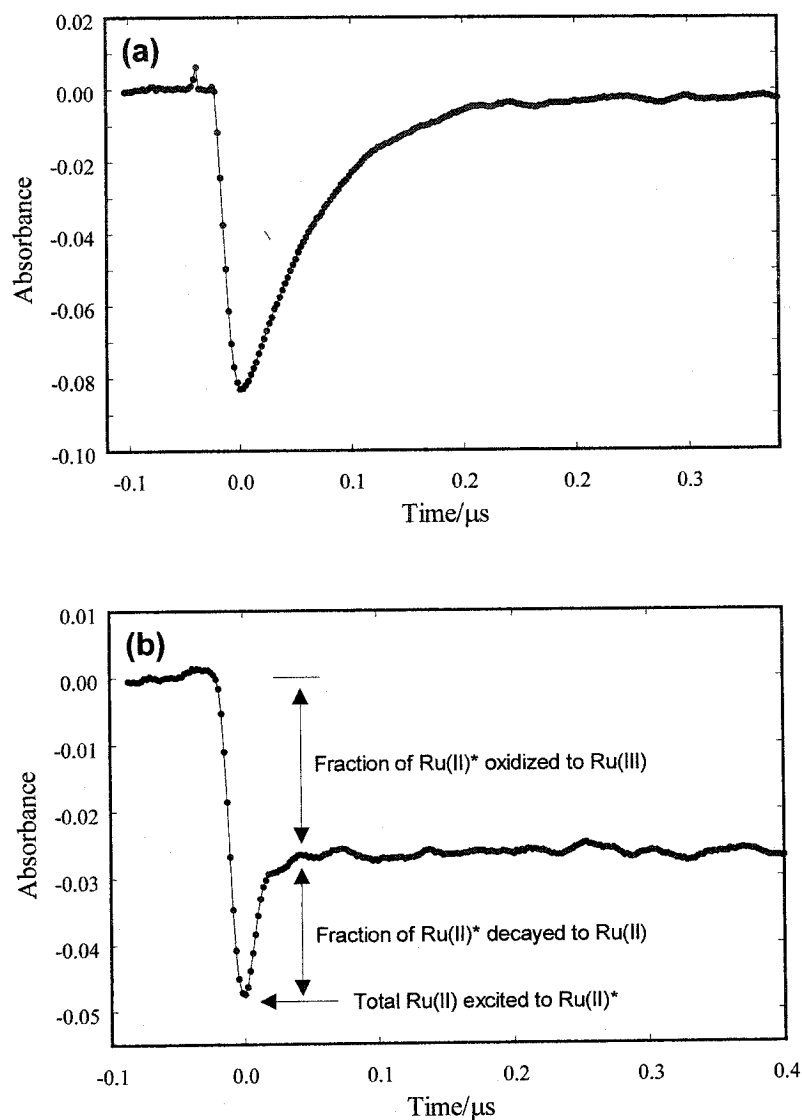


Figure 2-4. Kinetic trace acquired at 450 nm following the 355-nm laser irradiation of Ru(dmeob)₃ in nitrogen-purged, aqueous solutions in the (a) absence or (b) presence of 100 mM [Ru(NH₃)₆]Cl₃. Figure (b) indicates an Ru(II)*-to-Ru(III) conversion efficiency of approximately 60%.

Table 2-5. Percentages of Ru(II)* oxidized to Ru(III) by 100 mM [Ru(NH₃)₆]Cl₃ for various tris(bipyridyl)ruthenium complexes.

Complex	% oxidation ^a
Ru(dmeob) ₃	60
Ru(dmb) ₃	> 98
Ru(bpy) ₂ (dmb)	> 95
Ru(bpy) ₃	> 95
Ru(dmeb) ₂ (dmb)	88
Ru(dmeb) ₃	55
Ru(dfmb) ₂ (dmb)	48
Ru(dfmb) ₃	23

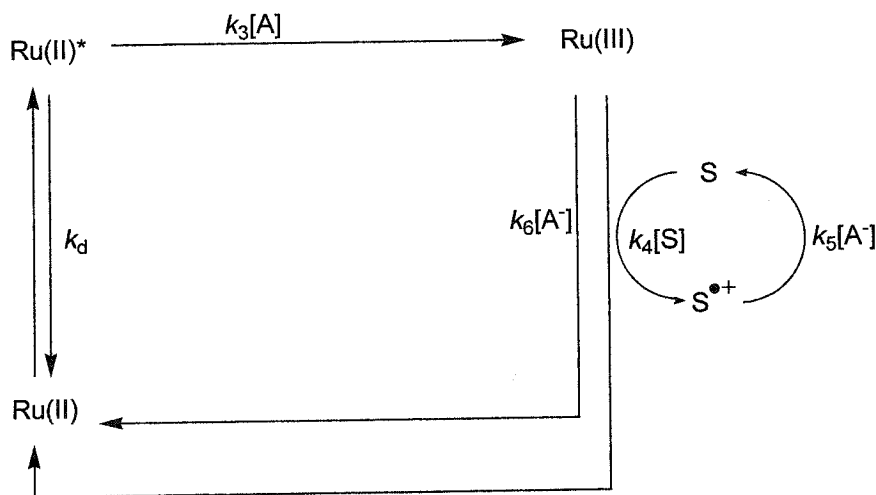
^a Values are typically reproducible to within 5%.

2.2.3 Substrate oxidation by Ru(III)

Since Ru(II)* states were not reduced to Ru(I) by the various substrates at the concentrations studied, yet were oxidized to Ru(III) by the electron acceptor, the pathways in Scheme 2-1 can be simplified by removal of the route of initial Ru(II)* reduction to yield Scheme 2-6. The Ru(III) state generated *via* oxidation of Ru(II)* can return to the initial, stable Ru(II) state by two methods, namely charge recombination with the reduced acceptor ($k_6[A^-]$) and oxidation of the substrate ($k_4[S]$). The monitoring of Ru(II) bleaching recovery at 450 nm therefore serves as a convenient indicator of substrate oxidation, which would lead to an increased rate of observed Ru(II) recovery. Since the charge recombination process $k_6[A^-]$ can be approximated to first-order kinetics

in the vicinity of $1 \times 10^5 \text{ s}^{-1}$ at moderate time scales (e.g. $40 \text{ } \mu\text{s}$), the observed recovery of Ru(II), k_{obs} , is a pseudo first-order process comprised of $k_6[\text{A}^-]$ and $k_4[\text{S}]$, where $k_{\text{obs}} = k_6[\text{A}^-] + k_4[\text{S}]$. Similar to previous analyses, the second-order rate constant k_4 can be extracted from a plot of k_{obs} as a function of $[\text{S}]$.

In addition, the radical cation generated can also undergo charge recombination with the reduced acceptor, $k_5[\text{A}^-]$. However, this does not affect the kinetic analyses, as the recovery rate of Ru(II) is used to infer substrate oxidation rather than the direct monitoring of radical cation formation. The latter was not considered due to two main reasons: the radical cations were not observed, and they may naturally decay by other reactions at a rate greater than which they were formed.



Scheme 2-6. Intramolecular substrate oxidation in the presence of an irreversible electron acceptor, depicting the route of initial Ru(II)* oxidation.

A representative kinetic trace is provided in Figure 2-5, which shows the effect of varying concentrations of 4-methoxycumene on the rate constant for the recovery of the Ru(II) state of Ru(dfmb)₂(dmb). In this plot, it is evident that a certain amount of Ru(II)*, corresponding to an Ru(II) absorption of about -0.027, is formed from the laser pulse, observed as bleaching. Afterwards, about half of the bleaching rapidly recovers, *i.e.*, the decay of Ru(II)* to Ru(II). Thus, the balance corresponds to the amount of Ru(II)* converted to Ru(III). This then slowly recovers to Ru(II), the rate constant of which is dependent on substrate concentration. It is important to emphasize that in such plots, the portion of the trace used for kinetic fits (k_{obs}) is that which is *after* the rapid recovery, the portion corresponding to the conversion of Ru(III) to Ru(II).

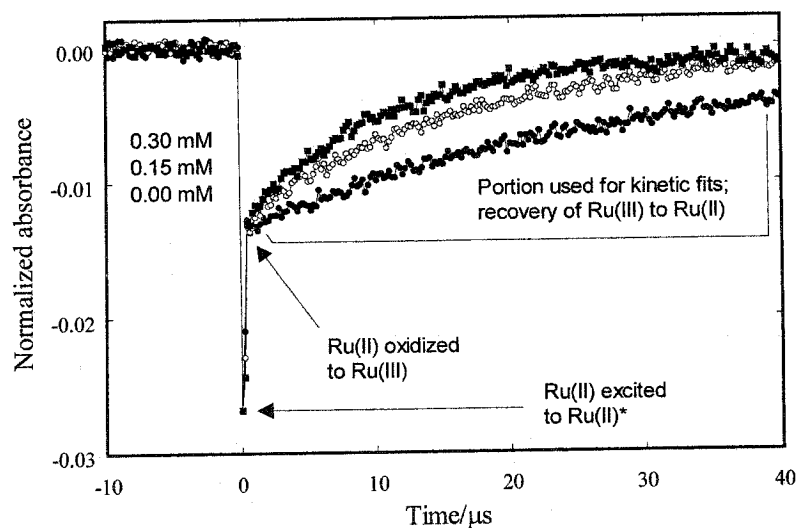


Figure 2-5. Kinetic trace acquired at 450 nm following the 355-nm laser irradiation of Ru(dfmb)₂(dmb) in nitrogen-purged, aqueous 100 mM [Ru(NH₃)₆]Cl₃ in the presence of (●) 0.0 mM, (○) 0.15 mM, and (■) 0.30 mM 4-methoxycumene.

The observed, pseudo first-order rate constants of Ru(II) recovery, k_{obs} , were subsequently plotted against substrate concentration for each of the six substrates, ranging from Figure 2-6 for *trans*-anethole to Figure 2-11 for styrene. In the resulting linear plots, substrate oxidation by Ru(III) of the complexes was deemed to be statistically significant when the correlation coefficient (R^2) of the linear fits was large (greater than 0.9). Typically, correlation coefficients were either above or substantially below this value, facilitating the identification of positive oxidations. However, due to solubility constraints, some substrate concentrations were sub-millimolar, where slow, and hence not very useful, oxidations would have been undetectable, *i.e.*, $k_4[\text{S}] \ll k_6[\text{A}^-]$. Second-order rate constants for substrate oxidation, determined from the slope of the plots, are summarized in Table 2-6 along with the corresponding reduction-potential differences (ΔE). Not all combinations of substrate and complex were investigated, particularly those with highly negative ΔE values, as these would be largely thermodynamically unfavourable electron transfers.

Table 2-6. Second-order rate constants ($/10^8 \text{ M}^{-1} \text{ s}^{-1}$) and reduction potential differences ΔE (V) for substrate oxidation by Ru(III) states of tris(bipyridyl)ruthenium complexes.

Complex	<i>trans</i> - anethole	4- methoxy- cumene	<i>trans</i> - stilbene	<i>trans</i> - β - methyl- styrene	4- methyl- styrene	styrene
Ru(dmeob) ₃	-- (-0.53)	-- (-0.77)	nd (-0.68)	nd (-0.80)	nd (-1.07)	nd (-1.25)
Ru(dmb) ₃	-- (-0.23)	-- (-0.47)	nd (-0.38)	nd (-0.50)	nd (-0.77)	nd (-0.95)
Ru(bpy) ₂ (dmb)	-- (-0.06)	-- (-0.30)	-- (-0.21)	nd (-0.33)	nd (-0.60)	nd (-0.78)
Ru(bpy) ₃	0.21 (-0.06)	-- (-0.30)	-- (-0.21)	nd (-0.33)	nd (-0.60)	nd (-0.78)
Ru(dmeb) ₂ (dmb)	22 (+0.11)	1.1 (-0.13)	-- (-0.04)	-- (-0.16)	-- (-0.43)	nd (-0.61)
Ru(dmeb) ₃	26 (+0.22)	11 (-0.02)	1.2 (+0.07)	0.36 (-0.05)	-- (-0.32)	nd (-0.50)
Ru(dfmb) ₂ (dmb)	17 (+0.30)	2.0 (+0.06)	1.1 (+0.15)	-- (+0.03)	-- (-0.24)	-- (-0.42)
Ru(dfmb) ₃	23 (+0.42)	11 (+0.18)	1.2 (+0.27)	2.0 (+0.15)	0.97 (-0.12)	-- (-0.30)

No entry (--) denotes the absence of observable oxidation and nd denotes not determined. ΔE is shown in parentheses.

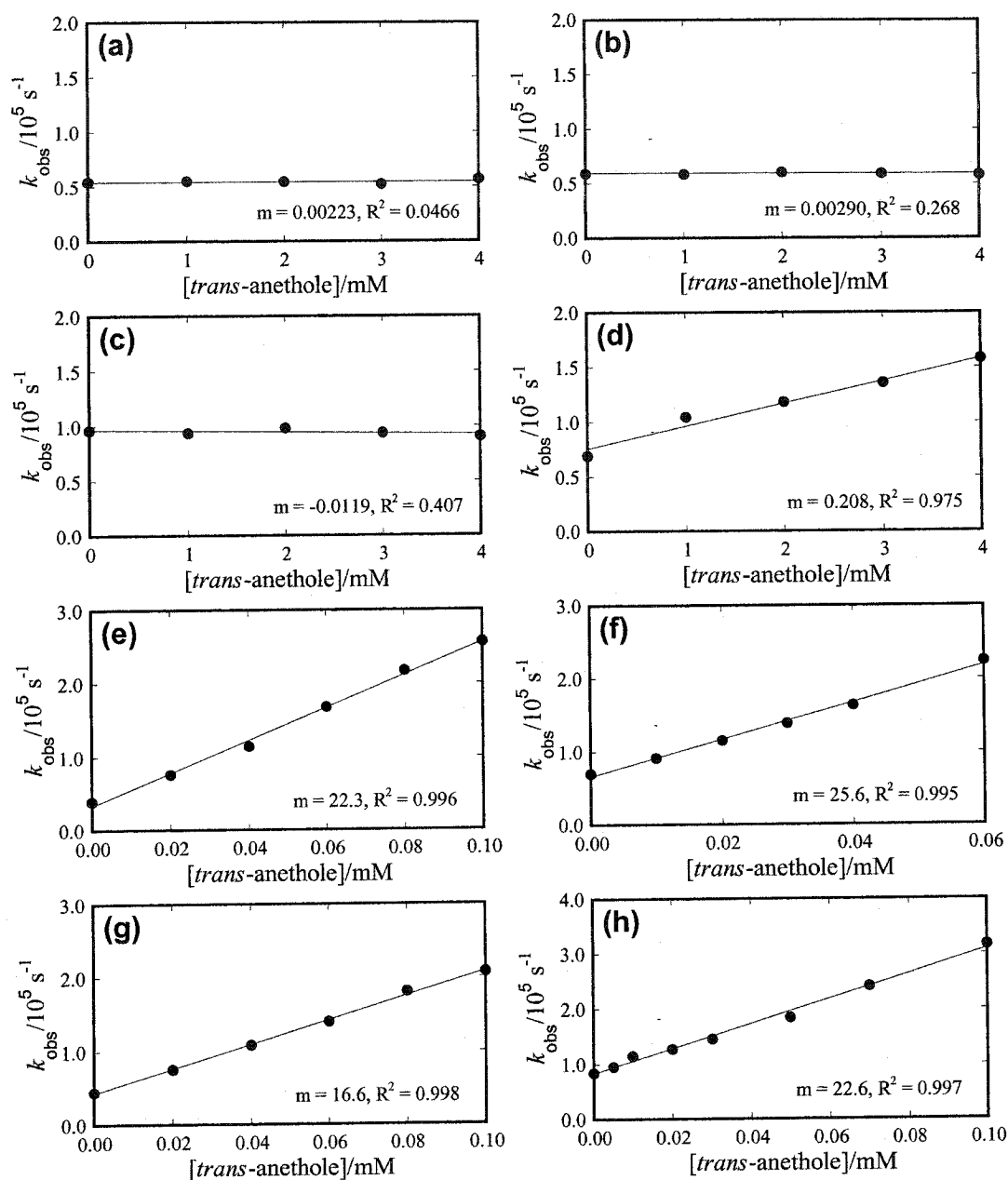


Figure 2-6. Observed rate constants for the recovery of Ru(II) of (a) Ru(dmeob)_3 , (b) Ru(dmb)_3 , (c) $\text{Ru(bpy)}_2(\text{dmb})$, (d) Ru(bpy)_3 , (e) $\text{Ru(dmeb)}_2(\text{dmb})$, (f) Ru(dmeb)_3 , (g) $\text{Ru(dfmb)}_2(\text{dmb})$, and (h) Ru(dfmb)_3 as a function of *trans*-anethole concentration, measured from kinetic traces monitored at 450 nm following 355-nm laser irradiation of nitrogen-saturated samples in 100 mM $[\text{Ru}(\text{NH}_3)_6]\text{Cl}_3$. Slope (m) in units of $10^8 \text{ M}^{-1} \text{ s}^{-1}$.

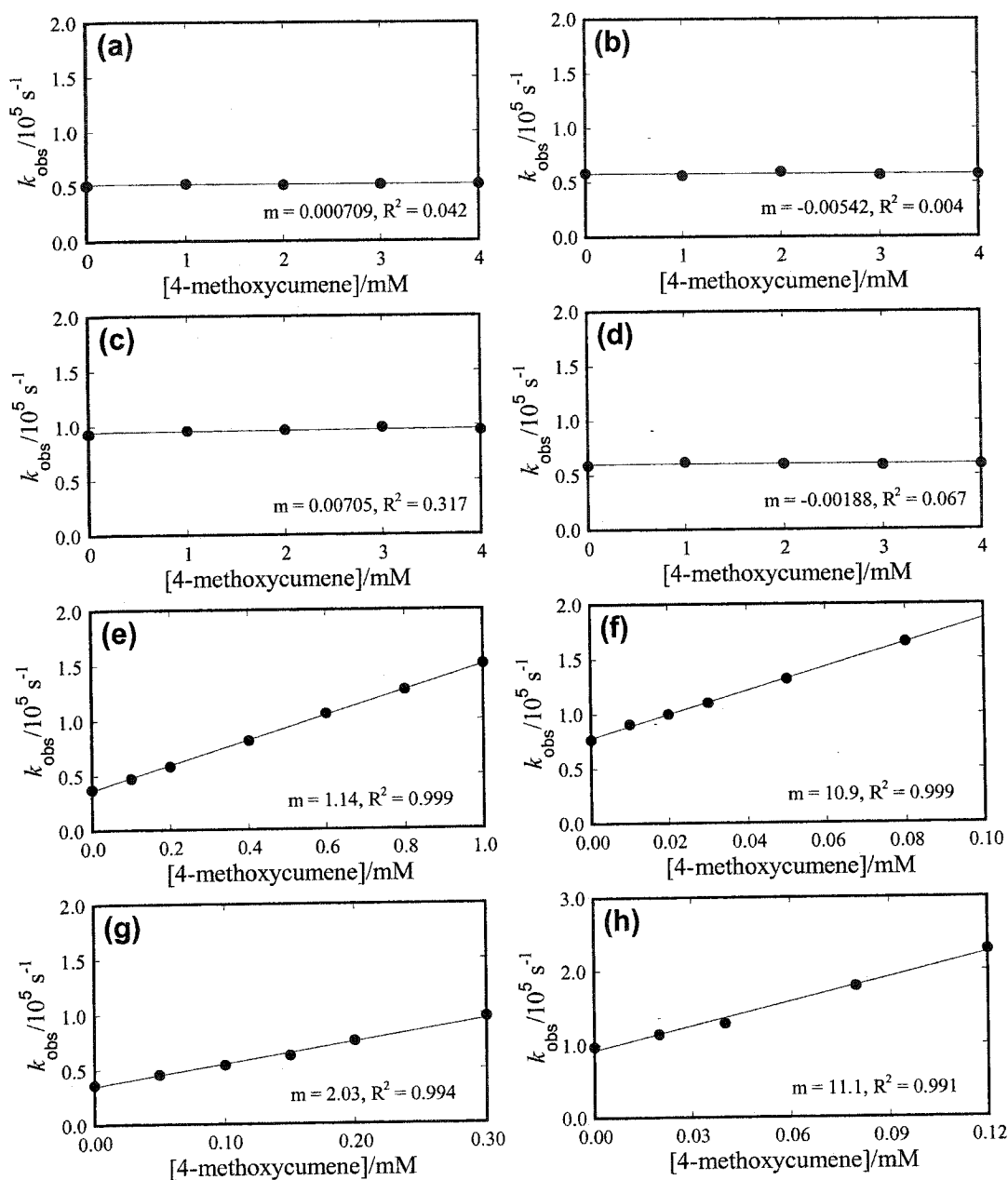


Figure 2-7. Observed rate constants for the recovery of Ru(II) of (a) $\text{Ru}(\text{dmeob})_3$, (b) $\text{Ru}(\text{dmb})_3$, (c) $\text{Ru}(\text{bpy})_2(\text{dmb})$, (d) $\text{Ru}(\text{bpy})_3$, (e) $\text{Ru}(\text{dmeb})_2(\text{dmb})$, (f) $\text{Ru}(\text{dmeb})_3$, (g) $\text{Ru}(\text{dfmb})_2(\text{dmb})$, and (h) $\text{Ru}(\text{dfmb})_3$ versus 4-methoxycumene concentration, measured from kinetic traces monitored at 450 nm following 355-nm laser irradiation of nitrogen-saturated samples containing 100 mM $[\text{Ru}(\text{NH}_3)_6]\text{Cl}_3$. Slope (m) in units of $10^8 \text{ M}^{-1} \text{ s}^{-1}$.

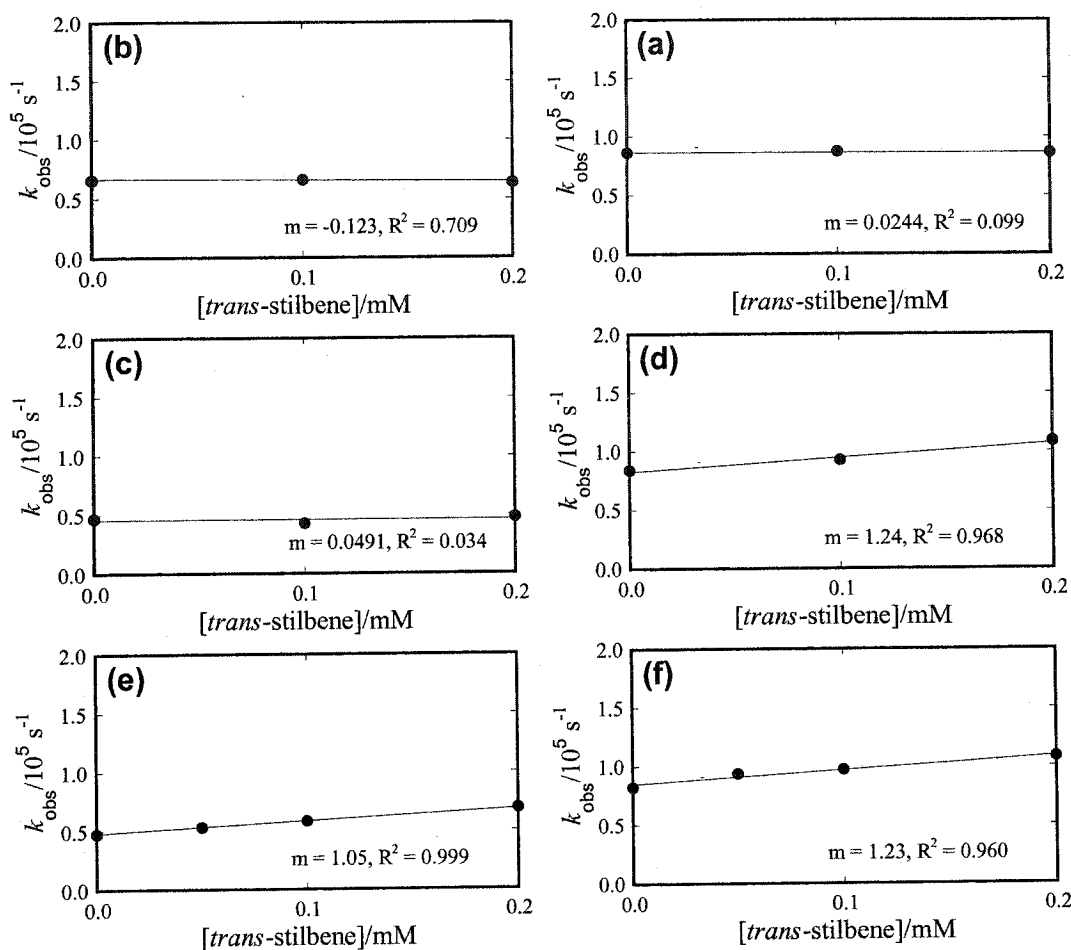


Figure 2-8. Observed rate constants for the recovery of Ru(II) of (a) $\text{Ru}(\text{bpy})_2(\text{dmb})$, (b) $\text{Ru}(\text{bpy})_3$, (c) $\text{Ru}(\text{dmeb})_2(\text{dmb})$, (d) $\text{Ru}(\text{dmeb})_3$, (e) $\text{Ru}(\text{dfmb})_2(\text{dmb})$, and (f) $\text{Ru}(\text{dfmb})_3$ as a function of *trans*-stilbene concentration. Rate constants were measured from kinetic traces monitored at 450 nm following 355-nm laser irradiation of nitrogen-saturated samples in 100 mM $[\text{Ru}(\text{NH}_3)_6]\text{Cl}_3$. Slope (m) in units of $10^8 \text{ M}^{-1} \text{ s}^{-1}$.

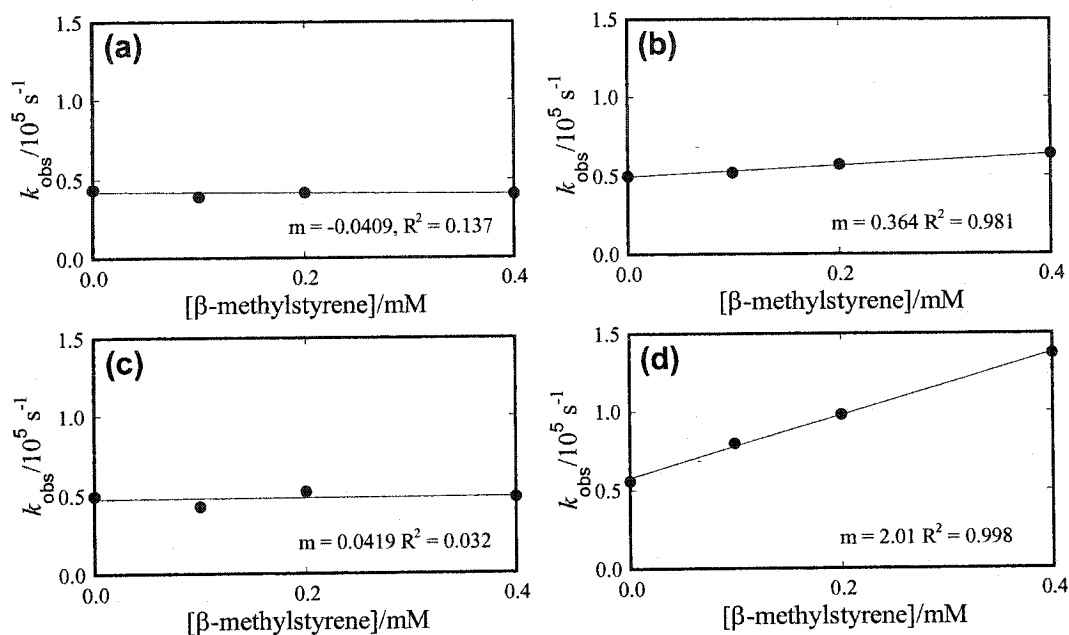


Figure 2-9. Observed rate constants for the recovery of Ru(II) of (a) $\text{Ru}(\text{dmeb})_2(\text{dmb})$, (b) $\text{Ru}(\text{dmeb})_3$, (c) $\text{Ru}(\text{dfmb})_2(\text{dmb})$, and (d) $\text{Ru}(\text{dfmb})_3$ as a function of β -methylstyrene concentration. Rate constants were measured from kinetic traces monitored at 450 nm following 355-nm laser irradiation of nitrogen-saturated samples in 100 mM $[\text{Ru}(\text{NH}_3)_6]\text{Cl}_3$. Slope (m) in units of $10^8 \text{ M}^{-1} \text{ s}^{-1}$.

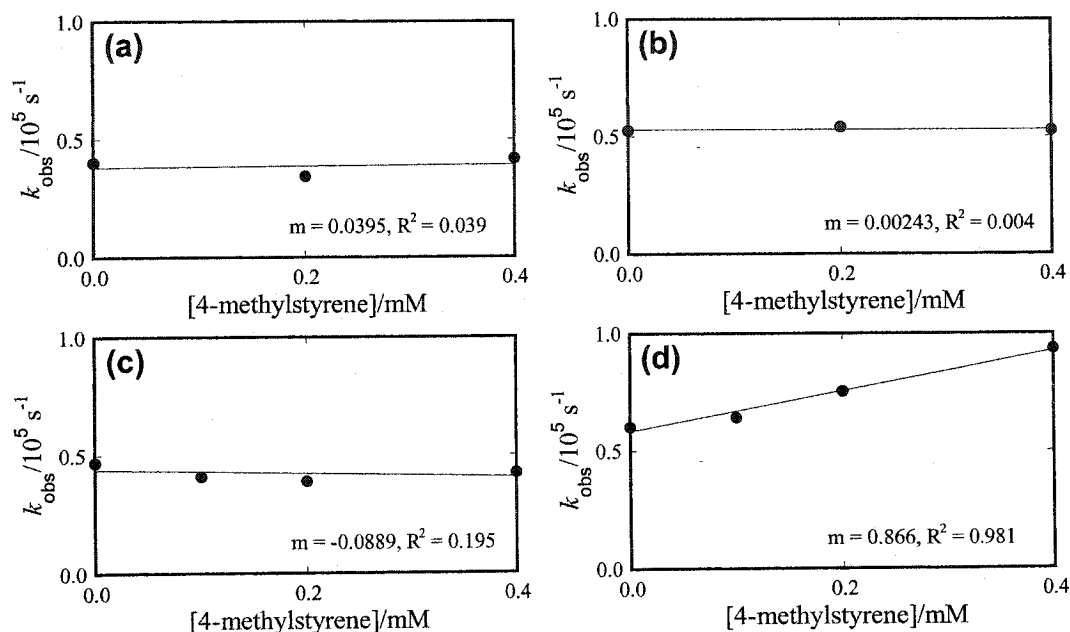


Figure 2-10. Observed rate constants for the recovery of Ru(II) of (a) $\text{Ru(dmeb)}_2(\text{dmb})$, (b) Ru(dmeb)_3 , (c) $\text{Ru(dfmb)}_2(\text{dmb})$, and (d) Ru(dfmb)_3 as a function of 4-methylstyrene, measured from kinetic traces at 450 nm following 355-nm laser irradiation of nitrogen-saturated samples in 100 mM $[\text{Ru}(\text{NH}_3)_6]\text{Cl}_3$. Slope (m) in units of $10^8 \text{ M}^{-1} \text{ s}^{-1}$.

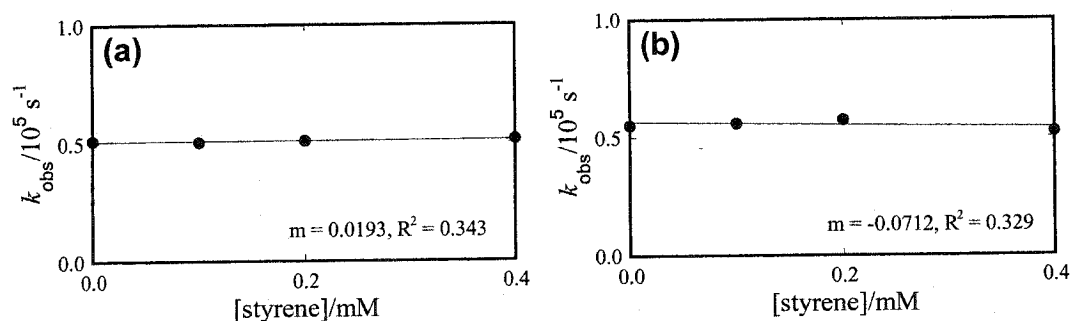


Figure 2-11. Observed rate constants for the recovery of Ru(II) of (a) Ru(dmeb)_3 and (b) Ru(dfmb)_3 as a function of styrene concentration, measured from kinetic traces monitored at 450 nm following 355-nm laser irradiation of nitrogen-saturated samples in 100 mM $[\text{Ru}(\text{NH}_3)_6]\text{Cl}_3$. Slope (m) in units of $10^8 \text{ M}^{-1} \text{ s}^{-1}$.

2.3 Discussion

This chapter demonstrates the utility of tris(bipyridyl)ruthenium complexes for the oxidation of organic substrates to their respective cations. Moreover, a perspective of the types of substrates that could be oxidized by Ru(II)* and Ru(III) states in aqueous solutions was gathered, along with the ligand substituents required for such oxidations; *i.e.* the selectivity of substrate oxidation.

2.3.1 Relationship between thermodynamics and kinetics

The correlation between thermodynamics and kinetics is one of the most important aspects of this chapter. Both the oxidation of Ru(II)* to Ru(III) by the electron acceptor, and the oxidation of the substrate by Ru(III), demonstrate that the kinetics of the electron transfer are dependent on the thermodynamic Gibbs free energy (ΔG°) of the transfer. This free energy term is related to the difference between the two reduction potentials (ΔE) of the associated half-reactions by the Nernst equation, 2.1.

$$\Delta G^\circ = -nF\Delta E \quad (2.1)$$

In this equation, n corresponds to the number of moles of electrons transferred in the reaction, which for the processes studied in this chapter is one; and F is Faraday's constant. Since the values of $-\Delta G^\circ$ and ΔE are directly proportional ($\Delta G^\circ \propto \Delta E$), the two terms are often used interchangeably.

However, while the Gibbs free energy parameter ΔG° is a measure of the thermodynamic feasibility of a reaction, it does not represent the true thermodynamic

“driving force.” Electron transfers that only involve a simple transfer of an electron are termed “outer sphere,” while those involving significant rearrangements of groups or atoms, for instance substantial bond-length modifications or hydride transfers, are termed “inner sphere.” In this chapter, it is obvious that the type of electron transfers studied are predominantly outer-sphere processes. For any electron transfer to occur, an acceptor and a donor need to be brought to close proximity so that orbital overlap is possible. The bringing together of two reactants to a reactive configuration for an outer-sphere electron transfer involves a significant reorganization of solvent molecules, notably changes in solvent coordination and polarization, both before and after the electron transfer. These reorganization processes require energy, the amount of which is denoted by the parameter λ . It can be envisioned then, that if the free energy ΔG° released by a seemingly exogenic electron transfer is insufficient to cover the reorganization energy, the addition of energy will be required.

The necessary addition of energy for an electron transfer to occur is somewhat analogous to the activation energy of a conventional chemical reaction that is governed by Arrhenius theory, where a higher activation energy results in a slower reaction. Similarly, there is a relationship between ΔG° , λ , and k_{et} , the rate of an electron transfer, in what is known as the Marcus theory of electron transfer. A combination of classical and semi-classical interpretations of the theory is best represented by equation 2.2.

$$k_{\text{et}} = K_{\text{el}} \nu_{\text{n}} \exp \left[\frac{-(\lambda + \Delta G^\circ)^2}{4\lambda RT} \right] \quad (2.2)$$

In this equation, K_{el} corresponds to the electronic transmission coefficient, ν_n the nuclear collision frequency, R the universal gas constant, and T the temperature; the product of the first two terms $K_{el}\nu_n$ is generally accepted to $1.0 \times 10^{11} \text{ s}^{-1}$.¹¹⁷

One of the most celebrated implications of Marcus theory is the formation of an inverted parabola, represented in Figure 2-12, when k_{et} is plotted against $-\Delta G^\circ$ according to equation 2.2. On the left side of the curve, known as the “normal region,” the theory predicts that k_{et} increases as the reaction becomes more exogonic (more negative ΔG°), reaching a maximum value at $-\Delta G^\circ = \lambda$. With highly exogonic reactions on the right-hand side, where $-\Delta G^\circ > \lambda$, the rate of electron transfer decreases in this “inverted region.” While the existence of such an inverted region has been confirmed for rigid, *intramolecular* processes (e.g. electron transfer through proteins and DNA), its presence in *intermolecular* electron transfers has been difficult to confirm and only recently did a report¹¹⁸ of the first definitive confirmation of the inverted region in intermolecular processes appear in the literature. One major factor that has hampered the observation of the inverted region is the diffusion-controlled limit of the solvent used, thereby requiring highly exogonic electron transfers before changes in rate are observable.

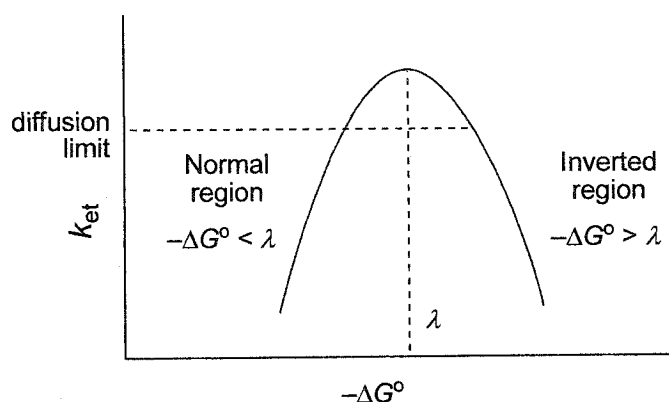


Figure 2-12. Marcus relationship between the rate (k_{et}) and the free energy (ΔG°) of an electron-transfer reaction.

It is important then, to have an approximate idea of the value of the reorganization energy. Since reorganization is attributed to changes in solvent molecule coordination and polarization, λ is dependent on the dielectric properties of a solvent as well as the distance of electron transfer. The value of λ for an outer-sphere process can be approximated by equation 2.3.

$$\lambda = (\Delta e)^2 \left[\frac{1}{2r_A} + \frac{1}{2r_D} - \frac{1}{d} \right] \left[\frac{1}{D_{\text{op}}} - \frac{1}{D_s} \right] \quad (2.3)$$

Here, Δe is the number of electrons transferred in the reaction (one); r_A and r_D are the radii of the acceptor and donor, respectively; and D_{op} and D_s are the respective optical and static dielectric constants for the solvent (for water, 1.77 and 785.5, respectively). As well, d corresponds to the distance of the electron transfer and can be approximated as the sum of r_A and r_D .

Reorganization energies have been calculated in the literature for electron transfers between $\text{Ru}(\text{bpy})_3$ or $\text{Ru}(\text{dmb})_3$ in their $\text{Ru}(\text{II})^*$ states and various organic compounds, including phenolate ions in water and aromatic amines in acetonitrile. In all cases, reorganization energies ranged between 0.81–0.87 eV.^{79,117} Since these organic compounds are not considerably different in size from the substrates investigated in this chapter, a reorganization energy of 0.8 eV can serve as reasonable approximation.

Thus, for electron transfer processes with $\Delta E < 0.8$ V, the reaction would lie in the normal region of the Marcus curve, where $-\Delta G^\circ < \lambda$, and the second-order rate constants of electron transfer would increase with ΔE or $-\Delta G^\circ$. The maximum rate of electron transfer would be observed at $\Delta E = +0.8$ V, but due to diffusional limits, the maximum would be achieved at a somewhat lower ΔE value (Figure 2-12).

2.3.2 Reactivity of $\text{Ru}(\text{II})^*$ excited states

In all experiments involving the use of $\text{Ru}(\text{II})^*$ as an oxidant or a reductant, the processes of oxidation or reduction were inferred by monitoring changes to the lifetime of the $\text{Ru}(\text{II})^*$ emission at 620 nm.

2.3.2.1 Reactivity with organic substrates

The use of $\text{Ru}(\text{II})^*$ states as oxidants (Scheme 2-4, k_1) was evaluated by monitoring changes to the $\text{Ru}(\text{II})^*$ emission lifetime after the addition of 4 mM *trans*-anethole (Table 2-3), the most easily oxidized substrate used in this study (Table 2-2). With all complexes, the presence of 4 mM *trans*-anethole did not noticeably quench the

Ru(II)* excited state, inferring that oxidation of the substrate to its radical cation did not occur at a detectable rate. The lifetime of the strongest Ru(II)* oxidant, Ru(dfmb)₃, was measured as 1089 ns ± 2%, corresponding to a rate constant $k_d = 9.18 \times 10^5 \text{ s}^{-1}$. Since oxidation was inferred from increases to the observed pseudo first-order decay according to the relationship $k_{\text{obs}} = k_d + k_1[\text{trans-anethole}]$, where k_{obs} would need to be greater than $9.34 \times 10^5 \text{ s}^{-1}$ to be significant based on the 2% error, only k_1 greater than $4.0 \times 10^6 \text{ M}^{-1} \text{ s}^{-1}$ would cause noticeable and significant changes to the Ru(II)* lifetime.

Based on the similarities between the reduction potentials of the (II)*/(I) couple of Ru(dfmb)₃ (Table 2-1) and that of the *trans*-anethole radical cation (Table 2-2), with a ΔE of about zero, it is not surprising that the electron transfer was too slow to be observable. Thus, the Ru(II)* states of other complexes, which are even weaker oxidants than Ru(dfmb)₃, were not able to oxidize *trans*-anethole. Since this easily oxidized substrate was not oxidized, the ability of Ru(II)* to oxidize the other substrates was not investigated, since such combinations would result in even lower ΔE values. Accounting for a reorganization energy of 0.8 V, even the electron transfer between Ru(II)* of Ru(dfmb)₃ and *trans*-anethole is endogonic.

2.3.2.2 Reactivity with electron acceptor

In experiments involving the electron acceptor [Ru(NH₃)₆]Cl₃, the Ru(II)* excited state functions as a reductant, leading to the generation of the stable, ground state Ru(III). Electron transfer between Ru(II)* and the acceptor was inferred from increases to the rate of Ru(II)* decay (Figure 2-2). Clearly, there is a noticeable trend between the second-

order rate constants of Ru(II)* quenching and ΔE . A maximum rate of about $2 \times 10^9 \text{ M}^{-1} \text{ s}^{-1}$, which is in the order of a diffusion-controlled reaction, was observed when ΔE was between +0.9 V to +1.2 V. Since the reorganization energy lies near +0.8 V, it is possible that these values may lie in the inverted region of the Marcus curve. However, both the diffusion limit and errors in ΔE forbid an accurate assessment. Nonetheless, the results show that Ru(II)* states featuring ligands containing electron-donating substituents are more rapidly oxidized to their Ru(III) states.

It is also possible to argue whether the quenching of Ru(II)* by the acceptor is indeed a result of electron transfer, or whether it is caused by a transfer of excited-state energy to the electron acceptor. However, both experimental evidence and theory provide strong support for the former. First, if quenching occurred by energy transfer, then Ru(II)* would be converted back to Ru(II) instead of oxidation to Ru(III). The kinetics of the Ru(II)* decay at 620 nm would therefore be identical with the recovery of Ru(II) bleaching at 450 nm, and this is certainly not the case (Figure 2-4). Second, the Forster theory of energy transfer¹¹⁹ proposes that, in order for possible energy transfer, there must be spectral overlap between the excited-state emission of Ru(II)* and the absorption of the quencher. Since the emission of Ru(II)* occurs near 620 nm, a wavelength at which $[\text{Ru}(\text{NH}_3)_6]\text{Cl}_3$ has no detectable absorption, it is clear that the mechanism of quenching by energy transfer can be ruled out. Literature data^{114,115} also suggests that the primary mode of Ru(II)* quenching by this acceptor is *via* oxidative electron transfer.

2.3.3 Reactivity of Ru(III) states with organic substrates

Although Ru(III) is generated *via* photoinduced electron transfer between Ru(II)* and an electron acceptor, the electron transfer between Ru(III) and a substrate is a standard electrochemical reaction. The only possible method of converting Ru(III) to Ru(II) is by reductive electron transfer, and therefore, energy transfer is not applicable. Rate constants for the intermolecular substrate oxidation by Ru(III), along with the corresponding potential differences (ΔE), are provided in Table 2-6.

Two discrepancies are noticeable in Table 2-6, both of which relate to reduction potentials. First, the rate constants suggest that Ru(dfmb)₂(dmb) is a weaker oxidant than Ru(dmeb)₃, contrary to data in Table 2-1. However, the potentials for Ru(dfmb)₂(dmb) were assumed to be similar to that of Ru(dfmb)₂(bpy). Yet, the substitution of bpy with the electron-donating dmb should decrease the oxidizing ability of a complex, so there is likely error in the assumption that the dmb and bpy derivatives have similar potentials.

Second, the rate constants observed for 4-methoxycumene (4-isopropylanisole) suggest that it is more easily oxidized than *trans*-stilbene, contrary to electrochemical data in Table 2-2 (+1.57 V and +1.48 V, respectively). It is important to note that there is likely some error and discrepancy in the reduction potentials found in the literature. For instance, a value of +1.46 was reported¹²⁰ for the derivative 4-ethylanisole, and as this derivative and 4-isopropylanisole are structurally similar, the value of +1.57 V for the latter appears to be excessively high. As well, the potentials in Table 2-2 were measured in acetonitrile, while the studies herein were performed in water. Solvent effects may also introduce additional error.

Nonetheless, the most easily oxidized substrate *trans*-anethole (Table 2-2) exhibited the highest rate constant of electron transfer, reaching nearly $2 \times 10^9 \text{ M}^{-1} \text{ s}^{-1}$ at a relatively low ΔE of +0.11 V when oxidized by the Ru(III) state of Ru(dmeb)₂(dmb). While this electron transfer is undoubtedly in the Marcus normal region, continued increases in ΔE , up to +0.42 V with the complex Ru(dfmb)₃, did not result in additional rate increases because the electron transfer is already occurring at the diffusion limit.

A maximum electron-transfer rate of only about $1 \times 10^9 \text{ M}^{-1} \text{ s}^{-1}$ was observed for the substrate 4-methoxycumene, at a ΔE of -0.02 V for oxidation by Ru(III) of Ru(dmeb)₃, as seen in Table 2-6. Under Marcus normal-region conditions, further increases to ΔE should increase the rate constant of electron transfer, since $1 \times 10^9 \text{ M}^{-1} \text{ s}^{-1}$ is somewhat lower than the diffusion limit. However, when ΔE was increased to +0.18 V, the rate did not change, suggesting that other factors limiting the rate may exist. One possible factor is the size of the substrate; not only do larger substrates diffuse more slowly, they may not be in the proper conformation required for orbital overlap and electron-transfer upon collision with the ruthenium complex. This explanation may also account for the maximum oxidation rate constant of about $1 \times 10^8 \text{ M}^{-1} \text{ s}^{-1}$ observed for the significantly larger substrate, and more insoluble, *trans*-stilbene between ΔE of +0.07 to +0.27 V.

Interestingly, substrate oxidation was observed even when ΔE was negative (Table 2-6), but at much slower rates; e.g. $2 \times 10^7 \text{ M}^{-1} \text{ s}^{-1}$ for *trans*-anethole and the Ru(III) state of Ru(bpy)₃, with $\Delta E = -0.06 \text{ V}$. As well, reorganization energy is also required, resulting in an electron transfer that is thermodynamically unfavourable.

2.3.4 Selective oxidation of organic substrates

While it may seem that the slow rates of electron transfer observed between some substrate-complex combinations in Table 2-6 are undesirable, this is in fact not the case. Photoinduced electron transfer is a useful method for generating reactive intermediates, and one problem that commonly arises with this method is the lack of selective oxidation of a single substrate, usually the one that is most easily oxidized, in a mixture of several substrates. This often occurs when the reduction potential of the oxidant is too high.

The solution to this problem lies in the use of oxidants that have easily modifiable electrochemical properties, and the results in this chapter strongly suggest that tris(bipyridyl)ruthenium complexes are useful for selective substrate oxidation for two reasons. First, the electrochemical properties of the complexes are easily manipulated *via* the relatively simple modification of ligand substituent and by the use of combinations of different ligands; for instance, only five ligands were used to prepare eight complexes (Table 2-6). Second, the rate constants that the complexes react with substrates are dependent on the electrochemical properties of both the complex and the substrate, suggesting that a complex can be “fine tuned” for the oxidation of a particular substrate.

2.4 Conclusion

The results presented in this chapter provide insight into the types of substrates that can be oxidized, as well as the second-order rate constants for their oxidation by tris(4,4'-disubstituted-2,2'-bipyridine)ruthenium complexes. More importantly, these results provide significant implications to the design of substrate-linked complexes for

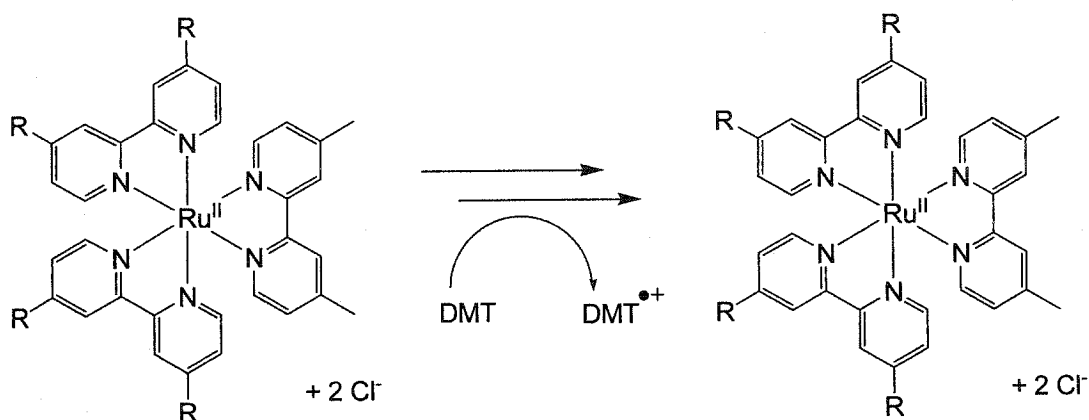
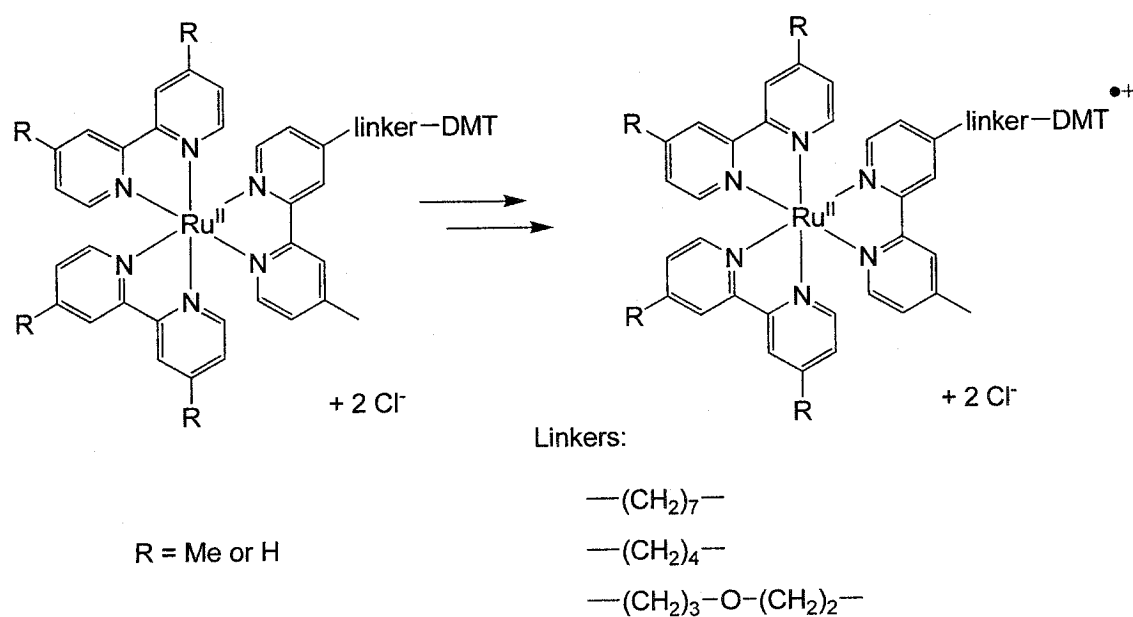
intramolecular oxidation. Since these linked complexes are intended for biological applications, it is critical that the photosensitizer core selectively oxidizes the linked substrate and not the other components present, *e.g.* the biomolecule. As mentioned in the last chapter, various literature studies have used transition-metal complexes to oxidize the biomolecule itself, and in these cases, the selectivity of oxidation is less important. However, for our intended studies, it would be ideal then to choose a photosensitizer core with the minimum electrochemical properties sufficient for oxidizing the substrate. For example, a photosensitizer core based on Ru(dmeb)₂(dmb) would be ideal for the oxidation of a linked *trans*-anethole moiety; the use of Ru(dfmb)₂(dmb) would not be necessary.

Chapter Three: Oxidation of *N,N*-Dimethyl-*p*-toluidine

3.1 Introduction

In the previous chapter, the range of organic substrates that could be oxidized by the Ru(II)* and Ru(III) states of a variety of substituted tris(bipyridyl)ruthenium complexes *via* intermolecular electron transfer was surveyed. This chapter now concentrates on the oxidation of the basic substrate *N,N*-dimethyl-*p*-toluidine (DMT) by two complexes, Ru(dmb)₃ and Ru(bpy)₂(dmb), *via* both intermolecular and intramolecular electron transfer, represented in Scheme 3-1. For the latter, DMT is covalently attached to the complexes by means of a linker. Specifically, this chapter investigates the effect of different linkers, methyl substitution on the bipyridine ligands, and pH on the rate and efficiency of DMT radical cation generation by Ru(II)* and Ru(III) states.

While the chapters in this thesis are in a sequence that seems to be a logical research progression, where it appears that the fundamental concepts derived in one chapter are applied to and expanded in the following, they are in fact not the case. The experiments performed in this chapter with DMT were actually carried out in order to explain some of the results observed for the oxidation of amino-substituted diphenylalkanes in the next chapter. DMT therefore serves as a simple yet reasonable model substrate for the more sophisticated amino-substituted diphenylalkanes.

Intermolecular oxidationIntramolecular oxidation

Scheme 3-1. Schematic of the inter- and intramolecular oxidation of *N,N*-dimethyl-*p*-toluidine (DMT) to its radical cation by tris(bipyridyl)ruthenium complexes.

The oxidation of DMT is more complicated than many of the substrates examined in the previous chapter, as it is relatively easily oxidized and has a reduction potential¹²¹

of +0.71 V *versus* SCE in acetonitrile for the radical cation; reduction potentials relative to NHE in water should be similar.⁷⁸ This reduction potential suggests that both the Ru(II)* and Ru(III) states of Ru(dmb)₃ and Ru(bpy)₂(dmb), Table 3-1, may be able to oxidize the substrate, leading to the introduction of an inherent problem: competition now exists for the Ru(II)* excited state, which may be reduced by the substrate to Ru(I) or oxidized to Ru(III) by an added sacrificial electron acceptor, such as [Ru(NH₃)₆]Cl₃.

Table 3-1. Relevant reduction potentials (V) for Ru(dmb)₃, Ru(bpy)₂(dmb), the substrate *N,N*-dimethyl-*p*-toluidine, and the electron acceptor [Ru(NH₃)₆]Cl₃.

Compound	III/II	II/I	II*/I	III/II*	(•+)/0
Ru(dmb) ₃	+1.10	-1.45	+0.64	-0.99	--
Ru(bpy) ₂ (dmb)	+1.27	-1.36	+0.79	-0.83	--
[Ru(NH ₃) ₆]Cl ₃	+0.10	--	--	--	--
DMT	--	--	--	--	+0.71

Potentials are from published data^{71,82,121,122} and those relative to SCE in acetonitrile, except for the electron acceptor, which is relative to NHE in water.

From the reduction potentials in Table 3-1, it is apparent that the oxidation of the Ru(II)* excited states of both complexes to Ru(III) by the acceptor is more thermodynamically favourable than the corresponding reduction of Ru(II)* to Ru(I) by the substrate. However, these thermodynamic values do not address the kinetic aspects of

the competitive reactions, particularly where both the concentration of DMT and electron acceptor are variable in the intermolecular electron transfers and where the effective concentration of an intramolecularly linked DMT is unknown.

3.2 Results

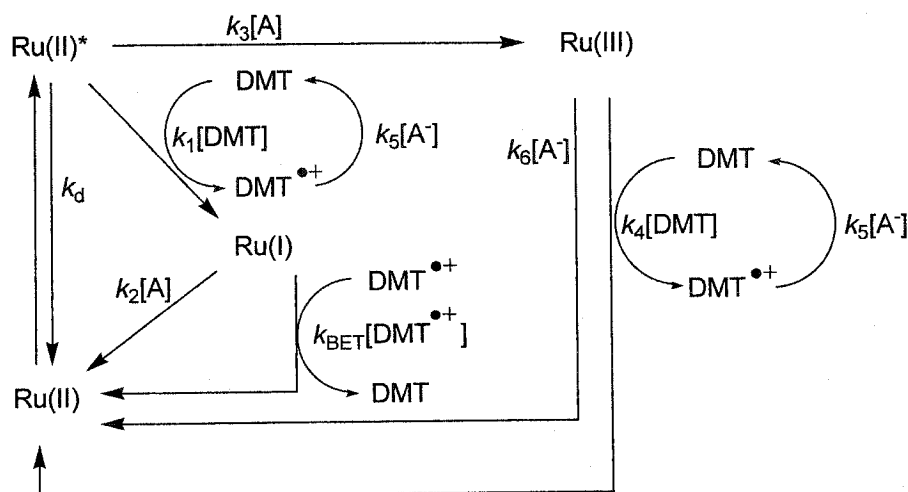
Inter- and intramolecular electron transfer experiments were carried out in 250 mM and 25 mM buffer solutions, respectively. The pH and buffers used were pH 3.2, sodium formate; 4.2, 4.7, 5.1, and 5.6, sodium acetate; and 6.5, sodium phosphate.

3.2.1 Intermolecular oxidation

As discussed in the previous chapter, the exploitation of Ru(III) states over Ru(II)* for substrate oxidation is more favourable. Ru(III) has a higher oxidizing ability and regenerates the initial Ru(II) state upon substrate oxidation, while Ru(II)* is a weaker oxidant and also generates an undesirable and highly reducing Ru(I) that may undergo relatively fast charge recombination with the newly formed substrate radical cation. Nonetheless, both Ru(II)* and Ru(III) states were evaluated as an oxidant for DMT.

Potential pathways for the intermolecular oxidation of DMT, as postulated from the reduction potentials (Table 3-1), are presented in Scheme 3-2. In the previous chapter, the competition for Ru(II)* by the substrates were essentially a non-issue, as the substrates examined therein were relatively difficult to oxidize and required the higher oxidizing power of Ru(III). As well, the relatively high concentration of electron acceptor used relative to the substrates ensured that the oxidation of Ru(II)* to Ru(III) was the

predominant process. However, with DMT, the similarities between the reduction potentials of its radical cation and the Ru(II)^* states of the two complexes (Table 3-1) suggest that Ru(II)^* may be a feasible oxidant and that the route of Ru(II)^* to Ru(I) via bimolecular rate constant $k_1[\text{DMT}]$ may be important.



Scheme 3-2. Possible routes for the intermolecular oxidation of DMT in the presence of a reversible electron acceptor, $[\text{Ru}(\text{NH}_3)_6]\text{Cl}_3$, denoted as A.

3.2.1.1 Intermolecular oxidation by Ru(II)^*

To assess the feasibility of DMT oxidation by the Ru(II)^* excited states of Ru(dmb)_3 and $\text{Ru(bpy)}_2(\text{dmb})$, $k_1[\text{DMT}]$, the rate of Ru(II)^* decay was monitored at 370 nm in the *absence* of any electron acceptor at various pH and DMT concentrations. Without any acceptor present, the only possible routes of Ru(II)^* consumption are k_d and $k_1[\text{DMT}]$, the sum of which constitutes the observed, pseudo first-order rate constant for Ru(II)^* decay, k_{obs} . Second-order rate constants for the oxidation of DMT were

determined from the slopes of pseudo first-order rate plots of the observed rate of Ru(II)* disappearance as a function of DMT concentration ($k_{\text{obs}} = k_d + k_1[\text{DMT}]$). In all experiments, DMT was varied up to 4 mM by adding stock acetonitrile solutions of DMT to the nitrogen-purged, buffered solutions of the complexes. Any changes to the pH of the buffered solutions, as well as dilution by up to 1% acetonitrile, were deemed negligible.

In the absence of any DMT, the Ru(II)* lifetime measured for Ru(dmb)₃ after 355 nm excitation under nitrogen was 330 ns, corresponding to a decay of $3.0 \times 10^6 \text{ s}^{-1}$ that was reproducible to within 2% (*i.e.*, $3.0 \pm 0.1 \times 10^6 \text{ s}^{-1}$). Lifetimes were similar in pure water and in 250 mM buffer at all pH values investigated. When the solutions were supplemented with up to 4 mM DMT, no measurable increases in the rate of Ru(II)* decay were observed at all pH values studied, suggesting that the oxidation of DMT by Ru(II)* was too slow to impact significantly the Ru(II)* decay. Since the decay in the absence of DMT is $3.0 \pm 0.1 \times 10^6 \text{ s}^{-1}$, only decay increases of $0.2 \times 10^6 \text{ s}^{-1}$ would be observable and experimentally significant. At 4 mM DMT, this increase corresponds to a second-order rate constant for the reaction between DMT and Ru(II)* of $5 \times 10^7 \text{ M}^{-1} \text{ s}^{-1}$, which is therefore the minimum detectable rate. It is interesting that this reaction occurs in acetonitrile⁷⁹ at $6.3 \times 10^7 \text{ M}^{-1} \text{ s}^{-1}$, which is near the predicted minimum detectable rate.

For Ru(bpy)₂(dmb), the Ru(II)* lifetime measured under similar conditions was 475 ns, also reproducible to within 2%, corresponding to a decay of $2.1 \pm 0.1 \times 10^6 \text{ s}^{-1}$, independent of pH or buffer. When up to 4 mM DMT was added, changes in the pseudo first-order decay of Ru(II)* were observed only at pH 5.1 and above, inferring the oxidation of DMT by Ru(II)*. A typical kinetic trace is shown in Figure 3-1. The second-

order rate constants for this reaction (k_1), extracted from pseudo first-order plots (Figure 3-2) increased with pH, from $0.57 \times 10^8 \text{ M}^{-1} \text{ s}^{-1}$ at pH 5.1, to $1.2 \times 10^8 \text{ M}^{-1} \text{ s}^{-1}$ at pH 5.6, and finally $2.3 \times 10^8 \text{ M}^{-1} \text{ s}^{-1}$ at pH 6.5. However, no changes to the decay upon the addition of DMT were observed at pH values 4.7 and lower, although, like $\text{Ru}(\text{dmb})_3$, the minimum detectable rate constant is about $5 \times 10^7 \text{ M}^{-1} \text{ s}^{-1}$.

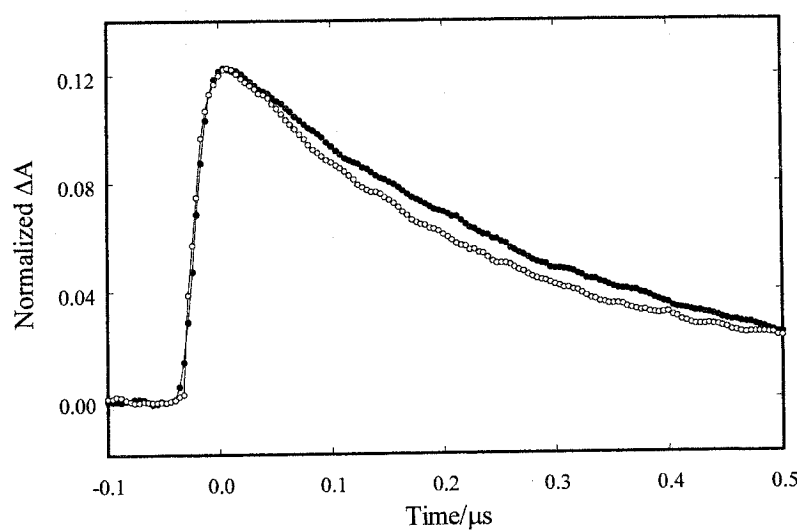


Figure 3-1. Time-resolved kinetic trace of $\text{Ru}(\text{II})^*$ monitored at 370 nm following 355-nm laser irradiation of $\text{Ru}(\text{bpy})_2(\text{dmb})$ in nitrogen-saturated 250 mM sodium phosphate pH 6.5 containing (●) 0 mM or (○) 4 mM DMT.

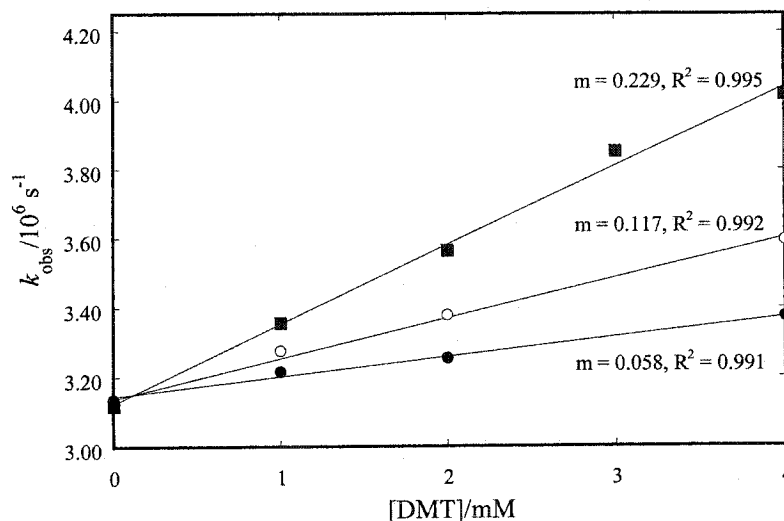


Figure 3-2. Observed rate constants for the decay of Ru(II)^* of $\text{Ru(bpy)}_2(\text{dmb})$ as a function of DMT at pH (●) 5.1, (○) 5.6, and (■) 6.5, measured from kinetic traces monitored at 370 nm following 355-nm laser irradiation. Slope (m) in units of $10^9 \text{ M}^{-1} \text{ s}^{-1}$.

The oxidation of DMT by the Ru(II)^* excited state, $k_1[\text{DMT}]$, was observed for $\text{Ru(bpy)}_2(\text{dmb})$, and only at higher pH values, but not for Ru(dmb)_3 . These observations correlate with those predicted from the previous chapter, where the presence of electron-donating groups on the bipyridine ligands reduces the rate of substrate oxidation, as well as with the reduction potentials of the two complexes (Table 3-1). More importantly, these results show that the competition for the Ru(II)^* excited state of Ru(dmb)_3 by up to 4 mM DMT at all pH studied is negligible; for $\text{Ru(bpy)}_2(\text{dmb})$, the competition may be significant at pH 5.1 or above. As well, the pH-dependence of the electron transfer suggests that only the unprotonated form of DMT can be oxidized; further details are gathered from experiments in the following section.

3.2.1.2 Intermolecular oxidation by Ru(III)

While the reductive quenching of Ru(II)* states by aromatic amines in acetonitrile has been documented in the literature,⁷⁹ no data related to oxidation of these amines by Ru(III) exists. Thus, this section characterizes the oxidation of DMT by the Ru(III) states of the complexes Ru(dmb)₃ and Ru(bpy)₂(dmb).

Like the experiments carried out in the previous chapter, Ru(III) states were generated *via* the oxidative quenching of Ru(II)* excited states by the electron acceptor [Ru(NH₃)₆]Cl₃. Data in Table 2-4 suggest that this acceptor quenches the Ru(II)* excited states of Ru(dmb)₃ and Ru(bpy)₂(dmb) at approximately $2 \times 10^9 \text{ M}^{-1} \text{ s}^{-1}$. Thus, we postulated that, at 60 mM [Ru(NH₃)₆]Cl₃, the competition between Ru(II)* reduction by 4 mM DMT ($k_1[\text{DMT}]$), which proceeds at no greater than $2.3 \times 10^8 \text{ M}^{-1} \text{ s}^{-1}$ even for Ru(bpy)₂(dmb), and oxidation by the acceptor ($k_3[\text{A}]$) should preferentially favour the latter. The concentration of acceptor was chosen such that the rate constant of Ru(II)* oxidation would be at least 100-fold greater than that of reduction, based on respective concentrations and rate constants of 60 mM at $2 \times 10^9 \text{ M}^{-1} \text{ s}^{-1}$ *versus* 4 mM at $2.3 \times 10^8 \text{ M}^{-1} \text{ s}^{-1}$.

The MLCT absorption of the Ru(II) ground state was conveniently monitored at 450 nm, like the experiments in the previous chapter, to infer substrate oxidation. Thus, any process that consumes Ru(II) would result in a bleach, or negative absorption, and the subsequent regeneration of Ru(II) from Ru(III) would be observed in the form of a bleaching recovery. The monitoring wavelength of 450 nm also overlaps the absorption band of the DMT radical cation (420-540 nm, with a maximum near 485 nm, as

determined by the direct 308-nm photoionization of aqueous DMT; lit.¹²³ 470 nm in acetonitrile), allowing both Ru(II) recovery and radical cation formation by route $k_4[\text{DMT}]$ to be monitored simultaneously.

When buffered solutions of Ru(dmb)_3 without any DMT were irradiated in the presence of 60 mM $[\text{Ru}(\text{NH}_3)_6]\text{Cl}_3$ and monitored at 450 nm (measured $\epsilon = 1.26 \times 10^4$) at very short time scales to capture rapid absorption changes, approximately 3 μM of the Ru(II)^* excited state was initially produced, inferred from the bleaching of ground-state Ru(II) . Small fluctuations in sample concentration and laser power were responsible for variations in the amounts of Ru(II)^* produced. Nevertheless, typically 10% of the total bleaching recovered within the time of the laser pulse, implying that 90% of the excited state was rapidly oxidized to Ru(III) by the electron acceptor. With $\text{Ru(bpy)}_2(\text{dmb})$, also monitored at 450 nm (measured $\epsilon = 1.30 \times 10^4$), similar concentrations of the Ru(II)^* state were generated upon excitation, but 25-30% of the bleaching recovered immediately after the laser pulse, indicating that only 70-75% of Ru(II)^* was oxidized to Ru(III) . These phenomena are illustrated in Figure 3-3, and for both complexes, the percentages of Ru(III) generated were pH-independent. The lower efficiency of Ru(II)^* to Ru(III) conversion for $\text{Ru(bpy)}_2(\text{dmb})$, despite its longer excited-state lifetime, is most likely attributed to its higher III/II^* reduction potential (Table 3-1), rendering it more difficult to oxidize.

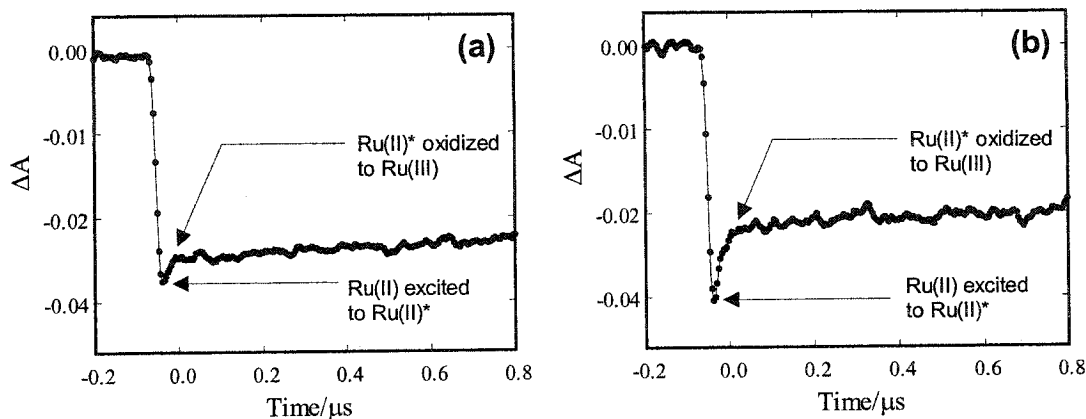


Figure 3-3. Time-resolved kinetic trace monitored at 450 nm following 355-nm laser irradiation of (a) $Ru(dmb)_3$ and (b) $Ru(bpy)_2(dmb)$ in nitrogen-saturated 250 mM sodium phosphate pH 6.5 containing 60 mM $[Ru(NH_3)_6]Cl_3$. Kinetic traces were similar at other pH values investigated.

When no DMT was present to reduce $Ru(III)$ to $Ru(II)$, a slow recovery of bleaching was observed for both complexes (Figure 3-3). This is attributed to the bimolecular charge recombination of $Ru(III)$ and reduced acceptor, $k_6[A^-]$. At short time scales, the second-order recovery could be approximated to a first-order growth of around $1 \times 10^5 s^{-1}$. Hence, the minimum rate of intermolecular oxidation by $Ru(III)$ that can be reliably observed at 4 mM DMT would be approximately $5 \times 10^6 M^{-1} s^{-1}$, in the form of an increase in the rate of $Ru(II)$ recovery.

Upon the addition of up to 4 mM DMT to laser-flash irradiation solutions of $Ru(dmb)_3$ and $Ru(bpy)_2(dmb)$, the amount of $Ru(II)^*$ converted to $Ru(III)$ remained constant at 90% for the former complex and 70-75% for the latter, regardless of pH. This suggests that the predominant mechanism of $Ru(II)^*$ deactivation in the presence of both

electron acceptor and DMT was oxidation to Ru(III), $k_3[A]$, as we had expected from the high concentration of acceptor relative to DMT. Once Ru(III) was generated, the oxidation of DMT was inferred from increases in the pseudo first-order recovery at 450 nm corresponding to the reduction of Ru(III) to Ru(II). The Ru(II) recovery rate for both complexes increased with the addition of up to 4 mM DMT at all pH values, indicating that the Ru(III) states of both complexes were able to oxidize DMT, as anticipated from the reduction potentials (Table 3-1). Representative kinetic traces are shown in Figure 3-4 (a). The recovery of the Ru(II) bleaching at 450 nm also rises above baseline at high DMT levels. This observation is attributed to the absorption of the DMT radical cation ($\lambda_{\text{max}} \approx 490$ nm) that is also seen in the transient absorption spectra Figure 3-4 (b).

The observed pseudo first-order recoveries in the kinetic traces are comprised of a sum of two rate constants, the approximated, first-order $k_6[A^-]$ and the second-order $k_4[\text{DMT}]$. Pseudo first-order rate plots were used for the extraction of second-order rate constants for the electron transfer between Ru(III) states and DMT, and are shown in Figure 3-5 for Ru(dmb)₃ and Figure 3-6 for Ru(bpy)₂(dmb). Corresponding rate-constant data are summarized in Table 3-2, which clearly shows the substituent effect on the rate of DMT oxidation. Errors for the rate constants are estimated to be within 3%. It is interesting that a plot (Figure 3-7) of the second-order rate constants for DMT oxidation by the Ru(III) states of Ru(bpy)₂(dmb) versus those for Ru(dmb)₃ is linear with slope = 1.15, suggesting that the former complex is capable of oxidizing DMT 15% faster than the latter.

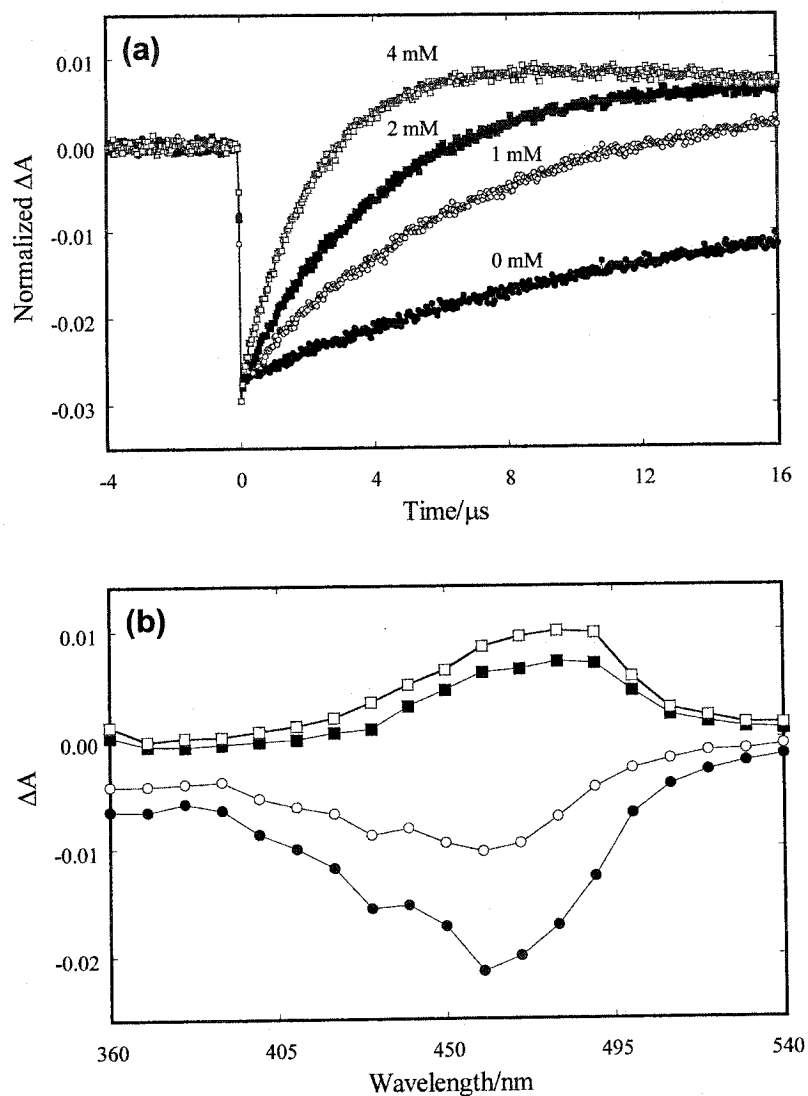


Figure 3-4. (a) Time-resolved kinetic trace of Ru(II) monitored at 450 nm following 355-nm laser irradiation of Ru(dmb)₃ in nitrogen-saturated 250 mM sodium acetate pH 4.2 with 60 mM [Ru(NH₃)₆]Cl₃ and (●) 0 mM, (○) 1 mM, (■) 2 mM, or (□) 4 mM DMT. (b) Transient absorption spectra collected (●) 0.080 μs , (○) 0.72 μs , (■) 3.6 μs , and (□) 6.0 μs after irradiation of the same compound under similar conditions with 4 mM DMT.

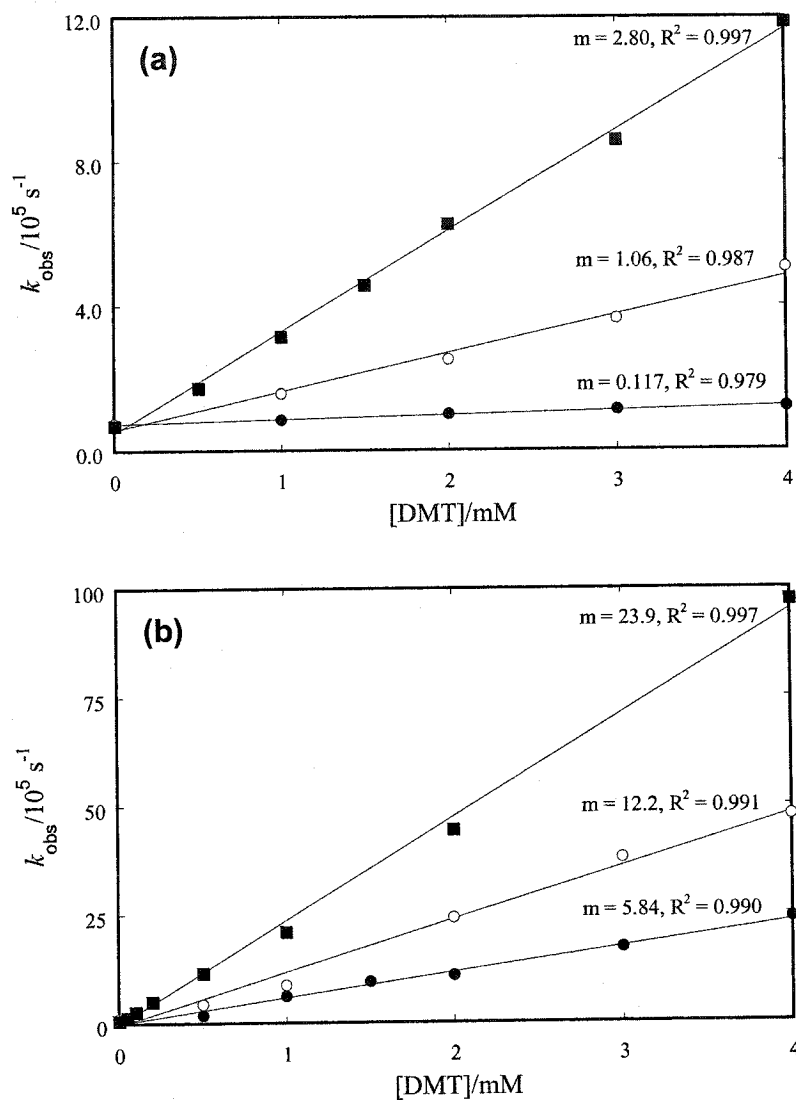


Figure 3-5. Observed rate constants for the recovery of Ru(II) of Ru(dmb)₃ as a function of DMT concentration at pH (a) (●) 3.2, (○) 4.2, (■) 4.7; (b) (●) 5.1, (○) 5.6, (■) 6.5. Rate constants were measured from kinetic traces monitored at 450 nm following 355-nm laser irradiation in the presence of 60 mM [Ru(NH₃)₆]Cl₃. Slope (m) in units of $10^8 \text{ M}^{-1} \text{ s}^{-1}$.

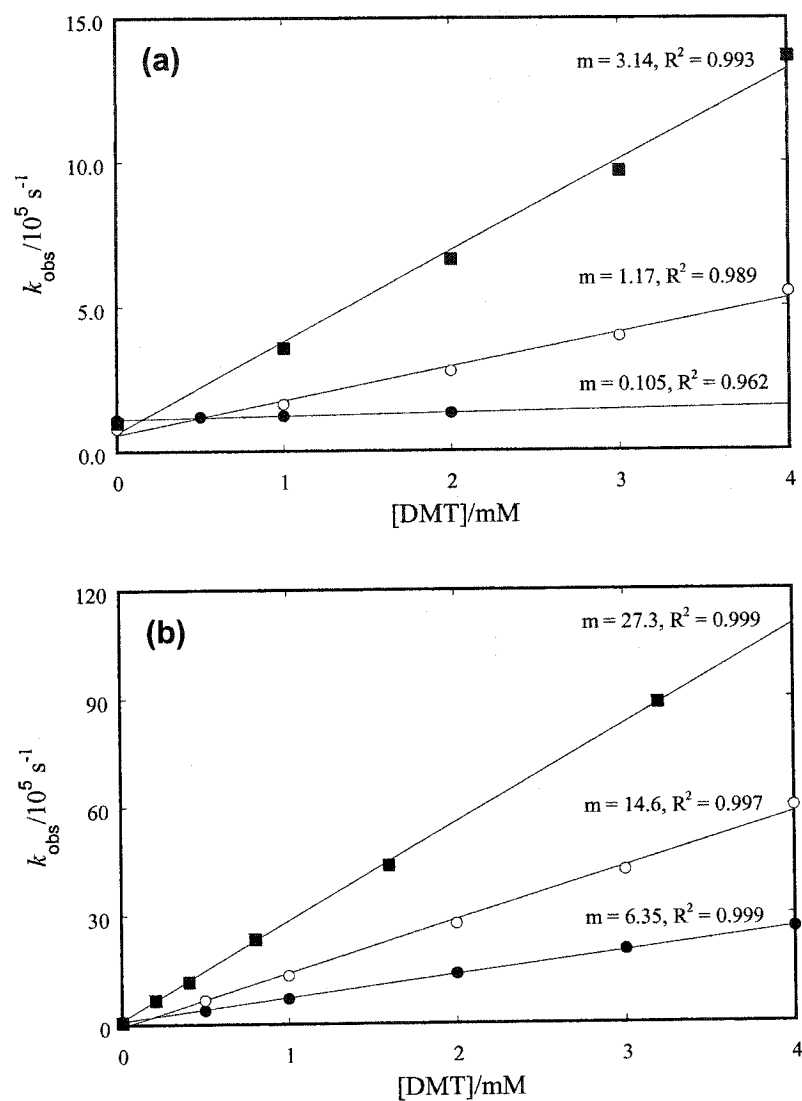
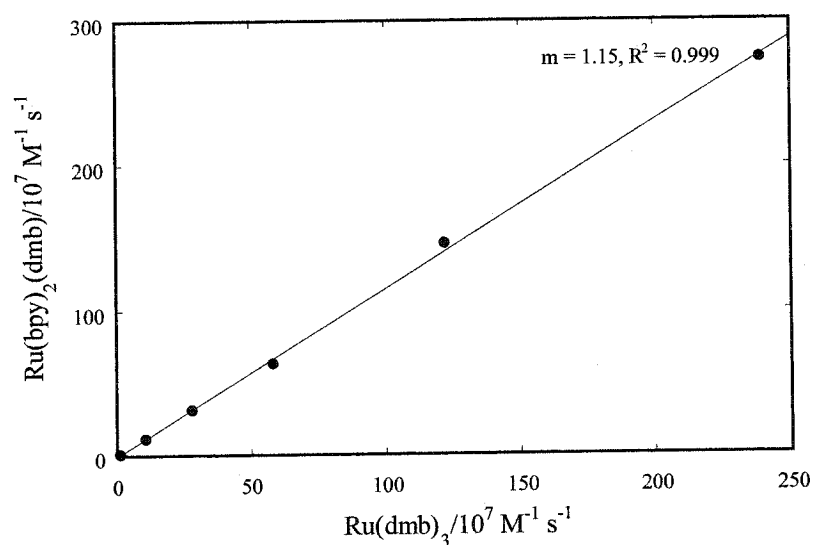


Figure 3-6. Observed rate constants for the recovery of Ru(II) of Ru(bpy)₂(dmb) as a function of DMT concentration at pH (a) (●) 3.2, (○) 4.2, (■) 4.7; (b) (●) 5.1, (○) 5.6, (■) 6.5. Rate constants were measured from kinetic traces monitored at 450 nm following 355-nm laser irradiation in the presence of 60 mM [Ru(NH₃)₆]Cl₃. Slope (m) in units of 10⁸ M⁻¹ s⁻¹.

Table 3-2. Second-order rate constants ($/10^7 \text{ M}^{-1} \text{ s}^{-1}$) for the oxidation of DMT by Ru(III) states of Ru(dmb)_3 and $\text{Ru(bpy)}_2(\text{dmb})$ as a function of pH.

Complex	pH					
	3.2	4.2	4.7	5.1	5.6	6.5
Ru(dmb)_3	1.2	11	28	58	120	240
$\text{Ru(bpy)}_2(\text{dmb})$	1.1	12	31	64	150	270

**Figure 3-7.** Comparison of the second-order rate constants for the oxidation of DMT by the Ru(III) state of $\text{Ru(bpy)}_2(\text{dmb})$ to the oxidation by Ru(dmb)_3 at pH 3.2-6.5.

One question remains; why is the second-order rate constant dependent on pH? It was postulated earlier that this dependence was primarily due to DMT protonation to yield its conjugate acid, DMTH⁺, which cannot be easily oxidized to its radical cation. Should this be true, then the measured second-order rate constant (k_{pH}) should be directly related to some maximum rate (k_{max}) that occurs when the total added substrate is entirely in its base form. Protonation decreases the proportion of the base form, and accordingly, k_{pH} should be proportional to k_{max} relative to the fraction of the total substrate in the base form, as represented in equation 3.1.

$$k_{\text{pH}} = k_{\text{max}} \left(\frac{[\text{Base}]}{[\text{Total}]} \right) = k_{\text{max}} \left(\frac{[\text{DMT}]}{[\text{DMT}] + [\text{DMTH}^+]} \right) \quad (3.1)$$

The fraction of the total substrate that is in the base form is related to the dissociation constant K_a of the conjugate acid, DMTH⁺, as well as the $[\text{H}^+]$, shown in equation 3.2.

$$K_a = \frac{[\text{DMT}][\text{H}^+]}{[\text{DMTH}^+]} \quad (3.2)$$

Substitution of equation 3.2 into the $[\text{DMTH}^+]$ variable of 3.1 yields 3.3.

$$k_{\text{pH}} = k_{\text{max}} \left(\frac{[\text{DMT}]}{[\text{DMT}] + \frac{[\text{DMT}][\text{H}^+]}{K_a}} \right) = k_{\text{max}} \left(\frac{K_a}{K_a + [\text{H}^+]} \right) \quad (3.3)$$

At low acid (high pH), the $[\text{H}^+]$ term is negligible and k_{pH} approaches k_{max} , while at high $[\text{H}^+]$ (low pH), the denominator becomes large and results in a low k_{pH} . At the midpoint is

an inflection point, when $K_a = [H^+]$ and the ratio of [DMT] to $[DMTH^+]$ is 1:1 (pK_a); here, $k_{pH} = \frac{1}{2} k_{max}$. This equation can also be conveniently written as shown in 3.4.

$$k_{pH} = k_{max} \left(\frac{K_a}{K_a + 10^{-pH}} \right) \quad (3.4)$$

To verify the proposal that the dependence of the second-order DMT oxidation rate constants on pH is primarily influenced by DMT protonation, equation 3.4 was fit to data in Table 3-2 to produce the plots, resembling acid-base titration curves, shown in Figure 3-8. The excellent fit of equation 3.4 to the data affirms the protonation hypothesis, and, in addition, pK_a values extracted (≈ 5.7) are in line with literature¹²⁴ and calculated values of 5.5 and 5.7 (ACD Labs pK_a software), respectively.

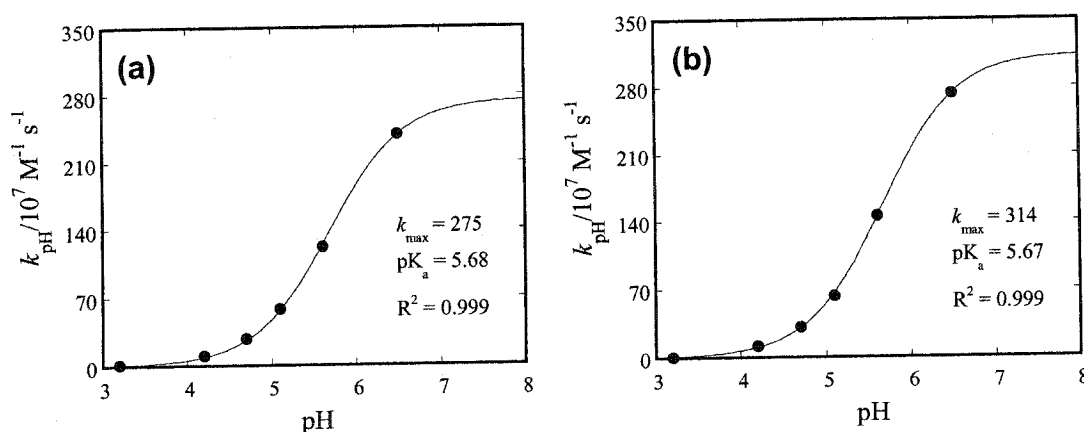


Figure 3-8. Apparent second-order rate constants for the oxidation of DMT by Ru(III) states of (a) Ru(dmb)_3 and (b) $\text{Ru(bpy)}_2(\text{dmb})$ in as a function of pH.

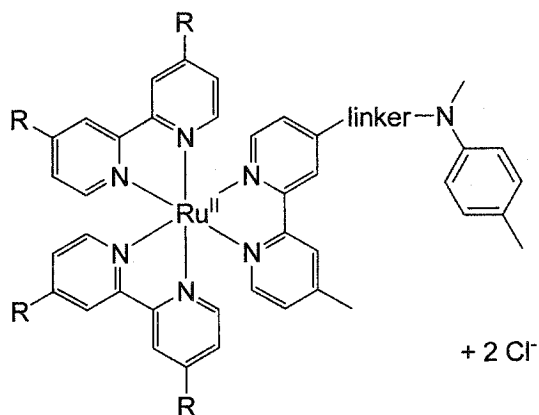
In summary, the results presented in this intermolecular section demonstrate three important points. First, the efficiency of the oxidation Ru(II)^* to Ru(III) by the electron acceptor, $k_3[\text{A}]$, was not affected by the presence of up to the solubility limit of DMT (4 mM), suggesting that this process is preferred over the competitive reduction to Ru(I) , $k_1[\text{A}]$. Of course, this competitive reduction may be significant at higher DMT concentrations. Second, both the Ru(II)^* and Ru(III) states of $\text{Ru(bpy)}_2(\text{dmb})$ can oxidize DMT faster than the respective states of Ru(dmb)_3 , consistent with substituent effects. Finally, the bimolecular rate constants observed for DMT oxidation are in agreement with the titration-curve behaviour expected for the amount of unprotonated DMT as a function of pH, inferring that DMT protonation is responsible for the lower rate constants seen at low pH. It is important to note though, these are *apparent* rate constants and the actual, second-order rate of DMT free-base oxidation (k_{max}) remains pH-independent.

3.2.2 Intramolecular oxidation

To study the oxidation of DMT covalently attached to tris(bipyridyl)ruthenium, six complexes were prepared (Scheme 3-3). In this linking strategy, one of the *N*-methyl groups on DMT was replaced with one of three flexible, long-chained linkers; this substitution of a methyl group with an alkyl chain is not expected to alter significantly its properties, and for convenience, the linked substrate will herein be referred to as linked DMT. On the other end of the linker, either four, six, or seven linker atoms away, is a photosensitizer core corresponding to one of the unlinked counterparts, Ru(dmb)_3 or $\text{Ru(bpy)}_2(\text{dmb})$. Both four- and seven-atom linkers are polymethylenes, while the six-

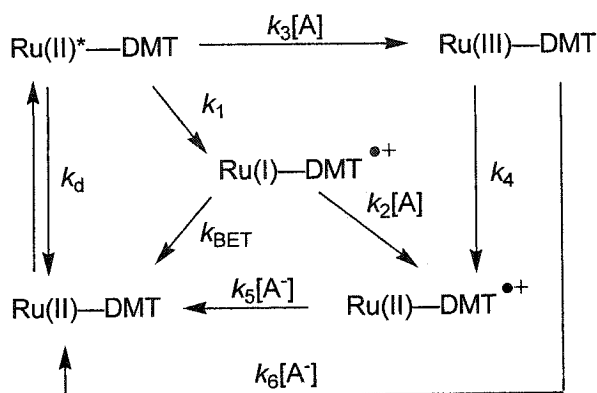
atom version contains an ether oxygen located near the centre of the linker. The choice of different linker lengths was rationalized by the possibility that some hydrophobic environments, such as enzyme active sites, may be deeply buried and distant from the hydrophilic, aqueous exterior, where the charged ruthenium photosensitizer core would most likely reside. The presence of an oxygen allowed the determination of the effect of a simple heteroatom substitution, as well as providing for a linker that is presumably more hydrophilic than one comprised solely of methylene carbons. Overall, the purpose was to evaluate the outcome of various linkers and of pH on the oxidation process, as well as whether the effect of methyl substitution on the ligands previously observed in intermolecular experiments are also applicable to intramolecular oxidation.

The kinetic pathways associated with intramolecular oxidation are different from those for intermolecular oxidation (Scheme 3-2) in that any process associated with DMT now becomes unimolecular. In this intramolecular set of routes (Scheme 3-4), k_1 , k_4 , and k_{BET} are now first-order rate constants. However, intramolecular oxidation is somewhat more complicated than the intermolecular counterpart. While the competition between $k_3[\text{A}]$ and $k_1[\text{DMT}]$ in the intermolecular oxidation studies clearly favoured the latter at up to 4 mM DMT, that assumption cannot be extended here for the simple reason that the effective concentration of a linked DMT moiety is unknown. Due to the presence of competitive pathways $k_3[\text{A}]$ and k_1 , the concentration of acceptor was maintained at a relatively high level, 60 mM, in the hope that $k_3[\text{A}]$ would be the predominant route over k_1 . This concentration of 60 mM is slightly lower than that used in the previous chapter, 100 mM, since the acceptor also absorbs light at 355 nm.

General structureDesignation of complexes

<u>R</u>	<u>Linker</u>	<u>Abbreviation</u>
Me	—(CH ₂) ₇ —	Ru(dmb) ₂ (C ₇ -NT)
Me	—(CH ₂) ₄ —	Ru(dmb) ₂ (C ₄ -NT)
Me	—(CH ₂) ₃ -O-(CH ₂) ₂ —	Ru(dmb) ₂ (C ₃ OC ₂ -NT)
H	—(CH ₂) ₇ —	Ru(bpy) ₂ (C ₇ -NT)
H	—(CH ₂) ₄ —	Ru(bpy) ₂ (C ₄ -NT)
H	—(CH ₂) ₃ -O-(CH ₂) ₂ —	Ru(bpy) ₂ (C ₃ OC ₂ -NT)

Scheme 3-3. *N,N*-Dimethyl-*p*-toluidine linked to tris(bipyridyl)ruthenium. Corresponding unlinked complexes are Ru(dmb)₃ for R = Me and Ru(bpy)₂(dmb) for R = H.



Scheme 3-4. Possible routes for the intramolecular oxidation of DMT linked to tris(bipyridyl)ruthenium in the presence of a reversible electron acceptor, denoted as A.

3.2.2.1 Intramolecular oxidation by Ru(II)*

To assess the feasibility of intramolecular DMT oxidation by Ru(II)* states (k_1), the excited state lifetimes of the complexes at various pH were measured at 370 nm after 355-nm laser-flash irradiation in the *absence* of an electron acceptor. These results are summarized in Table 3-3. Without the acceptor, the only available pathways present are k_d , k_1 , and k_{BET} , and those responsible for the decay of Ru(II)* are k_d and k_1 . Since k_d is a property of the photosensitizer core and presumably remains constant, any changes observed to the lifetime of Ru(II)* can be attributed to increases to the rate of k_1 . Oxidation of the linked substrate is therefore inferred by changes to the Ru(II)* lifetime. In these lifetime measurements, the concentration of linked complexes in the laser-flash irradiation samples was at relatively low levels (8-12 μM), minimizing any possible intermolecular electron transfer between two linked complexes.

Table 3-3. Excited-state lifetimes of DMT-linked tris(bipyridyl)ruthenium complexes in pH-buffered, nitrogen-purged solutions.

Complex	Lifetime/ns ^a					
	pH 3.2	4.2	4.7	5.1	5.6	6.5
Ru(dmb) ₂ (C ₇ -NT)	330	305	312	308	315	305
Ru(dmb) ₂ (C ₄ -NT)	335	330	327	320	310	282
Ru(dmb) ₂ (C ₃ OC ₂ -NT)	325	303	298	290	268	249
Ru(bpy) ₂ (C ₇ -NT)	488	465	452	444	436	410
Ru(bpy) ₂ (C ₄ -NT)	487	457	414	393	357	296
Ru(bpy) ₂ (C ₃ OC ₂ -NT)	450	340	282	227	161	104

^aLifetimes reproducible to within 5 ns.

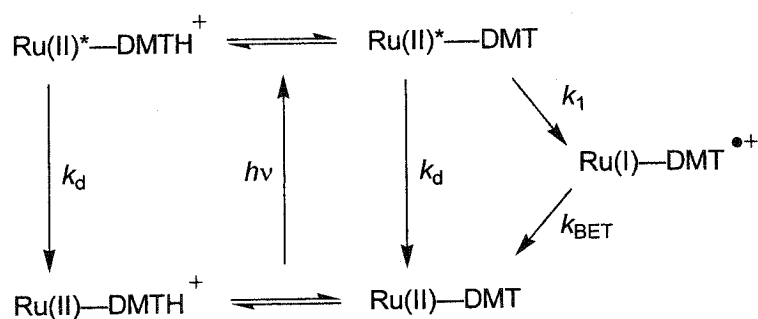
At low pH (3.2), the lifetimes (Table 3-3) for the linked complexes where R = Me or R = H were comparable to those of unlinked Ru(dmb)₃ or Ru(bpy)₂(dmb), respectively; *i.e.* the presence of a large, linked moiety does not substantially impact the excited-state lifetimes. However, at higher pH values, the effect of linkers on the Ru(II)* lifetimes was noticeable (Table 3-3). Typically, the lifetimes followed the trend of linker type ether < four-carbon < seven-carbon, inferring that the rate of intramolecular DMT oxidation (k_1) is greatest for the ether linker and slowest for the long, alkyl chain. This result was surprising considering that the ether linker is longer than the four-carbon polymethylene linker and yet has a much faster electron transfer. This phenomenon will be discussed later on.

Substituent effects were also seen for the linked complexes, consistent with trends previously established. When the ligands were substituted with $R = \text{Me}$, effects similar to the Ru(II)^* intermolecular experiments with the corresponding photosensitizer cores Ru(dmb)_3 or $\text{Ru(bpy)}_2(\text{dmb})$ were observed (section 3.2.1.1). While the lifetime of $\text{Ru(bpy)}_2(\text{dmb})$ was reduced by DMT at pH 5.1-6.5, no reduction was observed with Ru(dmb)_3 . Likewise, more drastic reductions were seen in the lifetimes of $R = \text{H}$ complexes compared to those of $R = \text{Me}$ when the pH was increased; this effect is most noticeable when comparing $\text{Ru(dmb)}_2(\text{C}_3\text{OC}_2\text{-NT})$ to $\text{Ru(bpy)}_2(\text{C}_3\text{OC}_2\text{-NT})$.

The remaining question is: why do DMT oxidation rate constants by Ru(II)^* increase with pH? In the intermolecular experiments with unlinked DMT, high acidity simply reduces the amount of oxidizable, unprotonated DMT. However, the DMT-linked complexes are more sophisticated in that protonation occurs on the linked substrate. Thus, the total amount of complex is distributed amongst a dynamic equilibrium of Ru(II)-DMT and Ru(II)-DMTH^+ unexcited forms. Protonation of the distant, linked substrate should not affect the light-absorption properties of photosensitizer core, and excitation should produce a mixture of $\text{Ru(II)}^*\text{-DMT}$ and $\text{Ru(II)}^*\text{-DMTH}^+$ in the same ratio as the unprotonated forms. With the former, Ru(II)^* can decay back to the ground state (k_d) or undergo intramolecular electron transfer via k_1 to produce Ru(I)-DMT^{*+} , which subsequently back-electron transfers (k_{BET}). However, with the protonated $\text{Ru(II)}^*\text{-DMTH}^+$, substrate oxidation (k_1) cannot occur, leaving Ru(II)^* decay (k_d) as the only possible route. Although the base and conjugate acid species are in dynamic

equilibrium, these long lifetimes observed at low pH could possibly indicate that the deprotonation of linked DMTH^+ is slower than Ru(II)^* decay.

As a whole, the role of pH is to govern the possible Ru(II)^* -deactivation pathways that may occur (Scheme 3-5). Thus, at very low pH, where the majority of the linked DMT exists as DMTH^+ , k_d is the principal route. Conversely, at high pH, most of the linked DMT exists in the base form and therefore k_1 is available. Of course, for k_1 , a property of the linker and substitution on the ligands, to be the predominant route, it needs to be faster than k_d . It is necessary to emphasize that, for a given complex, the actual rate constant k_1 should not vary with pH. Rather, the observed shortening of Ru(II)^* lifetime with increasing pH are attributed to an increase in the amount of Ru(II)^* -DMT relative to Ru(II)^* - DMTH^+ , thereby allowing a larger proportion of the total Ru(II)^* to access the k_1 pathway of excited-state deactivation.



Scheme 3-5. Possible routes for the deactivation of Ru(II)^* in DMT-linked tris(bipyridyl)ruthenium complexes. Oxidation of linked DMT is possible at high pH.

Although intramolecular oxidation of DMT was inferred by a reduction in Ru(II)* lifetime, the formation of DMT radical cation near 485 nm was not detected. The transient absorption spectra of the DMT-linked complexes at all pH values studied strikingly resembled the spectra of their respective photosensitizer cores. Representative spectra are shown in Figure 3-9, and the significant bands are the decay of Ru(II)* absorption near 370 nm, the recovery of the Ru(II) ground state near 450 nm, and the luminescence of Ru(II)* near 630 nm, all of which feature similar kinetics. The inability to observe DMT radical cation near 485 nm despite substantial Ru(II)* lifetime reduction suggests that when DMT is oxidized by Ru(II)* *via* route k_1 , the resultant radical ion undergoes fast charge recombination with Ru(I), k_{BET} . In other words, $k_{\text{BET}} > k_1$, and DMT serves as a mediator for the energy-wasting, intramolecular deactivation of Ru(II)*. In this futile cycle, the initial Ru(II) state is regenerated with no net radical cation production. These deductions are consistent with the virtually identical kinetics observed for the three bands, as well as with literature data¹²⁵ indicating that charge recombination between DMT radical cation and a similarly linked Ru(I) is very rapid ($> 10^8 \text{ s}^{-1}$).

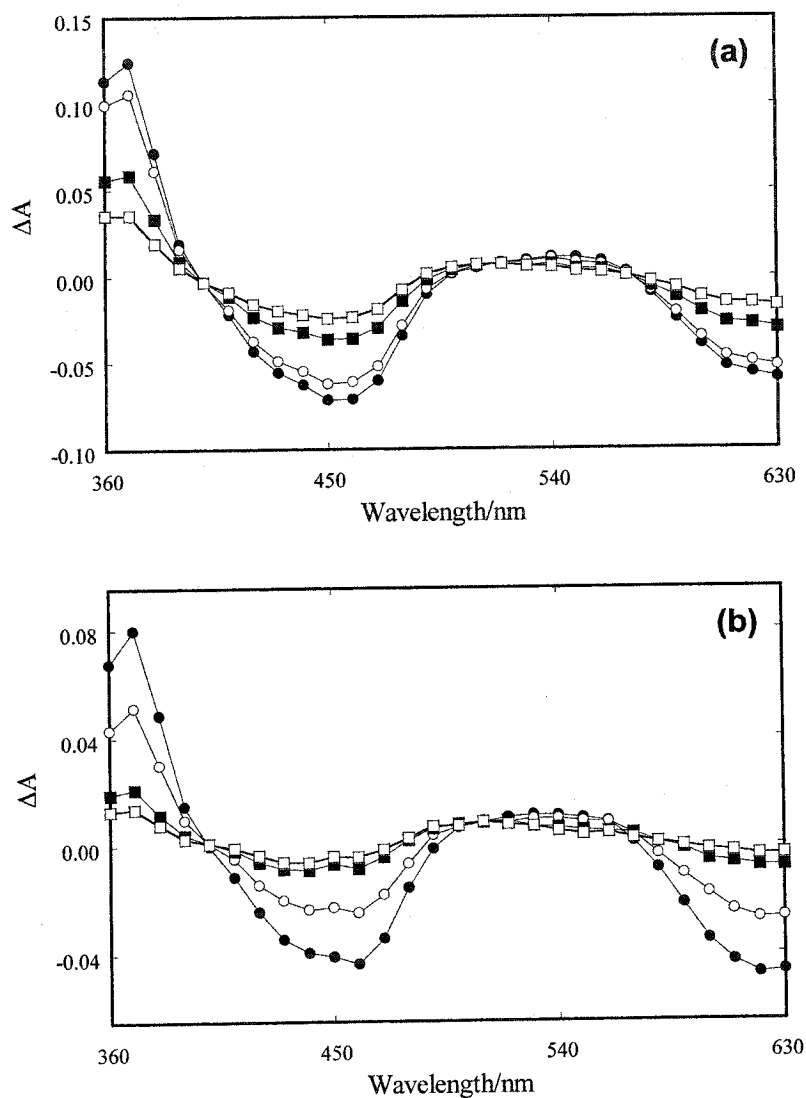


Figure 3-9. Transient absorption spectra obtained (●) 0.008 μ s, (○) 0.072 μ s, (■) 0.36 μ s, and (□) 0.60 μ s following 355-nm laser irradiation of (a) Ru(bpy)₂(dmb) in nitrogen saturated neat water and (b) Ru(bpy)₂(C₃OC₂-NT) in nitrogen-saturated 25 mM sodium phosphate pH 6.5.

3.2.2.2 Intramolecular oxidation by Ru(III)

The intramolecular Ru(II)* excited-state studies in the previous section suggest that for complexes capable of fast electron transfer, such as Ru(bpy)₂(C₃OC₂-NT), there is substantial energy-wasting deactivation of Ru(II)* by k_1 and k_{BET} to regenerate Ru(II) with no radical cation production. In this section, experiments were performed to determine if an electron acceptor, 60 mM [Ru(NH₃)₆]Cl₃, can competitively oxidize Ru(II)* by route $k_3[\text{A}]$ faster than Ru(II)* reduction by the substrate (k_1). The Ru(III) state generated from this process can subsequently oxidize the linked DMT moiety to its radical cation (k_4) or undergo intermolecular charge recombination with the reduced acceptor, $k_6[\text{A}^-]$. Like k_1 , the rate of k_4 is presumed to be dependent on the linker and the substitution on the bipyridyl ligands.

Since Ru(II)* rapidly lost through k_1 and k_{BET} affords no radical cation, a smaller total yield of radical cation was predicted for cases where k_1 is significantly larger than $k_3[\text{A}]$. As the proportion of Ru(II)* deactivated by k_1 varies with pH, the yield of radical cation should, in this case, decrease with increasing pH. Unfortunately, the large number of possible kinetic pathways shown in Scheme 3-4 complicated the analysis, and to overcome this difficulty, two key parameters representative of the efficiency of radical cation generation were measured. These are t_{max} , the time required for the absorption of the DMT radical cation to reach its maximum value, and Φ , the relative quantum yield of radical cation generation determined by comparing the maximum amount of radical

cation produced at 485-490 nm relative to the total amount of Ru(II)*, measured as Ru(II) bleaching at 450 nm.

The two efficiency parameters were calculated as follows, using representative kinetic traces in Figure 3-10. Firstly, the total Ru(II)* formed from the laser flash was measured at short time scales (Figure 3-10a) as the most negative value of Ru(II) bleaching at 450 nm (parameter ΔA_{max} 450 nm); here, the absorption is -0.0167 . This absorption was converted to concentration using the measured extinction coefficient of the corresponding photosensitizer cores at 450 nm, $12600 \text{ M}^{-1} \text{ cm}^{-1}$ for Ru(dmb)₃ and $13000 \text{ M}^{-1} \text{ cm}^{-1}$ for Ru(bpy)₂(dmb). Secondly, the time required for the absorption of the radical cation, Figure 3-10 (c), at 485 nm (parameter ΔA_{max} 485 nm) to reach its maximum is estimated to be $t_{\text{max}} \approx 55 \text{ } \mu\text{s}$, and corresponds to an absorption of 0.0023 . This absorption was converted to concentration using an extinction coefficient of $10400 \text{ M}^{-1} \text{ cm}^{-1}$ for the DMT radical cation.¹²³ Finally, the relative quantum yield is the absolute value of the ratio of the maximum concentration of radical cation produced relative to that of Ru(II)*. Using these values for Ru(dmb)₂(C₇-NT), which features Ru(dmb)₃ as the corresponding core, affords a relative quantum yield of 17%. It is interesting to note that bleaching at 485 nm was also observed due to the broad MLCT absorption of the Ru(II), but this does not interfere with the calculations, since it is presumed that all Ru(III) has been reduced back to the Ru(II) at t_{max} . Though not used for efficiency calculations, Figure 3-10 (b) depicts Figure 3-10 (a) at the longer time scales used for kinetic fits to determine the rate of the slow component.

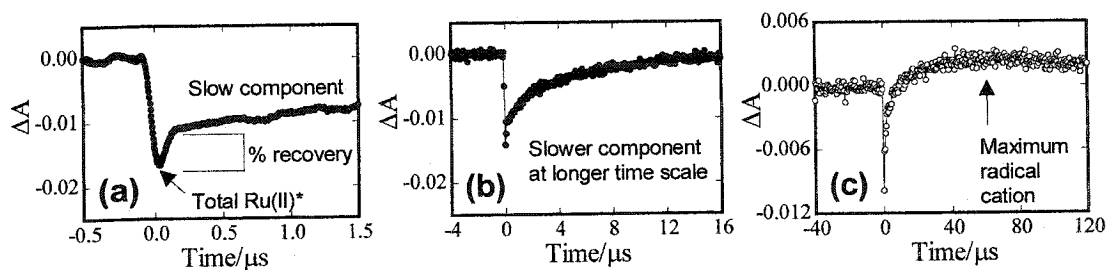


Figure 3-10. Determination of the efficiency of radical cation generation by comparing the (a) Ru(II) bleaching at 450 nm to (c) the absorption of the DMT radical cation at 485 nm at longer time scale; (b) depicts the 450 nm recovery at longer time scale.

3.2.2.2.1 Irradiation of the slowest complex: Ru(dmb)₂(C₇-NT)

For laser-flash experiments with the “slowest complex” Ru(dmb)₂(C₇-NT), which has a relatively small k_1 as inferred from the excited-state lifetimes (Table 3-3), it was postulated that this route of Ru(II)* deactivation would be minimal. As a result, oxidation of Ru(II)* by the acceptor, $k_3[A]$, should be able to compete with relatively slow k_1 , leading to reasonable yields of radical cation generated through Ru(III) (k_4). However, a slow k_1 also indicates that substrate oxidation by Ru(III), k_4 , would be slow, inferring that a large proportion of Ru(III) may be lost via $k_6[A^-]$.

In the presence of the electron acceptor, laser irradiation of Ru(dmb)(C₇-NT) afforded kinetic traces shown in Figure 3-11, and relevant data extracted from these traces are shown in Table 3-4. Immediately following laser irradiation, 2-3 μ M of Ru(II)* was produced and detected in the form of Ru(II) bleaching at 450 nm (Figure 3-11 a, d, g, j, m, p). Typically 30% of the initial bleaching recovered within the duration of the laser pulse *regardless of pH*, inferring that the remaining 70% Ru(II)* was oxidized by

the acceptor to Ru(III). These data were collected at short timescales to maximize acquisition resolution. These observations implies that the oxidation of Ru(II)* to Ru(III) for this complex was not as efficient as for the representative unlinked Ru(dmb)₃, where only 10% of the initial bleaching recovered within the time frame of the laser pulse (Figure 3-4). Large alkyl substituents on the bipyridyl ligands have been shown to reduce the rate of intermolecular Ru(II)* quenching,⁷⁹ and the presence of a DMT moiety would be expected to do the same. Nonetheless, this observation shows that the electron acceptor ($k_3[A]$) can effectively compete with the deactivation of Ru(II)*, k_1 , in agreement with earlier predictions. The predominant route of linked DMT oxidation for this complex is therefore characterized by an initial Ru(II)* oxidation to Ru(III).

After the initial, pH-independent $\approx 30\%$ rapid recovery of the 450-nm bleaching following the laser pulse, the balance continued to rise on longer timescales (Figure 3-11 b, e, h, k, n, q; Table 3-4) due to a mixture of charge recombination ($k_6[A^-]$) and intramolecular DMT oxidation (k_4). This slower component, designated k_{obs} , was strongly dependent on pH. At higher pH values, a larger proportion of the DMT moiety exists in the oxidizable base form, while at low pH, the protonated DMT moiety needs to equilibrate slowly with the base form. Thus, at high pH, where Ru(III) is more rapidly converted to Ru(II) by substrate oxidation (k_4), the rate of charge recombination ($k_6[A^-]$) becomes less significant and results in improved efficiency of radical-cation generation (Table 3-4). This is illustrated at 485 nm in (Figure 3-11 c, f, i, l, o, r), where the absorption rises above baseline in all cases, but is more pronounced at higher pH, inferring more radical cation formation.

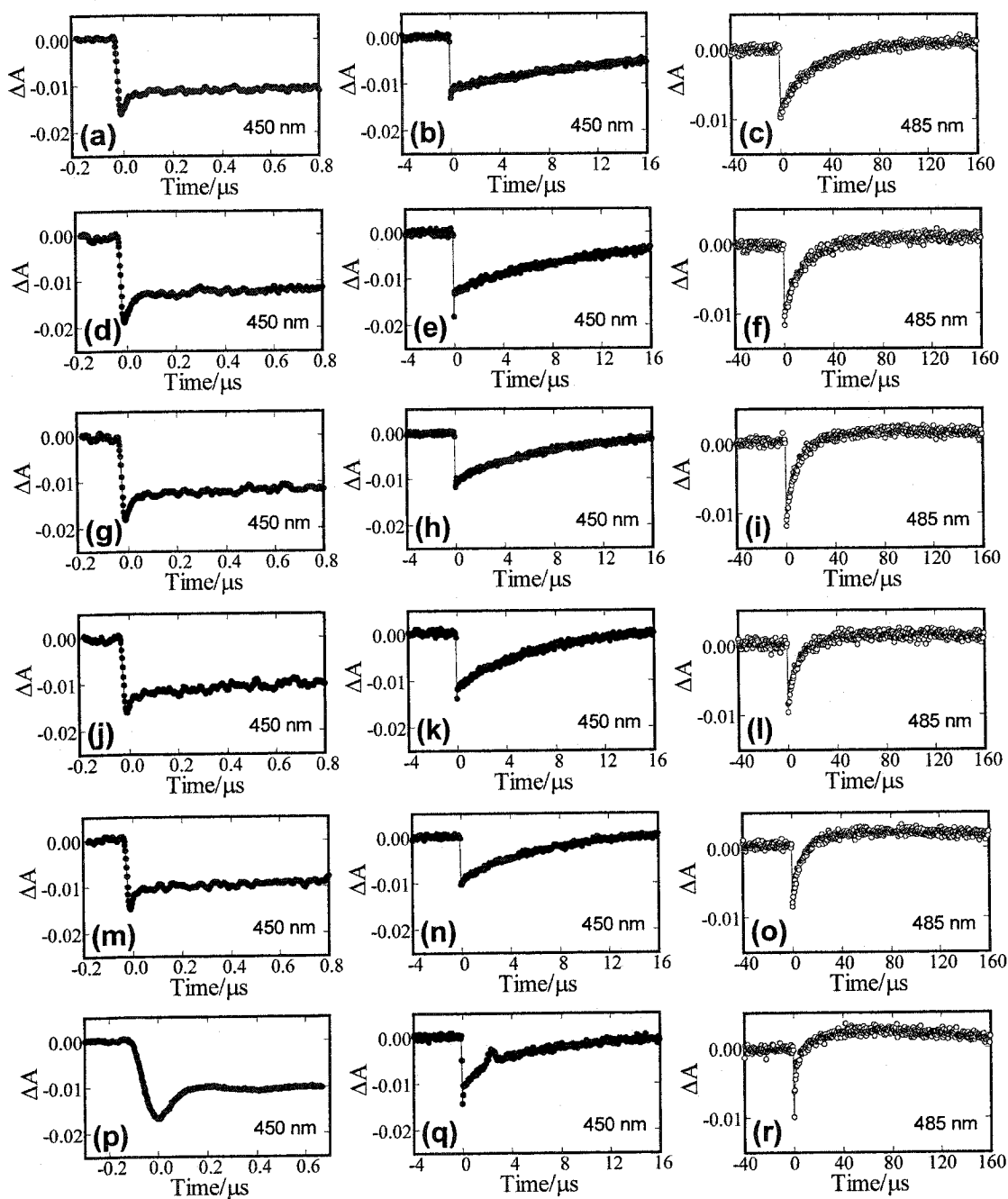


Figure 3-11. Time-resolved kinetic trace collected at (●) 450 nm and (○) 485 nm after 355-nm laser irradiation of $\text{Ru(dmb)}_2(\text{C}_7\text{-NT})$ in buffered 60 mM $[\text{Ru}(\text{NH}_3)_6]\text{Cl}_3$ at pH (a-c) 3.2, (d-f) 4.2, (g-i) 4.7, (j-l) 5.1, (m-o) 5.6, and (p-r) 6.5.

Table 3-4. Parameters acquired from the laser-flash irradiation of Ru(dmb)₂(C₇-NT) in the presence of buffered, nitrogen-purged 60 mM [Ru(NH₃)₆]Cl₃.

pH	ΔA_{max} 450 nm	% fast rise ^a	k_{obs}^b /10 ⁶ s ⁻¹	ΔA_{max} 485 nm	t_{max} /μs	Φ
3.2	-0.0160	28	0.046	0.0008	135	0.061
4.2	-0.0190	32	0.070	0.0010	90	0.064
4.7	-0.0180	28	0.093	0.0017	80	0.11
5.1	-0.0160	25	0.11	0.0014	70	0.11
5.6	-0.0147	29	0.12	0.0021	60	0.17
6.5	-0.0167	34	0.29	0.0023	55	0.17

Data in this table are extracted from Figure 3-11. ^aPercentage of the bleaching at 450 nm that rapidly recovered after the laser flash. ^bRecovery of the slower component after the fast rise at 450 nm.

3.2.2.2.2 Irradiation of the fastest complex: Ru(bpy)₂(C₃OC₂-NT)

Of the six DMT-linked complexes studied, the Ru(II)* excited-state lifetime of Ru(bpy)₂(C₃OC₂-NT) in the absence of electron acceptor was most susceptible to pH variations (Table 3-3). Such a behaviour infers that the intramolecular oxidation of linked DMT by Ru(II)* *via* route k_1 is the fastest of all complexes, and that at high pH, a significant portion of Ru(II)* would decay by this route. Consequently, in the presence of an electron acceptor, an uncertainty lies in whether $k_3[A]$ can effectively compete with the Ru(II)*-consuming k_1 . Amid this uncertainty, two scenarios are predicted. In the first and presumably more-desirable case, k_1 is still sufficiently slow compared to $k_3[A]$ and observations similar to Ru(dmb)₂(C₇-NT) would be seen: the amount of Ru(II)* oxidized

to Ru(III) would remain similar regardless of pH, and the efficiency of radical cation generation would increase with pH. In the second and presumably less-desirable scenario, the electron acceptor cannot compete with k_1 , resulting in a wastage of Ru(II)* as well as low radical-cation yields. Such a scenario would be expected to be observed in the form of rapid Ru(II) bleaching recovery *without* radical cation formation.

Laser-flash irradiation of Ru(bpy)₂(C₃OC₂-NT) in the presence of 60 mM [Ru(NH₃)₆]Cl₃ at various pH afforded kinetic traces (Figure 3-12) that are clearly different from those collected for the slowest complex, Ru(dmb)₂(C₇-NT) (Figure 3-11). In particular, the percentage of the bleaching at 450 nm that immediately recovered within the time frame of the laser pulse gradually increased with pH (Table 3-5). In fact, at pH 5.6 and 6.5 (Figure 3-12 m-r), not only did a complete recovery of the 450-nm bleaching occur within the laser pulse, the signal rapidly rose above baseline levels concomitant with prompt radical cation generation at 485 nm. After this rapid rise, a slower, second component followed. The proportion of the rapid growth relative to the total growth also increased with pH, even though quantum yields of DMT radical cation formation remained high. Since the DMT radical cation has a broad absorption that extends into the 450 nm region, the kinetic traces at 450 nm measure both the recovery of Ru(II) and radical cation formation. These unexpected traces suggest that at high pH values, both prompt Ru(II) regeneration and radical cation formation occurred, causing the signal to rise above baseline levels within the time frame of the laser pulse. The slower continued growth on the other hand, is likely attributed to oxidation of linked DMT by the small amount of Ru(III) formed.

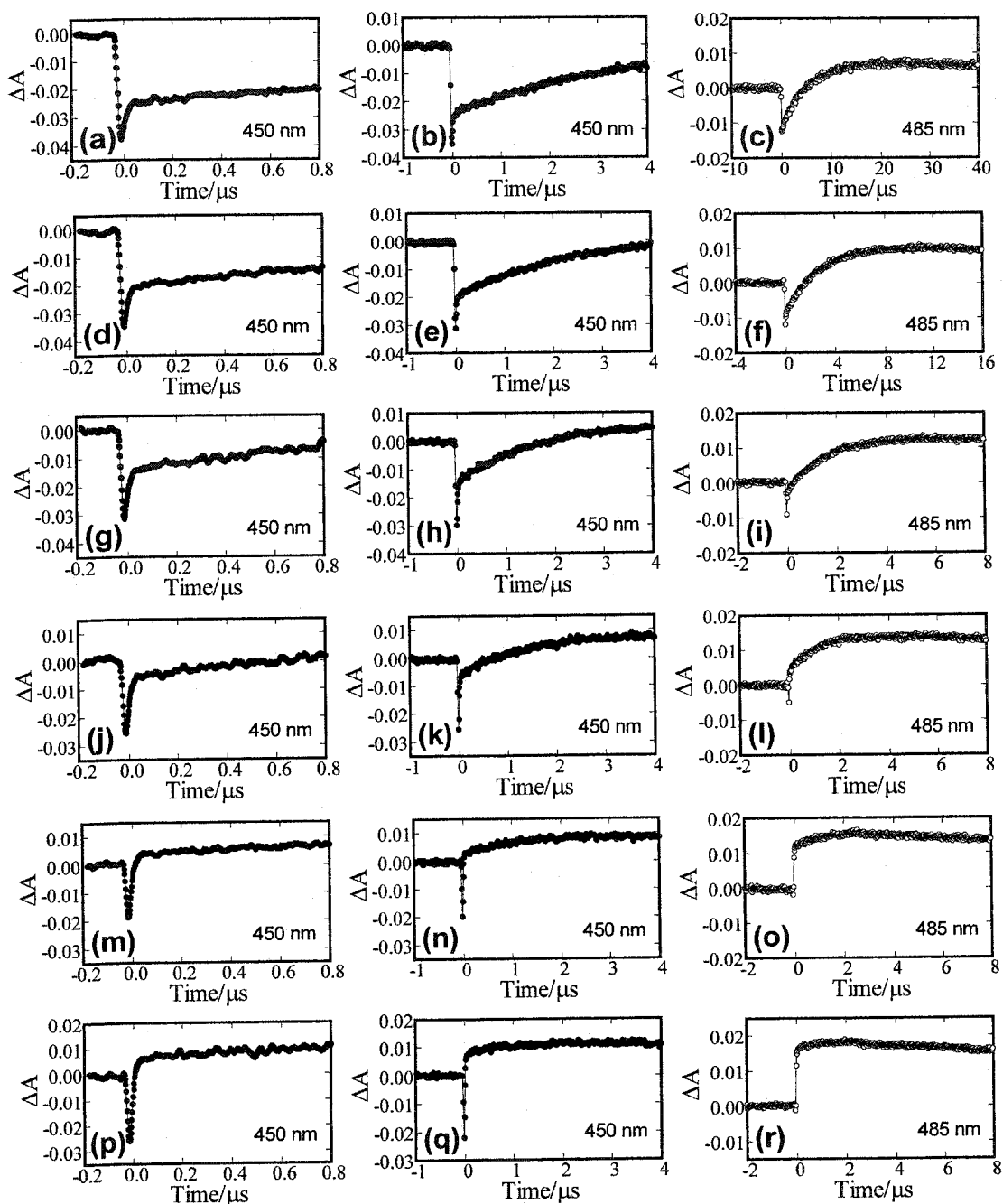


Figure 3-12. Time-resolved kinetic trace collected at (●) 450 nm and (○) 485 nm after 355-nm laser irradiation of $\text{Ru}(\text{bpy})_2(\text{C}_3\text{OC}_2\text{-NT})$ in buffered 60 mM $[\text{Ru}(\text{NH}_3)_6]\text{Cl}_3$ at pH (a-c) 3.2, (d-f) 4.2, (g-i) 4.7, (j-l) 5.1, (m-o) 5.6, and (p-r) 6.5.

Table 3-5. Parameters acquired from the laser-flash irradiation of Ru(bpy)₂(C₃OC₂-NT) in the presence of buffered, nitrogen-purged 60 mM [Ru(NH₃)₆]Cl₃.

pH	ΔA_{max} 450 nm	% fast rise ^a	k_{obs}^b /10 ⁶ s ⁻¹	ΔA_{max} 485 nm	$t_{\text{max}}/\mu\text{s}$	Φ
3.2	-0.0212	39	0.17	0.0052	25	0.31
4.2	-0.0347	42	0.42	0.010	11	0.36
4.7	-0.0314	54	0.70	0.013	7.0	0.50
5.1	-0.0256	80	1.0	0.014	4.0	0.67
5.6	-0.0185	> 100	1.6	0.015	3.0	1.0
6.5	-0.0228	> 100	> 2	0.019	2.5	1.0

Data in this table are extracted from Figure 3-12. ^aPercentage of the bleaching at 450 nm that rapidly recovered after the laser flash. ^bRecovery of the slower component after the fast rise at 450 nm.

It is obvious then, that these results do not support the first possible scenario where the electron acceptor competitively oxidizes the Ru(II)* excited state ($k_3[A]$) and prevents it from undergoing reduction to Ru(I) by k_1 . For this scenario to hold true, the percentage of the recovery that occurs immediately after the laser pulse needs to remain relatively constant throughout the pH range studied, and this is obviously not the case with Ru(bpy)₂(C₃OC₂-NT). As well, unity relative quantum yields are not possible when the oxidation of Ru(II)* to Ru(III) is at most 70%, suggesting that another mechanism of substrate oxidation is responsible for the large amount of radical cation produced.

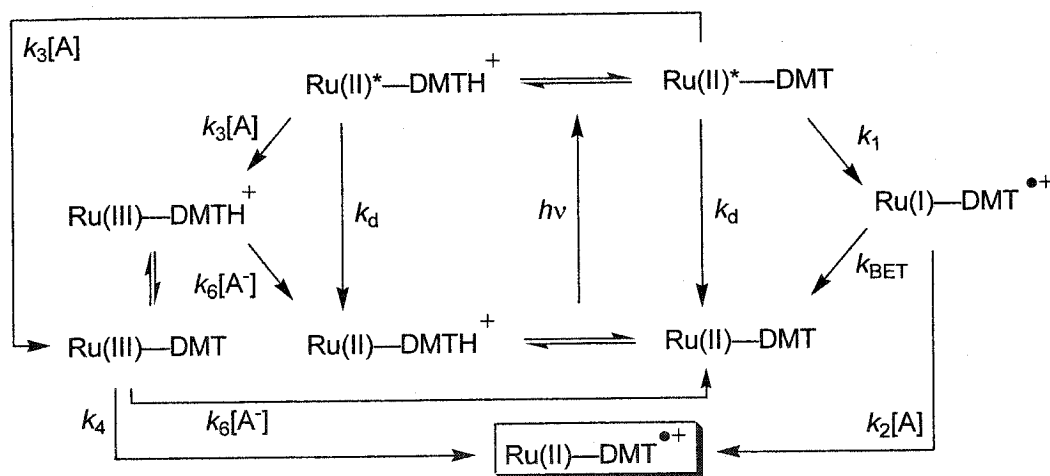
The pH-dependence of the rapid recovery of the bleaching following the laser-flash suggests that more Ru(II) is quickly regenerated at higher pH. While this would be

consistent with the observations predicted for the second possible scenario, where $k_3[A]$ is insufficient to compete with k_1 , which along with k_{BET} would result in the rapid regeneration of Ru(II), there is an important contradiction. At high pH, where k_1 would be predominant as indicated from excited-state lifetimes, more Ru(II)* would be diverted through the energy-wasting k_1 and k_{BET} pathway, and the quantum yield should decrease with increasing pH. Instead, the exact opposite was observed.

Therefore, the kinetic traces collected do not support either of the two proposed scenarios. Their biphasic character, where a large portion of the total rise occurs in the form of a rapid recovery following the laser pulse, indicates that a combination of two mechanisms exists. In order for the Ru(II) bleaching at 450 nm to rise above the baseline, another transient absorption at 450 nm needs to be generated in approximately the same time frame. This transient is attributed to the DMT radical cation, which can be rapidly formed *via* electron transfer with the Ru(II)* excited state. It is proposed that the resultant, highly reductive Ru(I) state, which can undergo back-electron transfer with the radical cation, is quickly oxidized by the acceptor ($k_2[A]$) to regenerate the initial Ru(II) state (Scheme 3-4). In other words, the function of the electron acceptor also lies in the trapping of Ru(I), inferring that $k_2[A] > k_{\text{BET}}$.

In the last section, excited-state lifetime measurements suggested that only the unprotonated form of DMT can be oxidized by Ru(II)* and that the route of initial Ru(II)* reduction to Ru(I) is more significant at higher pH. These also apply to experiments with the electron acceptor, where pH continues to govern the routes of DMT oxidation (Scheme 3-6). At low pH values, excitation of the sample would provide

Ru(II)^* primarily as $\text{Ru(II)}^*-\text{DMTH}^+$, which can either decay (k_d) or be oxidized by the acceptor ($k_3[\text{A}]$). The latter process affords $\text{Ru(III)}-\text{DMTH}^+$, and since it is in a presumably slow, dynamic equilibrium with the base form, oxidation of the substrate can occur to regenerate Ru(II) , observed as a slow rise at 450 nm (second component). On the contrary, excitation of the sample at high pH affords Ru(II)^* mainly as $\text{Ru(II)}^*-\text{DMT}$, which can be oxidized by the acceptor ($k_3[\text{A}]$) or undergo electron transfer (k_1) to form the charge-separated $\text{Ru(I)}-\text{DMT}^{\bullet+}$. This Ru(I) state is then oxidized to $\text{Ru(II)}-\text{DMT}^{\bullet+}$ by $k_2[\text{A}]$, and it is this rapid combination of $k_1 + k_2[\text{A}]$ that results in the prompt rise above baseline at 450 nm immediately after the laser pulse. A small percentage of Ru(II)^* is also oxidized at pH 6.5 to Ru(III) by $k_3[\text{A}]$, which is observed as the second, slower component of the rise at 450 nm.



Scheme 3-6. Possible routes for the oxidation of linked DMT by Ru(II)^* and Ru(III) in the presence of an electron acceptor, denoted as A.

At high pH, radical cation is generated primarily *via* an initial reduction of the Ru(II)* excited state to Ru(I) due to the high k_1 for this “fast” Ru(bpy)₂(C₃OC₂-NT) complex, where the right-hand side of Scheme 3-6 predominates, with $k_1 > k_3[A]$. On a similar note, the left-hand side would apply at low pH, where an initial oxidation of Ru(II)* to Ru(III) by route $k_3[A]$ predominates. Thus, it can be envisioned that as pH increases from a low to high value, the mechanism by which Ru(II)* is consumed would shift from the left side to the right, *i.e.*, from a predominant initial Ru(II)* oxidation to a reduction. At an intermediate pH, both mechanisms would co-exist and are suggested by the kinetic traces (Figure 3-12) in the form a fast rise followed by a second, slower component.

The initially unwanted pathway of initial Ru(II)* reduction is in fact advantageous in many respects. In this pathway, the radical cation is formed by direct electron transfer with the Ru(II)* excited state. This route is more efficient than the one involving Ru(III), since the conversion of Ru(II)* to Ru(III) by the electron acceptor does not occur with complete efficiency. As well, the Ru(III) oxidant can also undergo charge recombination with the reduced acceptor, $k_6[A^-]$, further reducing the amount of Ru(III) available for substrate oxidation. This recombination is avoided with the Ru(I) route. Although the pathway of initial Ru(II)* reduction is favoured by a high pH, it is also necessary that k_1 , a property based on linker and ligand substitution, be sufficiently fast in order for the initial reduction to predominate.

3.2.2.2.3 Irradiation of other complexes

As inferred from the Ru(II)* excited-state lifetimes (Table 3-3), the remaining four DMT-linked complexes feature k_1 values bordered by those of the slowest and fastest complexes, Ru(dmb)₂(C₇-NT) and Ru(bpy)₂(C₃OC₂-NT), respectively. With the slow Ru(dmb)₂(C₇-NT), DMT radical cation was generated from Ru(III) states independent of pH, while with the fast Ru(bpy)₂(C₃OC₂-NT), Ru(II)* to Ru(I) reduction was predominate at high pH. Thus, for the four “intermediate” complexes, it was proposed that the initial Ru(II)* reduction would be more significant when complexes contained bpy ligands over dmb, and with linkers that are more conductive (ether > C₄ > C₇).

Based on Ru(II)* excited-state lifetime data (Table 3-3), Ru(bpy)₂(C₇-NT) appeared to be the second-slowest complex for intramolecular electron transfer (k_1). Laser-flash irradiation of this complex in the presence of 60 mM [Ru(NH₃)₆]Cl₃ at various pH afforded kinetic traces shown in Figure 3-13, which were used to extract relevant data summarized in Table 3-6. At pH 3.2, approximately 38% of the Ru(II) bleaching at 450 nm recovered immediately after the laser pulse. Since the excited-state lifetime of this complex at pH 3.2 (Table 3-3; 488 ns) is comparable to that of corresponding unlinked Ru(bpy)₂(dmb), 485 ns, the route of Ru(II)* reduction at this pH is negligible. Thus, 62% of the Ru(II)* is directly converted to Ru(III) by the acceptor ($k_3[A]$) in the absence of k_1 competition. This value serves as a baseline for the (bpy)₂ complexes and is slightly less than the 70% observed for the (dmb)₂ complexes, similar to the trend observed for the corresponding unlinked complexes (70% *versus* 90%).

As the pH increased to 6.5 for Ru(bpy)₂(C₇-NT), so did the percentages of the prompt bleaching recoveries observed at 450 nm; however, the magnitude of the prompt recoveries were nowhere near those seen for the fast complex Ru(bpy)₂(C₃OC₂-NT) (Table 3-5). The value of k_1 for Ru(bpy)₂(C₇-NT) is such that the acceptor can still competitively oxidize the excited state to Ru(III), the predominant oxidant of DMT. Substituent effects are also noticeable, where k_{obs} , t_{max} , and Φ are higher than those obtained for the (dmb)₂ derivative with the same linker, Ru(dmb)₂(C₇-NT). These higher values are most likely attributed to a higher k_4 relative to $k_6[A^-]$, indicating that more Ru(II) is regenerated through DMT oxidation instead of charge recombination.

Table 3-6. Parameters acquired from the laser-flash irradiation of Ru(bpy)₂(C₇-NT) in the presence of buffered, nitrogen-purged 60 mM [Ru(NH₃)₆]Cl₃.

pH	ΔA_{max} 450 nm	% fast rise ^a	k_{obs}^b /10 ⁶ s ⁻¹	ΔA_{max} 485 nm	$t_{\text{max}}/\mu\text{s}$	Φ
3.2	-0.0202	38	0.066	0.0010	120	0.062
4.2	-0.0273	38	0.088	0.0021	65	0.096
4.7	-0.0278	37	0.13	0.0024	40	0.11
5.1	-0.0248	42	0.17	0.0028	30	0.14
5.6	-0.0207	44	0.20	0.0031	27	0.19
6.5	-0.0219	56	0.35	0.0048	20	0.27

Data in this table are extracted from Figure 3-13. ^aPercentage of the bleaching at 450 nm that rapidly recovered after the laser flash. ^bRecovery of the slower component after the fast rise at 450 nm.

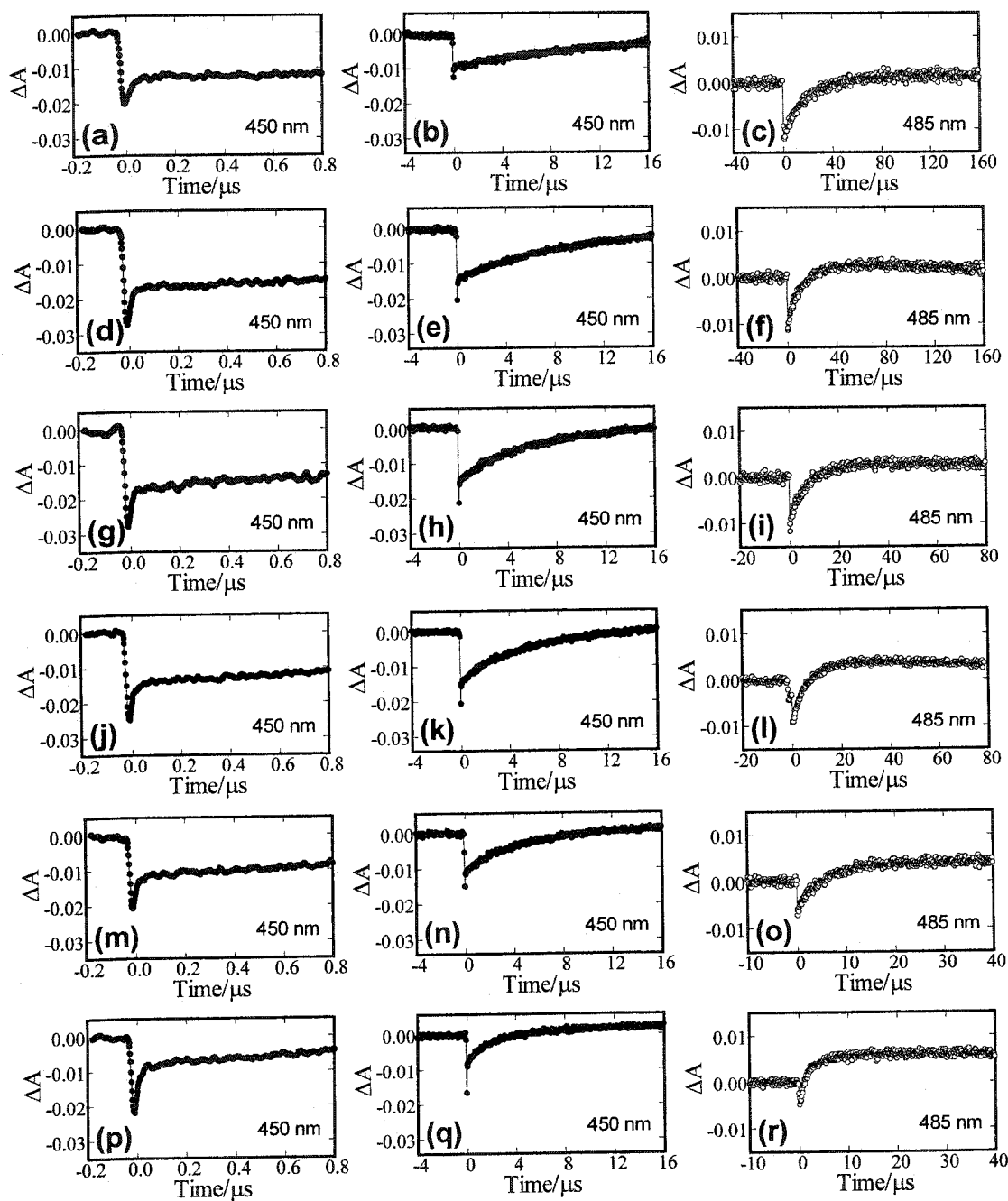


Figure 3-13. Time-resolved kinetic trace collected at (●) 450 nm and (○) 485 nm after 355-nm laser irradiation of $\text{Ru}(\text{bpy})_2(\text{C}_7\text{-NT})$ in buffered 60 mM $[\text{Ru}(\text{NH}_3)_6]\text{Cl}_3$ at pH (a-c) 3.2, (d-f) 4.2, (g-i) 4.7, (j-l) 5.1, (m-o) 5.6, and (p-r) 6.5.

For the remaining complexes $\text{Ru(dmb)}_2(\text{C}_4\text{-NT})$, $\text{Ru(bpy)}_2(\text{C}_4\text{-NT})$, and $\text{Ru(dmb)}_2(\text{C}_3\text{OC}_2\text{-NT})$, which are in the order of increasing k_1 based on Ru(II)^* lifetimes (Table 3-3), the kinetic traces acquired at 450 nm following excitation in the presence of 60 mM $[\text{Ru}(\text{NH}_3)_6]\text{Cl}_3$ were as predicted. Kinetic traces and relevant extracted data are shown in Figures 3-14 to 3-17 and Tables 3-7 to 3-9, respectively. When the pH was increased, so did the amount of the bleaching that recovered immediately following the laser pulse, inferring rapid formation of DMT radical cation. This effect, as well as the improvement of radical cation generation efficiency, was more pronounced for complexes with a higher k_1 , such as $\text{Ru(dmb)}_2(\text{C}_3\text{OC}_2\text{-NT})$. These results are consistent with the dual mechanism of DMT oxidation and also demonstrate that both high pH and fast k_1 values are required for the mechanism of initial Ru(II)^* reduction to predominate.

It is interesting to note that the maximum efficiency of DMT radical cation generation, regardless of linker and ligand substitution, is achieved at pH 6.5. At this value, most of the complex is in the unprotonated state and available to access the preferential initial reduction route, k_1 . A comparison of efficiency parameters for the six complexes at this pH is presented in Table 3-10. Since DMT serves as a reasonable model for the sterically hindered, amino-substituted substrates used in the next chapter, these results suggest that substrate oxidation would proceed efficiently at biological pH, near 7.

Table 3-7. Parameters acquired from the laser-flash irradiation of Ru(dmb)₂(C₄-NT) in the presence of buffered, nitrogen-purged 60 mM [Ru(NH₃)₆]Cl₃.

pH	ΔA_{\max} 450 nm	% fast rise ^a	k_{obs}^b /10 ⁶ s ⁻¹	ΔA_{\max} 485 nm	t_{\max} /μs	Φ
3.2	-0.0233	29	0.071	0.0018	60	0.094
4.2	-0.0211	34	0.13	0.0024	38	0.14
4.7	-0.0223	33	0.22	0.0031	30	0.17
5.1	-0.0253	43	0.31	0.0037	16	0.18
5.6	-0.0229	48	0.41	0.0042	13	0.22
6.5	-0.0212	62	0.91	0.0052	6	0.30

Data in this table are extracted from Figure 3-14. ^aPercentage of the bleaching at 450 nm that rapidly recovered after the laser flash. ^bRecovery of the slower component after the fast rise at 450 nm.

Table 3-8. Parameters acquired from the laser-flash irradiation of Ru(bpy)₂(C₄-NT) in the presence of buffered, nitrogen-purged 60 mM [Ru(NH₃)₆]Cl₃.

pH	ΔA_{\max} 450 nm	% fast rise ^a	k_{obs}^b /10 ⁶ s ⁻¹	ΔA_{\max} 485 nm	t_{\max} /μs	Φ
3.2	-0.0356	45	0.088	0.0027	50	0.10
4.2	-0.0314	47	0.19	0.0035	25	0.14
4.7	-0.0311	48	0.28	0.0048	14	0.19
5.1	-0.0300	52	0.40	0.0055	12	0.23
5.6	-0.0360	68	0.43	0.0062	10	0.22
6.5	-0.0332	76	1.2	0.0078	4	0.32

Data in this table are extracted from Figure 3-15. ^aPercentage of the bleaching at 450 nm that rapidly recovered after the laser flash. ^bRecovery of the slower component after the fast rise at 450 nm.

Table 3-9. Parameters acquired from the laser-flash irradiation of Ru(dmb)₂(C₃OC₂-NT) in the presence of buffered, nitrogen-purged 60 mM [Ru(NH₃)₆]Cl₃.

pH	ΔA_{max} 450 nm	% fast rise ^a	k_{obs}^b /10 ⁶ s ⁻¹	ΔA_{max} 485 nm	$t_{\text{max}}/\mu\text{s}$	Φ
3.2	-0.0220	27	0.19	0.0043	30	0.24
4.2	-0.0251	40	0.33	0.0060	13	0.29
4.7	-0.0214	46	0.62	0.0084	9	0.48
5.1	-0.0170	66	0.97	0.0085	5	0.61
5.6	-0.0140	--	1.3	0.0092	3	0.80
6.5	-0.0247	--	> 2	0.019	2.5	0.91

Data in this table are extracted from Figure 3-16. ^aPercentage of the bleaching at 450 nm that rapidly recovered after the laser flash. ^bRecovery of the slower component after the fast rise at 450 nm.

Table 3-10. Radical cation generation efficiencies for DMT-linked complexes in nitrogen-purged 25 mM sodium phosphate, pH 6.5, with 60 mM [Ru(NH₃)₆]Cl₃.

Complex	$t_{\text{max}}/\mu\text{s}$	Φ
Ru(dmb) ₂ (C ₇ -NT)	55	0.17
Ru(dmb) ₂ (C ₄ -NT)	6	0.30
Ru(dmb) ₂ (C ₃ OC ₂ -NT)	2.5	0.91
Ru(bpy) ₂ (C ₇ -NT)	20	0.27
Ru(bpy) ₂ (C ₄ -NT)	4	0.32
Ru(bpy) ₂ (C ₃ OC ₂ -NT)	2	1.0

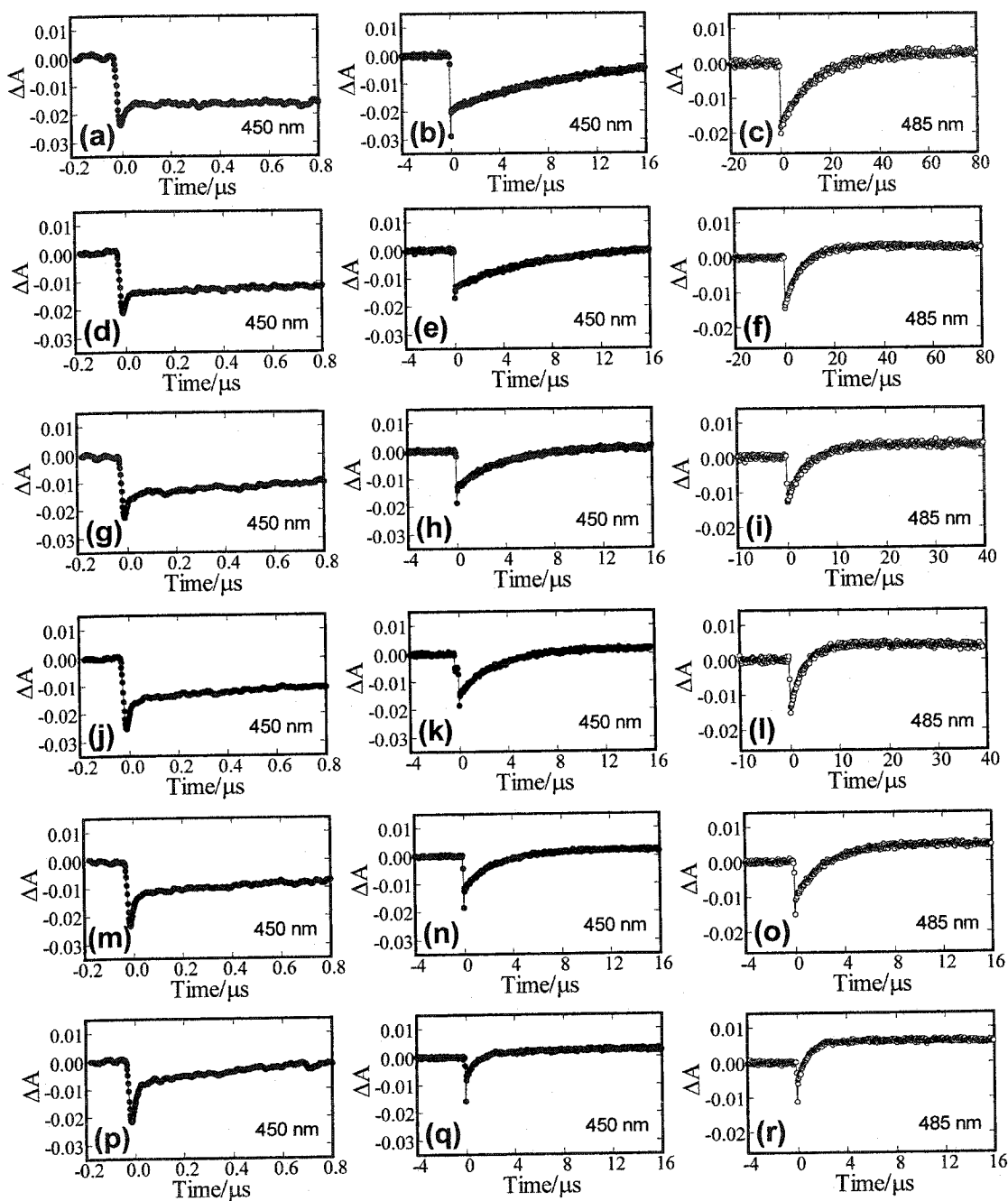


Figure 3-14. Time-resolved kinetic trace collected at (●) 450 nm and (○) 485 nm after 355-nm laser irradiation of $\text{Ru}(\text{dmb})_2(\text{C}_4\text{-NT})$ in buffered 60 mM $[\text{Ru}(\text{NH}_3)_6]\text{Cl}_3$ at pH (a-c) 3.2, (d-f) 4.2, (g-i) 4.7, (j-l) 5.1, (m-o) 5.6, and (p-r) 6.5.

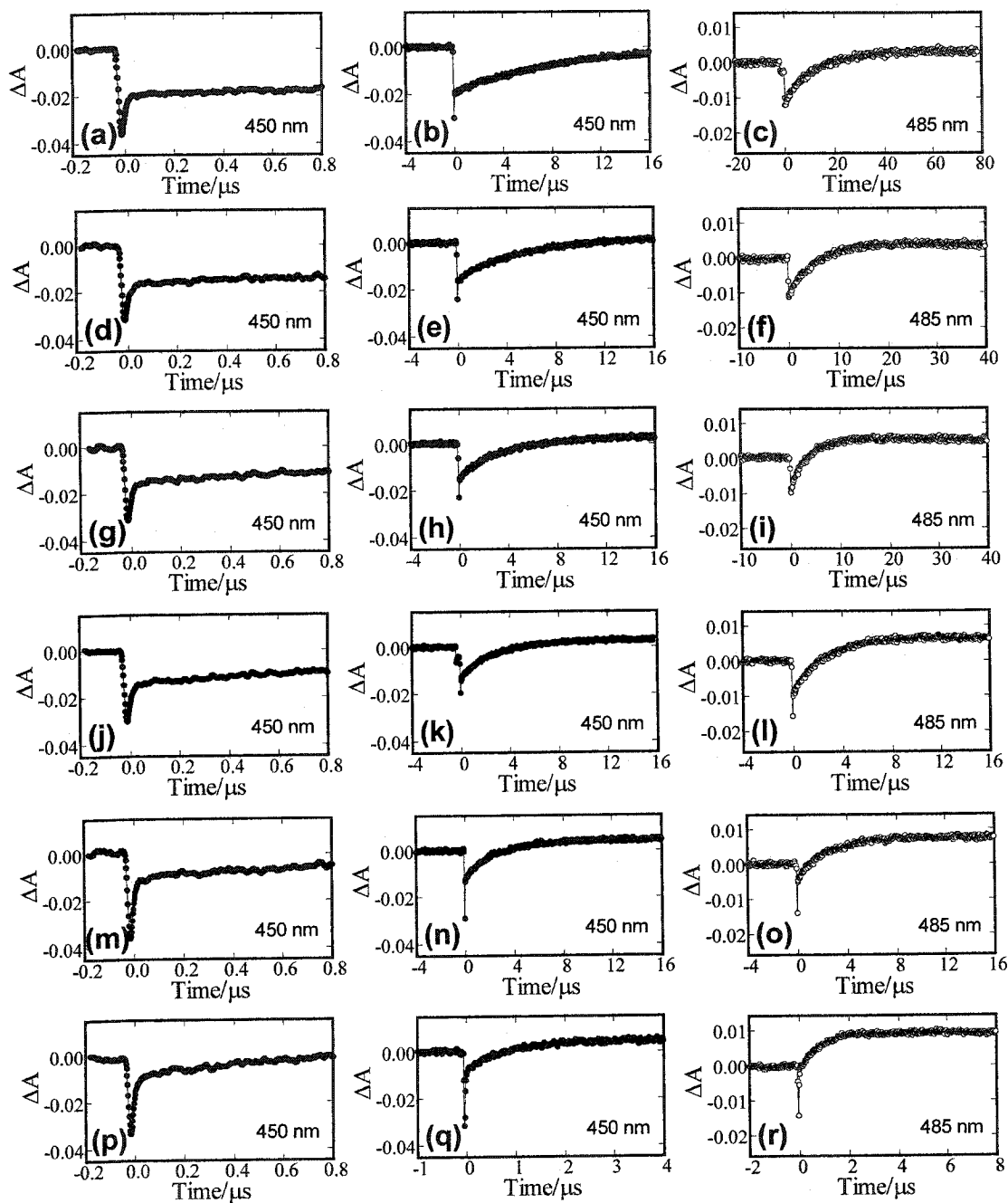


Figure 3-15. Time-resolved kinetic trace collected at (●) 450 nm and (○) 485 nm after 355-nm laser irradiation of $\text{Ru}(\text{bpy})_2(\text{C}_4\text{-NT})$ in buffered 60 mM $[\text{Ru}(\text{NH}_3)_6]\text{Cl}_3$ at pH (a-c) 3.2, (d-f) 4.2, (g-i) 4.7, (j-l) 5.1, (m-o) 5.6, and (p-r) 6.5.

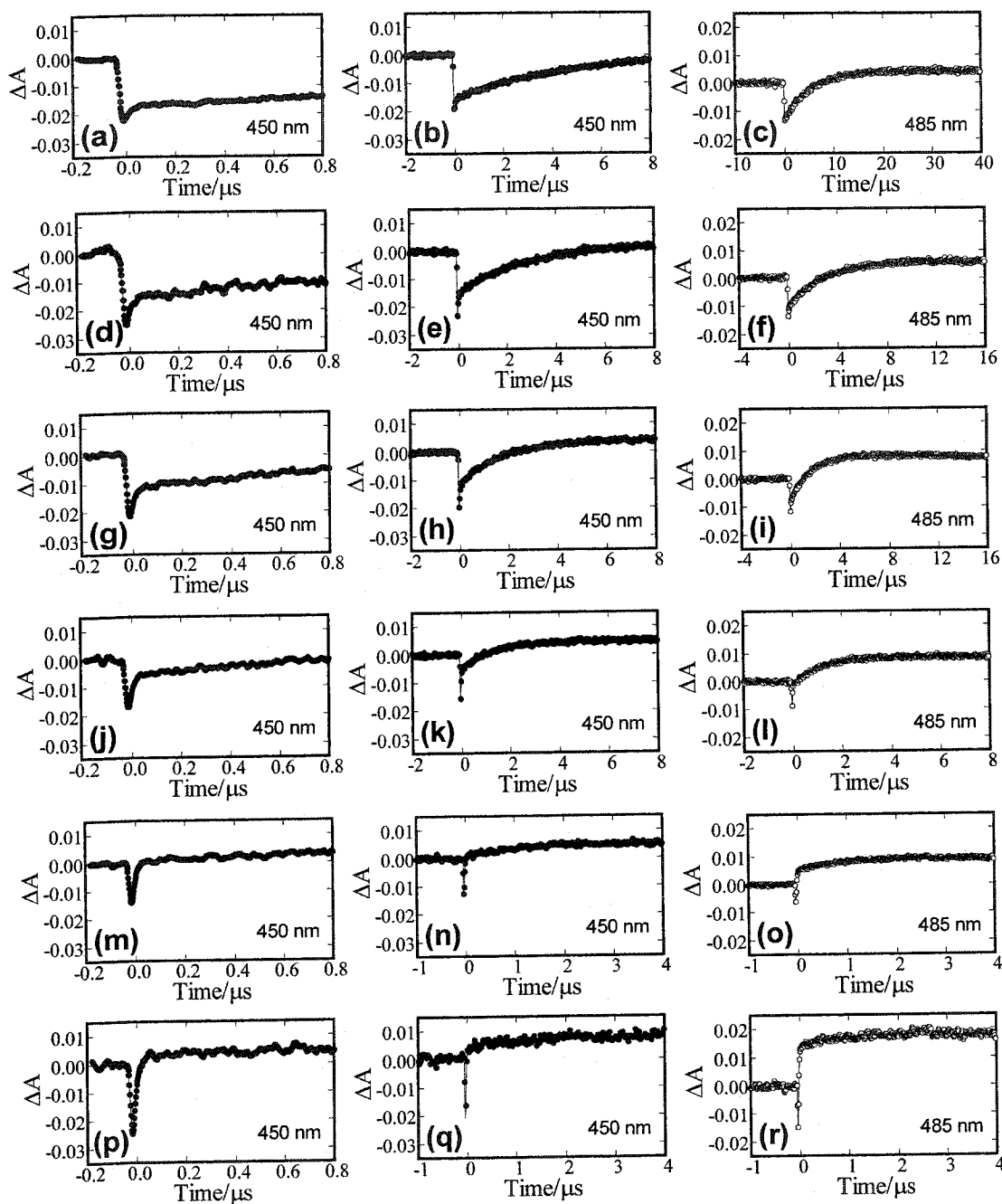


Figure 3-16. Time-resolved kinetic trace collected at (●) 450 nm and (○) 485 nm after 355-nm laser irradiation of $\text{Ru}(\text{dmb})_2(\text{C}_3\text{OC}_2\text{-NT})$ in buffered 60 mM $[\text{Ru}(\text{NH}_3)_6]\text{Cl}_3$ at pH (a-c) 3.2, (d-f) 4.2, (g-i) 4.7, (j-l) 5.1, (m-o) 5.6, and (p-r) 6.5.

3.3 Discussion

3.3.1 Electron acceptor as an Ru(I) oxidant

The results obtained in the previous section suggest that the preferential route of DMT oxidation, in the presence of a linker and photosensitizer core supporting rapid electron transfers, proceeds *via* an initial reduction of Ru(II)* to Ru(I). In this highly efficient yet unexpected mechanism, the function of the acceptor lies in the oxidation of Ru(I) back to Ru(II), not the intended conversion of Ru(II)* to Ru(III). The mechanism of Ru(II)* reduction is more efficient in that potentially all of the excited state produced could oxidize DMT, not just the amount converted to Ru(III) by the acceptor.

Moreover, the primary function of the electron acceptor as a Ru(I) oxidant is unconventional. A survey of the literature indicated that in almost all cases, the primary purpose of an acceptor is to oxidize the Ru(II)* excited state to Ru(III). The excited state does not directly act upon the substrate. Of course, the Ru(III) state is rather advantageous in that it is a stronger oxidizing agent than the corresponding excited state (Table 3-1), allowing a broader range of substrates to be oxidized. In addition, unlike the short-lived Ru(II)*, the Ru(III) state is stable and long-lived, permitting the oxidation of substrates that are either slowly oxidized or in low concentration.

The only literature instance where the electron acceptor serves to oxidize Ru(I) is found in a report last year by Engstrom *et al.*,⁷¹ where they covalently linked a ruthenium-based photosensitizer core to the heme-containing, electron-transfer protein cytochrome *c*. Here, laser-flash irradiation of the complex induced the reduction of

Ru(II)* to Ru(I) by the heme moiety, with an intramolecular electron-transfer rate of $1.5 \times 10^6 \text{ s}^{-1}$. Under anoxic conditions without any electron acceptor, the subsequent back-electron transfer between Ru(I) and the oxidized heme was observed at $7 \times 10^3 \text{ s}^{-1}$, an unexpectedly slow value. However, when either dissolved oxygen or the electron acceptor $[\text{Co}(\text{NH}_3)_5\text{Cl}]\text{Cl}_2$ was present, the Ru(I) species was rapidly converted to Ru(II), effectively blocking the relatively slow back-electron transfer pathway and leaving the oxidized heme. These pathways are analogous to the k_1 , k_{BET} , and $k_2[\text{A}]$ pathways featured in Scheme 3-4. It is accepted that the solubility of oxygen at 20 °C and 760 mm Hg is near 0.3 mM, and if it is assumed that the reaction of Ru(I) and oxygen is diffusion-controlled ($\approx 10^9 \text{ M}^{-1} \text{ s}^{-1}$), then the calculated $k_2[\text{A}]$ of $3 \times 10^5 \text{ s}^{-1}$ is substantially larger than k_{BET} between Ru(I) and oxidized heme. Hence, in this instance, oxygen is an acceptable trapping agent for Ru(I).

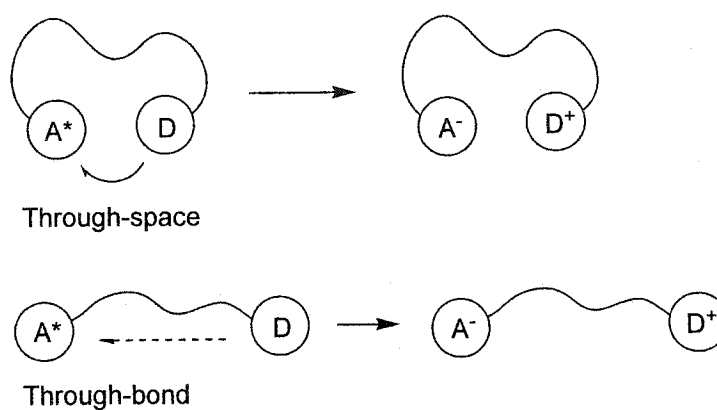
For the DMT-linked complexes, however, oxygen would not be an appropriate for Ru(I) trapping due to its low solubility. The Ru(II)* lifetime of $\text{Ru}(\text{bpy})_2(\text{C}_3\text{OC}_2\text{-NT})$ at pH 6.5 in the absence of an electron acceptor was measured at 104 ns (Table 3-3), corresponding to a decay of $1 \times 10^7 \text{ s}^{-1}$. This decay is a combination of k_1 and k_d , but the latter should contribute to only about one-fifth of the total decay, based on the 485 ns lifetime of the unlinked photosensitizer core $\text{Ru}(\text{bpy})_2(\text{dmb})$. Thus, Ru(II)* is primarily consumed *via* route k_1 . The inability to observe radical cation infers that $k_{\text{BET}} \geq k_1$, and in order for Ru(I) to be efficiently trapped, $k_2[\text{A}]$ needs to be at least 10^7 s^{-1} , depending on the value of k_{BET} . Since 60 mM $[\text{Ru}(\text{NH}_3)_6]\text{Cl}_3$ was able to trap successfully Ru(I), as inferred from the high quantum yield of radical cation, and if it is assumed that k_2 is

diffusion-controlled ($\approx 10^9 \text{ M}^{-1} \text{ s}^{-1}$), then it can be deduced that k_{BET} is in the vicinity of 10^7 s^{-1} for $\text{Ru}(\text{bpy})_2(\text{C}_3\text{OC}_2\text{-NT})$. This estimation is in line with literature data¹²⁵ for DMT linked by an ultrashort, single-methylene linker, $4 \times 10^8 \text{ s}^{-1}$.

3.3.2 Effect of linker

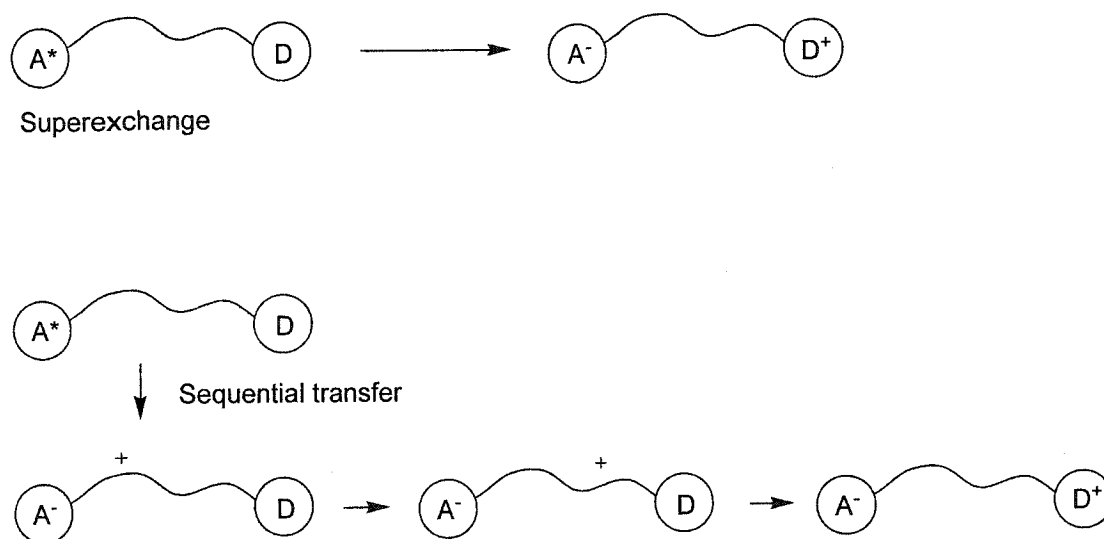
Intramolecular electron transfer between a donor and an acceptor connected by means of a linker (bridge) over long distances has recently been an area of intense study due to its biological significance.^{126,127} For instance, long-distance electron transfer over proteins forms the basis of one of the most important, light-driven, biochemical reactions, photosynthesis.¹²⁸ Similarly, the conductive nature of the fundamental molecule DNA leads to many implications, including the possibility of oxidative damage at a site distant from the original oxidation.^{129,130} As well, DNA has promising applications in the field of nanotechnology, where it can function as conductive nanowires used for charge injection and for connecting molecular devices.¹³¹⁻¹³³

From the simplest perspective, electron transfer between a linked donor and acceptor can occur *via* two methods, namely through-space or through-bond. In the former, the donor and the acceptor are sufficiently close to permit orbital overlap and subsequent electron transfer. In this mode, the function of the linker is not to conduct charge, but to bring the donor and acceptor into close proximity. Whereas, in the through-bond method, the linker acts as a conductive highway on which electrons may travel. These two modes are schematically illustrated in Scheme 3-7, where an excited acceptor accepts an electron from the donor.



Scheme 3-7. Schematic representation of through-space and through-bond electron transfer between a linked donor (D) and an excited acceptor (A*).

The through-bond mode of electron transfer can be further described by two mechanisms, superexchange (tunneling) and sequential transfer (hopping), and there is a continuous debate in the literature as to which mechanism is responsible for electron transfer between linked donor-acceptor systems. With superexchange, no charge resides on the linker, and electron transfer occurs in a single step by means of orbital wavefunction overlap between the donor, linker, and acceptor. Alternatively, sequential transfer occurs as a discrete, multiple-step process, where the linker bears charge during the electron transfer. The theoretical aspects of these two mechanisms are beyond the scope of this thesis and are for convenience represented in the schematic shown in Scheme 3-8.



Scheme 3-8. Superexchange and sequential transfer mechanisms of through-bond electron transfer, where a linked donor (D) reduces an excited acceptor (A^*).

For the DMT-linked complexes, it is not possible, based on the studies performed, to differentiate between the through-space and through-bond modes of electron transfer, let alone superexchange or hopping. The donor and acceptor are connected by non-rigid linkers that do not restrict conformation, and it is reasonable to assume that both through-space and through-bond processes can occur. When the seven-carbon alkyl linker was replaced with the four-carbon version, the rate and efficiency of radical cation generation increased. The effect of a reduced distance between the donor and the acceptor is two fold; first, the rate of through-bond electron transfer would increase, and second, the rate of through-space electron transfer would also increase due to a reduction in the number of spatial conformations that can be attained with a shorter linker.

However, the electron transfer rate constants for the two complexes containing the six-atom ether linker were substantially faster than those with the short, four-carbon linker. Neither is conformationally restricted, and since the ether linker is longer, its contribution of the through-space process to the overall electron transfer should be smaller than with the four-carbon alkyl linker. As well, the more polar ether group may prefer an open, extended conformation in aqueous solutions, distancing the photosensitizer core from the substrate and causing a reduction in the through-space electron transfer.

Accordingly, the higher rate constants observed for the ether are better ascribed to an enhanced through-bond transfer. The presence of a highly polarizable oxygen atom may increase the probability of orbital-wavefunction overlap between the donor and acceptor moieties, resulting in faster superexchange. The enhanced conductivity of an oxygen-containing linker is analogous to the rigid, highly conjugated linkers that have been optimized for rapid charge transfer.^{69,134} As well, the oxygen may aid in stabilizing any short-lived charge that may form on the linker due to sequential transfer.

In order to distinguish between the through-bond and through-space modes of linker-mediated electron transfer, further experiments are necessary. Some literature studies¹³⁵ on electron transfer between linked donors and acceptors involved the addition of β -cyclodextrin, which has been suggested to promote linker elongation *via* self-insertion between the donor and the acceptor. The overall effect is the distancing of the donor and acceptor moieties, leading to a reduction of through-space interaction, and similar studies on these DMT-linked complexes would prove interesting.

3.4 Conclusion

In this chapter, the tris(bipyridyl)ruthenium-sensitized oxidation of linked *N,N*-dimethyl-*p*-toluidine to its respective radical cation was demonstrated. The oxidation of this substrate serves as a reasonable model for the sterically hindered substrates that are investigated in the subsequent chapter. Moreover, this model substrate emphasized that several general considerations need to be taken into account when designing complexes intended for the delivery of reactive intermediates to remote sites. Specifically, if the behaviour of these short-lived intermediates in remote sites is to be studied, it is desirable to optimize their rate of generation.

Of significant importance is the linker, which can serve as a molecular wire for the flow of electrons between the substrate and the photosensitizer core. If the rapid route of substrate oxidation *via* an initial Ru(II)* reduction to Ru(I) is desired, then k_1 needs to be significantly faster than k_d and $k_3[A]$. However, increasing k_1 by means of a more-conductive linker would logically also increase k_{BET} . As a result, excessively fast conditions can lead to a futile cycle, which takes place when k_{BET} exceeds $k_2[A]$. Similarly, a slow linker would favour the less-efficient Ru(III) route instead of Ru(I), resulting in slow radical cation generation. While it appears that it is essential to seek a compromise between the two scenarios, the importance of the linker may in fact be less significant in the presence of biomolecules such as proteins. The conductive nature of proteins raises the possibility that electron transfer between the substrate and the photosensitizer core may proceed through the protein instead of the linker.

In the intramolecularly linked complexes, the effect of substituent was also apparent. Substitution on the bipyridyl ligands serves to modify the electrochemical properties (thermodynamics) of the complexes with relative synthetic ease. In turn, the thermodynamics of an electron-transfer reaction are directly linked to the rate at which it occurs by Marcus theory, where in the normal region, the rate of an electron transfer increases as the reaction is more thermodynamically favourable. Substrate oxidation by Ru(II)* of the two photosensitizer cores of Ru(dmb)₃ and Ru(bpy)₂(dmb) yields ΔG° values of -0.07 V and $+0.08$ V, respectively. Similarly, oxidation by Ru(III) of the same complexes affords respective ΔG° of $+0.39$ V and $+0.56$ V. These potential differences are significantly lower than the typical reorganization energies of 0.5-1.0 V, which place them in the Marcus normal region and explain the faster electron transfers observed for the Ru(bpy)₂(dmb) photosensitizer core. Thus, it is beneficial to have electron-withdrawing ligands, which increase the rate of electron transfer.

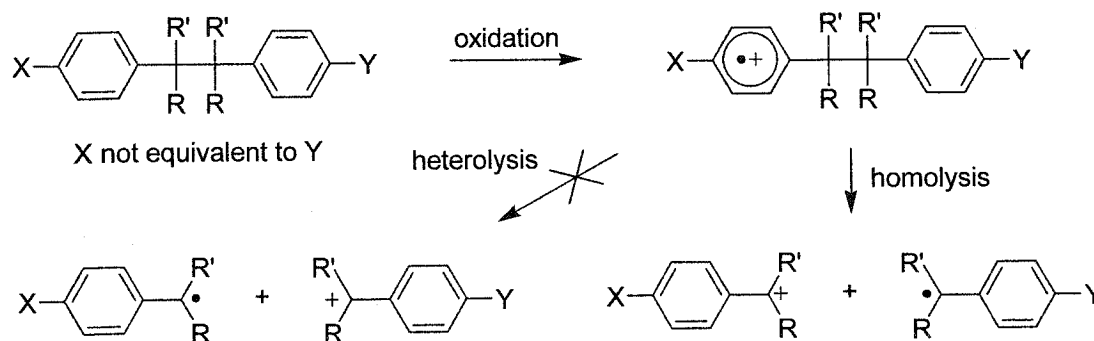
Chapter Four: Intramolecular Oxidation of Diphenylalkanes

4.1 Introduction

While the previous chapter describes the intramolecular oxidation of a linked substrate to its respective radical cation by tris(bipyridyl)ruthenium complexes, this chapter extends those concepts and examines linked, sterically hindered substrates that can undergo fragmentation upon oxidation.⁶¹ These substrate-linked complexes could be used to “deliver” carbocations to hydrophobic sites of enzymes, synthetic peptides, and other biomolecules in a controlled, photoactivated manner. It is anticipated that the linked, hydrophobic substrate moiety will bind to the hydrophobic regions of the biomolecule, and upon laser-flash irradiation, oxidation, and fragmentation, an unlinked carbocation will be delivered, as schematically represented in Scheme 1-2. The tris(bipyridyl)ruthenium photosensitizer core functions only as an oxidant, and the fragmentation of the radical cation lies independent of the photosensitizer.

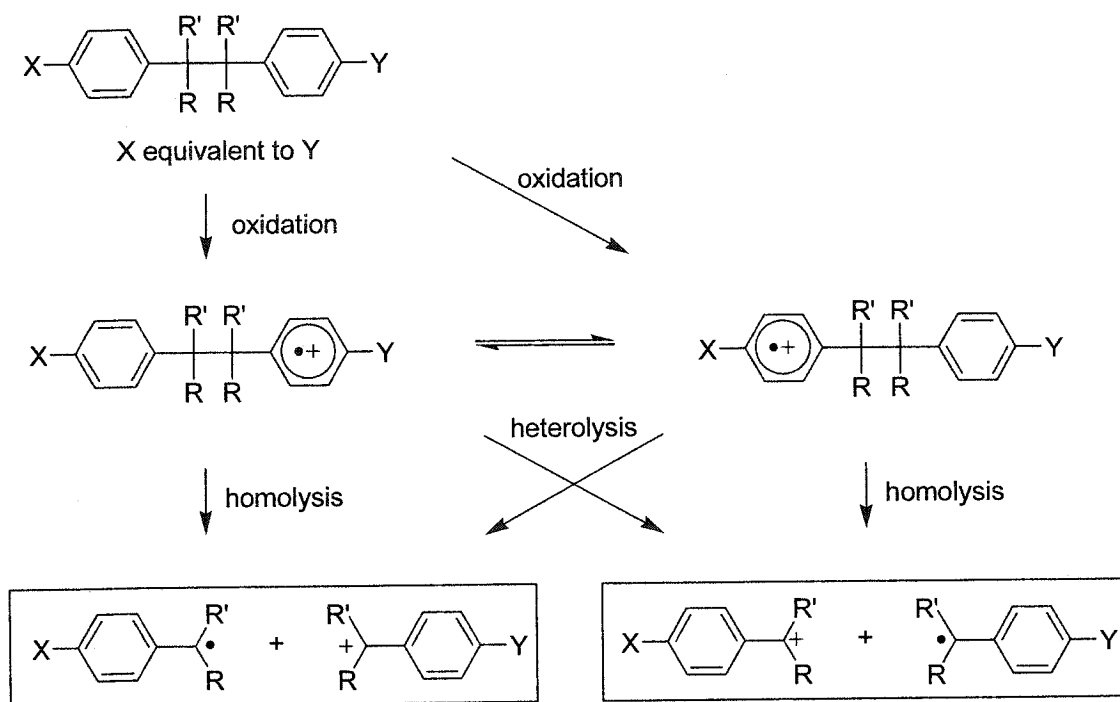
The substrates studied in this chapter feature a diphenylalkane moiety that is hindered about the central C-C bond (Scheme 4-1), where oxidation to their respective radical cations induces cleavage to form 4-substituted α,α -dialkylbenzyl carbocations and radicals.^{61,136} In cases where the substrate is unsymmetrically 4,4'-disubstituted, both the radical cation and the resultant carbocation are expected to form on the terminus more able to stabilize the charge, denoted by substituent X in this general schematic. In this example, the X substituent is typically a better electron-donating group than Y, and also

more easily oxidized. The presence of two possible routes of cleavage, homolysis and heterolysis, has been termed *mesolysis*.^{136,137} In this example, where heterolysis would result in the formation of less-stable products, the homolytic route should predominate.



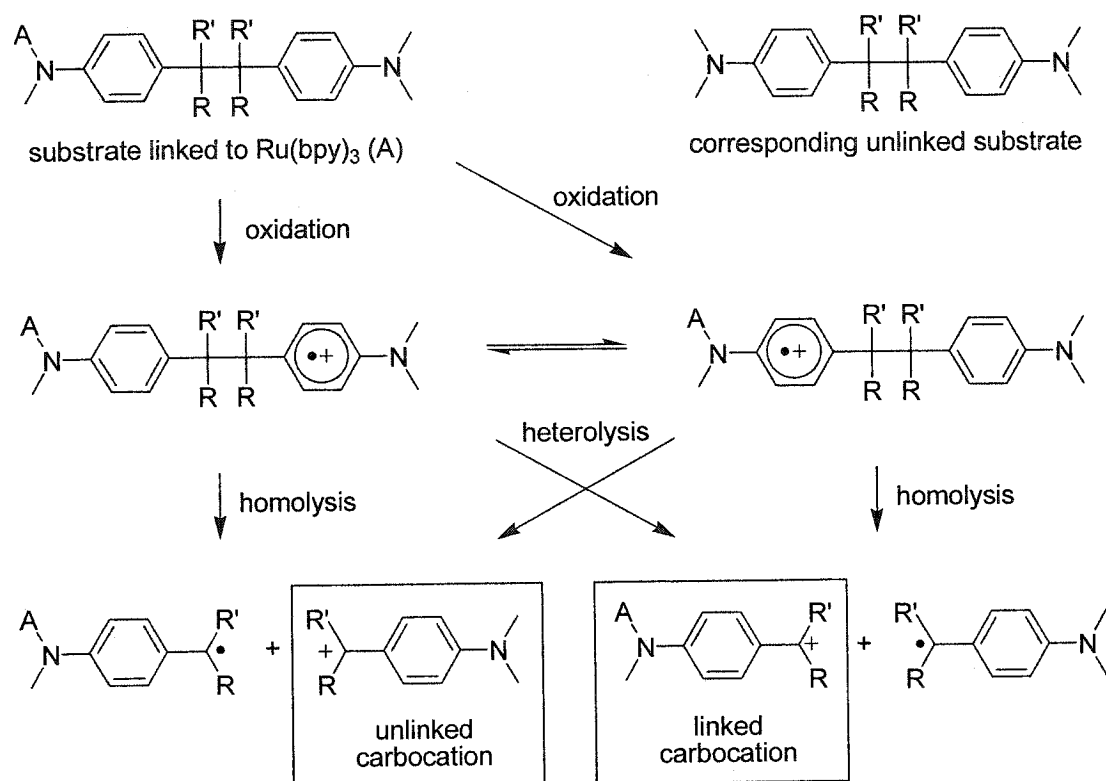
Scheme 4-1. Oxidation of an unsymmetrical diphenylalkane substrate to its respective radical cation, which can undergo fragmentation to afford a carbocation and a radical. Both the radical cation and the carbocation are generated on the terminus, herein shown as the X-substituted, more able to stabilize the positive charge.

If a substrate were symmetrically substituted, where both X and Y substituents are identical or equivalent (e.g. *N,N*-dimethylamino and *N*-alkyl-*N*-methylamino are deemed equivalent), as shown in Scheme 4-2, then it can be assumed both termini will be oxidized. Thus, it is likely the radical cation would be formed on both fragments in equal proportion. Following cleavage, the amount of X-substituted carbocation would be equal to the amount of the Y-substituted, regardless of the pathway favoured. Of course, since the X and Y substituents are equivalent, they would not be easily distinguished by absorption spectroscopy.



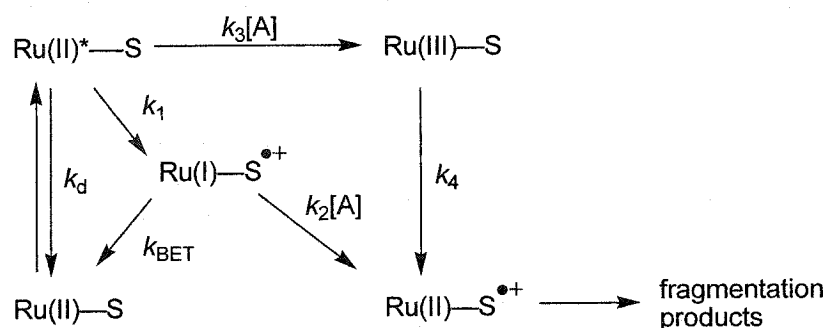
Scheme 4-2. Oxidation of a symmetrical diphenylalkane substrate to its respective radical cation. The equivalent nature of X and Y suggests that the radical cations will be equally distributed amongst both forms. Cleavage by heterolysis or homolysis should afford X- and Y-substituted carbocations in equal proportions.

This argument can be applied to substrates linked to tris(bipyridyl)ruthenium, as shown in Scheme 4-3, where one *N*-methyl group of a symmetrical substrate is replaced with an alkyl chain linked to the photosensitizer core. In this context, this replacement is considered equivalent, and the substrate will be referred to as symmetrical. Thus, the radical cation would be generated on both termini, with cleavage producing carbocations, half linked and the other half free. However, this would only be true if the photosensitizer equally oxidizes both termini or if a rapid equilibrium between the two is achieved.



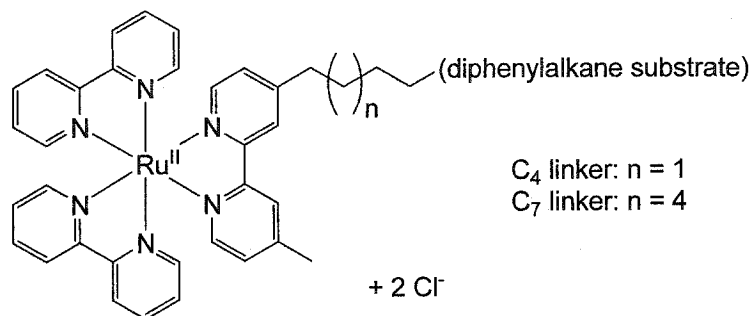
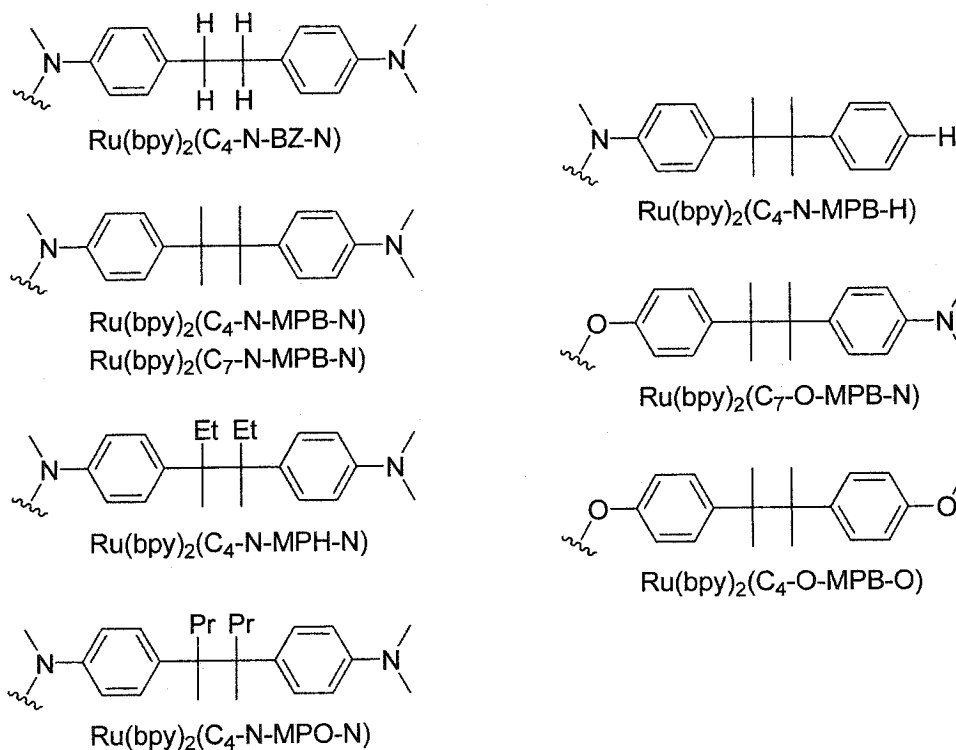
Scheme 4-3. Corresponding symmetrical diphenylalkane substrate linked by an alkyl chain to a tris(bipyridyl)ruthenium photosensitizer core (denoted by A). Half of the carbocations formed would remain linked, while the other half would be free.

Like the linked DMT studied in the previous chapter, two pathways of oxidation are also possible with these linked complexes (Scheme 4-4). However, a difference exists between these studies and those of DMT, in that an irreversible sacrificial electron acceptor, $[\text{Co}(\text{NH}_3)_5\text{Cl}]\text{Cl}_2$, was used herein rather than the reversible $\text{Ru}(\text{NH}_3)_6\text{Cl}_3$. This cobalt-based acceptor decomposes to $\text{Co}^{2+}(\text{aq})$ upon reduction,¹³⁸ and the $\text{Co}(\text{III})/\text{Co}(\text{II})$ potential⁸² of 1.92 V indicates that back-electron transfer with either $\text{Ru}(\text{III})$ or the substrate radical cation will not be favourable.



Scheme 4-4. Intramolecular substrate oxidation in the presence of an irreversible electron acceptor. Two routes of substrate oxidation are present and are distinguished by an initial Ru(II)* reduction to Ru(I) by k_1 or an initial Ru(II)* oxidation to Ru(III) by k_3 .

A variety of hydrophobic, diphenylalkane substrates were prepared and covalently linked to water-soluble ruthenium photosensitizer cores (Scheme 4-5). Results from the previous chapter indicated that complexes with two unlinked bpy ligands, as opposed to dmb, would be better for the oxidation of linked aromatic amines. Thus, in this chapter, only complexes in the form of Ru(bpy)₂(substrate-linked-ligand) were investigated. The substrates used in these linked complexes differ by 4,4'-substitution as well as the alkyl groups at the fragmenting C-C bond, so that these effects on the kinetics of fragmentation and hence radical cation generation could be studied. As the focus of this chapter is to demonstrate the ability of ruthenium complexes to oxidize diphenylalkane substrates and to measure rate constants for the radical cation fragmentations in aqueous solutions, most substrates were linked using only the four-carbon alkyl linker (C₄).

General structureDiphenylalkane substrates and designation of linked complexes

Scheme 4-5. Diphenylalkane substrates, comprised of bibenzyl (BZ), 2,3-dimethyl-2,3-diphenylbutane (MPB), 3,4-dimethyl-3,4-diphenylhexane (MPH), and 4,5-dimethyl-4,5-diphenyloctane (MPO) centres, linked to tris(bipyridyl)ruthenium. Corresponding unlinked substrates have a methyl group in place of the alkyl-linked photosensitizer.

4.2 Results

All studies were at pH 7.2 in nitrogen-purged 10 mM sodium phosphate. At this pH, substrates containing aniline nitrogens are expected to be unprotonated.

4.2.1 Excited-state lifetime measurements

In order to evaluate linked-substrate oxidation by Ru(II)* states (k_1), the excited state lifetimes of the complexes were measured at 370 nm after 355-nm laser-flash irradiation in the *absence* of an electron acceptor (Table 4-1). Under these conditions, only pathways are k_d , k_1 , and k_{BET} (Scheme 4-4) are available, and any electron transfer between the substrate and Ru(II)* by k_1 would result in a decreased excited-state lifetime.

Table 4-1. Excited-state lifetimes of tris(bipyridyl)ruthenium complexes linked to diphenylalkane substrates in 10 mM sodium phosphate pH 7.2.

Substrate-linked complex	Lifetime/ns
Ru(bpy) ₂ (C ₄ -N-BZ-N)	66 ± 3
Ru(bpy) ₂ (C ₄ -N-MPB-N)	83 ± 4
Ru(bpy) ₂ (C ₄ -N-MPH-N)	71 ± 3
Ru(bpy) ₂ (C ₄ -N-MPO-N)	69 ± 4
Ru(bpy) ₂ (C ₄ -N-MPB-H)	220 ± 3
Ru(bpy) ₂ (C ₄ -O-MPB-N)	412 ± 7
Ru(bpy) ₂ (C ₇ -O-MPB-O)	480 ± 2
Ru(bpy) ₂ (C ₇ -N-MPB-N)	63 ± 3

The lifetime of $\text{Ru}(\text{bpy})_2(\text{C}_7\text{-O-MPB-O})$ is virtually identical with that of $\text{Ru}(\text{bpy})_2(\text{dmb})$, an unlinked complex that is representative of the photosensitizer cores of the substrate-linked complexes and has a measured lifetime of 475 ns. These similar lifetimes suggest that the substrate was not oxidized by the $\text{Ru}(\text{II})^*$ excited state, as anticipated from the difference in reduction potentials of the two species involved; the reference unlinked complex has a $\text{Ru}(\text{II})^*/\text{Ru}(\text{I})$ reduction potential of +0.79 V (Table 2-1), while that of the dianisole substrate radical cation⁶¹ is +1.84 V. As well, this negative result demonstrates that the attachment of a large substrate to the photosensitizer core does not significantly impact its lifetime.

Complexes containing linked substrates with at least one aniline nitrogen exhibited noticeable excited-state lifetime reductions. These are attributed to the presence of an intramolecular electron transfer pathway, k_1 , that contributes to the depletion of $\text{Ru}(\text{II})^*$. Moreover, the degree of lifetime reduction was highly dependent on the structure of the linked substrate. While a clustered range of lifetimes (63-83 ns) was observed for complexes featuring aniline functionalities on both termini of the diphenylalkane substrate moiety, lifetimes for the complexes containing only one aniline, $\text{Ru}(\text{bpy})_2(\text{C}_4\text{-N-MPB-H})$ and $\text{Ru}(\text{bpy})_2(\text{C}_4\text{-O-MPB-N})$, were less remarkable at 220 and 412 ns, respectively. These longer lifetimes infer that the electron transfer process (k_1) in these complexes are slower, and their possible causes are discussed later on. As well, it is interesting to note that the presence of a longer linker in $\text{Ru}(\text{bpy})_2(\text{C}_7\text{-N-MPB-N})$ actually increases the electron transfer rate somewhat relative to the four-carbon linked complex, $\text{Ru}(\text{bpy})_2(\text{C}_4\text{-N-MPB-N})$.

In all cases, as with the linked *N,N*-dimethyl-*p*-toluidine studied in the previous chapter, no transients corresponding to the absorption of the aromatic-amine radical cations ($\lambda_{\text{max}} \approx 485 \text{ nm}$) were detected. These observations suggest that rapid charge recombination between Ru(I) and the radical cation ($k_{\text{BET}} > k_1$) occurred. Results in the literature¹²⁵ indicate that the back-electron transfer for a similar system occurs at a high rate of approximately $1.5 \times 10^8 \text{ s}^{-1}$. The net result is an energy-wasting pathway ($k_1 + k_{\text{BET}}$) that consumes Ru(II)* yet produces no radical cation.

4.2.2 Laser-flash irradiation with an electron acceptor

The addition of an irreversible electron acceptor $[\text{Co}(\text{NH}_3)_5\text{Cl}]\text{Cl}_2$ (15 mM; near solubility limit) to the laser-flash irradiation solutions introduces two pathways, $k_2[\text{A}]$ and $k_3[\text{A}]$, that are responsible for the oxidation of Ru(I) and Ru(II)* to Ru(II) and Ru(III), respectively (Scheme 4-4). As discussed in the previous chapter, two competitive routes exist for the consumption of Ru(II)*, k_1 and $k_3[\text{A}]$, and are distinguished by an initial excited-state oxidation or reduction, respectively. Under conditions where k_1 is slow, Ru(II)* would be irreversibly oxidized by the acceptor to Ru(III). Likewise, a very fast k_1 would lead to the reduction of Ru(II)* to Ru(I) by the substrate, where subsequent oxidation of Ru(I) by $k_2[\text{A}]$ regenerates Ru(II), effectively halting the energy-wasting k_{BET} .

4.2.2.1 Generation of radical cations

Radical-cation generation is normally deduced from the direct observation of the radical cation absorption band, which for aromatic amines typically has a maximum near 485-490 nm. However, for radical cations that do not absorb in a useful spectral region, such as the dianisole radical cation that can be formed from the complex $\text{Ru}(\text{bpy})_2(\text{C}_7\text{-O-MPB-O})$, generation needs to be inferred from the recovery of Ru(II) bleaching from Ru(III), k_4 , similar to studies in Chapter 2. Thus, the kinetic trace for this complex, shown in Figure 4-1 (a), was recorded at 450 nm to monitor ground-state Ru(II). Immediately after the laser pulse, a portion of the Ru(II)* excited-state is oxidized to Ru(III) by the electron acceptor, and this is observed as a negative signal due to the consumption of Ru(II). No recovery of the bleaching was observed over a time scale of 120 μs after the laser pulse. This trace resembles that of the unlinked reference $\text{Ru}(\text{bpy})_2(\text{dmb})$, shown in Figure 4-1 (b), where the Ru(III)-to-Ru(II) recovery is not possible since there is no substrate available for oxidation. The electron acceptor used is irreversible, and thus no conversion from Ru(III) to Ru(II) can occur in the absence of oxidizable substrate. Consequently, it is concluded that oxidation of the linked substrate in $\text{Ru}(\text{bpy})_2(\text{C}_7\text{-O-MPB-O})$ did not occur; the reduction potential of the Ru(III)/Ru(II) couple (+1.27 V) is insufficient to oxidize the substrate (+1.84 V for the corresponding radical cation) at a reasonable rate to be observed.

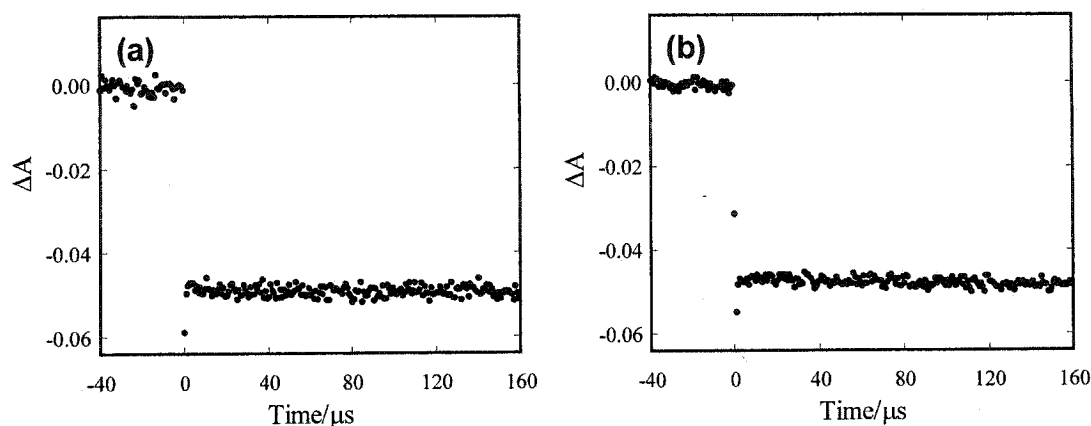
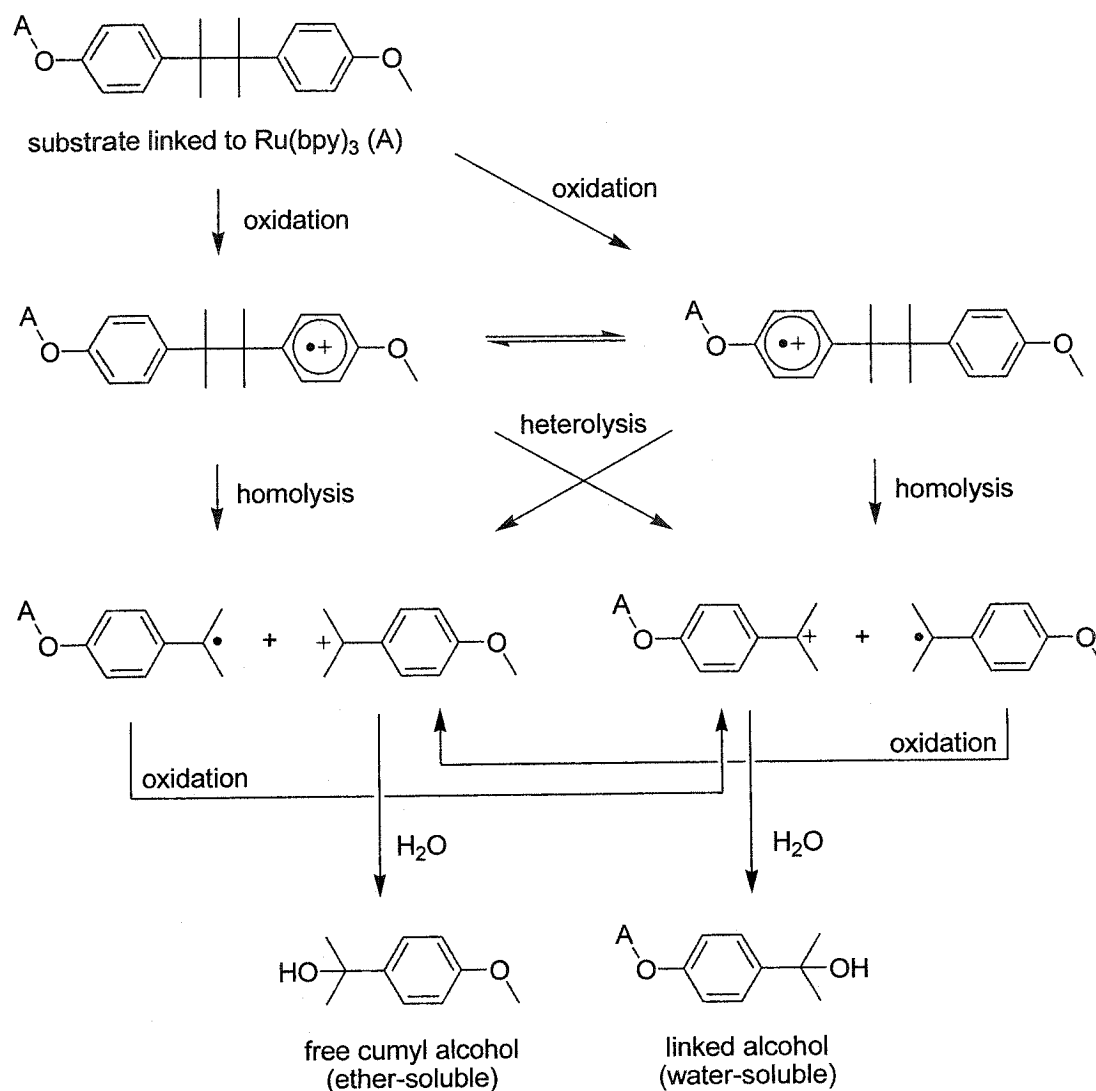


Figure 4-1. Time-resolved kinetic trace monitored at 450 nm following 355-nm laser irradiation of (a) $\text{Ru}(\text{bpy})_2(\text{C}_7\text{-O-MPB-O})$ and (b) $\text{Ru}(\text{bpy})_2(\text{dmb})$ in nitrogen-saturated 10 mM sodium phosphate pH 7.2 containing 15 mM $[\text{Co}(\text{NH}_3)_5\text{Cl}]\text{Cl}_2$.

To determine whether the endothermic electron transfer for the complex $\text{Ru}(\text{bpy})_2(\text{C}_7\text{-O-MPB-O})$ can actually occur, but at very slow rates, product studies were performed. A mixture of nitrogen-purged 10 mM $[\text{Co}(\text{NH}_3)_5\text{Cl}]\text{Cl}_2$ and 0.1 mM $\text{Ru}(\text{bpy})_2(\text{C}_7\text{-O-MPB-O})$ was irradiated with a mercury lamp equipped with a Pyrex filter (300 nm cut-off). After five minutes of irradiation, the initially brown/orange photolysis mixture turned black, and the irradiation was halted. The ethereal extract of the photolysis was analyzed by ^1H NMR and GC-MS, and only one compound was detected. This compound was unequivocally identified as 4-methoxycumyl alcohol, with ^1H NMR (CDCl_3 , 250 MHz) δ (ppm): 1.56 (s, 6H), 2.60 (br s, 1H), 3.78 (s, 3H), 6.88 (d, 2H, 8.6 Hz), 7.41 (d, 2H, 8.7 Hz); and GC-MS m/z : 166 ($\text{M}^{\bullet+}$, 2%), 148 ($\text{M}^{\bullet+} - \text{H}_2\text{O}$, 100%). Any other organic compounds formed from the photolysis that are not linked to the

ruthenium complex would have been expected to be ether-soluble, and thus the absence of other compounds in the extracts indicates that 4-methoxycumyl alcohol is the sole photoproduct. This product could only have been formed from the cleavage of the linked substrate, but surprisingly, no radical-derived product, expected to be the radical dimer 4,4'-dimethoxybicumene, was detected (Scheme 4-6). These observations could possibly be explained by the oxidation of the *p*-methoxycumyl radical, by the electron acceptor, to its carbocation (reduction potential $(+)/(•) = -0.14$ V relative to SCE in CH_3CN)¹³⁹, which subsequently reacted with water to form the alcohol. However, it still remains unclear why the inferred oxidation occurred with the mercury-lamp photolysis, but not with laser-flash photolysis experiments. It is possible that with the mercury-lamp photolysis, an oxidizing species other than Ru(III) is generated, and thus, further work is suggested to demonstrate that in this photolysis, the oxidizing species is indeed Ru(III).

The other substrate-linked complexes listed in Scheme 4-5, feature one or two aniline functionalities. In laser-flash photolysis experiments carried out with a cobalt-based electron acceptor, absorption was monitored at 490 nm where the *N,N*-dialkyl-*p*-toluidine radical cation has a strong absorption, and where interference from the MLCT absorption of ground-state Ru(II) is relatively small. Kinetic traces obtained from the laser-flash irradiation of these substrate-linked complexes are illustrated in Figure 4-2 through Figure 4-8.



Scheme 4-6. Formation of *p*-methoxycumyl alcohol from the mercury-lamp photolysis of a mixture of 10 mM $[\text{Co}(\text{NH}_3)_5\text{Cl}]\text{Cl}_2$ and 0.1 mM $\text{Ru}(\text{bpy})_2(\text{C}_7\text{-O-MPB-O})$. The photosensitizer core and alkyl chain are denoted as A. No radical-derived product was detected, suggesting the oxidation of the radical to the carbocation.

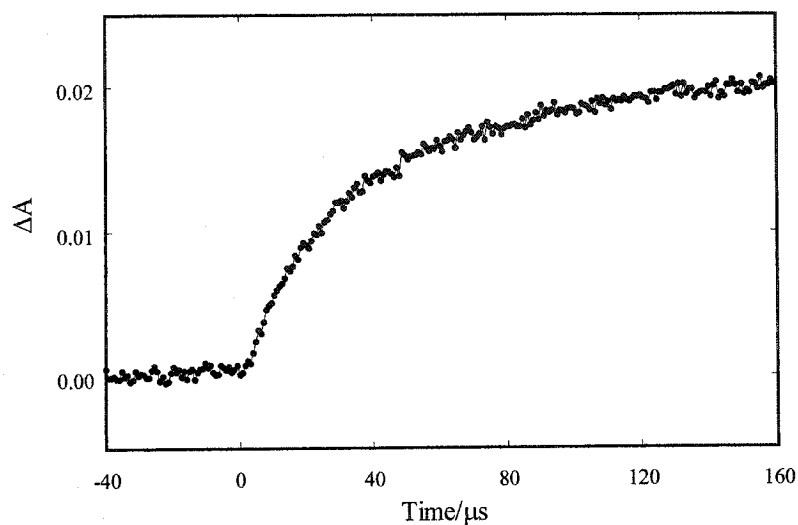


Figure 4-2. Time-resolved kinetic trace monitored at 490 nm following 355-nm laser irradiation of $\text{Ru}(\text{bpy})_2(\text{C}_4\text{-O-MPB-N})$ in nitrogen-saturated 10 mM sodium phosphate pH 7.2 containing 15 mM $[\text{Co}(\text{NH}_3)_5\text{Cl}]\text{Cl}_2$.

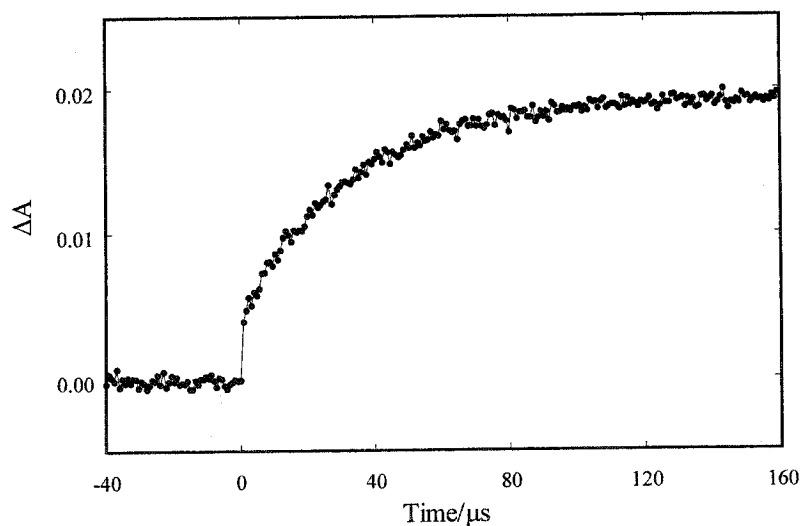


Figure 4-3. Time-resolved kinetic trace monitored at 490 nm following 355-nm laser irradiation of $\text{Ru}(\text{bpy})_2(\text{C}_4\text{-N-MPB-H})$ in nitrogen-saturated 10 mM sodium phosphate pH 7.2 containing 15 mM $[\text{Co}(\text{NH}_3)_5\text{Cl}]\text{Cl}_2$.

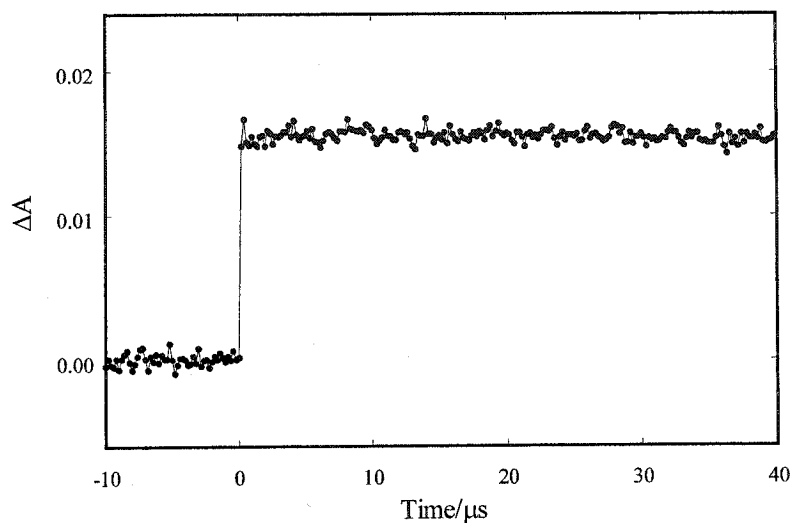


Figure 4-4. Time-resolved kinetic trace monitored at 490 nm following 355-nm laser irradiation of $\text{Ru}(\text{bpy})_2(\text{C}_4\text{-N-BZ-N})$ in nitrogen-saturated 10 mM sodium phosphate pH 7.2 containing 15 mM $[\text{Co}(\text{NH}_3)_5\text{Cl}]\text{Cl}_2$.

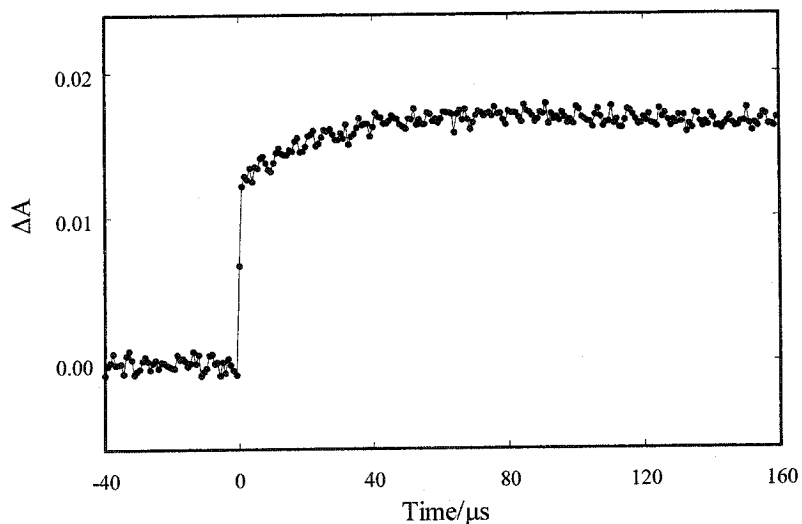


Figure 4-5. Time-resolved kinetic trace monitored at 490 nm following 355-nm laser irradiation of $\text{Ru}(\text{bpy})_2(\text{C}_4\text{-N-MPB-N})$ in nitrogen-saturated 10 mM sodium phosphate pH 7.2 containing 15 mM $[\text{Co}(\text{NH}_3)_5\text{Cl}]\text{Cl}_2$.

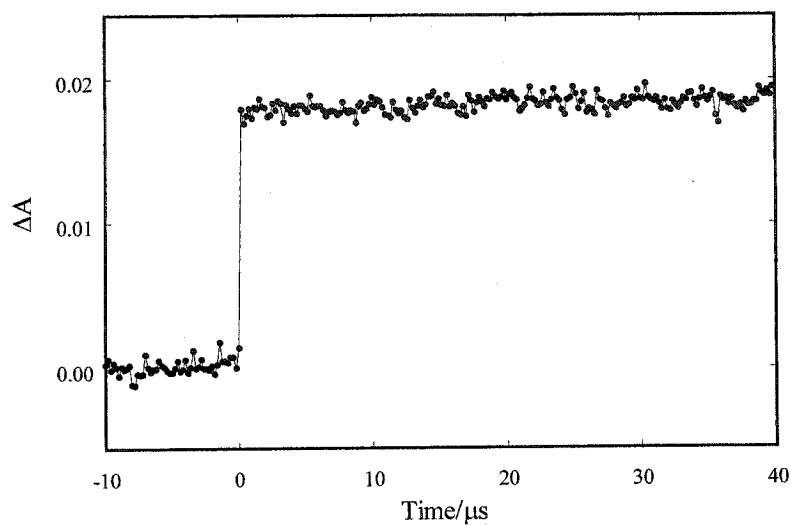


Figure 4-6. Time-resolved kinetic trace monitored at 490 nm following 355-nm laser irradiation of $\text{Ru}(\text{bpy})_2(\text{C}_7\text{-N-MPB-N})$ in nitrogen-saturated 10 mM sodium phosphate pH 7.2 containing 15 mM $[\text{Co}(\text{NH}_3)_5\text{Cl}]\text{Cl}_2$.

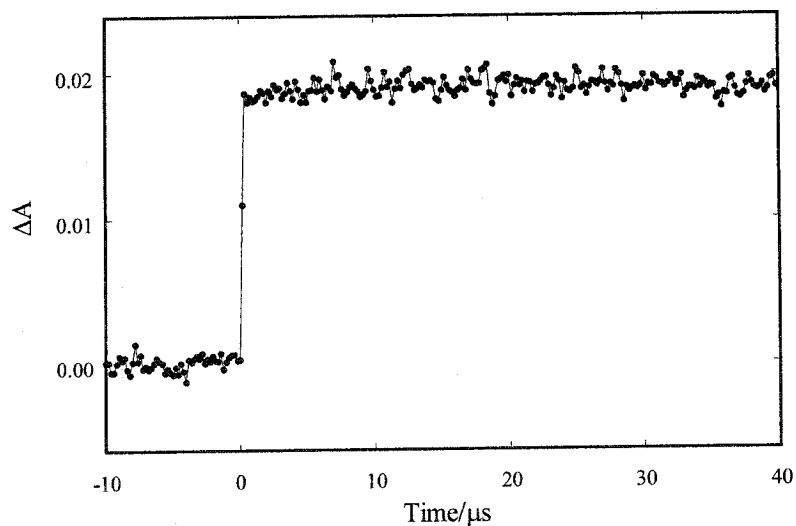


Figure 4-7. Time-resolved kinetic trace monitored at 490 nm following 355-nm laser irradiation of $\text{Ru}(\text{bpy})_2(\text{C}_4\text{-N-MPH-N})$ in nitrogen-saturated 10 mM sodium phosphate pH 7.2 containing 15 mM $[\text{Co}(\text{NH}_3)_5\text{Cl}]\text{Cl}_2$.

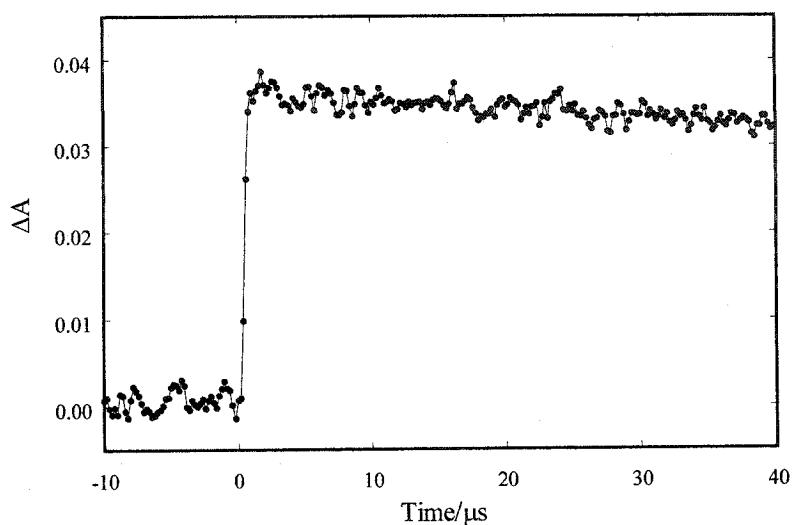


Figure 4-8. Time-resolved kinetic trace monitored at 490 nm following 355-nm laser irradiation of $\text{Ru}(\text{bpy})_2(\text{C}_4\text{-N-MPO-N})$ in nitrogen-saturated 10 mM sodium phosphate pH 7.2 containing 15 mM $[\text{Co}(\text{NH}_3)_5\text{Cl}]\text{Cl}_2$.

Laser-flash irradiation of the substrate-linked $\text{Ru}(\text{bpy})_2(\text{C}_4\text{-O-MPB-N})$ complex in the presence of the electron acceptor resulted in the monoexponential formation of the corresponding substrate cation at 490 nm (Figure 4-2) at a relatively slow rate constant of $2.4 \times 10^4 \text{ s}^{-1}$. The recovery of Ru(II) bleaching was also concomitantly observed at 450 nm with similar kinetics (not shown), suggesting that the radical cation is indeed a product of Ru(III) oxidation, k_4 . The monoexponential property of the radical cation growth indicates that virtually all of the radical cation produced is formed *via* k_4 ; this is feasible due to the relatively slow k_1 (412 ns; Table 4-1) for this complex, allowing the acceptor to oxidize efficiently $\text{Ru}(\text{II})^*$ to $\text{Ru}(\text{III})$ *via* $k_3[\text{A}]$. Hence, with this complex, the

predominant mechanism of radical cation formation proceeds by an initial Ru(II)* oxidation.

In contrast, biexponential kinetics were observed for the generation of radical cation derived from the Ru(bpy)₂(C₄-N-MPB-H) complex (Figure 4-3). After laser-flash irradiation in the presence of the electron acceptor, a rapid growth ($> 10^7 \text{ s}^{-1}$) corresponding to approximately 25% of the total radical cation produced was observed, followed by the balance (75%) at a substantially reduced rate of $3.0 \times 10^4 \text{ s}^{-1}$. This complex has a moderate k_1 based on its excited-state lifetime of 220 ns (Table 4-1), which allows for competition between an initial Ru(II)* reduction (k_1) or oxidation ($k_3[\text{A}]$). Ru(I) generated via the initial-reduction route is rapidly trapped by the acceptor ($k_2[\text{A}]$) to prevent charge recombination with the radical cation (k_{BET}), while Ru(III) resulting from initial oxidation returns to Ru(II) more gradually *via* electron transfer with the substrate (k_4).

For complexes with a faster k_1 (Table 4-1), such as Ru(bpy)₂(C₄-N-MPB-N) with a lifetime of 83 ns, the effect of competition becomes more significant (Figure 4-5). The kinetic trace recorded for the radical cation growth remains biphasic, and the fraction of initial, fast component ($> 10^7 \text{ s}^{-1}$) now corresponds to approximately 78% of the total growth, with the remaining 22% occurring at a slower rate of $4.2 \times 10^4 \text{ s}^{-1}$. Likewise, about three-quarters of the total radical cation is generated primarily through the route of initial Ru(II)* reduction, k_1 .

For complexes with even lower excited-state lifetimes of 63-71 ns (Table 4-1), the kinetic traces illustrating radical cation growth again showed monoexponential

behaviour, Figures 4-4, Ru(bpy)₂(C₄-N-BZ-N); 4-5, Ru(bpy)₂(C₇-N-MPB-N); 4-7, Ru(bpy)₂(C₄-N-MPH-N); and 4-8, Ru(bpy)₂(C₄-N-MPO-N). Kinetic traces for these complexes show that complete radical cation formation occurs rapidly ($> 10^7 \text{ s}^{-1}$) without a second, slower component. With these complexes, k_1 is significantly faster than $k_3[A]$, and the Ru(II)* excited state is reduced to Ru(I); in this scenario, the primary route of radical cation generation is an initial Ru(II)* reduction.

Rate constants for the generation of radical cations from the corresponding substrate-linked complexes in the presence of the electron acceptor, as well as the fraction of radical cation generated by the fast component, are summarized in Table 4-2. Clearly, a trend exists where the percentage of the radical cation generated by the fast component increases with decreasing excited-state lifetime (Table 4-1), supporting the proposal that the fast component originates from Ru(I) formation.

Essentially, all substrate-linked complexes except that of Ru(bpy)₂(C₄-O-MPB-O) demonstrated radical cation formation. For complexes with asymmetrical substrates, Ru(bpy)₂(C₄-O-MPB-N) and Ru(bpy)₂(C₄-N-MPB-H), the presence of absorption near 485 nm suggests that the radical cation is most likely situated on the aniline moiety. Interestingly, the oxidation of these asymmetrical substrates to their corresponding radical cations is substantially slower than the substrates containing only one aniline moiety. As well, the introduction of a longer, C₇ linker increased the rate of electron transfer, contrary to results from the previous chapter. These observations and issues are later addressed in the discussion.

Table 4-2. Radical cation generation rate constants for tris(bipyridyl)ruthenium complexes linked to diphenylalkane substrates in 10 mM sodium phosphate pH 7.2 containing 15 mM $[\text{Co}(\text{NH}_3)_5\text{Cl}]\text{Cl}_2$.

Substrate-linked complex	Rate constants/s ⁻¹ (fraction of total growth)
$\text{Ru}(\text{bpy})_2(\text{C}_4\text{-N-BZ-N})$	$> 10^7$ (100%)
$\text{Ru}(\text{bpy})_2(\text{C}_4\text{-N-MPB-N})$	$> 10^7$ (78%), $4.2 \pm 0.2 \times 10^4$ (22%)
$\text{Ru}(\text{bpy})_2(\text{C}_4\text{-N-MPH-N})$	$> 10^7$ (100%)
$\text{Ru}(\text{bpy})_2(\text{C}_4\text{-N-MPO-N})$	$> 10^7$ (100%)
$\text{Ru}(\text{bpy})_2(\text{C}_4\text{-N-MPB-H})$	$> 10^7$ (25%), $3.0 \pm 0.2 \times 10^4$ (75%)
$\text{Ru}(\text{bpy})_2(\text{C}_4\text{-O-MPB-N})$	$2.4 \pm 0.1 \times 10^4$ (100%)
$\text{Ru}(\text{bpy})_2(\text{C}_7\text{-N-MPB-N})$	$> 10^7$ (100%)
$\text{Ru}(\text{bpy})_2(\text{C}_4\text{-O-MPB-O})$	No radical cation

4.2.2.2 Fragmentation of radical cations

In this section, the radical cations of amino-substituted diphenylalkane substrates linked to tris(bipyridyl)ruthenium are evaluated for fragmentation and aminobenzyl carbocation generation. Quite simply, the radical cations (490 nm) were monitored at longer timescales along with potential carbocation formation at 380 nm, which is near the absorption maximum^{136,140} of α,α -dialkyl-*N,N*-dialkylbenzyl carbocations. Transient absorption spectra were also acquired to illustrate the absorption bands of the radical cation and carbocation, and are presented with the kinetic traces in Figure 4-9 through

Figure 4-15. Pertinent rate constants, determined from the decay of the radical cation at 490 nm and the growth of the carbocation at 380 nm, are summarized in Table 4-3.

The fragmentation of the linked radical cations, along with the production of carbocation, was inferred from the presence of concomitant decay and growth processes observed at 490 nm and 380 nm, respectively. Carbocation production was observed for complexes linked to symmetrical substrates that are sterically hindered about the central carbon-carbon bond; *i.e.* those of the form N-MPB-N, N-MPH-N, and N-MPO-N. Transient absorption spectra for complexes with these linked substrates show isosbestic points near 435 nm, consistent with literature values.^{136,140} No carbocation was produced from the substrate radical cation of the complex $\text{Ru}(\text{bpy})_2(\text{C}_4\text{-N-BZ-N})$, Figure 4-9, supporting the idea that a hindered C-C bond is essential for radical cation fragmentation.

No carbocation was produced from either of the complexes with unsymmetrical substrates. These complexes are interesting in that the carbocation, had the radical cations fragmented, would have remained at the more stable terminus, that of the aniline functionality. Thus, $\text{Ru}(\text{bpy})_2(\text{C}_4\text{-N-MPB-H})$, Figure 4-13, would have produced free, unsubstituted cumyl radicals, while with $\text{Ru}(\text{bpy})_2(\text{C}_4\text{-O-MPB-N})$, Figure 4-14, all of the aminobenzyl carbocations would have been unlinked.

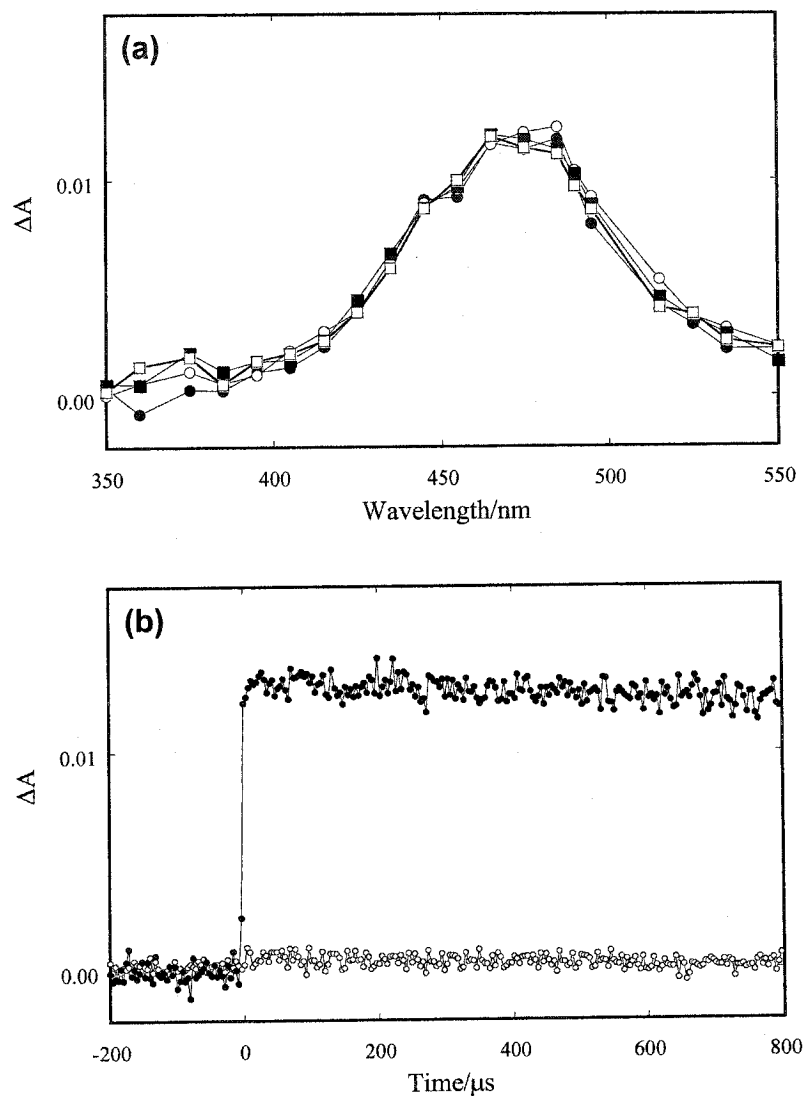


Figure 4-9. (a) Transient absorption spectra obtained (\bullet) 24 μ s, (\circ) 80 μ s, (\blacksquare) 360 μ s, and (\square) 600 μ s following 355-nm laser irradiation of $\text{Ru}(\text{bpy})_2(\text{C}_4\text{-N-BZ-N})$ in nitrogen-saturated 10 mM sodium phosphate pH 7.2 containing 15 mM $[\text{Co}(\text{NH}_3)_5\text{Cl}]\text{Cl}_2$. (b) Time-resolved kinetic traces monitored at (\bullet) 490 nm and (\circ) 380 nm for the same compound under identical conditions.

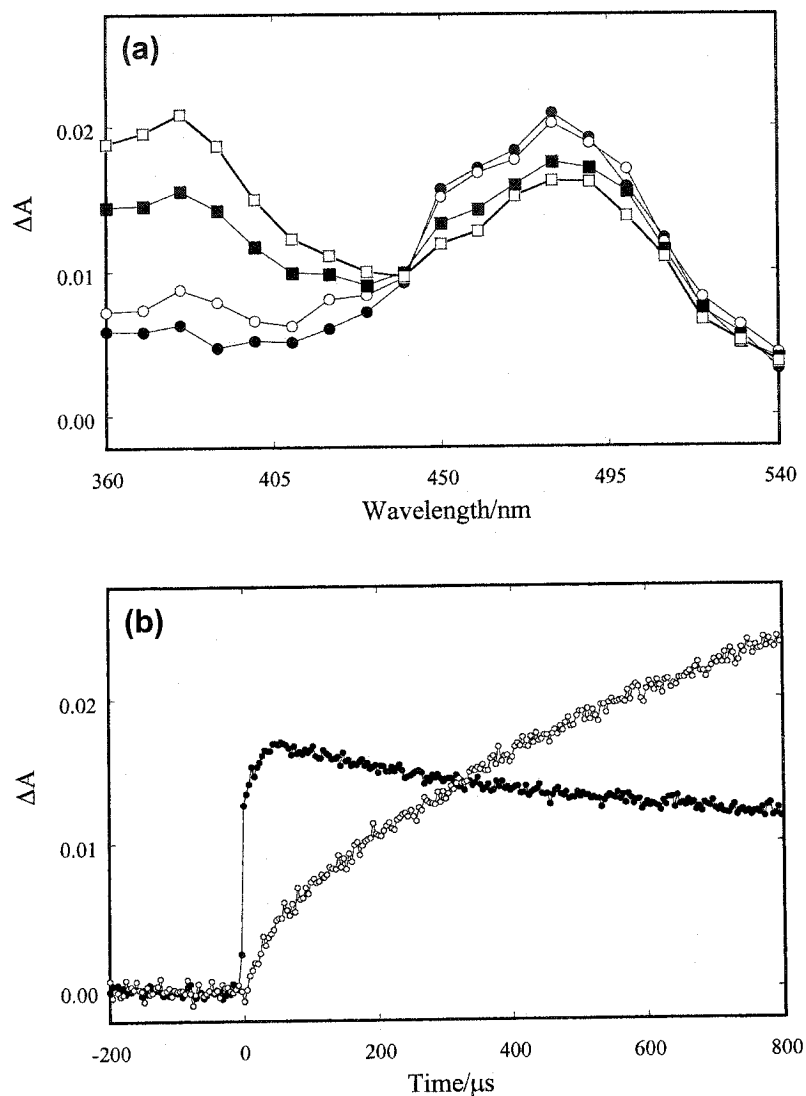


Figure 4-10. (a) Transient absorption spectra obtained (●) 24 μ s, (○) 80 μ s, (■) 360 μ s, and (□) 600 μ s following 355-nm laser irradiation of Ru(bpy)₂(C₄-N-MPB-N) in nitrogen-saturated 10 mM sodium phosphate pH 7.2 containing 15 mM [Co(NH₃)₅Cl]Cl₂. (b) Time-resolved kinetic traces monitored at (●) 490 nm and (○) 380 nm for the same compound under identical conditions.

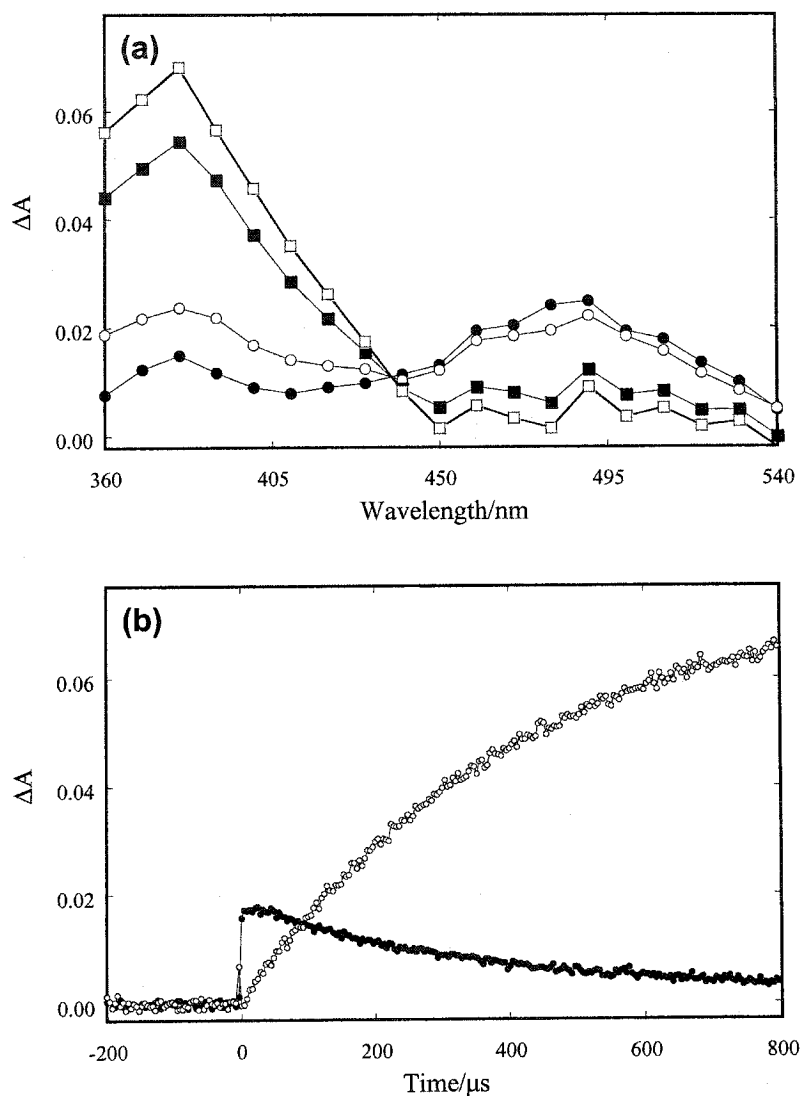


Figure 4-11. (a) Transient absorption spectra obtained (●) 44 μ s, (○) 96 μ s, (■) 360 μ s, and (□) 600 μ s following 355-nm laser irradiation of Ru(bpy)₂(C₄-N-MPH-N) in nitrogen-saturated 10 mM sodium phosphate pH 7.2 containing 15 mM [Co(NH₃)₅Cl]Cl₂. (b) Time-resolved kinetic traces monitored at (●) 490 nm and (○) 380 nm for the same compound under identical conditions.

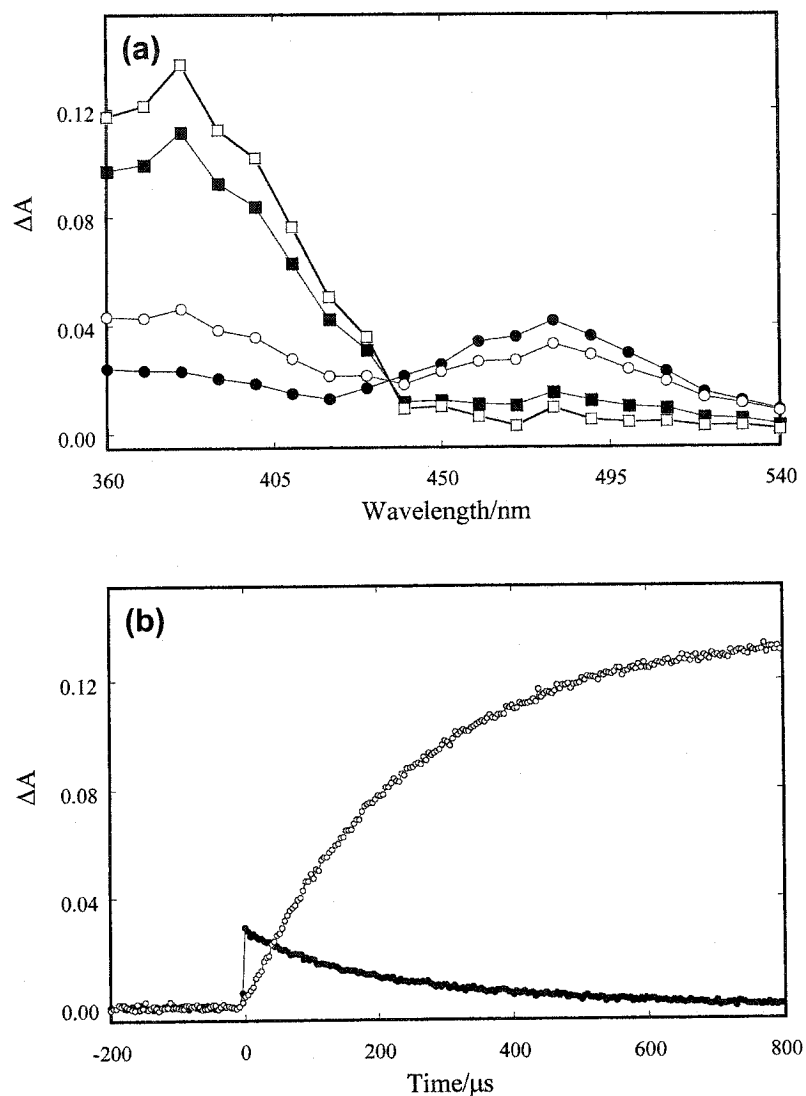


Figure 4-12. (a) Transient absorption spectra obtained (●) 44 μ s, (○) 96 μ s, (■) 360 μ s, and (□) 600 μ s following 355-nm laser irradiation of Ru(bpy)₂(C₄-N-MPO-N) in nitrogen-saturated 10 mM sodium phosphate pH 7.2 containing 15 mM [Co(NH₃)₅Cl]Cl₂. (b) Time-resolved kinetic traces monitored at (●) 490 nm and (○) 380 nm for the same compound under identical conditions.

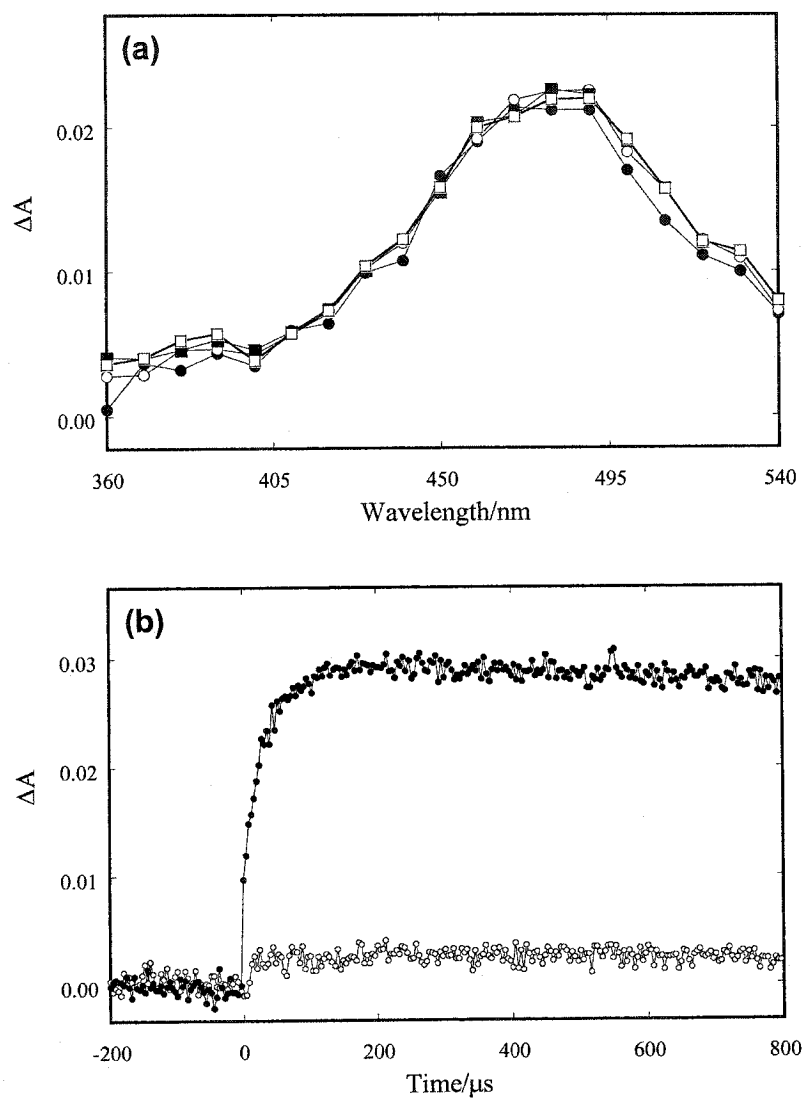


Figure 4-13. (a) Transient absorption spectra obtained (●) 88 μ s, (○) 204 μ s, (■) 440 μ s, and (□) 664 μ s following 355-nm laser irradiation of Ru(bpy)₂(C₄-N-MPB-H) in nitrogen-saturated 10 mM sodium phosphate pH 7.2 containing 15 mM [Co(NH₃)₅Cl]Cl₂. (b) Time-resolved kinetic traces monitored at (●) 490 nm and (○) 380 nm for the same compound under identical conditions.

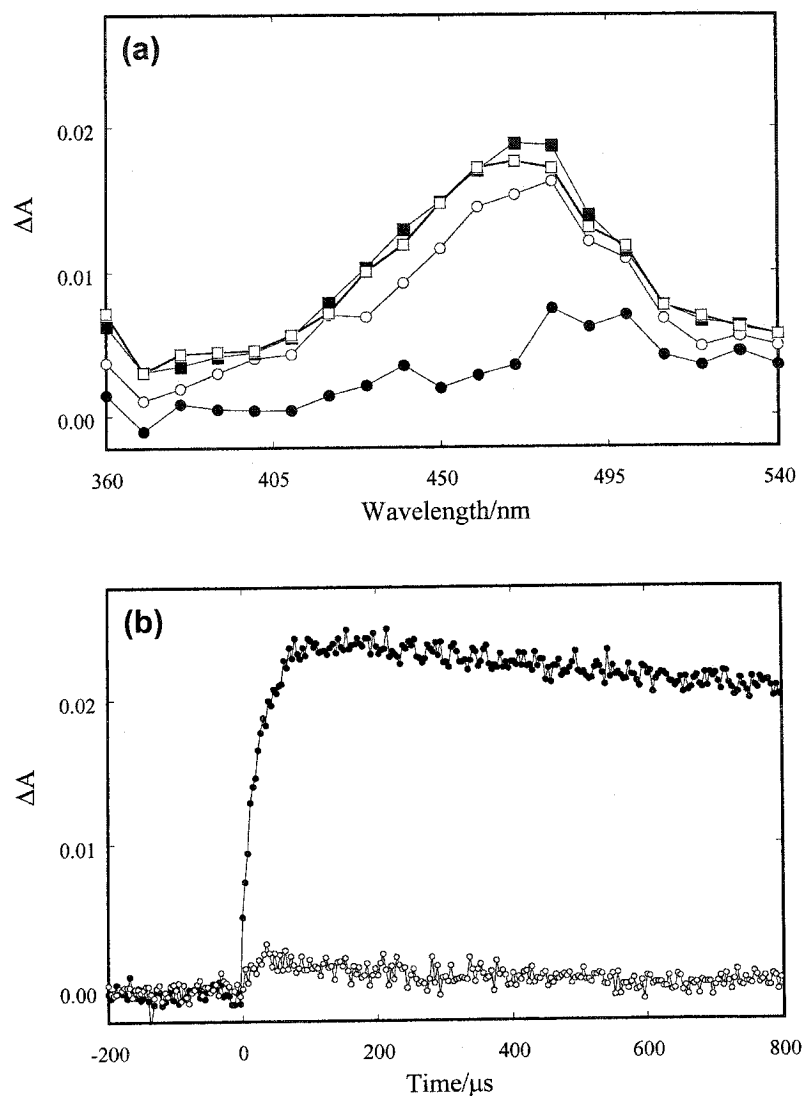


Figure 4-14. (a) Transient absorption spectra obtained (●) 24 μ s, (○) 80 μ s, (■) 360 μ s, and (□) 600 μ s following 355-nm laser irradiation of $\text{Ru}(\text{bpy})_2(\text{C}_4\text{-O-MPB-N})$ in nitrogen-saturated 10 mM sodium phosphate pH 7.2 containing 15 mM $[\text{Co}(\text{NH}_3)_5\text{Cl}]\text{Cl}_2$. (b) Time-resolved kinetic traces monitored at (●) 490 nm and (○) 380 nm for the same compound under identical conditions.

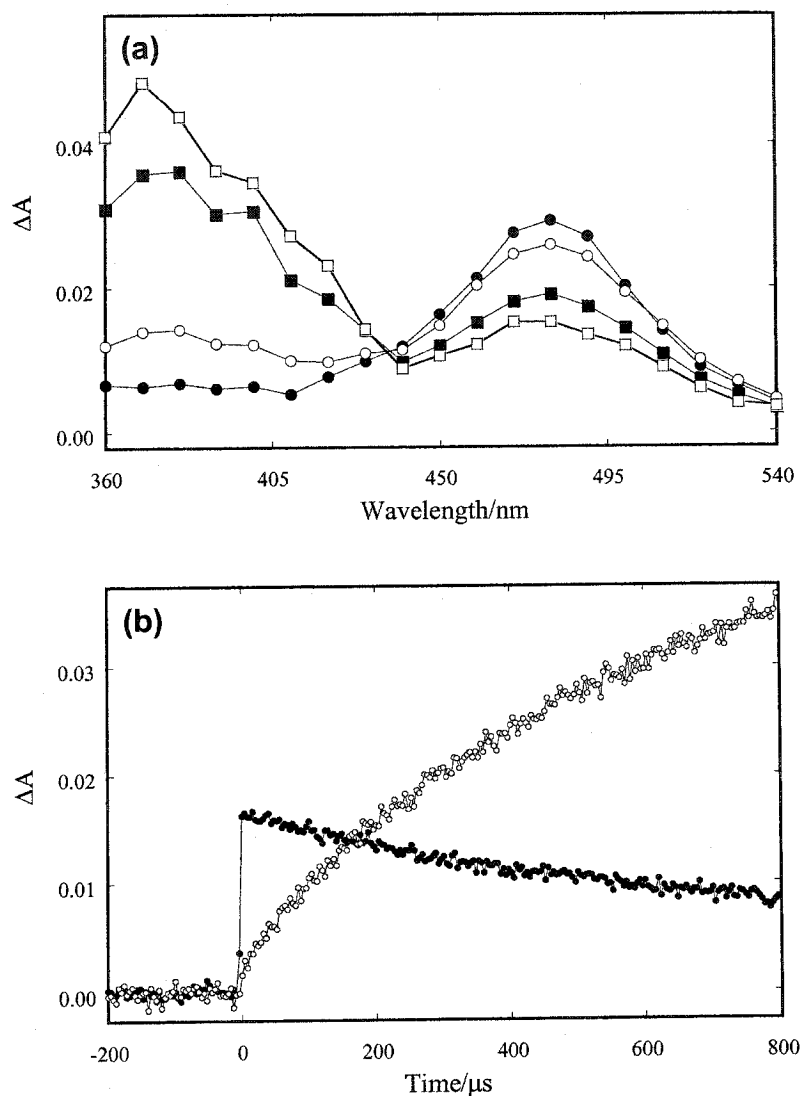


Figure 4-15. (a) Transient absorption spectra obtained (●) 24 μ s, (○) 80 μ s, (■) 360 μ s, and (□) 600 μ s following 355-nm laser irradiation of Ru(bpy)₂(C₇-N-MPB-N) in nitrogen-saturated 10 mM sodium phosphate pH 7.2 containing 15 mM [Co(NH₃)₅Cl]Cl₂. (b) Time-resolved kinetic traces monitored at (●) 490 nm and (○) 380 nm for the same compound under identical conditions.

While the kinetics of radical cation fragmentation for some of the corresponding unlinked, non-polar diphenylalkane substrates have been studied in organic solvents and are highly sensitive to small changes in solvent composition, no data exist for aqueous solutions. Herein, rate constants in water were measured by linking the diphenylalkane substrates to water-soluble Ru complexes, and these rate constants, along with literature values where available, are provided for comparison in Table 4-3. It is clear then, that the experimental values acquired herein differ considerably from literature values. Such differences may be caused by solvent effects or the different temperatures used in the literature studies. In other words, it was not possible to predict the rate of radical fragmentation based on literature data, and the choosing of appropriate substrates to link to the complexes was almost entirely based on trial and error.

Of particular interest is the complex $\text{Ru}(\text{bpy})_2(\text{C}_4\text{-N-MPB-H})$, where the radical cation did not rapidly fragment (Figure 4-13; Table 4-3). Literature data¹⁴⁰ suggested that the corresponding radical cation, that of 2,3-dimethyl-2-[4-(*N,N*-dimethylamino)phenyl]-3-phenylbutane, fragments and produces carbocation at a rate of $1 \times 10^5 \text{ s}^{-1}$ at 20 °C in 2:1 acetonitrile:water, and it is argued that rate constants observed in this solvent mixture are similar to those in water. However, attempts to reproduce this result *via* direct photoionization at 266 nm in the same solvent mixture were unsuccessful. The radical cation was produced, but it did not rapidly fragment or afford carbocation.

Table 4-3. Rate constants for the decay of amino-substituted diphenylalkane radical cations and the growth of corresponding aminobenzyl carbocations in nitrogen-saturated 10 mM sodium phosphate pH 7.2 containing 15 mM [Co(NH₃)₅Cl]Cl₂. Literature values are for the fragmentation of the unlinked radical cations of the corresponding substrates.

Substrate-linked complex	Rate constants/s ⁻¹		
	Radical cation decay	Carbocation growth	Literature value and conditions
Ru(bpy) ₂ (C ₄ -N-BZ-N)	$< 1.0 \times 10^3$	--	--
Ru(bpy) ₂ (C ₇ -N-MPB-N)	$1.6 \pm 0.2 \times 10^3$	$1.7 \pm 0.1 \times 10^3$	> 5.0 at -25 °C in 5% MeOH in DCM ¹⁴¹
Ru(bpy) ₂ (C ₄ -N-MPB-N)	$2.0 \pm 0.2 \times 10^3$	$1.6 \pm 0.1 \times 10^3$	same as above
Ru(bpy) ₂ (C ₄ -N-MPB-N) measured at 27 °C	$3.1 \pm 0.1 \times 10^3$	$3.3 \pm 0.1 \times 10^3$	same as above
Ru(bpy) ₂ (C ₄ -N-MPH-N)	$2.8 \pm 0.1 \times 10^3$	$2.5 \pm 0.1 \times 10^3$	--
Ru(bpy) ₂ (C ₄ -N-MPO-N)	$4.4 \pm 0.1 \times 10^3$	$4.1 \pm 0.1 \times 10^3$	--
Ru(bpy) ₂ (C ₄ -N-MPB-H)	$< 1.0 \times 10^3$	--	0.7 at 22 °C in 5% MeOH in DCM; ¹³⁶ 1×10^5 at 20 °C in 2:1 CH ₃ CN:H ₂ O ¹⁴⁰
Ru(bpy) ₂ (C ₄ -O-MPB-N)	$< 1.0 \times 10^3$	--	7.9×10^{-2} at -25 °C in 5% MeOH in DCM ¹⁴¹

4.3 Discussion

Two concepts are covered in this chapter, namely the oxidation of diphenylalkane substrates to their corresponding radical cations, as well as the fragmentation of the resulting radical cations.

4.3.1 Radical cation generation

Like the results obtained for the tris(bipyridyl)complexes linked to *N,N*-dimethyl-*p*-toluidine in the previous chapter, there is a clear trend between Ru(II)* excited-state lifetimes (Table 4-1) and the rate constants of radical cation generation (Table 4-2). Two pathways of substrate oxidation are possible (Scheme 4-4) and are characterized by an initial Ru(II)* reduction to Ru(I) by k_1 or oxidation to Ru(III) by $k_3[A]$. For complexes with long excited-state lifetimes, such as Ru(bpy)₂(C₄-O-MPB-N), 412 ns, virtually all radical cation is generated *via* the slow oxidation of the substrate by Ru(III), with a rate constant of $2.4 \times 10^4 \text{ s}^{-1}$ corresponding to k_4 . For Ru(bpy)₂(C₄-N-MPB-H), which has a shorter excited-state lifetime of 220 ns, a fast component now appears and the slow component increases to $3.0 \times 10^4 \text{ s}^{-1}$. Similarly, for Ru(bpy)₂(C₄-N-MPB-N) with an excited-state lifetime of 83 ns, k_4 increases to $4.0 \times 10^4 \text{ s}^{-1}$, but the percentage of this slow component is much smaller. This correlation between higher k_4 and shorter excited-state lifetime (faster k_1) is not surprising, since a substrate capable of reducing Ru(II)* at a faster rate should also reduce Ru(III) more rapidly. However, the percentage of radical cation generated by the Ru(III) pathway decreases as k_1 increases, due to the presence of the competitive Ru(II)* reduction to Ru(I) by the substrate.

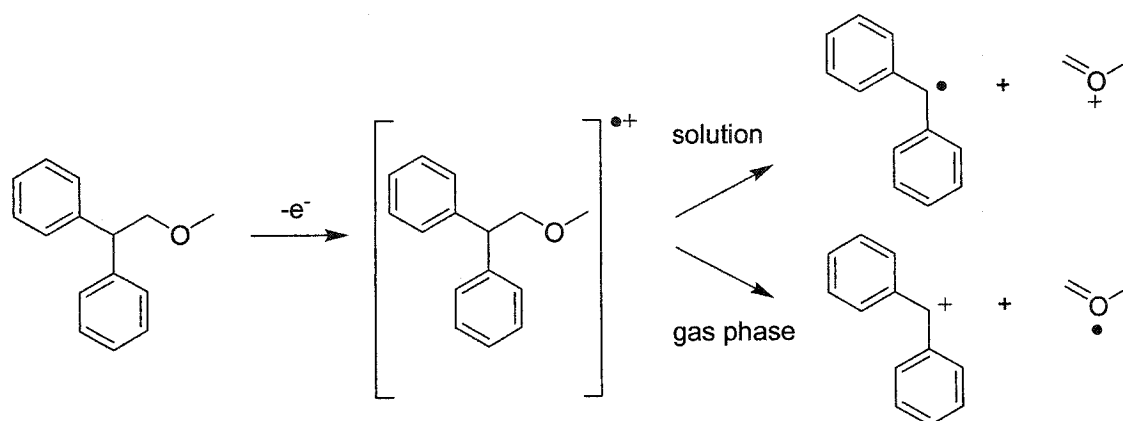
In contrast with the linked *N,N*-dimethyl-*p*-toluidine in the previous chapter, the replacement of the C₄ linker in the Ru(bpy)₂(C₄-N-MPB-N) complex with a C₇ to yield Ru(bpy)₂(C₇-N-MPB-N) increased the rate of intramolecular electron transfer from the substrate to Ru(II)*, as evidenced by a decrease in the Ru(II)* lifetime of 83 ns for the former to 63 ns for the latter (Table 4-1). The higher rate for the longer linker is possibly attributed to conformational differences between the C₄- and C₇-linked derivatives. The linkers are not fixed in extended conformations, but are rather constantly undergoing dynamic change. As well, these polymethylene linkers, along with the attached substrates, make for a hydrophobic moiety that would favour a compact conformation that would minimize contact with water. The C₇ complex, with more non-polar methylenes, may have a higher propensity to adopt a more compact conformation than the C₄ complex, causing the substrate to be spatially closer to the photosensitizer.

Another unexpected observation relates to the electron-transfer rate constants of the complexes linked to unsymmetrical substrates. For electron transfers involving the intramolecular reduction of Ru(II)* to Ru(I), the substitution of the aniline moiety in Ru(bpy)₂(C₄-N-MPB-H) with an alkoxyphenyl in Ru(bpy)₂(C₄-O-MPB-N) decreases the rate (*k*₁, Table 4-1). Similarly, the rate of Ru(III)-to-Ru(II) reduction (*k*₄, Table 4-2) is faster with the Ru(bpy)₂(C₄-N-MPB-H) complex than with Ru(bpy)₂(C₄-O-MPB-N). The reduced rate constants observed for Ru(bpy)₂(C₄-O-MPB-N), where oxidation is presumed to occur at the aniline moiety, can possibly be explained by the increased distance between the photosensitizer core and the aniline. Such distance increases would lead to slower electron transfers.

Unexpectedly, the rate constants of electron transfer for the symmetrical complex $\text{Ru}(\text{bpy})_2(\text{C}_4\text{-N-MPB-N})$ are much faster than for the unsymmetrical $\text{Ru}(\text{bpy})_2(\text{C}_4\text{-N-MPB-H})$, both with $\text{Ru}(\text{II})^*$, Table 4-1, and $\text{Ru}(\text{III})$, Table 4-2. These complexes differ by the replacement of a terminal, unsubstituted phenyl moiety in $\text{Ru}(\text{bpy})_2(\text{C}_4\text{-N-MPB-H})$ with an aniline in $\text{Ru}(\text{bpy})_2(\text{C}_4\text{-N-MPB-N})$, and even though the terminal aniline moiety is further away than the moiety attached to the linker, higher rate constants were observed for the latter. This effect can may indicate that both aniline ends are oxidized, and that the faster oxidation is due to an effective doubling of the concentration of oxidizable groups.

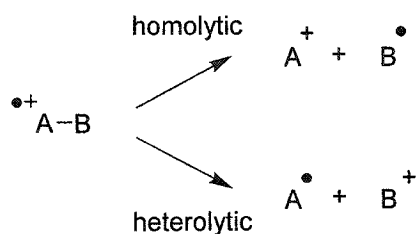
4.3.2 Radical cation fragmentation

Nearly three decades ago, Arnold and Maroulis¹⁴² reported the fragmentation of radical cations generated by electron-transfer photosensitization. In this landmark report, the irradiation of a mixture containing 2,2-diphenylethyl methyl ether and an electron-transfer sensitizer, for instance methyl 4-cyanobenzoate, resulted in cleavage of the former. The proposed mechanism (Scheme 4-7) suggests that the fragmentation of a radical ion into its separate radical and ion components proceeds in a direction that leads to the more stable fragments. In polar solvents, the diphenylmethyl radical and α -oxycarbonium ion are favoured, while the reverse is obtained in gas phase. Thus, two fundamental concepts stem from this report: (a) the oxidation of a neutral substrate to its radical cation induces bond fragmentation *via* activation energy reduction, and (b) fragmentation results in radical and ion pairs that are the most thermodynamically stable in their environment.



Scheme 4-7. Fragmentation of the radical cation of 2,2-diphenylethyl methyl ether into thermodynamically stable radical and cation components.

More recently, these fundamental concepts were extended to diphenylalkane derivatives by Maslak *et al.*,^{61,136,141,143-155} where neutral, substituted diphenylalkanes are converted their to corresponding radical ions to induce bond cleavage. For radical cations that originate from unsymmetrically substituted diphenylalkanes, represented as A-B in Scheme 4-8 below, two fragmentation mechanisms exist, homolytic and heterolytic. The presence of two possible mechanisms is termed *mesolytic*. Both mechanisms involve the removal of electron density about the fragmenting bond, resulting in the production of separate radical and cation fragments. In this scheme, the radical cation is generated with the positive charge localized on the more easily oxidized portion, A. Therefore, with the homolytic mode of cleavage, the charge remains associated with the A fragment, while with the heterolytic mode, the charge is transferred to the B fragment. With both modes, though more prominent with heterolysis, partial positive-charge transfer occurs over the fragmenting bond at the transition state (*i.e.* polarization).¹⁵²



Scheme 4-8. Generalized representation of mesolytic cleavage.

Due to the transition-state polarization in the mesolytic cleavage process, the amount of available charge density affects the rate at which the fragmentation occurs.⁶¹ The presence of electron-withdrawing substituents on the phenyl rings reduces the rate of cleavage, while the opposite occurs for electron-donating substituents. These effects may explain why fragmentation was observed with the complex $\text{Ru}(\text{bpy})_2(\text{C}_{(4/7)}\text{-N-MPB-N})$, but not with $\text{Ru}(\text{bpy})_2(\text{C}_4\text{-O-MPB-N})$ nor $\text{Ru}(\text{bpy})_2(\text{C}_4\text{-N-MPB-H})$, where an amino group ($\sigma^+ = -1.11$)¹⁵⁶ is substituted with either an alkoxy ($\sigma^+ = -0.65$) or a hydrogen ($\sigma^+ = 0.00$). However, these substitutions cannot fully account for the lack of cleavage, as 4,4'-dimethoxybicumene, an unlinked substrate with two methoxy groups, cleaves at an exceedingly high rate of $6.0 \times 10^8 \text{ s}^{-1}$ (0.5% MeOH in DCM). These discrepancies may lie in differences in the nature of the fragmentation activation energies for the corresponding radical cations, as well as in the difference in stability of the radical cation. Those containing one or more aniline substituents are most likely more stable than those containing only methoxy substituents.

A major contributor to the fragmentation rate constants is the degree of steric bulk adjacent to the fragmenting C-C bond. Rüchardt *et al.*¹⁵⁷⁻¹⁵⁹ first observed that the thermolysis rate constants for neutral, 4,4'-unsubstituted diphenylalkanes were highly dependent on the degree of steric strain at the C-C bond. The introduction of bulky substituents at that bond results in an increased bond length^{153,160} and a decreased bond dissociation energy,¹⁶¹ all of which result in reduction in the activation energy required for the mesolytic cleavage of radical cations.¹³⁶ According to the Hammond postulate,¹⁶² it can be envisioned that high-energy substrates containing bulky substituents are closer to the transition-state structure, where bond cleavage occurs and the fragments are separating, than their lower-energy, less-bulky counterparts. For these reasons, the rate constants of radical cation fragmentation (Table 4-3) increase when the linked substrates contain larger substituents adjacent to the fragmenting C-C bond.

Another interesting aspect of the radical cation fragmentation is the distribution between linked and unlinked carbocations, Scheme 4-3. In this scheme, four distinct products, two radicals and two carbocations, are generated, inferring that an average of two radical cation fragmentations are required for the production of a single unlinked carbocation. However, if the radicals are oxidized to their respective carbocations by the electron acceptor, then only two products, the unlinked and linked carbocations, can be produced and in a 1:1 ratio. Oxidation of the formed α,α -dialkyl-4-(*N,N*-dimethyl)benzyl radical is highly feasible, and although no literature reduction potential is available for the corresponding carbocation, this amino-substituted radical should be more easily oxidized than the previously discussed *p*-methoxycumyl radical (Scheme 4-6).

4.4 Conclusion and future work

The results presented in this chapter demonstrate that tris(bipyridyl)ruthenium complexes are practical for the generation of radical cations of diphenylalkane substrates under biocompatible conditions. While all symmetrical substrates containing aniline functionalities were oxidized, only those with sterically hindered central C-C bonds underwent fragmentation to afford carbocations. Rate constants for the radical cation generation and fragmentation processes were also measured.

The work presented in this thesis provides a methodology that could be used for the introduction of reactive, aminobenzyl carbocations to the hydrophobic sites of various biomolecules, including synthetic peptides. These carbocations could possibly be used as “probe” cations to investigate the stabilizing effects of the π -cation interaction, where stabilization may be inferred by changes to the carbocation lifetime.

If more reactive carbocations are desired, the results from Chapter Two suggest that the concept of ligand substitution could be used to permit oxidation of substrates that result in the generation of more-reactive carbocations. For instance, the addition of CF_3 groups to the bipyridyl ligands of $\text{Ru}(\text{bpy})_2(\text{C}_7\text{-O-MPB-O})$, which did not exhibit intramolecular substrate oxidation, results in $\text{Ru}(\text{dfmb})_2(\text{C}_7\text{-O-MPB-O})$, which is more likely to undergo intramolecular electron transfer with the linked substrate. Fragmentation of the resulting radical cation would result in the delivery of a highly reactive, 4-methoxycumyl cation. However, it is important to emphasize that the linked substrate should be more easily oxidized than the biomolecule being investigated.

However, additional work prior to the use of these substrate-linked complexes would be useful in order to fully elucidate the predominant mechanism of linker-mediated electron transfer in these complexes, *i.e.*, through-bond or through-space. Such work can likely be performed by computational investigations to determine the lowest-energy conformations of the complexes in water, as well as the extent of orbital overlap between the substrate and the ruthenium photosensitizer core. Additional laser-flash experiments in the presence of β -cyclodextrin, which can cause the linkers to adopt an extended conformation, may also provide valuable information.

Of course, it may also be possible to use these substrate-linked complexes without further studying their electron-transfer aspects. In this case, one category of biomolecules that can be used to verify the intended functionality of these complexes would be micelles, prior to experiments with synthetic peptides. This experiment is expected to be relatively simple, since the hydrophobic nature of the linked substrate should favour its incorporation into micelle interiors. Subsequent laser-flash irradiation would result in the delivery of a carbocation directly located within the micelle interior. Although micelle interiors do not necessarily contain carbocation-stabilizing aromatic groups, depending on the constituent lipids, the shielding of the carbocation from the nucleophilic, aqueous exterior environment is expected to result in enhanced carbocation lifetimes. Micelle studies are also advantageous in that could also possibly be used to study the electron transfer between the substrate and the photosensitizer core, as the linker is expected to be in an elongated form when the substrate is bound in the interior and the photosensitizer core is situated in the aqueous environment.

Peptide experiments are expected to be far more complicated than the micelle experiments, since substantial work will be necessary to design a peptide that contains a hydrophobic site capable of binding a photosensitizer-linked substrate. This work may involve computational modelling of substrate-peptide interactions in order to identify a possible cation-stabilizing, amino-acid sequence. Nonetheless, once a cation-stabilizing peptide is identified, the effect of small modifications in peptide sequence on the carbocation lifetime might be investigated to evaluate the changes in cation stabilization.

Chapter Five: Picosecond Dynamics of Ru(II)* Excited States

This chapter deviates significantly from the overall theme of the thesis, where tris(bipyridyl)ruthenium complexes are employed for radical cation generation, and instead briefly investigates the ultrafast photophysics of the excited states; *i.e.* the events occurring between time of initial excitation and the formation of the Ru(II)* state. The preliminary results presented herein are the result of a collaborative effort between the thesis author (compound preparation and characterization), Sherri A. McFarland (data acquisition and processing), and Karen A.W.Y. Cheng (instrument setup).

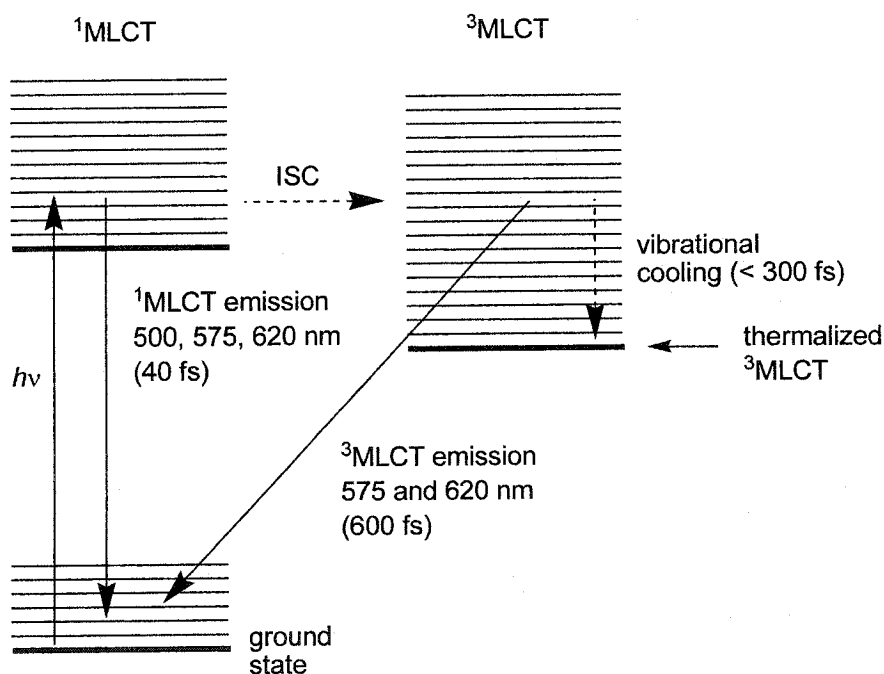
5.1 Introduction

The Ru(II)* excited states mentioned in the previous chapters are more accurately described as thermalized (vibrationally relaxed, lowest energy), $^3\text{MLCT}$ triplet states derived from the intersystem crossing of strongly coupled, non-thermalized (vibrationally hot, Franck-Condon) $^1\text{MLCT}$ singlet states. While the properties of the thermalized $^3\text{MLCT}$ state have been studied over the past few decades and are well-characterized in the literature, interest in the ultrafast dynamics leading up to the formation of this state has only been present in the last several years. Such interest was sparked by the importance of the non-thermalized, high-energy $^1\text{MLCT}$ state in solar-energy conversion devices, where electron injection has been proposed to occur from the high-energy MLCT state.^{163,164}

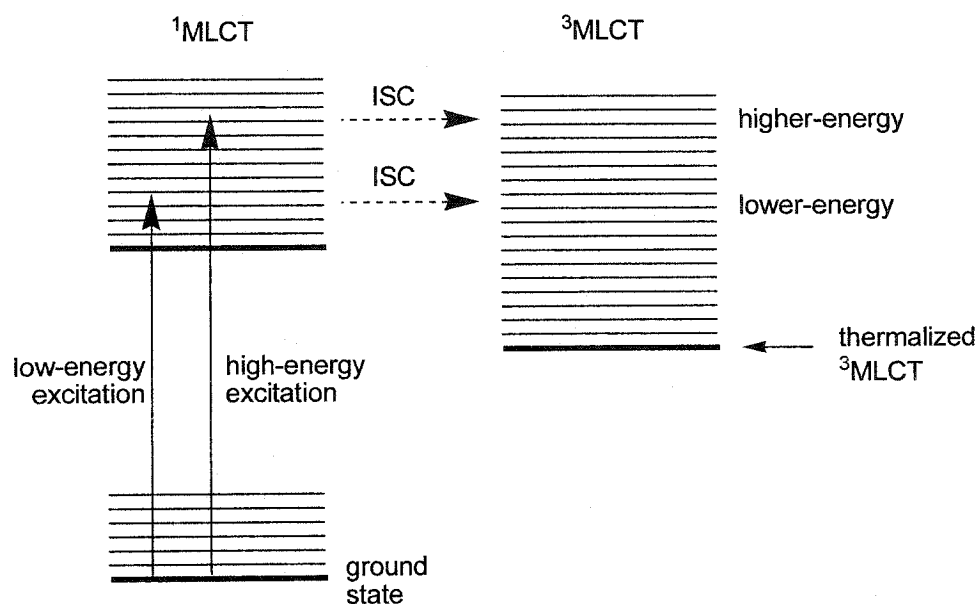
Previous fluorescence studies⁷⁶ with the complex Ru(bpy)₃ excited at 480 nm have shown that intersystem crossing (ISC) from non-thermalized ¹MLCT to the strongly coupled ³MLCT occurs with a lifetime of 40 fs, inferred from non-thermalized singlet emission at 500, 575, and 620 nm. However, the formation of the absorptive properties of the thermalized ³MLCT state does not occur until 300 fs after excitation.¹⁶⁵ The difference between these two lifetimes is therefore attributed to processes occurring on the triplet manifold related to vibrational cooling, including internal conversion, charge localization, vibrational relaxation, and redistribution of vibrational energy. Similarly, it can be argued that any process occurring with a lifetime greater than 40 fs also needs to originate from the triplet manifold. One of these processes is luminescence of non-thermalized ³MLCT at 575 nm and 620 nm with a lifetime of approximately 600 fs in acetonitrile.⁷⁶ This emission was not observed at 500 nm. All of these processes which may occur in the time frame between excitation and thermalized-³MLCT formation are shown in Scheme 5-1.

The ultrafast kinetics of excited states of transition-metal complexes are also strongly dependent on the wavelength of excitation.¹⁶⁶⁻¹⁶⁸ In recent studies, excitation wavelengths of 400, 410, and 480 nm were used to investigate the non-thermalized states of Ru(bpy)₃, where changes as small as 10 nm produced noticeable kinetic effects. At lower wavelengths (higher energy), a higher vibrational state on the singlet manifold is initially populated, allowing a larger range of higher-energy processes to occur. One example demonstrating the usefulness of high-energy excitation lies in TiO₂ nanocrystalline film devices with potential solar energy conversion applications, where

the rate constant of electron injection from the non-thermalized $^1\text{MLCT}$ state of the closely related complex $\text{Ru}(4,4'\text{-dicarboxy-2,2'}\text{-bipyridine})_2(\text{NCS})_2$ to TiO_2 was shown to be wavelength-dependent.¹⁶³ In other words, high-energy excitation populates a higher vibrational $^1\text{MLCT}$ state that undergoes more rapid electron injection; the non-thermalized $^1\text{MLCT}$ state is more easily oxidized when excited by higher energy. As well, the initially populated $^1\text{MLCT}$ state can also undergo intersystem crossing to the triplet manifold. Thus, high-energy excitation allows the population of vibrationally higher $^1\text{MLCT}$ and $^3\text{MLCT}$ states, as illustrated in Scheme 5-2.

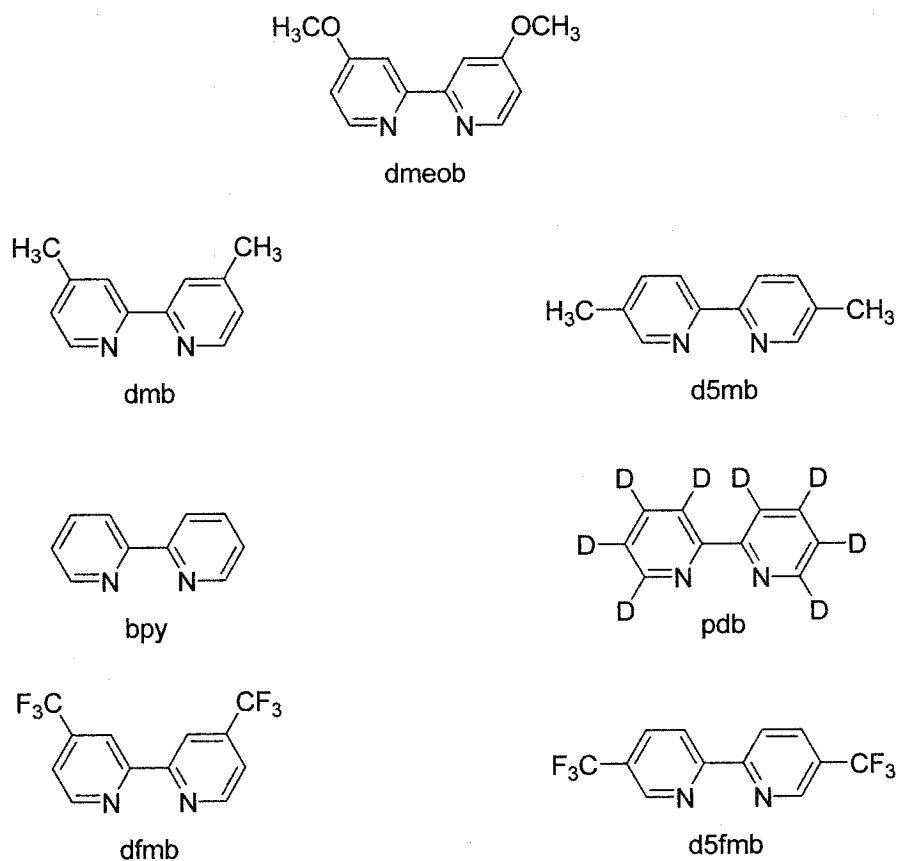


Scheme 5-1. Decay of non-thermalized states in $\text{Ru}(\text{bpy})_3$ determined by fluorescence techniques. Lifetimes of corresponding emissive processes are shown in parentheses.



Scheme 5-2. Accessing vibrationally higher $^1\text{MLCT}$ and $^3\text{MLCT}$ states by high-energy excitation of tri(bipyridyl)ruthenium complexes.

Despite the significance and importance of high-energy excitation on the excited-state dynamics of tris(bipyridyl)ruthenium complexes, no literature reports on the excitation of $\text{Ru}(\text{bpy})_3$ using wavelengths below 400 nm have been found. Thus, this chapter investigates the effect of higher-energy 388-nm excitation on the emissive properties of $\text{Ru}(\text{bpy})_3$, specifically non-thermalized emission near 500 nm on the ps timescale. As well, this chapter studies the picosecond dynamics of both homoleptic and heteroleptic complexes comprised of 4,4'- or 5,5'-disubstituted-2,2'-bipyridyl ligands, or perdeuterio-2,2'-bipyridine (Scheme 5-3) to provide preliminary insight on the effect of the substituent on excited-state dynamics. Attempts are also made to correlate picosecond dynamics to nanosecond decay of the luminescent, thermalized $^3\text{MLCT}$ state.



Scheme 5-3. Bipyridyl ligands used to investigate the picosecond dynamics of tris(bipyridyl)ruthenium excited at 388 nm.

5.2 Results

A streak camera that directly measures emission from the sample was used as the detection system, providing for picosecond resolution that is limited by the instrument response function (IRF). Emissive processes with lifetimes smaller than the IRF (3-5 ps) therefore cannot be accurately measured, as they would be observed as a rapid rise and

fall in emission corresponding to the IRF; such processes can only be assigned lifetimes of $< 3\text{-}5$ ps. On the other hand, a slow process with a significantly longer lifetime would appear as a standard kinetic trace. However, if both fast (< 5 ps) and slow (> 5 ps) processes are present with lifetime components τ_1 and τ_2 , respectively, the kinetic trace would be biexponential and feature a “tailed” appearance. These scenarios are illustrated in Figure 5-1, which show (a) the IRF only, (b) a sample with only a τ_1 emission where $\tau_1 < \text{IRF}$, and (c) a sample with both τ_1 and τ_2 components with $\tau_1 < \text{IRF}$ and $\tau_2 > \text{IRF}$. Clearly, (a) and (b) appear equivalent, while (c) features a second, slower component.

Thus, eighteen different homoleptic and heteroleptic complexes were prepared from a combination of seven ligands shown in Scheme 5-3 using methods outlined in the next chapter. Their spectroscopic properties were measured and are summarized in Table 5-1. These properties include ground-state MLCT absorption maxima, as measured on a UV spectrophotometer; the thermalized $^3\text{MLCT}$ emission maxima, as determined on a fluorimeter using an excitation wavelength of 450 nm; the thermalized $^3\text{MLCT}$ lifetime measured within 10 nm of the emission maximum (355-nm ns-laser excitation); and the non-thermalized MLCT emission at 500 nm (388-nm fs-laser excitation) measured by S. McFarland. Acquired picosecond-scale kinetic traces were in the form of either Figure 5-1 (a), for complexes with only a single τ_1 lifetime under 5 ps, or (b), for those with both fast and slow components, τ_1 and τ_2 respectively.

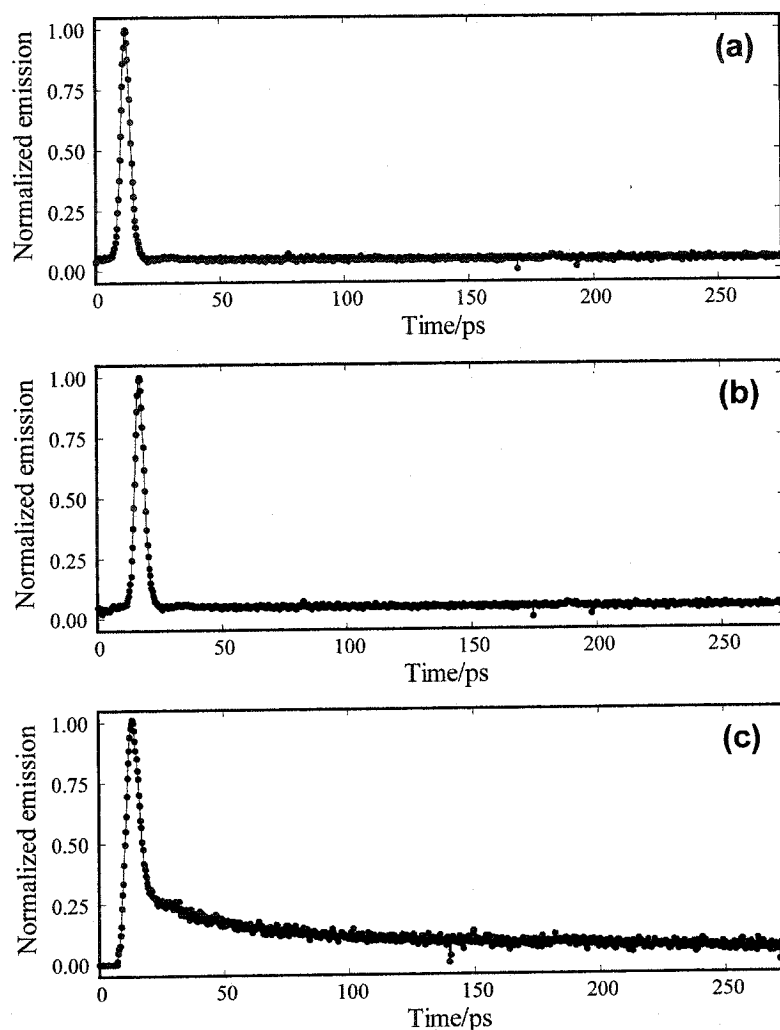


Figure 5-1. (a) Instrument response function measured using a suspension of corn starch in water. (b and c) Time-resolved kinetic traces monitored at 500 nm following 388-nm laser irradiation of aqueous (b) Ru(bpy)₃ with a single fast component and (c) Ru(dmb)₃ with biexponential kinetics comprised of a fast and slow component.

Table 5-1. Spectroscopic properties of tris(bipyridyl)ruthenium complexes in water.

Complex	Ru(II) $\lambda_{\text{abs}}/\text{nm}^a$	$^3\text{MLCT}$ $\lambda_{\text{em}}/\text{nm}^b$	$^3\text{MLCT}$ τ/ns^c	τ_1/ps^d	τ_2/ns^d
Ru(bpy) ₃	452	605	481	< 5	--
Ru(pdb) ₃	450	606	512	< 5	--
Ru(dmb) ₃	460	620	295	< 3	1.3
Ru(d5mb) ₃	444	597	481	< 5	--
Ru(dmeob) ₃	480	660	61	< 2	1.7
Ru(dfmb) ₃	455	611	848	< 5	3.2
Ru(bpy) ₂ (dmb)	456	614	391	< 5	--
Ru(bpy) ₂ (d5mb)	449	611	466	< 5	--
Ru(bpy) ₂ (dmeob)	460	625	282	< 5	--
Ru(bpy) ₂ (dfmb)	480	668	161	< 5	--
Ru(dmb) ₂ (bpy)	458	630	317	< 5	--
Ru(dmb) ₂ (dfmb)	494	710	91	< 5	--
Ru(dmb) ₂ (dmeob)	465	638	203	< 5	--
Ru(dfmb) ₂ (bpy)	473	637	334	< 5	--
Ru(dfmb) ₂ (dmb)	480	648	306	< 5	--
Ru(dfmb) ₂ (dmeob)	486	657	171	< 5	--
Ru(d5fmb) ₂ (bpy)	481	658	83	< 5	--
Ru(d5fmb) ₂ (d5mb)	485	660	68	< 5	--

^aGround-state MLCT absorption maximum. ^bEmission maximum of thermalized ³MLCT at 450-nm excitation. ^cLifetime of thermalized ³MLCT emission within 10 nm of λ_{em} after 355-nm excitation. ^dLifetimes of non-thermalized emission at 500 nm after 388-nm excitation; τ_2 lifetimes reproducible to about 1 ns.

All of the complexes investigated (Table 5-1) except for three of the six homoleptic complexes, Ru(dmb)₃, Ru(dmeob)₃, and Ru(dfmb)₃, afforded kinetic traces virtually identical with the one shown in Figure 5-1 (b) after 388-nm excitation. The rise and fall of the emission at 500 nm were both similar to the IRF, indicating that the emission lifetime τ_1 is less than the IRF (3-5 ps). It is important to note that the parameter τ_1 is a collection of all processes occurring faster than the IRF, and the inability to observe a τ_2 infers the absence of slower (> 5 ps) processes emitting at 500 nm.

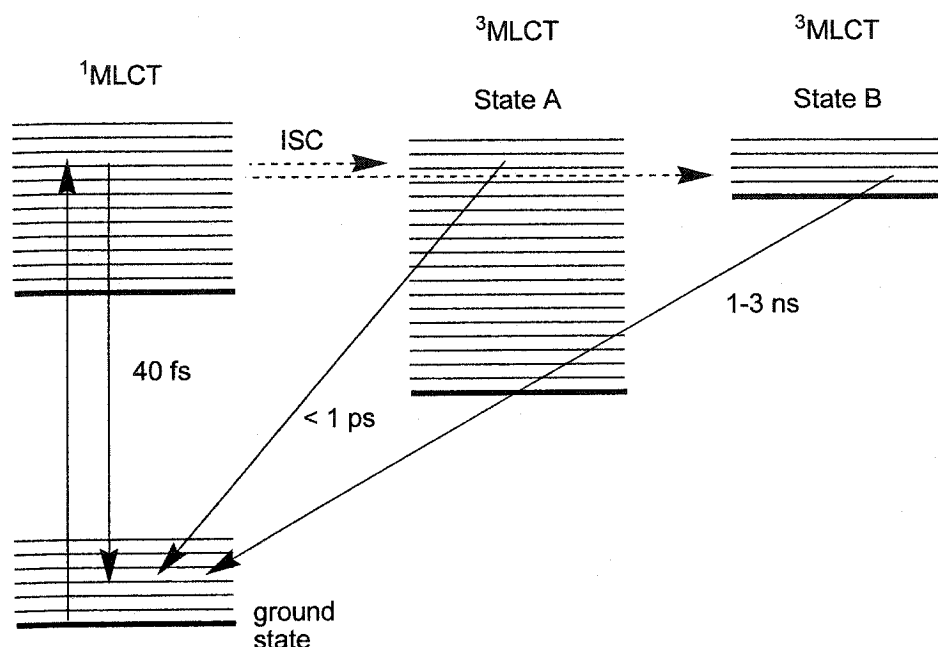
However, with the homoleptic Ru(dmb)₃, Ru(dmeob)₃, and Ru(dfmb)₃, kinetic traces of the type shown in Figure 5-1 (c) were obtained. Thus, in addition to the fast τ_1 , the emission decays of these three complexes also feature a slower, first-order component τ_2 . Only these three homoleptic complexes, which contain 4,4'-disubstituted ligands, exhibited τ_2 behaviour, and no other homoleptic or heteroleptic complexes showed τ_2 .

5.3 Discussion

The data collected for the 388-nm excitation of Ru(bpy)₃ are consistent with literature fluorescence data^{76,169} previously mentioned, as only a fast τ_1 component was observed at 500 nm. Where the excited-state dynamics following the initial population of the ¹MLCT state are complete in less than 1 ps after excitation (Scheme 5-1), and the IRF corresponds to a lifetime of 3-5 ps, the maximum time resolution that can be attained is approximately 1 ps even after mathematical deconvolution. This resolution-limited lifetime encompasses all processes, including the 40 fs and 600 fs non-thermalized ¹MLCT and ³MLCT emissions, respectively, as well as vibrational cooling.

A slower second component of emission (τ_2) was observed at 500 nm for the three complexes Ru(dmb)₃, Ru(dmeob)₃, and Ru(dfmb)₃. Kinetic traces for these complexes are of the type illustrated in Figure 5-1 (c), and the τ_2 values were determined to be in the range of 1-3 ns (Table 5-1) when measured using a slow sweep unit to trigger the streak camera. Since this time constant is significantly larger than the previously discussed 40 fs proposed for the ¹MLCT-to-³MLCT intersystem crossing of Ru(bpy)₃, it can be postulated that the observed τ_2 originates from a non-thermalized, high-energy state located on the triplet manifold, assuming that these three complexes have similar intersystem-crossing rate constants similar to Ru(bpy)₃.

A model we propose to account for the fast and slow emission components at 500 nm, τ_1 and τ_2 , respectively, is shown in Scheme 5-4, with the key feature being two ³MLCT states, A and B. While state A would be the state accessible by low-energy excitation and leads to the 600-fs emission observed by Bhasikuttan *et al.*⁷⁶ (Scheme 5-1), state B is proposed to be a higher-energy state. Emission from these two states encompasses the processes observed as τ_1 and τ_2 . As previously discussed (Scheme 5-2), excitation at a higher energy allows the initial population of a higher ¹MLCT state, which intersystem-crosses to a higher ³MLCT; high-energy excitation may thus permit access to both states A and B. However, it is not possible to distinguish if states A and B are indeed distinct electronic states, or whether state B is situated on a local minimum of the potential energy surface of state A.



Scheme 5-4. Schematic of the dual routes of non-thermalized emission from the triplet manifold. State B, a higher energy state, can be attained from high-energy excitation and initial population of the singlet state. Omitted are vibrational cooling processes.

In order for this kinetic model (Scheme 5-4) to carry any validity, two relatively straightforward assumptions need to be made. First, it needs to be assumed that state B in Scheme 5-4, the proposed origin of the slower component τ_2 , indeed originates from the rapid intersystem crossing of a vibrationally hot, Franck-Condon $^1\text{MLCT}$ state. Literature precedence¹⁷⁰⁻¹⁷² has shown that $^1\text{MLCT}$ and $^3\text{MLCT}$ states are strongly spin-orbit coupled at energies corresponding to excitation wavelengths of 380-500 nm, and thus excitation at 388 nm would permit a large range of $^1\text{MLCT}$ and $^3\text{MLCT}$ states to be accessed. It is reasonable to assume then, that state B is situated on the triplet manifold.

Second, it needs to be assumed that the wavelength of excitation, 388 nm, is indeed an MLCT excitation, where the initial electronic transition from ground state to the $^1\text{MLCT}$ state occurs. While the MLCT absorption band of $\text{Ru}(\text{bpy})_3$ is relatively broad, as shown in Figure 5-2, excitation at 388 nm is somewhat close to the singlet metal-centered $d-d$ transition.^{73,74} As discussed in the first chapter, this excitation involves the promotion of an electron from the π orbital of the metal to an empty σ^* orbital, also on the metal centre. However, such a $d-d$ transition, which is merely a redistribution of electrons within a set of d orbitals in a molecule with a centre of symmetry, are Laporte forbidden; *i.e.* ^1MC absorption is usually very weak. Thus, excitation at 388 nm would result in a state that is primarily $^1\text{MLCT}$ in character.^{170,173}

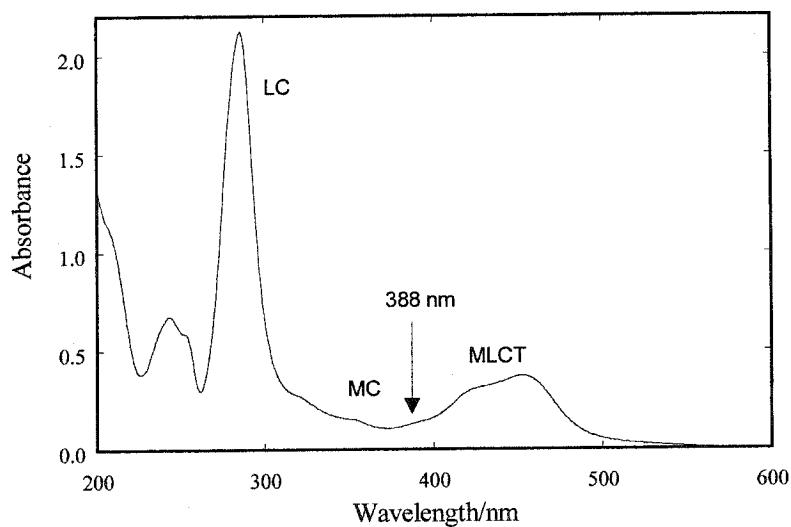


Figure 5-2. Ground-state absorption spectrum of $\text{Ru}(\text{bpy})_3$.

It was unexpected that none of the heteroleptic complexes, even those with three 4,4'-disubstituted ligands, exhibited a τ_2 component (Table 5-1). All lifetimes measured at 500 nm were limited by the IRF (< 5 ps). This suggests that both 4,4'-disubstitution and D_3 symmetry, that of a homoleptic complex, may be required for the appearance of τ_2 . However, these requirements are not yet fully understood and cannot be explained based solely on the results acquired here.

As well, there appears to be no correlation between the appearance of the slower τ_2 component and the λ_{abs} , λ_{em} , and thermalized $^3\text{MLCT}$ nanosecond-scale lifetimes of the complexes (Table 5-1). It is not possible at this point to predict whether τ_2 would be present based on these properties alone.

5.4 Conclusion

The preliminary results presented in this chapter reiterate the importance of excitation wavelength on the ultrafast dynamics of tris(bipyridyl)ruthenium non-thermalized excited states. At 388-nm excitation, both $\text{Ru}(\text{bpy})_3$ and $\text{Ru}(\text{pdb})_3$ exhibited similar kinetic behaviour, contrary to literature data indicating the appearance of a long-lived, non-thermalized emission from the excitation of $\text{Ru}(\text{pdb})_3$ at a higher wavelength. However, this long-lived, 1-3 ns emission was observed for homoleptic complexes with 4,4'-disubstituted ligands, suggesting that substitution and symmetry may influence the excited-state dynamics of tris(bipyridyl)ruthenium complexes.

The work presented herein may also have implications for the design of complexes for electron-injection applications. As previously discussed, electron injection

is thought to occur from a high-energy, non-thermalized excited state. Therefore, such a state that is long-lived may prove useful, as it may allow for improved electron-injection efficiency.

Chapter Six: Experimental

6.1 General procedures

Chemicals. All non-standard laboratory reagents were purchased from Aldrich Chemical Co. and used without further purification, unless otherwise indicated. Hexanes, DCM, EtOAc, and methanol were distilled prior to use. THF was dried by distillation over Na / benzophenone under nitrogen. TEA (Riedel-de-Haen) for chromatography was used as received. Anhydrous diethyl ether (ACP Chemicals, < 0.03% water) was used without additional drying.

Optical measurements. UV-visible absorption measurements were performed on a Varian Cary 100 Bio spectrophotometer in quartz cells with a 10 mm path length. Fluorescence measurements were conducted on a Photon Technology fluorimeter in square 10 mm quartz cuvettes. All measurements were performed at 20 ± 2 °C.

Chromatography. Column chromatography using silica gel or alumina was performed either by gravity or under vacuum. For TLC analyses requiring TEA, plates were washed with 3:1:1 hexanes:TEA:EtOAc and dried prior to use. Vanilla TLC dip reagent consisted of a solution of 9 g vanillin, 150 mL ethanol, 40 mL water, and 5 mL conc. H₂SO₄, and was used for the detection of unalkylated aniline NH₂ groups (yellow spot). Saturated aqueous iron(III) sulfate TLC dip was used for the detection of bipyridines (red spot). Developed plates were thoroughly dried to remove TEA before

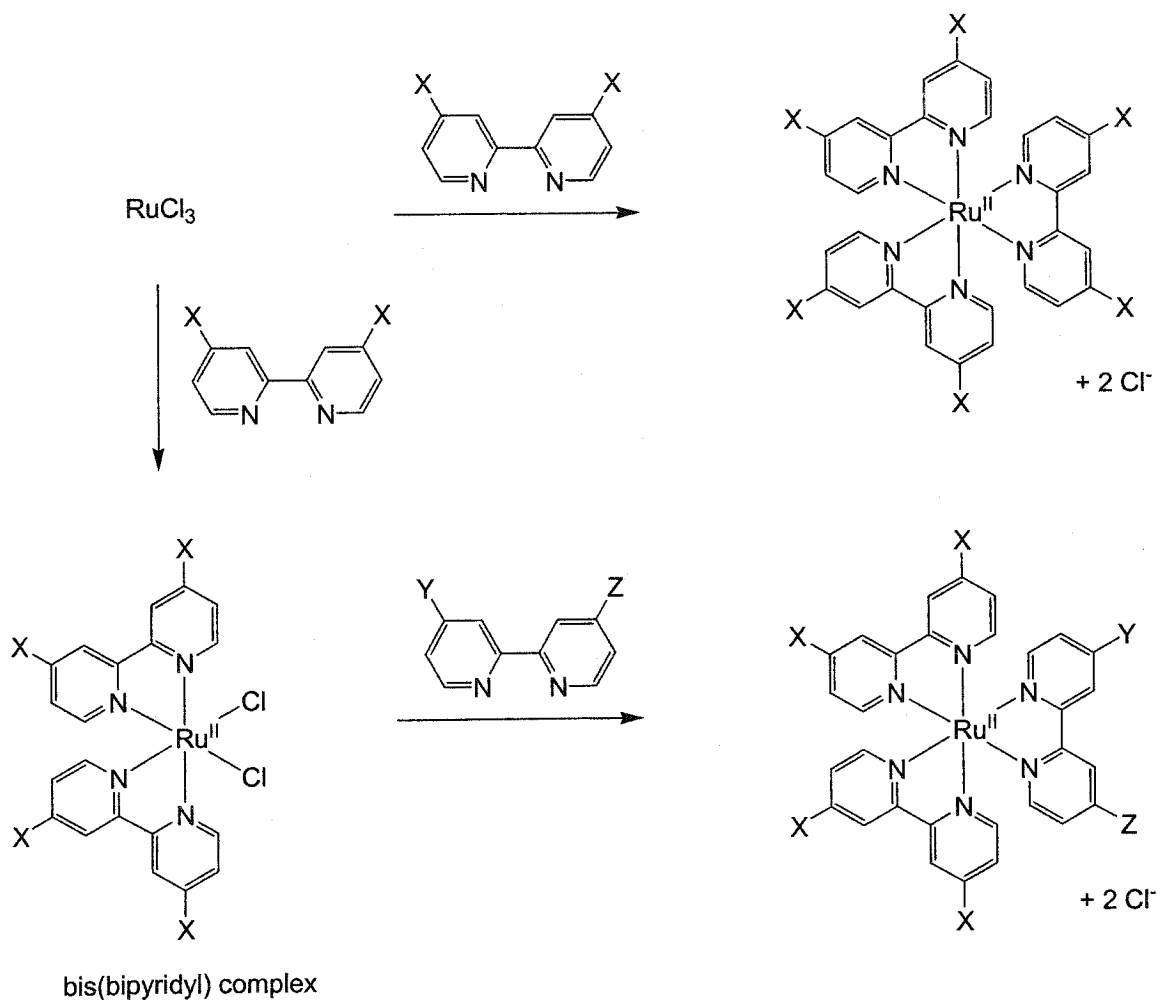
immersion in the dip, and bipyridines containing electron-withdrawing groups required heating after immersion in and removal from the reagent.

Analysis. NMR spectra were collected on Bruker AC-250 (^1H at 250 MHz and ^{13}C at 62.9 MHz), AMX-400 (^1H at 250 MHz), and AV-500 (^1H at 500 MHz and ^{13}C at 125.8 MHz) spectrometers at the Atlantic Region Magnetic Resonance Centre, and data were processed with Bruker WinNMR (AC-250 and AMX-400), Tecmag NTNMR (AC-250), and Bruker Xwin-NMR (AV-500) software. Chemical shifts were calibrated using residual solvent signals and are reported relative to tetramethylsilane. GC-MS was performed on a Perkin-Elmer Autosystem XL Turbomass instrument, while GC with a flame ionization detector was carried out on a Perkin-Elmer Autosystem 4000. Both were equipped with Supelco MDN-5S 30 m \times 0.25 mm \times 0.50 μm columns, and samples were usually diluted or dissolved in DCM for analysis. ESI-MS spectra were collected in methanol on a Thermo Finnigan LCQ Duo instrument on positive ion mode at the Dalhousie Mass Spectrometry Laboratory; reported m/z correspond to the most abundant isotope. Melting points were measured on a Fisher-Johns apparatus and are uncorrected. For compounds that have been previously reported in the literature, the spectral properties collected herein correspond to their literature values.

6.2 Synthesis of unlinked tris(bipyridyl)ruthenium complexes

The preparation of tris(bipyridyl)ruthenium complexes has been thoroughly reported in the literature. Usually, the synthesis of complexes involved the preparation and isolation of the bis(bipyridyl)ruthenium intermediate from RuCl_3 , followed by the

addition of a third ligand. Alternatively, homoleptic complexes may also be prepared directly from RuCl_3 , as illustrated in Scheme 6-1. Complexes were analyzed by NMR and ESI-MS.



Scheme 6-1. Outline of the coordination of bipyridyl ligands to ruthenium. Substituents X, Y, and Z on the 2,2'-bipyridine ligands may or may not be equivalent.

6.2.1 Bipyridyl ligands

The ligands 2,2'-bipyridine (bpy), 4,4'-dimethyl-2,2'-bipyridine (dmb), 4,4'-dimethoxy-2,2'-bipyridine (dmeob), and 5,5'-dimethyl-2,2'-bipyridine (d5mb) were obtained from commercial sources and recrystallized with EtOAc to remove insoluble matter and other impurities prior to coordination to ruthenium, and were typically isolated as white or pale crystals. Other ligands were synthesised as described below.

4,4'-Di(trifluoromethyl)-2,2'-bipyridine (dfmb) was prepared by the method of Furue *et al.*⁸¹ with modifications. Activated zinc powder was prepared by washing ground zinc with 0.5 M HCl followed by water, ethanol, and diethyl ether. The washed zinc was subsequently dried under vacuum at 120 °C overnight. Tetraethylammonium iodide was dried under vacuum at 110°C for 8 h, followed by 16 h in a vacuum dessicator containing P₂O₅. The activated zinc (1.96 g, 30 mmol) and tetraethylammonium iodide (20 mmol, 4.0 g) were combined with dibromobis(triphenylphosphine)nickel(II) (6.0 mmol, 4.5 g) under argon, to which argon-purged dry THF (70 mL) was added *via* cannula. After the dark suspension was stirred at room temperature for 30 min, 2-chloro-4-(trifluoromethyl)pyridine (20 mmol, 3.6 g, Matrix Scientific) was injected by syringe, and the reaction was stirred at 50°C for an additional 48 h under argon. The black slurry was poured into 2 M ammonium hydroxide (200 mL), mixed with chloroform (200 mL), and filtered. The organic layer was separated, dried with anhydrous Na₂SO₄, and evaporated *in vacuo*. Purification of the brown residue by SGCC using a gradient eluant of 0→5% EtOAc in hexanes afforded the desired product as a light yellow powder (mp

80-81 °C; lit.⁸¹ 81.5-82 °C) in 35% yield. ¹H NMR (CDCl₃, 250 MHz) δ (ppm): 7.60 (d, 2H, 4.8 Hz), 8.74 (s, 2H), 8.91 (d, 2H, 5.0 Hz). GC-MS *m/z*: 292 (100), 273 (33), 223 (67).

5,5'-Di(trifluoromethyl)-2,2'-bipyridine (d5fmb) was synthesized from 2-chloro-5-(trifluoromethyl)pyridine according to the preparation of dfmb. The product was isolated in 24% yield as a white powder (mp 109-111 °C; lit.⁸¹ 108.5-110 °C). ¹H NMR (CDCl₃, 250 MHz) δ (ppm): 8.10 (d, 2H, 8.8 Hz), 8.63 (d, 2H, 8.5 Hz), 8.96 (s, 2H). GC-MS *m/z*: 292 (100), 273 (34), 223 (60), 196 (83).

4,4'-Di(methylcarboxy)-2,2'-bipyridine (dmeb) was prepared according to literature procedures with modifications.¹⁷⁴ 2,2'-Bipyridyl-4,4'-dicarboxylic acid (5.0 mmol, 1.2 g, supplied by Sara van Rooy) was refluxed with stirring in thionyl chloride (40 mL) under nitrogen for 4 h, during which the solid dissolved. The yellow solution was evaporated *in vacuo* to yield a brown solid. Methanol (50 mL) was added, and the mixture was refluxed overnight under nitrogen. The solution was chilled to -10 °C, and the white crystals that had formed were collected, washed sequentially with water (2 × 10 mL), saturated aqueous NaHCO₃ (2 × 10 mL), water (3 × 10 mL), and cold methanol (2 × 3 mL), and dried overnight under vacuum to afford the product in 83% yield. ¹H NMR (CDCl₃, 250 MHz) δ (ppm): 4.00 (s, 6H), 7.92 (d, 2H, 4.3 Hz), 8.87 (d, 2H, 4.7 Hz), 8.97 (s, 2H). GC-MS *m/z*: 272 (6), 214 (100).

6.2.2 Bis(bipyridyl)ruthenium complexes

Although not specified in the abbreviated form, these complexes are of *cis* configuration. Ru(bpy)₂Cl₂ was purchased from Aldrich, while the others described below were prepared according to the classical procedure of Sullivan *et al.*¹⁷⁵ with modifications. These intermediates were typically not characterized by NMR due to their low solubility in a variety of common deuterated solvents.

cis-Bis[4,4'-bis(trifluoromethyl)-2,2'-bipyridyl]ruthenium(II) dichloride, Ru(dfmb)₂Cl₂. RuCl₃ hydrate (250 mg, Strem Chemicals) was combined with 4,4'-di(trifluoromethyl)-2,2'-bipyridine (2.0 mmol, 0.86 g), flame-dried lithium chloride (6.0 mmol, 0.25 g), and *N,N*-dimethylformamide (5 mL). After refluxing for 8 h under argon with stirring, the green solution turned blue. It was cooled to room temperature, and the reaction was quenched with acetone (15 mL). A purple powder, which appeared after overnight refrigeration, was collected on a fine sintered glass funnel, washed with water (2 × 2 mL) followed by diethyl ether (3 × 10 mL), and dried under vacuum (38% yield). λ_{max} absorption in ethanol: 388 and 533 nm.

cis-Bis[5,5'-bis(trifluoromethyl)-2,2'-bipyridyl]ruthenium(II) dichloride, Ru(d5fmb)₂Cl₂. RuCl₃ hydrate (0.88 mmol, 0.23 g, Strem Chemicals) was combined with 5,5'-di(trifluoromethyl)-2,2'-bipyridine (1.79 mmol, 522 mg), flame-dried lithium chloride (6.0 mmol, 0.25 g), and *N,N*-dimethylformamide (2 mL) and refluxed for 10 h. The blue

solution was removed from reflux, cooled to room temperature, and diluted with acetone (12 mL). Purple crystals, which appeared after overnight refrigeration, were separated from the blue mother liquor by filtration through a fine sintered glass funnel, washed with water (2×1 mL) followed by diethyl ether (3×5 mL), and dried under vacuum (67% yield). λ_{max} absorption in ethanol: 397 and 600 nm.

cis-Bis[4,4'-dimethyl-2,2'-bipyridyl]ruthenium(II) dichloride, $\text{Ru(dmb)}_2\text{Cl}_2 \cdot \text{RuCl}_3$ hydrate (1.0 mmol, 0.25 g) was combined with 4,4'-dimethyl-2,2'-bipyridine (2.0 mmol, 0.37 g, Strem Chemicals), flame-dried lithium chloride (6.0 mmol, 0.25 mg), and *N,N*-dimethylformamide (5 mL). After refluxing for 8 h under argon with stirring, the brown mixture turned purple and cooled to room temperature, and quenched with acetone (20 mL). A purple-red powder, which appeared after overnight refrigeration, was collected on a fine sintered glass funnel, washed with water (2×3 mL) followed by diethyl ether (5×10 mL), and dried under vacuum. However, the powder was not pure, for reasons as follows. When it was used in subsequent steps for the coordination of a third, different ligand, significant amounts of Ru(dmb)_3 were detected by ESI-MS, thus inferring its presence in the original powder. The purified form was obtained by resuspension of the powder in boiling 100 mM NaCl (75 mL) for 10 min,¹⁷⁶ whereby any Ru(dmb)_3 was presumed to have dissolved; the suspension was then cooled to 4 °C, and the purple crystals were collected by filtration and washed with water (2 mL) followed by diethyl ether (10 mL), in 12% yield.

cis-Bis[4,4'-bis(methylcarboxy)-2,2'-bipyridyl]ruthenium(II) dichloride, Ru(dmeb)₂Cl₂. The standard procedure of Sullivan *et al.*¹⁷⁵ was unsuccessful, as trace amounts of water present in the lithium chloride and the solvent most likely resulted in methyl ester hydrolysis. The product prepared from this method was water-soluble, which was not expected for bis(bipyridyl)ruthenium complexes. Thus, a modified alternate method¹⁷⁷ was carried out. 4,4'-Di(methylcarboxy)-2,2'-bipyridine (1.0 mmol, 0.27 g) was combined with anhydrous RuCl₃ (0.50 mmol, 0.11 g) in methanol (10 mL) and refluxed under argon. After 48 h, the mixture was cooled and dropped into diethyl ether (100 mL), causing a dark-purple precipitate to form. The precipitate was collected on a fine sintered glass funnel and washed sequentially with diethyl ether (3 × 20 mL), ethanol (2 mL), water (3 × 20 mL), ethanol (2 mL), and diethyl ether (10 mL). The orange filtrate, presumed to be the tris product, was discarded. The dry, purple powder was dissolved in *N,N*-dimethylformamide (4 mL), and the solution was supplemented with acetone (5 mL) and refrigerated overnight. Purple crystals that had formed were collected on a fine sintered glass funnel, washed with 2 mL water followed by ethanol (2 mL) and diethyl ether (5 mL), and dried under vacuum (38% yield).

6.2.3 Tris(bipyridyl)ruthenium complexes

Complexes were prepared according to the general procedures described below. Although not indicated in the abbreviated form, *e.g.* Ru(dmb)₃, all complexes were isolated as dichloride salts.

General procedure for the preparation of homoleptic complexes. RuCl_3 trihydrate (0.01–0.10 mmol, Strem Chemicals) was combined with 3.5 equivalents of the appropriate ligand and refluxed in 2–3 mL stirred ethylene glycol under nitrogen until the reaction mixture turned transparent and orange. Typically, the process required 5–30 min, except for ligands containing electron-withdrawing trifluoromethyl groups (12–24 h). After cooling to room temperature, the ethylene glycol solution was transferred to an Erlenmeyer flask and swirled with multiple portions of diethyl ether until the ethylene glycol was removed, leaving the dry, crude product adhering to the sides of the flask. Purification was carried out by the procedures outlined below.

General procedure for the preparation of heteroleptic complexes. The appropriate ligand (0.01–0.10 mmol) and 0.80 equivalents of the *cis*-bis(bipyridyl)ruthenium dichloride were refluxed in stirred 5:1 methanol:acetic acid¹⁷⁸ (10–25 mL) under argon. After the mixture turned transparent and bright orange (typically 10 min to 6 h), the reaction was cooled and evaporated *in vacuo* to yield the crude product. Purification was carried out as by procedures outlined below.

General procedure for purification by precipitation.^{179,180} Precipitation was normally used for the isolation of larger quantities of material (> 0.02 mmol). The crude product was dissolved in 1–5 mL acetonitrile, slowly dropped into anhydrous diethyl ether (100 mL) to extract any remaining ligand, and collected on a fine sintered glass funnel. The contents of the funnel were dissolved in a minimum amount of doubly distilled water (1–4 mL) and gently drawn through the filter by suction to remove water-insoluble components, for example $\text{Ru}(\text{bpy})_2\text{Cl}_2$. The orange aqueous solution was

combined with 5-10 mL acetonitrile or methanol and evaporated *in vacuo*. The further addition of one of the two solvents was usually necessary to facilitate the removal of water. Typical isolated yields were 60-90%.

General procedure for purification by size-exclusion chromatography.^{81,178} This method was ideal for small amounts of material (< 0.02 mmol), due to reduced manipulation relative to precipitation and hence a reduced loss of product. The crude product was dissolved in methanol (0.5 mL), loaded onto a Sephadex LH-20 column (30 cm × 3 cm diameter), and eluted with methanol at a flow rate of around 2 mL/min. The first coloured band (orange; 5-10 mL) to elute was collected and evaporated *in vacuo* to afford the product. Typical isolated yields were 80-90%.

Tris(2,2'-bipyridyl-d₈)ruthenium(II) dichloride, Ru(pdb)₃. Prepared from RuCl₃ trihydrate and pdb (99.8% atom D, CDN Isotopes).¹⁶⁹ ¹H NMR (CD₃OD, 250 MHz) δ (ppm): 7.52 (s), 7.84 (s), 8.18 (s), 8.77 (s); all signals are estimated to be of equal area and are not coupled, suggesting that no ligands present were exclusively H and that the H present was distributed evenly amongst the substitution positions. ESI-MS *m/z*: 297.3 (100%).

Tris(4,4'-dimethyl-2,2'-bipyridyl)ruthenium(II) dichloride, Ru(dmb)₃. Prepared from RuCl₃ trihydrate and dmb.⁸⁵ ¹H NMR (CD₃OD, 250 MHz) δ (ppm): 2.55 (s, 18H), 7.30 (d, 6H, 5.8 Hz), 7.57 (d, 6H, 5.8 Hz), 8.58 (s, 6H). ESI-MS *m/z*: 327.3 (100%).

Tris(5,5'-dimethyl-2,2'-bipyridyl)ruthenium(II) dichloride, Ru(d5mb)₃. Prepared from RuCl₃ trihydrate and d5mb.⁸⁵ ¹H NMR (CD₃OD, 250 MHz) δ (ppm): 2.25 (s, 18H), 7.55 (s, 6H), 7.94 (d, 6H, 7.9 Hz), 8.53 (d, 6H, 8.1 Hz). ESI-MS *m/z*: 327.2 (100%).

Tris(4,4'-dimethoxy-2,2'-bipyridyl)ruthenium(II) dichloride, Ru(dmeob)₃. Prepared from RuCl₃ trihydrate and dmeob.⁷⁸ ¹H NMR (CD₃OD, 250 MHz) δ (ppm): 4.03 (s, 18H), 7.06 (d, 6H, 6.7 Hz), 7.60 (d, 6H, 6.7 Hz), 8.26 (s, 6H). ESI-MS *m/z*: 375.2 (100%) and 750.0 (5%).

Tris[4,4'-bis(trifluoromethyl)-2,2'-bipyridyl]ruthenium(II) dichloride, Ru(dfmb)₃. Prepared from RuCl₃ trihydrate and dfmb.⁸¹ ¹H NMR (CD₃OD, 250 MHz) δ (ppm): 7.85 (d, 6H, 5.2 Hz), 8.16 (d, 6H, 5.8 Hz), 9.38 (s, 6H). ESI-MS *m/z*: 489.0 (100%), 977.0 (15%).

Tris(4,4'-bis(methylcarboxy)-2,2'-bipyridyl)ruthenium(II) dichloride, Ru(dmeb)₃. Prepared from RuCl₃ trihydrate and dmeb,¹⁷⁴ though the isolated product underwent virtually complete transesterification where all methyl groups were replaced by ethylene glycol. The product was converted back to the methyl derivative by refluxing overnight in methanol (100 mL) followed by purification *via* precipitation. ¹H NMR (CD₃OD, 250 MHz) δ (ppm): 4.03 (s, 6H), 7.98 (d, 2H, 5.5 Hz), 8.05 (d, 6H, 5.5 Hz), 9.22 (s, 2H). ESI-MS *m/z*: 459.1 (100%), 918.0 (30%).

Bis(2,2'-bipyridyl)(4,4'-dimethyl-2,2'-bipyridyl)ruthenium(II) *dichloride*,

$\text{Ru}(\text{bpy})_2(\text{dmb})$.¹⁸¹ Prepared from $\text{Ru}(\text{bpy})_2\text{Cl}_2$ and dmb. ^1H NMR (CD_3OD , 250 MHz) δ (ppm): 2.56 (s, 6H), 7.29 (d, 2H, 5.2 Hz), 7.48 (m, 4H), 7.58 (d, 2H, 5.8 Hz), 7.79 (m, 4H), 8.09 (t, 4H, 7.8 Hz), 8.58 (s, 2H), 8.67 (d, 4H, 8.2 Hz). ESI-MS m/z : 299.3 (100%).

Bis(2,2'-bipyridyl)(5,5'-dimethyl-2,2'-bipyridyl)ruthenium(II) *dichloride*,

$\text{Ru}(\text{bpy})_2(\text{d5mb})$.¹⁸² Prepared from $\text{Ru}(\text{bpy})_2\text{Cl}_2$ and d5mb. ^1H NMR (CD_3OD , 250 MHz) δ (ppm): 2.26 (s, 6H), 7.53 (m, 6H), 7.83 (d, 4H, 5.5 Hz), 7.96 (d, 2H, 8.6 Hz), 8.15 (t, 4H, 7.6 Hz), 8.57 (d, 2H, 8.2 Hz), 8.75 (d, 4H, 7.9 Hz). ESI-MS m/z : 299.2 (100%), 597.1 (20%), 632.8 (10%).

Bis(2,2'-bipyridyl)(4,4'-dimethoxy-2,2'-bipyridyl)ruthenium(II) *dichloride*,

$\text{Ru}(\text{bpy})_2(\text{dmeob})$.¹⁸³ Prepared from $\text{Ru}(\text{bpy})_2\text{Cl}_2$ and dmeob. ^1H NMR (CD_3OD , 250 MHz) δ (ppm): 4.03 (s, 6H), 7.05 (d, 1H, 2.8 Hz), 7.08 (d, 1H, 2.8 Hz), 7.48-7.53 (m, 6H), 7.80 (d, 2H, 5.1 Hz), 7.91 (d, 2H, 5.1 Hz), 8.10 (m, 4H), 8.29 (d, 2H, 2.5 Hz), 8.69 (d, 4H, 8.0 Hz). ESI-MS m/z : 315.2 (100%).

Bis(2,2'-bipyridyl)[4,4'-bis(trifluoromethyl)-2,2'-bipyridyl]ruthenium(II) *dichloride*,

$\text{Ru}(\text{bpy})_2(\text{dfmb})$.⁸¹ Prepared from $\text{Ru}(\text{bpy})_2\text{Cl}_2$ and dfmb.⁸¹ ^1H NMR (CD_3OD , 250 MHz) δ (ppm): 7.56 (m, 4H), 7.85 (m, 6H), 8.19 (m, 6H), 8.80 (d, 4H, 7.5 Hz), 9.32 (s, 2H). ESI-MS m/z : 353.3 (100%).

Bis(4,4'-dimethyl-2,2'-bipyridyl)(2,2'-bipyridyl)ruthenium(II) dichloride,

$\text{Ru(dmb)}_2(\text{bpy})$.¹⁸¹ Prepared from $\text{Ru(dmb)}_2\text{Cl}_2$ and bpy. ^1H NMR (CD_3OD , 250 MHz) δ (ppm): 2.55 (s, 12H), 7.29 (m, 4H), 7.45 (t, 6.1 Hz, 2H), 7.59 (m, 4H), 7.80 (d, 5.2 Hz, 2H), 8.07 (m, 2H), 8.56 (s, 4H), 8.67 (d, 8.2 Hz, 2H). ESI-MS m/z : 313.2 (100%) and 625.1 (4%).

Bis(4,4'-dimethyl-2,2'-bipyridyl)(4,4'-dimethoxy-2,2'-bipyridyl)ruthenium(II) dichloride,

$\text{Ru(dmb)}_2(\text{dmeob})$. Prepared from $\text{Ru(dmb)}_2\text{Cl}_2$ and dmeob. ^1H NMR (CD_3OD , 250 MHz) δ (ppm): 2.57 (s, 6H), 2.59 (s, 6H), 4.04 (s, 6H), 7.05 (d, 1H, 2.8 Hz), 7.08 (d, 1H, 2.8 Hz), 7.29 (d, 2H, 5.8 Hz), 7.33 (d, 2H, 5.8 Hz), 7.53 (d, 2H, 6.4 Hz), 7.60 (d, 2H, 5.8 Hz), 7.70 (d, 2H, 5.5 Hz), 8.28 (d, 2H, 2.8 Hz), 8.56 (s, 4H). ESI-MS m/z : 685.1 (100%) and 343.2 (20%).

Bis(4,4'-dimethyl-2,2'-bipyridyl)[4,4'-bis(trifluoromethyl)-2,2'-bipyridyl]ruthenium(II)

dichloride, $\text{Ru(dmb)}_2(\text{dfmb})$. Prepared from $\text{Ru(dmb)}_2\text{Cl}_2$ and dfmb. ^1H NMR (CD_3OD , 250 MHz) δ (ppm): 2.59 (s, 12H), 7.34 (2d, 4H), 7.60 (2d, 4H), 7.79 (d, 2H, 4.9 Hz), 8.15 (d, 2H, 5.8 Hz), 8.60 (s, 4H), 9.28 (s, 2H). ESI-MS m/z : 381.1 (70%), 761.0 (100%).

Bis[4,4'-bis(methylcarboxy)-2,2'-bipyridyl](2,2'-bipyridyl)ruthenium(II) dichloride,

$\text{Ru(dmeb)}_2(\text{dmb})$. Prepared from $\text{Ru(dmeb)}_2\text{Cl}_2$ and dmb⁸⁰ by refluxing in neat methanol in the absence of acetic acid. ^1H NMR (CD_3OD , 250 MHz) δ (ppm): 2.58 (s, 6H), 4.03 (s,

12H), 7.33 (d, 2H, 5.2 Hz), 7.57 (d, 2H, 5.8 Hz), 7.93 (d, 2H, 4.6 Hz), 8.02 (m, 6H), 8.61 (s, 2H), 9.20 (s, 4H). ESI-MS m/z : 415.2 (65%), 829.0 (100%).

Bis[4,4'-bis(trifluoromethyl)-2,2'-bipyridyl](2,2'-bipyridyl)ruthenium(II) dichloride, Ru(dfmb)₂(bpy).⁸¹ Prepared from Ru(dfmb)₂Cl₂ and bpy. ¹H NMR (CD₃OD, 250 MHz) δ (ppm): 7.56 (2d, 2H), 7.85 (m, 6H), 8.13-8.25 (m, 6H), 8.78 (d, 2H, 7.5 Hz), 9.35 (s, 4H). ESI-MS m/z : 421.2 (100%), 876.5 (7%).

Bis[5,5'-bis(trifluoromethyl)-2,2'-bipyridyl](2,2'-bipyridyl)ruthenium(II) dichloride, Ru(d5fmb)₂(bpy).⁸¹ Prepared from Ru(d5fmb)₂Cl₂ and bpy. ¹H NMR (CD₃OD, 250 MHz) δ (ppm): 7.59 (t, 2H, 6.1 Hz), 7.88 (d, 2H, 5.5 Hz), 7.96 (s, 2H), 8.17 (s, 2H), 8.24 (t, 2H, 8.3 Hz), 8.60 (2d, 4H), 8.79 (d, 2H, 8.0 Hz), 9.12 (d, 4H, 8.6 Hz). ESI-MS m/z : 421.2 (100%).

Bis[4,4'-bis(trifluoromethyl)-2,2'-bipyridyl](4,4'-dimethyl-2,2'-bipyridyl)ruthenium(II) dichloride, Ru(dfmb)₂(dmb). Prepared from Ru(dfmb)₂Cl₂ and dmb. ¹H NMR (CD₃OD, 250 MHz) δ (ppm): 2.60 (s, 6H), 7.37 (d, 5.2 Hz, 2H), 7.61 (d, 5.5 Hz, 2H), 7.80 (d, 5.5 Hz, 2H), 7.85 (d, 5.5 Hz, 2H), 8.12 (d, 6.1 Hz, 2H), 8.16 (d, 6.1 Hz, 2H), 8.63 (s, 2H), 9.34 (s, 4H). ESI-MS m/z : 435.0 (100%), 869.0 (65%).

Bis[5,5'-bis(trifluoromethyl)-2,2'-bipyridyl](5,5'-dimethyl-2,2'-bipyridyl)ruthenium(II) dichloride, Ru(d5fmb)₂(d5mb). Prepared from Ru(d5fmb)₂Cl₂ and d5mb. ¹H NMR (CD₃OD, 250 MHz) δ (ppm): 2.29 (s, 6H), 7.68 (s, 2H), 7.95 (s, 2H), 8.04 (d, 2H, 7.6 Hz), 8.15 (s, 2H), 8.61 (m, 6H), 9.13 (m, 4H). ESI-MS *m/z*: 435.1 (100%), 597.1 (20%), 868.9 (22%).

Bis[4,4'-bis(trifluoromethyl)-2,2'-bipyridyl](4,4'-dimethoxy-2,2'-bipyridyl)ruthenium(II) dichloride, Ru(dfmb)₂(dmeob). Prepared from Ru(dfmb)₂Cl₂ and dmeob. ¹H NMR (CD₃OD, 250 MHz) δ (ppm): 4.05 (s, 6H), 7.09 (d, 1H, 2.8 Hz), 7.11 (d, 1H, 2.8 Hz), 7.53 (d, 2H, 6.7 Hz), 7.78 (d, 2H, 5.8 Hz), 7.88 (d, 2H, 5.9 Hz), 8.16 (d, 2H, 6.1 Hz), 8.21 (d, 2H, 5.8 Hz), 8.34 (d, 2H, 2.8 Hz), 9.33 (s, 4H). ESI-MS *m/z*: 451.1 (100%), 936.5 (10%).

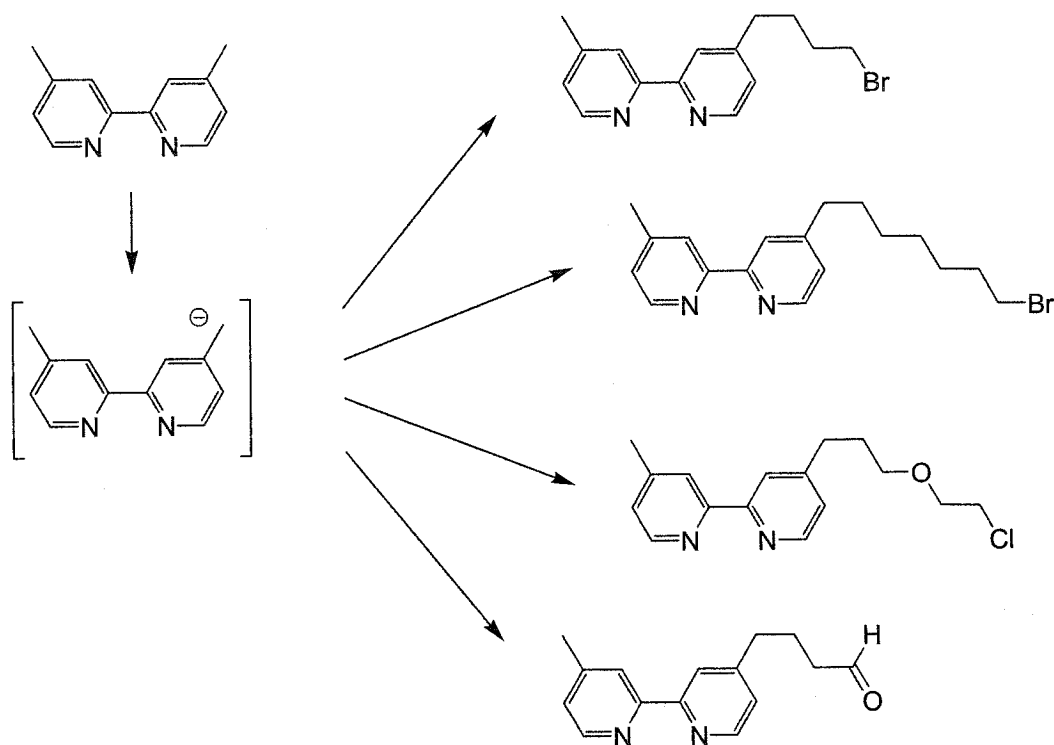
6.3 Synthesis of substrate-linked tris(bipyridyl)ruthenium complexes

The preparation of substrate-linked complexes consisted of key steps. 4,4-Dimethyl-2,2'-bipyridine was functionalized *via* the attachment of a linker, to which a substrate was then covalently attached. Coordination of the substrate-linked bipyridine to Ru(dmb)₂Cl₂ or Ru(bpy)₂Cl₂ afforded the final product.

6.3.1 Functionalized bipyridines

Although the functionalization of 4,4-dimethyl-2,2'-bipyridine was previously investigated by M. Clay,¹⁸⁰ further optimization of the procedures was necessary to

facilitate product isolation and to improve overall yields. These functionalized bipyridines were typically prepared *via* the addition of an alkyl halide to the anion of 4,4'-dimethyl-2,2'-bipyridine, as shown in Scheme 6-2.



Scheme 6-2. Outline of the preparation of functionalized bipyridines.

4-(4-Bromobutyl)-4'-methyl-2,2'-bipyridine. Excess lithium diisopropylamide (15 mmol, 7.5 mL of 2 M solution in THF) was added to a stirred solution of 4,4'-dimethyl-2,2'-bipyridine (10 mmol, 1.8 g) in dry THF (150 mL) under argon in a flame-dried flask cooled in a salt-ice bath. After stirring for 60 min, the brown solution was transferred by cannula to a rapidly stirred, cooled solution of 1,3-dibromopropane (20 mmol, 4.0 g, 2.0

mL) in dry THF under argon (50 mL). The reaction mixture was stirred for an additional 6 h, during which time the ice melted and the reaction mixture turned yellow. Water (50 mL) was added, and the mixture was stirred for 10 min to quench the reaction. Brine (150 mL) was then added, and the aqueous fraction was extracted with chloroform (75 mL). The combined organic fractions were dried with anhydrous MgSO_4 and evaporated *in vacuo*. Purification of the resulting oil by SGCC, whereby any remaining 1,3-dibromopropane was removed by elution with neat hexanes prior to elution with 97:3 hexanes:TEA, yielded the desired product as a thick, amber oil in 70% yield. ^1H NMR (CDCl_3 , 250 MHz) δ (ppm): 1.89 (m, 4H), 2.43 (s, 3H), 2.72 (t, 2H, 7.1 Hz), 3.42 (t, 2H, 6.1 Hz), 7.12 (d, 2H, 4.6 Hz), 8.22 (s, 2H), 8.54 (2d, 2H). GC-MS m/z : 304 (3), 225 (100), 197 (50), 184 (75).

4-(7-Bromoheptyl)-4'-methyl-2,2'-bipyridine. Prepared and isolated according to the preparation of 4-(4-bromobutyl)-4'-methyl-2,2'-bipyridine, except 1,6-dibromohexane (20 mmol, 4.8 g, 3.0 mL) was used in place of 1,3-dibromopropane. The product was isolated as a clear, amber oil that solidified upon standing in 65% yield. ^1H NMR (CDCl_3 , 250 MHz) δ (ppm): 1.36 (m, 6H), 1.69 (m, 2H), 2.43 (m, 2H), 2.42 (s, 3H), 2.68 (t, 2H, 7.3 Hz), 3.38 (t, 2H, 7.3 Hz), 7.12 (d, 2H, 4.9 Hz), 8.21 (s, 2H), 8.53 (2d, 2H). GC-MS m/z : 346 (0.5), 267 (23), 197 (33), 184 (100).

4'-[3-(2-Chloroethoxy)propyl]-4-methyl-2,2'-bipyridine. Excess lithium diisopropylamide (15 mmol, 7.5 mL of 2 M solution in THF) was added to a stirred solution of 4,4'-

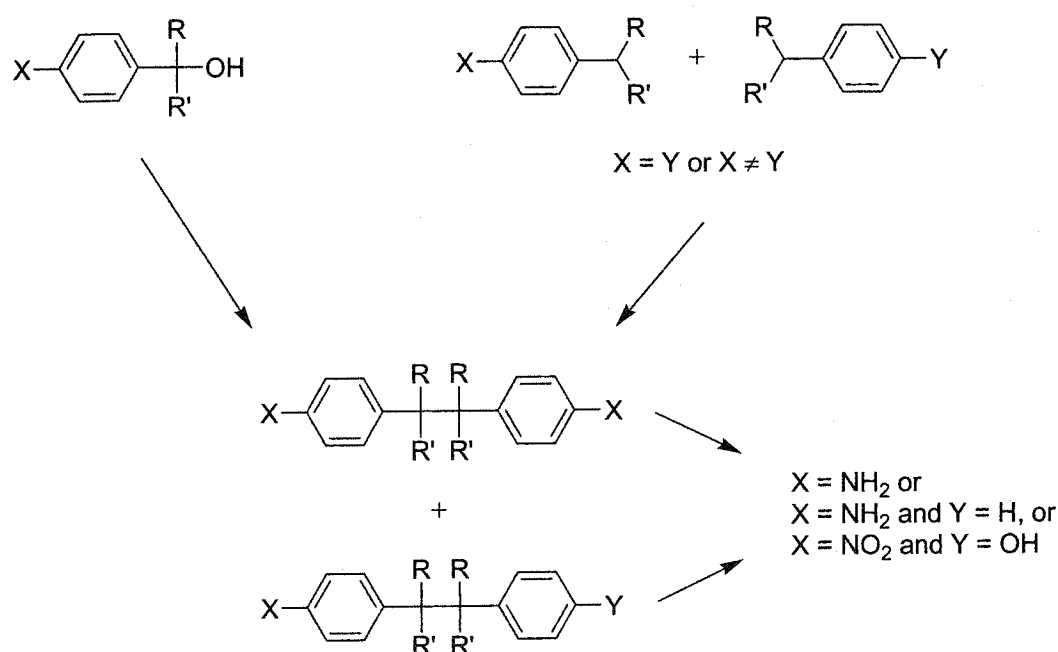
dimethyl-2,2'-bipyridine (10 mmol, 1.84 g) in dry THF (150 mL) under argon pressure in a flame-dried flask cooled in a salt-ice bath. After stirring the brown mixture for 60 min, bis(2-chloroethyl) ether (20 mmol, 2.9 g, 2.4 mL) was rapidly added. The mixture was stirred for an additional 48 h, during which time the ice melted and the reaction mixture turned yellow. Water (50 mL) was added, and the mixture was stirred for 10 min to quench the reaction. Brine (200 mL) was then added, and the aqueous fraction was extracted with chloroform (75 mL). The combined organic fractions were dried with copious amounts of anhydrous MgSO_4 and evaporated *in vacuo*. Purification of the orange oil by SGCC, whereby any remaining bis(2-chloroethyl) ether was removed by elution with neat DCM prior to elution with 92:3:3 hexanes:TEA:EtOAc, yielded the desired product as a waxy, light pink solid in 65% yield. ^1H NMR (CDCl_3 , 250 MHz) δ (ppm): 1.96 (quintet, 2H, 7.2 Hz), 2.45 (s, 3H), 2.81 (t, 2H, 7.3 Hz), 3.50 (t, 2H, 6.1 Hz), 3.62 (t, 2H, 4.9 Hz), 3.65 (t, 2H, 4.9 Hz), 7.10 (d, 2H, 4.9 Hz), 8.19 (s, 2H), 8.50 (d, 2H, 4.9 Hz). GC-MS m/z : 289 (0.5), 255 (91), 184 (100).

4'-(3-Formylpropyl)-4-methyl-2,2'-bipyridine was prepared according to literature procedures with modifications.¹⁸⁴ Excess lithium diisopropylamide (36 mmol, 18 mL of 2 M solution in THF) was added to a stirred solution of 4,4'-dimethyl-2,2'-bipyridine (24 mmol, 4.5 g) in dry THF (400 mL) under argon pressure in a flame-dried flask cooled in a salt-ice bath. The brown mixture was stirred for 60 min, and 2-(2-bromoethyl)-1,3-dioxane (28 mmol, 5.4 g, 3.8 mL) was injected. The reaction stirred for an additional 24 h, during which the ice melted and the reaction turned dark blue. GC-MS analysis of a

small, extracted sample of the reaction mixture indicated that virtually all starting bipyridine had been converted to the corresponding acetal (GC-MS m/z = 298). Water (100 mL) was added, and the mixture was stirred for 10 min to quench the reaction, causing it to turn orange. Brine (200 mL) was then added and stirred, and the aqueous fraction was extracted with DCM (2×150 mL). The organic fractions were combined, washed with brine (200 mL), dried with anhydrous MgSO_4 , and evaporated *in vacuo* to afford a brown oil. Purification of the oil by SGCC using a gradient eluant of 0→20% EtOAc in hexanes containing 5% TEA afforded the acetal, which was pure by GC-MS and TLC analysis (alumina; 4:1 hexanes:EtOAc; aqueous iron(III) sulfate dip), as a thick, yellow oil that solidified upon standing in 75% yield. When the aldehyde was required for use, the acetal (1.0 mmol, 0.30 g) was dissolved in 1 M HCl (10 mL) and stirred under argon at 55 °C; higher temperatures led to rapid decomposition. After 4 h, the solution was neutralized with saturated aqueous NaHCO_3 and extracted with DCM (2×75 mL). The combined organic fractions were dried with anhydrous Na_2SO_4 and evaporated *in vacuo* to afford the product as a clear, yellow oil. The aldehyde was pure by TLC analysis (silica; 5:1:1 hexanes:EtOAc:TEA; aqueous iron(III) sulfate dip) and was used within one week without further purification; decomposition of unused material occurred over several months at -15 °C. ^1H NMR (CDCl_3 , 250 MHz) δ (ppm): 2.04 (quintet, 2H, 7.3 Hz), 2.44 (s, 3H), 2.51 (t, 2H, 7.3 Hz), 2.75 (t, 2H, 7.8 Hz), 7.14 (d, 2H, 4.2 Hz), 8.24 (s, 2H), 8.55 (2d, 2H), 9.79 (s, 1H). GC-MS m/z : 240.

6.3.2 Diphenylalkane substrates

The amino-substituted diphenylalkanes, either with free NH_2 substituents or in the *N,N*-dimethylamino form, were air-sensitive and slowly turned yellow and decomposed over several weeks at room temperature, unless purged with argon and stored at -15°C . As a result, rapid manipulations were required throughout the syntheses to minimize their exposure to air. The diphenylalkane cores were typically prepared *via* the coupling of substituted phenylalkanes or phenylalcohols, followed by a series of functional group interconversions or additions, as shown in Scheme 6-3.



Scheme 6-3. Outline of the preparation of diphenylalkane substrates.

6.3.2.1 Amino-substituted 2,3-dimethyl-2,3-diphenylbutane

2,3-Dimethyl-2,3-diphenylbutane was prepared according to literature procedures^{146,157} with modifications. Cumene (0.25 mol, 30 g, 35 mL) was combined with di-*tert*-butyl peroxide (0.75 mol, 111 g, 140 mL) and refluxed under nitrogen in a 125 °C oil bath. Samples were taken periodically for GC analysis (FID detector), and after ten days, approximately 80% of the starting material had been consumed. The reaction mixture was removed from reflux and cooled to -15 °C, during which large, white crystals formed. The crystals were collected, washed with cold methanol (2 × 50 mL), and dried under vacuum to yield the desired product in 62% yield. ¹H NMR (CDCl₃, 250 MHz) δ (ppm): 1.23 (s, 12H), 7.25-7.35 (m, 10H). GC-MS *m/z*: 119 (100), 103 (12), 91 (64).

2,3-Dimethyl-2,3-di(4-nitrophenyl)butane was prepared according to literature nitration procedures.^{153,185} A stirred solution of 2,3-dimethyl-2,3-diphenylbutane (25 mmol, 6 g) in acetic anhydride (200 mL) was placed in a water bath at room temperature. Conc. HNO₃ (100 mmol, 7 mL) was slowly added at a rate such that the temperature of the reaction mixture remained near room temperature. (Note: acetyl nitrate formed in the reaction can explode at temperatures above approximately 50 °C). The reaction mixture was stirred for 9 h, during which time copious amounts of white precipitate had formed, which was filtered through a fine sintered-glass funnel. The precipitate was washed sequentially with acetic anhydride (50 mL), water (3 × 100 mL), and ethanol (2 × 50 mL), and dried under

vacuum. The product, isolated in *ca.* 30% yield, was not soluble in any common solvent and was not characterized at this stage.

2,3-Dimethyl-2,3-di(4-aminophenyl)butane and *2,3-dimethyl-2-(4-aminophenyl)-3-phenylbutane* were prepared by Pd/C-catalyzed reduction of the corresponding nitro derivatives in the presence of hydrazine.¹⁵² The insoluble *2,3-dimethyl-2,3-di(4-nitrophenyl)butane* (3.7 mmol, 1.2 g), hydrazine hydrate (29 mmol, 1.5 g, 1.4 mL), and 10% Pd/C (0.5 g) were combined in methanol (500 mL). The grey suspension was refluxed under nitrogen pressure for 45 min, during which the white starting material dissolved. The catalyst was removed by filtration through a fine sintered-glass funnel, and the filtrate was evaporated *in vacuo* to afford a white residue (1.0 g). The residue was dissolved in CH₂Cl₂ (200 mL), washed with 250 mM sodium phosphate buffer at pH 6.5 (3 × 100 mL), dried with anhydrous Na₂SO₄, and evaporated *in vacuo*. TLC analysis (silica; DCM; detection by UV and vanilla dip) revealed two compounds (*R_f* = 0.0 and 0.3); when 10% TEA was added to the eluant, both spots advanced (*R_f* = 0.6 and 0.9). The two compounds were separated by SGCC, where the high-*R_f* compound was eluted with neat DCM; the addition of 5% TEA eluted the low-*R_f* component. The former was identified by ¹H NMR as the monoamino derivative, which originated from incomplete nitration, while the latter was the diamino product in 91% yield. ¹H NMR (CDCl₃, 250 MHz) δ (ppm) for the monoamino derivative: 1.25 (s, 6H), 1.29 (s, 6H), 3.55 (br s, 2H), 6.53 (d, 2H, 8.5 Hz), 6.83 (d, 2H, 8.5 Hz), 7.13 (m, 5H); for the diamino product: 1.24 (s, 12H), 3.54 (br s, 4H), 6.53 (d, 4H, 8.6 Hz), 6.86 (d, 4H, 8.5 Hz).

6.3.2.2 Amino-substituted 3,4-diethyl-3,4-diphenylhexane

Unlike the preparation of 2,3-dimethyl-2,3-diphenylbutane, the preparation of 3,4-diethyl-3,4-diphenylhexane by the di-*tert*-butyl peroxide dimerization of 3-phenylpentane was not attempted due in part to the unavailability of the latter at a reasonable cost. The ability of two bulky radicals to dimerize spontaneously was also questionable, particularly when the dimerization of cumene to form the less-hindered 2,3-dimethyl-2,3-diphenylhexane was already a slow process. The best approach then, appeared to be a titanium-mediated coupling of 3-phenyl-3-pentanol.

3-Phenyl-3-pentanol. An oven-dried, three-necked flask equipped with a condenser under nitrogen pressure was loaded with Mg turnings (0.38 mol, 9.3 g, washed sequentially with 1 M HCl, water, and ethanol, and oven-dried before use) and dry THF (200 mL). Bromobenzene (0.38 mol, 60 g, 40 mL) was dissolved in dry THF (300 mL) and placed in a dropping funnel. A portion (30 mL) of the bromobenzene solution was added to the stirred Mg/THF mixture, and the flask was gently warmed to initiate the reaction. After the reaction started, the heat was removed, and the remainder of the bromobenzene solution was added at a rate such that the reflux was maintained (ca. 30 min). The reaction mixture was stirred for an additional hour, after which 3-pentanone (0.38 mol, 33 g, 40 mL) was introduced dropwise over 30 min. The reaction was stirred for an additional 3 h and then quenched with saturated aqueous NH_4Cl (600 mL). The mixture was extracted with diethyl ether (3×300 mL), and the organic fractions were combined, dried with anhydrous Na_2SO_4 , and evaporated *in vacuo* to yield a clear, yellow oil.

Distillation of the oil under vacuum (3 mm Hg, 59-62°C) afforded the product as a clear, colourless oil in 93% yield. It was pure by TLC analysis (silica gel, 1:1 hexanes:DCM) and GC-MS; m/z : 164 (0.5), 146 (40), 135 (100), 117 (70).

3,4-Diethyl-3,4-diphenylhexane. A literature procedure^{152,157} for the coupling of 3-phenyl-3-pentanol *via* the addition 40% HBr in acetic acid to the neat alcohol followed by reduction with zinc seemed appropriate, but the acid at the 40% level was not commercially available. Substitution with the 30% variety was carried out, but the reaction did not occur and no product was obtained despite numerous attempts. Instances of the coupling of sterically hindered alcohols are scarce in the literature, and the only feasible method¹⁸⁶ involved low-valent titanium; a more modern lanthanum procedure¹⁸⁷ was less practical and also formed undesired side products. Titanium(III) chloride (0.15 mol, 5.0 g, pre-weighed in a nitrogen-filled glove bag into several flame-dried sample vials) was added to a flame-dried flask containing dry THF (700 mL) under argon pressure with stirring. The purple slurry was slowly supplemented with LiAlH₄ (50 mmol, 1.90 g), during which gas evolution occurred and the mixture turned black. After stirring for 15 min, 3-phenyl-3-pentanol (50 mmol, 8.2 g) was added. The reaction was heated to reflux, and small samples (1 mL) were periodically removed, quenched with water, and extracted for GC analysis. After 6 d, the black mixture was removed from reflux, quenched with water (300 mL), and extracted with diethyl ether (3 × 200 mL). The dark organic fractions were combined, washed with water (3 × 100 mL) followed by brine (2 × 100 mL), and dried over anhydrous Na₂SO₄. The clear, ethereal solution was

evaporated *in vacuo* to yield a thick and clear, colourless oil. NMR analysis (^1H and ^{13}C) of the oil indicated that the reaction was ca. 80% complete, with no evidence of side products. The thick oil was crystallized from methanol-water to afford the desired product as long, white crystals in 63% yield. ^1H NMR (CDCl_3 , 250 MHz) δ (ppm): 0.63 (t, 12H, 7.0 Hz), 2.00 (q, 8H, 7.0 Hz), 6.95-7.13 (m, 10H); ^{13}C NMR (CDCl_3 , 62.9 MHz) δ (ppm): 10.45, 25.44, 51.58, 125.11, 126.40, 130.13, 144.65.

3,4-Diethyl-3,4-di(4-nitrophenyl)hexane and *3,4-diethyl-3-(4-nitrophenyl)-4-phenylhexane*. A stirred solution of 3,4-diethyl-3,4-diphenylhexane (8.5 mmol, 2.5 g) in acetic anhydride (75 mL) was cooled in an ice bath. Conc. nitric acid (36 mmol, 2.5 mL) was added dropwise at a rate such that the temperature of the reaction remained below room temperature. The progress of the reaction was monitored by TLC analysis (spotted silica plate dried at 60 °C for 20 min prior to development with 1:1 hexanes:DCM), and after 4 h, all starting material had been consumed and the intensities of the spots corresponding to the mono- and dinitro products (R_f of 0.5 and 0.3, respectively) were approximately equal. The reaction mixture was poured into ice water (300 mL) and stirred until the acetic anhydride was hydrolyzed. The aqueous mixture was extracted with hexanes (5 \times 100 mL), and the organic fractions were combined, washed with saturated aqueous NaHCO_3 (2 \times 100 mL), dried with anhydrous Na_2SO_4 , and evaporated *in vacuo*. The resulting oil was purified by SGCC using a gradient eluant of 0 \rightarrow 50% DCM in hexanes to yield the mono- and dinitro products, which were subsequently crystallized from methanol-water to afford white crystals in respective yields of 20% and 25%. Mononitro

product ^1H NMR (CDCl_3 , 250 MHz) δ (ppm): 0.75 (2t, 12H), 2.03 (m, 8H), 6.88 (m, 2H), 7.02 (d, 2H, 8.8 Hz), 7.15 (m, 3H), 7.97 (d, 2H, 8.8 Hz). Dinitro product ^1H NMR (CDCl_3 , 250 MHz) δ (ppm): 0.75 (t, 12H, 7.1 Hz), 2.02 (m, 8H, 7.1 Hz), 7.04 (d, 4H, 9.0 Hz), 8.01 (d, 4H, 8.8 Hz); ^{13}C NMR (CDCl_3 , 62.9 MHz) δ (ppm): 10.5, 25.7, 52.8, 121.7, 130.8, 145.8, 151.9.

3,4-Diethyl-3,4-di(4-aminophenyl)hexane. A stirred mixture of 3,4-diethyl-3,4-di-(4-nitrophenyl)hexane (1.0 mmol, 384 mg), hydrazine hydrate (6 mmol, 0.28 mL, 0.30 g), and 10% Pd/C (250 mg) in methanol (75 mL) was heated under argon in an oil bath at 50 °C; the product decomposed at refluxing temperatures. After 45 min, TLC analysis (alumina; 9:1 hexanes:EtOAc) revealed one UV-active spot that turned yellow when dipped in vanilla reagent. The reaction mixture was filtered through a fine sintered glass funnel, and the filtrate was evaporated *in vacuo*. The yellow residue was redissolved in DCM (75 mL) and washed with 250 mM sodium phosphate buffer pH 6.5 (2 \times 50 mL) to remove any remaining hydrazine, and the organic fraction was dried with anhydrous Na_2SO_4 and evaporated again. Purification on a short, silica gel column using 95:5 DCM:TEA as an eluent afforded the desired product as a thick, light yellow oil in 85% yield. ^1H NMR (CDCl_3 , 250 MHz) δ (ppm): 0.71 (t, 12H, 6.9 Hz), 1.95 (q, 8H, 6.9 Hz), 3.62 (br s, 4H), 6.54 (d, 4H, 8.2 Hz), 6.80 (d, 4H, 8.2 Hz); ^{13}C NMR (CDCl_3 , 62.9 MHz) δ (ppm): 6.30, 21.31, 46.68, 109.17, 126.61, 130.66, 138.97. This compound was not successfully linked to a bipyridine.

3,4-Diethyl-3-(4-aminophenyl)-4-phenylhexane was prepared by reduction of the corresponding mononitro compound following the preparation of the diamino derivative above in the same mol quantities, except the reaction mixture was heated to reflux without any noticeable product decomposition. Purification on a short, silica gel column using neat DCM as an eluent afforded the desired product as a clear, colourless oil in 95% yield. ^1H NMR (CDCl_3 , 250 MHz) δ (ppm): 0.73 (2t, 12H), 2.03 (m, 8H), 3.56 (br s, 2H), 6.55 (d, 2H, 8.6 Hz), 6.78 (d, 2H, 8.8 Hz), 7.05 (m, 2H), 7.20 (m, 3H); ^{13}C NMR (CDCl_3 , 62.9 MHz) δ (ppm): 10.39, 10.45, 25.41, 25.46, 50.78, 51.64, 113.36, 124.89, 126.24, 130.13, 130.80, 134.57, 143.39, 144.83.

6.3.2.3 Amino-substituted 3,4-dimethyl-3,4-diphenylhexane

The synthesis of this derivative was greatly simplified by the commercial availability of the unsubstituted starting material at a relatively low cost. However, substantial purification of the purchased material was required.

meso-3,4-Dimethyl-3,4-diphenylhexane. Acros Organics 3,4-dimethyl-3,4-diphenylhexane (98% grade; unspecified stereochemistry) was received as a yellow, waxy semisolid, and, although pure by GC, it contained at least five major components by TLC analysis (silica; hexanes). Thus, the commercial material was purified by SGCC, using petroleum ether as a eluant, to afford a clear, colourless oil. ^1H -NMR analysis indicated that the oil was an approximately 1:1 mixture of *meso*:DL stereoisomers.¹⁵⁷ Initial crystallization of the oil in methanol resulted in a white powder that was approximately

3:2 *meso*:DL, and the powder was recrystallized twice more to afford the desired *meso* product as square, colourless crystals (mp 98-100 °C; lit.¹⁵⁷ 97 °C). ¹H NMR (CDCl₃, 250 MHz) δ (ppm): 0.59 (t, 6H, 7.3 Hz), 1.27 (s, 6H), 1.49 (m, 2H), 2.26 (m, 2H), 6.95 (m, 4H), 7.22 (m, 6H).

meso-3,4-Dimethyl-3,4-di(4-nitrophenyl)hexane. A stirred suspension of *meso*-3,4-dimethyl-3,4-diphenylhexane (3.0 mmol, 0.80 g) in stirred acetic anhydride (150 mL) was cooled in an ice bath. Conc. HNO₃ (5.6 mmol, 4.0 mL) was added dropwise over 15 min, after which the ice bath was removed and the reaction mixture was allowed to stir at room temperature. After 6 h, during which time the starting material had dissolved, TLC analysis (spotted silica plate dried at 60 °C for 20 min prior to development with 1:1 hexanes:DCM) indicated the presence of both mononitro (R_f = 0.8) and dinitro (R_f = 0.4) products. The light-yellow mixture was poured into cold water (500 mL) and stirred until the acetic anhydride was hydrolyzed. The aqueous mixture was extracted with hexanes (4 × 150), and the organic fractions were combined, washed with 1 M potassium carbonate (2 × 100 mL) followed by brine (100 mL), dried with anhydrous Na₂SO₄, and evaporated *in vacuo*. Purification of the yellow residue by SGCC using a gradient eluant of 20→40% DCM in hexanes afforded the mono- and dinitro derivatives as light yellow oils, which formed off-white powders in respective yields of 30% and 40% upon crystallization from methanol. Desired product ¹H NMR (CDCl₃, 250 MHz) δ (ppm): 0.60 (t, 6H, 7.0 Hz), 1.34 (s, 6H), 1.62 (m, 2H), 2.22 (m, 2H), 7.08 (d, 4H, 8.6 Hz), 8.05 (d, 4H, 9.0 Hz); ¹³C NMR (CDCl₃, 62.9 MHz) δ (ppm): 8.96, 20.88, 27.75, 49.17, 121.92, 130.46, 146.02,

151.11. *erythro*-3,4-dimethyl-3-(4-nitrophenyl)-4-phenylhexane (not used for subsequent studies) ^1H NMR (CDCl_3 , 250 MHz) δ (ppm): 0.61 (2t, 6H), 1.29 (s, 3H), 1.35 (s, 3H), 1.58 (m, 2H), 2.25 (m, 2H), 6.92 (m, 2H), 7.05 (d, 2H, 8.2 Hz), 7.19 (m, 3H), 8.02 (d, 2H, 9.0 Hz) ; ^{13}C NMR (CDCl_3 , 62.9 MHz) δ (ppm): 9.08, 20.84, 27.55, 27.71, 48.36, 49.21, 121.53, 125.84, 126.81, 129.64, 130.61, 142.53, 145.75, 152.35.

meso-3,4-Dimethyl-3,4-di(4-aminophenyl)hexane. The corresponding dinitro compound (1.0 mmol, 356 mg) was combined with hydrazine hydrate (6 mmol, 0.28 mL, 0.30 g) and 10% Pd/C (0.1 g) in methanol (50 mL) and refluxed under argon. After 15 min, TLC analysis (silica; DCM) indicated that the starting material had been consumed. The reaction mixture was filtered through a fine sintered glass funnel, and the filtrate was evaporated *in vacuo*. The residue was redissolved in DCM (100 mL) and washed with 25 mM sodium phosphate buffer at pH 7 (75 mL) to remove remaining hydrazine. After drying with anhydrous Na_2SO_4 , the organic fraction was evaporated *in vacuo* to afford a white powder. Purification of the powder by SGCC using a gradient eluant of 30 \rightarrow 70% DCM in hexanes containing 5% TEA afforded the product as a clear, colourless oil in 80% yield. ^1H NMR (CDCl_3 , 250 MHz) δ (ppm): 0.59 (t, 6H, 7.3 Hz), 1.19 (s, 6H), 1.45 (m, 2H), 2.13 (m, 2H), 6.54 (d, 4H, 8.6 Hz), 6.76 (d, 4H, 8.3 Hz).

6.3.2.4 Amino-substituted 4,5-dimethyl-4,5-diphenyloctane

2-Phenyl-2-pentanol. Phenylmagnesium bromide (0.15 mol, 50 mL of 3 M solution) was transferred *via* cannula to a flame-dried flask containing diethyl ether (400 mL) stirred under argon pressure in an ice bath. A solution of 2-pentanone (0.18 mol, 15.5 g, 19.5 mL) in diethyl ether (30 mL) was slowly introduced into the flask, during which the reaction mixture formed a white precipitate. The ice bath was then removed, and the reaction was stirred at room temperature. After 3 h, the reaction was quenched with 1 M ammonium chloride (250 mL) and water (200 mL), causing the white precipitate to dissolve. The ethereal solution was separated, and the aqueous fraction was extracted with diethyl ether (200 mL). The combined organic fractions were washed with brine (200 mL), dried with anhydrous MgSO_4 , and evaporated *in vacuo* to afford a thick, yellow oil. Vacuum distillation of the oil (10 mm Hg, bp 104–05 °C) afforded pure product as a clear, light yellow oil in 72% yield. GC-MS *m/z*: 164 (2), 146 (32), 131 (68), 121 (100). The product was also prepared from acetophenone and propylmagnesium bromide, but the similarity in the boiling points of the product and acetophenone complicated the distillation.

meso-4,5-Dimethyl-4,5-diphenyloctane. Titanium(III) chloride (36 mmol, 5.5 g, one Aldrich “5 g” bottle) was added to a flamed-dried flask containing stirred dry THF (250 mL) under argon pressure at room temperature. The purple solution was slowly supplemented with LiAlH_4 (12 mmol, 0.50 g), and the resulting black mixture was stirred for 15 min prior to the addition of 2-phenyl-2-pentanol (14 mmol, 2.4 g) by syringe. After

heating to reflux for 24 h, a small sample was removed, quenched with an equivalent volume of water, and analyzed by GC-MS; virtually no starting material remained. The mixture was cooled to room temperature, and the reaction was quenched with 1 M ammonium chloride (100 mL), water (150 mL), and an additional diethyl ether (150 mL). The black ethereal layer was washed with water (3×150 mL), and the resulting colourless solution was washed with brine (100 mL), dried with anhydrous Na_2SO_4 , and evaporated *in vacuo* to yield a clear, colourless oil. A single crystallization of the oil in methanol afforded the *meso* product¹⁵⁷ as white, needle-like crystals (mp 107-108 °C; lit.¹⁵⁷ 107 °C) in 28% yield. ^1H NMR (CDCl_3 , 250 MHz) δ (ppm): 0.83 (m, 8H), 1.07 (m, 2H), 1.29 (s, 6H), 1.47 (m, 2H), 2.09 (m, 2H), 6.94 (m, 4H), 7.16 (m, 6H).

meso-4,5-Dimethyl-4,5-di(4-nitrophenyl)octane. A stirred solution of *meso*-4,5-dimethyl-4,5-diphenyloctane (3.0 mmol, 0.88 g) in acetic anhydride (100 mL) was cooled in an ice bath. Conc. HNO_3 (5.0 mmol, 3.5 mL) was added dropwise over 15 min, after which the ice bath was removed, and the reaction mixture was stirred overnight at room temperature. TLC analysis (spotted silica plate dried at 60 °C for 20 min prior to development with 1:1 hexanes:DCM) indicated the presence of both mononitro ($R_f = 0.9$) and dinitro ($R_f = 0.5$) products. The amber mixture was poured into cold water (400 mL) and stirred until the acetic anhydride was hydrolyzed. The aqueous mixture was extracted with hexanes (4×100 mL), and the organic fractions were combined, washed with saturated aqueous NaHCO_3 (2×200 mL) followed by brine (150 mL), dried with

anhydrous Na_2SO_4 , and evaporated *in vacuo* to yield a thick, yellow oil. Purification of the oil by SGCC using a gradient eluant of 0→30% DCM in hexanes afforded the mono- and dinitro derivatives as clear, light yellow oils in respective yields of 40% and 25%. Desired product ^1H NMR (CDCl_3 , 250 MHz) δ (ppm): 0.75 (m, 2H), 0.85 (t, 6H, 6.7 Hz), 1.11 (m, 2H), 1.36 (s, 6H), 1.59 (m, 2H), 2.07 (m, 2H), 7.06 (d, 4H, 8.2 Hz), 8.04 (d, 4H, 9.2 Hz); ^{13}C NMR (CDCl_3 , 62.9 MHz) δ (ppm): 14.88, 17.83, 21.48, 37.76, 48.92, 121.88, 130.26, 146.02, 151.57. *erythro*-4,5-dimethyl-4-(4-nitrophenyl)-5-phenyloctane (not used for subsequent studies) ^1H NMR (CDCl_3 , 250 MHz) δ (ppm): 0.83 (m, 8H), 1.10 (m, 2H), 1.32 (s, 3H), 1.38 (s, 3H), 1.59 (m, 2H), 2.10 (m, 2H), 6.91 (m, 2H), 7.04 (d, 2H, 8.5 Hz), 7.19 (m, 3H), 8.02 (d, 2H, 9.2 Hz); ^{13}C NMR (CDCl_3 , 62.9 MHz) δ (ppm): 15.01, 17.95, 21.46, 37.72, 37.78, 48.14, 48.98, 121.51, 125.82, 126.79, 129.43, 130.38, 143.05, 145.73, 152.79.

meso-4,5-Dimethyl-4,5-di(4-aminophenyl)octane. Despite the presence of bulky substituents, decomposition of this compound in refluxing methanol was not observed. The corresponding dinitro derivative (0.60 mmol, 0.23 g) was refluxed with hydrazine hydrate (6.0 mmol, 0.28 mL, 0.30 g) and 10% Pd/C (150 mg) in methanol (50 mL) under argon. After 30 min, the reaction mixture was cooled for several minutes and filtered through a fine sintered glass funnel. The filtrate was evaporated *in vacuo*, and the resulting residue was dissolved in DCM (75 mL) and washed with 100 mM sodium phosphate buffer at pH 7 (75 mL) to remove any remaining hydrazine. The organic

fraction, which was pure by TLC analysis (silica; 9:1:1 hexanes: DCM:TEA; vanilla dip), was dried with anhydrous Na₂SO₄ and evaporated *in vacuo* to afford a clear, colourless oil in 92% yield. ¹H NMR (CDCl₃, 250 MHz) δ (ppm): 0.82 (m, 8H), 1.07 (m, 2H), 1.21 (s, 6H), 1.42 (m, 2H), 1.98 (m, 2H), 3.55 (br s, 4H), 6.53 (d, 4H, 8.5 Hz), 6.74 (d, 4H, 8.0 Hz).

6.3.2.5 Amino- and oxygen-substituted 2,3-dimethyl-2,3-diphenylbutane

Similar to the preparation of 2,3-dimethyl-2,3-diphenylbutane, preparation of these unsymmetrical derivatives was carried out *via* the di-*tert*-butyl peroxide coupling of two different precursors.

4-Isopropylphenyl acetate was prepared according to standard protocols with modifications.¹⁸⁸ 4-Isopropylphenol (0.11 mol, 15 g) was dissolved in stirred 3 M NaOH (50 mL) and diluted with approximately 150 g crushed ice. Acetic anhydride (0.14 mol, 15 g, 16 mL) was added, and the yellow reaction mixture was stirred for an additional 10 min. After the ice had melted, the cloudy mixture was extracted with diethyl ether (3 × 75 mL). The organic fractions were combined, washed with 5% NaOH (2 × 100 mL) to remove residual starting material, brine (2 × 100 mL), dried with anhydrous MgSO₄, and evaporated *in vacuo* to afford a yellow oil. Simple distillation afforded the product as a clear, colourless oil (bp 257-259 °C; lit.¹⁸⁹ 54.8-55.2 °C at 0.1 mm) in 92% yield. ¹H NMR (CDCl₃, 250 MHz) δ (ppm): 1.23 (d, 6H, 7.0 Hz), 2.27 (s, 3H), 2.92 (m, 1H), 6.99 (d, 2H, 8.9 Hz), 7.21 (d, 2H, 8.6 Hz). GC-MS *m/z*: 178 (20), 136 (60), 121 (100).

2,3-Dimethyl-2-(4-acetoxyphenyl)-3-(4-nitrophenyl)butane. A mixture of 4-isopropylphenyl acetate (0.10 mol, 18 g), cumene (0.10 mol, 12 g, 14 mL) and di-*tert*-butyl peroxide (0.40 mol, 58 g, 74 mL) was refluxed under argon in an oil bath. After 12 d, GC analysis indicated that the conversion to 2,3-dimethyl-2-(4-acetoxyphenyl)butane was approximately 60%, and the reaction mixture was cooled and evaporated *in vacuo* to yield a thick, amber oil. The oil was divided into several portions, each of which were subjected to SGCC using a gradient eluant of 0→5% EtOAc in hexanes. Fractions containing 2,3-dimethyl-2-(4-acetoxyphenyl)butane (determined by GC analysis), which co-eluted with the starting material 4-isopropylphenyl acetate, were pooled and evaporated *in vacuo* to yield a clear, colourless oil (10 g). A portion (2.5 g) of the oil was dissolved in acetic anhydride (100 mL), and the solution was cooled in an ice bath and slowly supplemented with conc. nitric acid (25 mmol, 1.8 mL) over 20 min. After stirring overnight, the yellow solution was poured into cold water (400 mL) and stirred until the acetic anhydride was hydrolyzed. The aqueous suspension was extracted with hexanes (4 × 100 mL), and the combined organic fractions were washed with saturated aqueous NaHCO₃ (3 × 100 mL) followed by brine (100 mL), dried with anhydrous Na₂SO₄, and evaporated *in vacuo*. Purification of the yellow residue by SGCC using a gradient eluant of 0→20% EtOAc in hexanes; the solid was recrystallized in hexanes to afford the product as yellow crystals in 7% yield. ¹H NMR (CDCl₃, 250 MHz) δ (ppm): 1.32 (s, 6H), 1.36 (s, 6H), 2.29 (s, 3H), 6.90 (d, 2H, 8.9 Hz), 6.99 (d, 2H, 8.9 Hz), 7.14 (d, 2H, 8.8 Hz), 8.01 (d, 2H, 8.8 Hz). ¹³C NMR (CDCl₃, 62.9 MHz) δ (ppm): 21.08, 24.90, 43.38, 44.44, 113.03, 119.74, 121.66, 129.32, 143.11, 145.79, 148.70, 154.63, 169.37.

2,3-Dimethyl-2-(4-hydroxyphenyl)-3-(4-nitrophenyl)butane. A mixture of 2,3-dimethyl-2-(4-acetoxyphenyl)butane (1.0 mmol, 0.34 g), 2 M HCl (10 mL), and methanol (90 mL) was refluxed under nitrogen. After 4 h, when TLC analysis (silica gel; 4:1 hexanes:EtOAc) indicated that all of the starting material had been consumed, the mixture was diluted with water (50 mL) and evaporated *in vacuo* to remove the methanol. The aqueous suspension containing an off-white precipitate was neutralized with saturated aqueous NaHCO₃ and extracted with DCM (3 × 75 mL). The organic fractions were combined, dried with anhydrous Na₂SO₄, and evaporated *in vacuo* to yield the desired product as a thick, yellow oil in 95% yield. ¹H NMR (CDCl₃, 250 MHz) δ (ppm): 1.31 (s, 6H), 1.37 (s, 6H), 6.70 (d, 2H, 8.2 Hz), 6.87 (d, 2H, 7.6 Hz), 7.16 (d, 2H, 8.3 Hz), 8.03 (d, 2H, 8.0 Hz). ¹³C NMR (CDCl₃, 62.9 MHz) δ (ppm): 24.92, 24.96, 42.95, 44.54, 113.61, 121.57, 129.39, 129.50, 137.74, 145.62, 153.61, 155.17.

6.3.2.6 Oxygen-substituted 2,3-dimethyl-2,3-diphenylbutane

The symmetrical nature of this compound, where both phenyl moieties are 4,4'-disubstituted with oxygen, greatly facilitated the synthesis. The di-*tert*-butyl peroxide coupling procedure was employed here as well.

2,3-Dimethyl-2,3-di(4-hydroxyphenyl)butane. A mixture of 4-isopropylphenyl acetate (25 mmol, 4.5 g) and di-*tert*-butyl peroxide (100 mmol, 14.5 g, 18.5 mL) was refluxed under argon in an oil bath. After 8 d, GC analysis indicated that the coupling reaction was approximately 80% complete, and the reaction mixture was cooled and evaporated *in*

vacuo to yield an orange oil that solidified upon standing. The residue was purified by SGCC using a gradient eluant of 0→40% EtOAc in hexanes to afford the diacetoxyl derivative as a white powder in 45% yield. The light-yellow powder (5.5 mmol, 1.9 g) was combined with methanol (250 mL) and 2 M HCl (25 mL) and refluxed overnight, after which TLC analysis (silica; DCM) indicated that the hydrolysis was complete. The methanol was removed by evaporation *in vacuo*, and the remaining aqueous suspension was neutralized with saturated aqueous NaHCO₃. DCM (100 mL) was added to dissolve the yellow residue, and the aqueous fraction was extracted with additional DCM (2 × 100 mL). The combined organic fractions were dried with anhydrous MgSO₄ and evaporated *in vacuo* to afford the desired product as a light yellow solid in 95% yield (mp 208-210 °C; lit.¹⁹⁰ 210 °C). ¹H NMR (CDCl₃, 250 MHz) δ (ppm): 1.28 (s, 12H), 3.81 (s, 2H), 6.65 (d, 4H, 8.9 Hz), 6.90 (d, 4H, 8.9 Hz). GC-MS *m/z*: 135.

2,3-Dimethyl-2-(4-hydroxyphenyl)-3-(4-methoxyphenyl)butane. Iodomethane (5.0 mmol, 0.71 g, 0.31 mL), anhydrous potassium carbonate (ca. 20 mmol, 3 g), 18-crown-6 (0.20 mmol, 50 mg), and the desmethyl starting material (5 mmol, 1.2 g) were combined in reagent-grade acetone (100 mL). The mixture was refluxed overnight under nitrogen, after which TLC analysis (silica; DCM) indicated the presence of dimethoxy (*R_f* = 0.9) and monomethoxy (*R_f* = 0.5) products, as well as remaining dihydroxy starting material (*R_f* = 0.2). The reaction mixture was filtered through a fine sintered glass funnel, and the filtrate was evaporated *in vacuo*. The brown residue was redissolved with water (50 mL) and diethyl ether (200 mL), and the organic fraction was washed with brine (50 mL),

dried with anhydrous MgSO_4 , and evaporated *in vacuo*. Purification of the resulting brown solid by SGCC using a gradient eluant of 25 \rightarrow 50% DCM in hexanes afforded the desired solid in 30% yield. ^1H NMR (CDCl_3 , 250 MHz) δ (ppm): 1.27 (s, 12H), 3.79 (s, 3H), 4.03 (s, 1H), 6.63 (d, 2H, 8.5 Hz), 6.71 (d, 2H, 8.9 Hz), 6.90 (d, 2H, 8.9 Hz), 6.95 (d, 2H, 8.8 Hz). GC-MS m/z : 135 and 149 in approximately equal intensities. Also isolated was 2,3-dimethyl-2,3-di(4-methoxyphenyl)-butane in 20% yield; ^1H NMR (CDCl_3 , 250 MHz) δ (ppm): 1.27 (s, 12H), 3.79 (s, 6H), 6.72 (d, 4H, 8.9 Hz), 6.95 (d, 4H, 8.8 Hz).

6.3.3 Bipyridine-linked substrates

The linking of substrates to halide-functionalized bipyridines typically involved refluxing the two components in acetonitrile for up to several days. However, these relatively vigorous conditions were typically not suitable for the linking of diphenylalkane substrates, which are thermolabile when possessing bulky substituents.¹⁵⁷ In these instances, the room-temperature linkage of an aldehyde-functionalized bipyridine was required. The aldehyde method is actually more convenient than the halide method due to a combined one-pot linkage and subsequent methylation, but this method was not devised until the decomposition became apparent. The structures of substrate-linked ligands are provided in Scheme 3-3 for DMT and Scheme 4-5 for diphenylalkanes.

4-{7-[*N*-Methyl-*N*-tolylamino]heptyl}-4'-methyl-2,2'-bipyridine ($\text{C}_7\text{-NT}$). A mixture of 4-(7-bromoheptyl)-4'-methyl-2,2'-bipyridine (2 mmol, 0.7 g) and *p*-toluidine (5.0 mmol,

0.55 g) in acetonitrile (50 mL) was refluxed for 4 d under nitrogen, after which TLC analysis (alumina, 95:5 hexanes:EtOAc, iron(III) sulfate dip) indicated that all starting bromide had been consumed. The solvent was evaporated *in vacuo*, and the orange residue was redissolved in DCM (5 mL) and loaded onto a silica gel column. The unreacted *p*-toluidine (detected by spotting on silica TLC plates and visualized using vanilla dip) was removed by eluting the column with DCM, after which the column was washed with neat hexanes and the eluant was switched to a gradient of 0→15% EtOAc in hexanes containing 3% TEA. The des-*N*-methyl product was isolated as a waxy yellow solid in 55% yield; ^1H NMR (CDCl_3 , 250 MHz) δ (ppm): 1.2-1.6 (m, 10H), 2.23 (s, 3H), 2.44 (s, 3H), 2.69 (t, 2H, 7.3 Hz), 3.07 (t, 2H, 7.0 Hz), 6.52 (d, 2H, 8.6 Hz), 6.97 (d, 2H, 8.3 Hz), 7.12 (d, 2H, 4.9 Hz), 8.22 (s, 2H), 8.54 (d, 2H, 4.0 Hz). NaBH_3CN (2 mmol, 120 mg), glacial acetic acid (4 mmol, 240 μL), 37% aqueous HCHO (4.0 mmol, 0.33 g, 0.30 mL), and the des-*N*-methyl product (0.20 g, 0.50 mmol) were suspended in acetonitrile (50 mL) and stirred at room temperature under nitrogen. After 24 h, the reaction was evaporated *in vacuo*, and the white residue was dissolved in a mixture of chloroform (50 mL) and saturated aqueous NaHCO_3 (75 mL). The organic fraction was washed with brine (2×50 mL), dried with anhydrous Na_2SO_4 , and evaporated *in vacuo* to afford an orange oil. Purification of the oil on SGCC using an eluant of 3:97 TEA:hexanes afforded the desired product as a thick, yellow oil in 55% yield. ^1H NMR (CDCl_3 , 250 MHz) δ (ppm): 1.3-1.4 (m, 6H), 1.54 (quintet, 2H, 7.4 Hz), 1.69 (quintet, 2H, 7.3 Hz), 2.24 (s, 3H), 2.44 (s, 3H), 2.68 (t, 2H, 7.6 Hz), 2.87 (s, 3H), 3.25 (t, 2H, 7.3 Hz), 6.62 (d, 2H, 8.6

Hz), 7.02 (d, 2H, 8.0 Hz), 7.12 (m, 2H), 8.24 (s, 2H), 8.54 (m, 2H); ^{13}C NMR (CDCl_3 , 62.9 MHz) δ (ppm): 20.20, 21.18, 26.50, 27.10, 29.29, 29.33, 30.36, 35.50, 38.45, 53.12, 112.58, 121.27, 122.03, 123.91, 124.61, 125.14, 129.66, 129.73, 147.44, 148.09, 148.93, 148.97, 152.78, 156.13.

4-{4-[N-Methyl-N-tolylamino]butyl}-4'-methyl-2,2'-bipyridine ($\text{C}_4\text{-NT}$). This compound was prepared according to the preparation of C_7NT , except 4-(4-bromobutyl)-4'-methyl-2,2'-bipyridine was used. However, the following one-pot preparation by means of the aldehydic bipyridine followed by methylation was more convenient. Acetonitrile (50 mL), 4-(3-formylpropyl)-4'-methyl-2,2'-bipyridine (0.50 mmol, 0.12 g), NaBH_3CN (4.0 mmol, 0.24 g), glacial acetic acid (8 mmol, 0.5 mL), and *p*-toluidine (2.0 mmol, 0.22 g) were combined and stirred under nitrogen. After 24 h, the mixture was supplemented with 37% aqueous HCHO (8.0 mmol, 0.65 g, 0.60 mL) and NaBH_3CN (4.0 mmol, 0.24 g) and stirred for an additional 12 h. The solvent was evaporated *in vacuo*, and the residue was dissolved in a mixture of chloroform (75 mL) and saturated aqueous NaHCO_3 (25 mL). The chloroform fraction was dried with anhydrous MgSO_4 and evaporated *in vacuo*. The resulting orange oil was purified by SGCC, whereby *N,N*-dimethyl-*p*-toluidine was eluted with DCM prior to changing the eluant to 97:3 hexanes:TEA, to afford the desired product as a clear, colourless oil in 32% yield. ^1H NMR (CDCl_3 , 250 MHz) δ (ppm): 1.67 (m, 4H), 2.24 (s, 3H), 2.44 (s, 3H), 2.72 (t, 2H, 7.3 Hz), 2.86 (s, 3H), 3.29 (t, 2H, 6.9 Hz), 6.62 (d, 2H, 8.5 Hz), 7.02 (d, 2H, 8.6 Hz), 7.12 (m, 2H), 8.23 (s, 2H), 8.55 (2d, 2H); ^{13}C NMR (CDCl_3 , 62.9 MHz) δ (ppm): 20.20,

21.20, 26.35, 28.05, 35.37, 38.54, 52.89, 112.67, 121.24, 122.03, 123.86, 124.67, 126.82, 129.69, 148.14, 148.94, 149.06, 152.34, 156.04, 126.20.

4-{3-[2-(N-Methyl-N-tolylamino)ethoxy]propyl}-4'-methyl-2,2'-bipyridine (C_3OC_2 -NT).

The relatively unreactive 4'-[3-(2-chloroethoxy)propyl]-4-methyl-2,2'-bipyridine (0.50 mmol, 0.13 g) was first converted to the iodide form by refluxing with flame-dried sodium iodide (5.0 mmol, 0.75 g) in reagent acetone (30 mL) under nitrogen. After 24 h, the cloudy mixture containing precipitated NaCl was evaporated *in vacuo*, and the white residue was dissolved in a mixture of DCM (75 mL) and water (50 mL). The organic fraction was dried with anhydrous Na_2SO_4 and evaporated *in vacuo*, and the resultant brown oil was analyzed by ^{13}C NMR and determined to contain ca. 4:1 iodide:chloride derivatives. The crude iodide was subsequently combined with *p*-toluidine (2.0 mmol, 0.21 g) in acetonitrile (20 mL) and refluxed for 24 h under nitrogen, after which the reaction mixture was evaporated *in vacuo* to afford a brown oil. The oil was purified by SGCC, whereby leftover *p*-toluidine was eluted with neat DCM prior switching the eluant to 92:3:3 hexanes:TEA:EtOAc. The des-*N*-methyl product was isolated as a clear, colourless oil in 63% yield; 1H NMR ($CDCl_3$, 250 MHz) δ (ppm): 1.96 (quintet, 2H, 7.2 Hz), 2.22 (s, 3H), 2.40 (s, 3H), 2.77 (t, 2H, 7.6 Hz), 3.25 (t, 2H, 4.9 Hz), 3.45 (t, 2H, 6.3 Hz), 3.59 (t, 2H, 5.2 Hz), 3.98 (br s, 1H), 6.55 (d, 2H, 8.5 Hz), 6.96 (d, 2H, 8.5 Hz), 7.10 (d, 2H, 4.9 Hz), 8.24 (2s, 2H), 8.53 (2d, 2H); ^{13}C NMR ($CDCl_3$, 62.9 MHz) δ (ppm): 20.42, 21.20, 30.17, 31.93, 44.02, 69.25, 69.83, 113.33, 121.33, 122.01, 124.00, 124.70, 126.70, 129.72, 145.99, 148.12, 148.94, 149.08, 151.93, 155.98, 156.19. $NaBH_3CN$ (1.0

mmol, 60 mg), glacial acetic acid (2.0 mmol, 0.12 mL), 37% aqueous HCHO (2.0 mmol, 0.16 g, 0.15 mL), and the des-*N*-methyl product (0.12 g, 0.32 mmol) were suspended in acetonitrile (25 mL) and stirred under nitrogen pressure at room temperature. After 24 h, the reaction mixture was evaporated *in vacuo*, and the yellow residue was dissolved in a mixture of hexanes (50 mL) and saturated aqueous NaHCO₃ (50 mL). The organic fraction was dried with anhydrous Na₂SO₄ and evaporated *in vacuo* to afford a clear, colourless oil, in 60% yield, that was pure by TLC (silica gel; 9:1 hexanes:TEA) and NMR analyses. ¹H NMR (CDCl₃, 250 MHz) δ (ppm): 1.97 (t, 2H, 7.6 Hz), 2.24 (s, 3H), 2.43 (s, 3H), 2.76 (t, 2H, 7.6 Hz), 2.95 (s, 3H), 3.43 (t, 2H, 6.3 Hz), 3.55 (2t, 6H), 6.65 (d, 2H, 8.6 Hz), 7.02 (d, 2H, 8.6 Hz), 7.10 (2d, 2H), 8.23 (s, 3H), 8.53 (d, 2H, 5.2 Hz); ¹³C NMR (CDCl₃, 62.9 MHz) δ (ppm): 20.23, 21.20, 30.31, 31.93, 39.20, 52.80, 68.32, 70.05, 112.52, 121.33, 122.03, 124.05, 124.67, 125.45, 129.69, 147.25, 148.14, 148.94, 149.03, 152.08, 156.02, 156.18.

4-{7-[*N*-Methyl-*N*-(4-{2,3-dimethyl-3-[4-(*N,N*-dimethylamino)phenyl]butan-2-yl}phenyl)]amino}heptyl-4'-methyl-2,2'-bipyridine (C₇-N-MPB-N). A mixture of 4-(7-bromoheptyl)-4'-methyl-2,2'-bipyridine (1.0 mmol, 0.35 g) and 2,3-dimethyl-2,3-di(4-aminophenyl)butane (3.0 mmol, 0.80 mg) was refluxed in acetonitrile (75 mL) under nitrogen pressure. The reaction mixture was monitored daily by TLC analysis (alumina; 9:1 hexanes:EtOAc; aqueous iron(III) sulfate dip), and after 7 d, the mixture was cooled and evaporated *in vacuo* to afford a brown oil. The oil was purified by SGCC using a gradient eluant of 0→10% EtOAc in hexanes containing 3% TEA; fractions were spotted

onto filter paper and those testing positive with both vanilla and aqueous iron(III) sulfate dips were combined and evaporated *in vacuo* to yield a yellow solid in 42% yield. The des-*N,N,N'*-trimethyl solid was then combined with NaBH₃CN (3.0 mmol, 0.18 g), glacial acetic acid (5.0 mmol, 0.30 g, 0.30 mL), and 37% aqueous HCHO (4 mmol, 0.3 g, 0.3 mL) in acetonitrile (100 mL) and stirred under nitrogen. The reaction mixture was periodically sampled, spotted onto filter paper, and tested by vanilla dip. After 24 h, the white suspension was evaporated *in vacuo*, and the white residue was redissolved in chloroform (150 mL) and saturated aqueous NaHCO₃ (100 mL). The organic fraction was washed with brine (2 × 100 mL), dried with anhydrous MgSO₄, and evaporated *in vacuo* to afford an off-white solid. Purification of the solid by SGCC using a gradient eluant of 0→5% EtOAc in hexanes containing 3% TEA afforded the desired product as a clear, colourless oil in 78% yield. ¹H NMR (CDCl₃, 250 MHz) δ (ppm): 1.27 (s, 12H), 1.38 (m, 6H), 1.58 (quintet, 2H, 6.9 Hz), 1.72 (quintet, 2H, 7.0 Hz), 2.44 (s, 3H), 2.69 (t, 2H, 7.8 Hz), 2.90 (s, 3H), 2.92 (s, 6H), 3.27 (t, 2H, 7.5 Hz), 6.56 (d, 2H, 8.9 Hz), 6.62 (d, 2H, 8.9 Hz), 6.98 (2d, 4H), 7.13 (d, 2H, 4.9 Hz), 8.26 (s, 2H), 8.56 (m, 2H); ¹³C NMR (CDCl₃, 62.9 MHz) δ (ppm): 21.23, 25.34, 26.70, 27.13, 29.38, 30.39, 35.51, 38.23, 40.75, 42.88, 42.96, 52.94, 110.46, 111.09, 122.03, 123.93, 124.63, 129.33, 134.61, 135.58, 147.03, 148.16, 148.27, 152.81, 156.11.

4-{4-[*N*-Methyl-*N*-(4-{2,3-dimethyl-3-[4-(*N,N*-dimethylamino)phenyl]butan-2-yl}phenyl)]amino}butyl-4'-methyl-2,2'-bipyridine (C₄-N-MPB-N). A mixture of 4-(3-formylpropyl)-4'-methyl-2,2'-bipyridine (0.50 mmol, 0.12 g), NaBH₃CN (4.0 mmol, 0.24

g), glacial acetic acid (8 mmol, 0.5 mL), and 2,3-dimethyl-2,3-di(4-aminophenyl)butane (1.0 mmol, 0.27 g) was suspended in acetonitrile (70 mL) and stirred under nitrogen at room temperature. The disappearance of the aldehyde was monitored by TLC analysis (alumina, 50:50 hexanes:DCM, aqueous iron(III) sulfate and vanilla dips). After 24 h, the reaction mixture was supplemented with 37% aqueous HCHO (8.0 mmol, 0.65 g, 0.70 mL) and NaBH₃CN (8.0 mmol, 0.48 g) and stirred for an additional 24 h. The reaction mixture was evaporated *in vacuo*, and saturated aqueous NaHCO₃ (50 mL) and chloroform (100 mL) were added to dissolve the residue. The organic fraction was separated, washed with brine (2 × 25 mL), dried with anhydrous MgSO₄, and evaporated *in vacuo* to afford an orange oil. Purification of the oil by SGCC using an eluant of 97:3 hexanes:TEA afforded the desired product as a clear, colourless oil that formed a white solid upon standing (20 % yield). ¹H NMR (CDCl₃, 250 MHz) δ (ppm): 1.25 (s, 12H), 1.70 (m, 4H), 2.44 (s, 3H), 2.75 (t, 2H, 7.3 Hz), 2.89 (s, 3H), 2.92 (s, 6H), 3.31 (t, 2H, 7.0 Hz), 6.52-6.62 (2d, 4H), 6.94-7.01 (2d, 4H), 7.13 (m, 2H), 8.25 (s, 2H), 8.55 (m, 2H); ¹³C NMR (CDCl₃, 62.9 MHz) δ (ppm): 21.20, 25.37, 26.55, 28.07, 35.41, 38.29, 40.76, 42.91, 42.96, 52.72, 110.58, 111.11, 121.26, 122.03, 123.88, 124.67, 129.31, 129.40, 134.87, 135.57, 146.97, 148.12, 148.31, 148.96, 149.06, 152.36, 156.05, 156.22.

4-[4-(*N*-Methyl-*N*-{4-[(2,3-dimethyl-3-phenyl)butan-2-yl]phenyl})amino]butyl-4'-methyl-2,2'-bipyridine (C₄-N-MPB-H). A solution of 4-(4-bromobutyl)-4'-methyl-2,2'-bipyridine (0.20 mmol, 60 mg) and 2,3-dimethyl-2-(4-aminophenyl)-3-phenylbutane (0.30 mmol, 75 mg) in acetonitrile (30 mL) was refluxed under argon and periodically

monitored by TLC analysis (alumina; hexanes:EtOAc 8:2). After the starting bromide had been consumed (5 d), the orange mixture was evaporated *in vacuo*. The resulting solid was subjected to SGCC; the column was first eluted with neat DCM to remove the remaining unlinked amine, and following a rinse with neat hexanes, the eluant was switched to a gradient of 0→5% EtOAc in hexanes containing 5% TEA. The des-*N*-methyl derivative of the desired product was isolated as a clear, colourless oil in 75% yield. ^1H NMR (CDCl_3 , 250 MHz) δ (ppm): 1.29 (s, 6H), 1.33 (s, 6H), 1.71 (quintet, 2H, 6.7 Hz), 1.84 (quintet, 2H, 7.9 Hz), 2.45 (s, 3H), 2.77 (t, 2H, 7.6 Hz), 3.15 (t, 2H, 6.6 Hz), 3.55 (br s, 1H), 6.47 (d, 2H, 8.5 Hz), 6.90 (d, 2H, 8.5 Hz), 7.17 (m, 6H), 8.31 (s, 2H), 8.59 (2d, 2H). The des-*N*-methyl derivative (0.15 mmol, 70 mg), NaBH_3CN (0.3 mmol, 0.02 g), glacial acetic acid (4.0 mmol, 0.24 mL) and 37% aqueous HCHO (2.0 mmol, 0.16 g, 0.15 mL) were suspended in acetonitrile (40 mL) and stirred for 4 h. The white suspension was evaporated *in vacuo*, and the residue was redissolved in a mixture of saturated aqueous NaHCO_3 (50 mL) and DCM (100 mL). The organic fraction was separated, dried with anhydrous Na_2SO_4 , and evaporated *in vacuo* to afford a yellow oil. Purification of the oil by SGCC using an eluant of 95:5 hexanes:TEA afforded the desired product as a clear, colourless oil in 80% yield. ^1H NMR (CDCl_3 , 250 MHz) δ (ppm): 1.28 (s, 6H), 1.32 (s, 6H), 1.71 (m, 4H), 2.46 (s, 3H), 2.77 (t, 2H, 7.0 Hz), 2.91 (s, 3H), 3.34 (t, 2H, 6.7 Hz), 6.55 (d, 2H, 8.9 Hz), 6.95 (d, 2H, 8.6 Hz), 7.18 (m, 6H), 8.29 (s, 2H), 8.58 (2d, 2H); ^{13}C NMR (CDCl_3 , 62.9 MHz) δ (ppm): 22.10, 25.17, 26.40, 27.95, 35.28, 38.16, 42.53, 43.80, 52.55, 110.42, 121.15, 121.92, 123.78, 124.58, 125.18,

126.43, 128.60, 129.23, 134.21, 146.94, 147.18, 148.03, 148.85, 148.97, 152.23, 155.92, 156.11.

4-[4-{2,3-Dimethyl-3-[4-(*N,N*-dimethylamino)phenyl]butan-2-yl}phenoxybutyl]-4'-methyl-2,2'-bipyridine (C₄-O-MPB-N). A mixture of 4-(4-bromobutyl)-4'-methyl-2,2'-bipyridine (0.25 mmol, 75 mg), potassium carbonate (2.5 mmol, 0.35 g), 18-crown-6 (0.05 mmol, 0.01 g), and 2,3-dimethyl-2-(4-hydroxyphenyl)-3-(4-nitrophenyl)butane (0.33 mmol, 0.10 g) was refluxed in acetone (25 mL) under nitrogen. After 8 h, TLC analysis (silica; hexanes:EtOAc:TEA 8:1:1) indicated that the starting bipyridine had disappeared. The reaction mixture was filtered through a fine sintered glass funnel, and the filtrate was evaporated *in vacuo* to afford a yellow oil. The oil was subjected to SGCC; the column was first eluted with neat DCM to remove the all non-bipyridine compounds, and following a rinse with neat hexanes, the eluant was switched to a gradient of 0→30% EtOAc in hexanes containing 5% TEA to elute the corresponding nitro product as a clear, colourless oil in 60% yield. ¹H NMR (CDCl₃, 250 MHz) δ (ppm): 1.29 (s, 6H), 1.34 (s, 6H), 1.88 (m, 4H), 2.43 (s, 3H), 2.78 (t, 2H, 7.0 Hz), 3.96 (t, 2H, 5.5 Hz), 6.70 (d, 2H, 8.5 Hz), 6.88 (d, 2H, 8.9 Hz), 7.15 (m, 4H), 8.00 (d, 2H, 8.9 Hz), 8.25 (d, 2H, 7.3 Hz), 8.56 (2d, 2H). A mixture of the nitro derivative (0.15 mmol, 75 mg), 10% Pd/C (50 mg), and excess hydrazine hydrate (1.0 mmol, 50 μL) was refluxed in methanol (50 mL) under argon. After 45 min, TLC analysis (alumina; hexanes:EtOAc 8:2) revealed only one spot that tested positive in separate iron(III) sulfate and vanilla dips. The mixture was filtered through a fine sintered glass funnel to remove the catalyst,

and the filtrate was evaporated *in vacuo*. Purification of the oily residue by SGCC using an eluant of 0→20% EtOAc in hexanes containing 5% TEA afforded the des-*N,N*-dimethyl product as a clear, colourless oil in 80% yield that solidified upon standing. ¹H NMR (CDCl₃, 250 MHz) δ (ppm): 1.26 (s, 6H), 1.27 (s, 6H), 1.88 (m, 4H), 2.45 (s, 3H), 2.79 (t, 2H, 7.4 Hz), 3.50 (br s, 2H), 3.98 (t, 2H, 5.8 Hz), 6.53 (d, 2H, 8.5 Hz), 6.72 (d, 2H, 8.6 Hz), 6.85 (d, 2H, 8.6 Hz), 6.98 (d, 2H, 8.6 Hz), 7.16 (m, 2H), 8.27 (d, 2H, 6.1 Hz), 8.58 (2d, 2H). NaBH₃CN (0.40 mmol, 25 mg), glacial acetic acid (4.0 mmol, 0.25 mL), 37% aqueous HCHO (2.0 mmol, 0.16 g, 0.15 mL), and the des-*N,N*-dimethyl product (0.12 mmol, 60 mg) were combined in acetonitrile (50 mL) and stirred overnight under argon. The white suspension was evaporated *in vacuo*, and saturated aqueous NaHCO₃ (50 mL) and DCM (75 mL) were added to dissolve the residue. The organic fraction was washed with brine (50 mL), dried with anhydrous Na₂SO₄, and evaporated *in vacuo*. The resultant oil was purified by SGCC using an eluant of 90:5:5 hexanes:TEA:EtOAc to afford the final product as a thick and clear, colourless oil in 65% yield. ¹H NMR (CDCl₃, 250 MHz) δ (ppm): 1.27 (s, 6H), 1.28 (s, 6H), 1.89 (m, 4H), 2.47 (s, 3H), 2.83 (t, 2H, 7.7 Hz), 2.93 (s, 6H), 3.99 (t, 2H, 5.5 Hz), 6.61 (d, 2H, 9.1 Hz), 6.73 (d, 2H, 8.9 Hz), 6.98 (2d, 4H), 7.16 (m, 2H), 8.22 (d, 2H, 6.1 Hz), 8.58 (2d, 2H); ¹³C NMR (CDCl₃, 62.9 MHz) δ (ppm): 21.31, 25.34, 25.47, 27.03, 29.05, 35.25, 40.84, 42.87, 43.33, 67.44, 111.25, 112.44, 121.60, 122.36, 124.12, 124.86, 129.36, 129.74, 135.31, 139.46, 148.44, 148.50, 148.98, 149.11, 152.63, 156.01, 156.17, 156.70.

4-{4-[N-Methyl-N-(4-{2-[4-(N,N-dimethylamino)phenyl]ethyl}phenyl)]amino}-butyl-4'-methyl-2,2'-bipyridine (C₄-N-BZ-N). 4,4'-Dinitrobibenzyl (2.0 mmol, 0.54 g, recrystallized in EtOAc) was combined with 10% Pd/C (250 mg) and hydrazine hydrate (15 mmol, 0.75 g, 0.70 mL) and refluxed in methanol under argon (200 mL). After 1 h, the black suspension was filtered through a fine sintered-glass funnel, and the methanol was removed from the filtrate *in vacuo*. The white residue was redissolved in DCM (250 mL) and 250 mM sodium phosphate buffer at pH 6.5 (100 mL), and the organic fraction was dried with anhydrous Na₂SO₄ and evaporated *in vacuo* to afford 4,4'-diaminobibenzyl in 95% yield as a white powder that was pure by TLC analysis (silica; 8:1:1 hexanes:TEA:EtOAc; vanilla dip). The 4,4'-diaminobibenzyl (0.40 mmol, 85 mg) was combined with 4-(4-bromobutyl)-4'-methyl-2,2'-bipyridine (0.20 mmol, 60 mg) and was refluxed under argon in acetonitrile (50 mL). After 12 h, during which the mixture turned orange, TLC analysis (alumina; 8:2 hexanes:EtOAc; aqueous iron(III) sulfate and vanilla dips) indicated that all of the starting bipyridine had been consumed. The reaction mixture was evaporated *in vacuo*, and the yellow oil was purified by SGCC using a gradient eluent of 0→50% DCM in hexanes containing 5% TEA. Fractions were analyzed by TLC (alumina; 8:2 hexanes:EtOAc), and those that were reasonably pure (one major UV-active spot that reacted to both iron(III) sulfate and vanilla dips) were pooled and evaporated *in vacuo* to afford a clear, colourless oil. The oil was redissolved in acetonitrile (75 mL) containing with NaBH₃CN (1.0 mmol, 60 mg), glacial acetic acid (2.0 mmol, 125 µL), and 37% aqueous HCHO (2.0 mmol, 160 mg, 150 µL), and stirred under argon. After 45 min, a sample of the reaction mixture was spotted on a silica TLC

plate, and vanilla dip testing indicated that the methylation was complete. The acetonitrile was removed by evaporation *in vacuo*, and the white residue was redissolved with saturated aqueous NaHCO₃ (75 mL) and chloroform (75 mL). The organic fraction was dried with MgSO₄ and evaporated *in vacuo* to afford a light yellow oil. Purification of the oil by SGCC using an eluant of 95:5 hexanes:TEA afforded the product as a clear, colourless oil in 30% yield. ¹H NMR (CDCl₃, 250 MHz) δ (ppm): 1.71 (m, 4H), 2.46 (s, 3H), 2.75 (t, 2H, 7.6 Hz), 2.80 (s, 4H), 2.90 (s, 3H), 2.94 (s, 6H), 3.33 (t, 2H, 7.0 Hz), 6.65 (d, 2H, 8.9 Hz), 6.73 (d, 2H, 8.5 Hz), 7.09 (m, 6H), 8.26 (s, 2H), 8.57 (m, 2H); ¹³C NMR (CDCl₃, 125.8 MHz) δ (ppm): 21.19, 26.48, 28.04, 35.39, 37.29, 37.32, 38.49, 40.97, 52.87, 112.54, 113.06, 121.26, 122.04, 123.86, 124.65, 128.99, 129.09, 130.00, 130.67, 147.69, 148.12, 148.96, 149.07, 152.33, 156.08, 156.25.

rac-[erythro-(4-{4-[*N*-Methyl-*N*-(4-{3,4-dimethyl-4-[4-(*N,N*-dimethylamino)-phenyl]hexan-3-yl}phenyl)]amino}butyl-4'-methyl-2,2'-bipyridine)] (C₄-N-MPH-N). A mixture of 4-(3-formylpropyl)-4'-methyl-2,2'-bipyridine (0.25 mmol, 60 mg), NaBH₃CN (2.0 mmol, 0.12 g), glacial acetic acid (4.0 mmol, 0.24 mL), and *meso*-3,4-dimethyl-3,4-di(4-aminophenyl)hexane (0.50 mmol, 0.15 g) was suspended in acetonitrile (50 mL) and stirred under argon. The disappearance of the aldehyde was monitored by TLC analysis (alumina, 50:50 hexanes:DCM, iron(III) sulfate and vanilla dips). After 90 min, the reaction mixture was supplemented with 37% aqueous HCHO (4.0 mmol, 0.32 g, 0.30 mL) and NaBH₃CN (4.0 mmol, 0.24 g), and after stirring for an additional 2 h, TLC analysis using vanilla dip indicated that all free amino groups had been alkylated. The

reaction mixture was evaporated *in vacuo*, and the white residue was redissolved with saturated aqueous NaHCO₃ (75 mL) and DCM (75 mL). The organic fraction was washed with brine (75 mL), dried over MgSO₄, and evaporated *in vacuo*. The oily, white residue was purified by SGCC using an eluant of 18:1:1 hexanes:DCM:TEA to afford the desired product as a clear, colourless oil in 30% yield. ¹H NMR (CDCl₃, 250 MHz) δ (ppm): 0.58 (t, 6H, 7.2 Hz), 1.19 (s, 6H), 1.40 (m, 2H), 1.73 (m, 4H), 2.18 (m, 2H), 2.46 (s, 3H), 2.77 (t, 2H, 7.3 Hz), 2.90 (s, 3H), 2.94 (s, 6H), 3.32 (t, 2H, 6.9 Hz), 6.55 (d, 2H, 9.2 Hz), 6.61 (d, 2H, 8.6 Hz), 6.88 (2d, 4H), 7.15 (m, 2H), 8.27 (br s, 2H), 8.57 (m, 2H); ¹³C NMR (CDCl₃, 62.9 MHz) δ (ppm): 9.40, 20.94, 21.34, 26.79, 27.83, 28.21, 35.55, 38.36, 40.82, 47.62, 47.67, 52.90, 110.65, 111.06, 121.41, 122.18, 124.01, 124.80, 130.67, 130.75, 131.74, 132.38, 146.97, 148.22, 148.27, 149.10, 149.22, 152.53, 156.22, 156.38. Also isolated was *meso*-3,4-dimethyl-3,4-di[4-(*N,N*-dimethylamino)phenyl]-hexane (25 mg) as a clear, colourless liquid that solidified upon standing; ¹H NMR (CDCl₃, 250 MHz) δ (ppm): 0.58 (t, 6H, 7.3 Hz), 1.20 (s, 6H), 1.40 (m, 2H), 2.19 (m, 2H), 2.94 (s, 12H), 6.61 (d, 4H, 8.9 Hz), 6.90 (d, 4H, 8.6 Hz); ¹³C NMR (CDCl₃, 62.9 MHz) δ (ppm): 9.12, 20.68, 27.55, 40.55, 47.38, 110.78, 130.41, 132.04, 147.93.

rac-[erythro-(4-{4-[*N*-Methyl-*N*-(4-{4,5-dimethyl-5-[4-(*N,N*-dimethylamino)-phenyl]octan-4-yl}phenyl)]amino}butyl-4'-methyl-2,2'-bipyridine)] (C₄-N-MPO-N). A mixture of 4-(4'-methyl-2,2'-bipyridyl)-butanal (0.25 mmol, 60 mg), NaBH₃CN (0.75 mmol, 45 mg), glacial acetic acid (2.0 mmol, 0.12 mL), and *meso*-4,5-dimethyl-4,5-di(4-

aminophenyl)octane (0.30 mmol, 97 mg) was suspended in acetonitrile (35 mL) and stirred under argon. After 45 min, the reaction mixture became cloudy, and TLC analysis (alumina, 50:50 hexanes:DCM, iron(III) sulfate and vanilla dips as indicators) indicated that the aldehyde had been consumed. The reaction mixture was supplemented with 37% aqueous HCHO (2.0 mmol, 0.16 g, 0.15 mL) and NaBH₃CN (2.0 mmol, 0.12 g), stirred for an additional 30 min, and evaporated *in vacuo*. The pale solid was redissolved in saturated aqueous NaHCO₃ (75 mL) and DCM (75 mL), and the organic fraction was washed with brine (75 mL), dried over MgSO₄, and evaporated *in vacuo*. The yellow oil was purified by SGCC using an eluant of 0→5% DCM in hexanes containing 5% TEA to afford the desired product as a clear, colourless oil in 55% yield. ¹H NMR (CDCl₃, 500 MHz) δ (ppm): 0.78 (t, 6H, 6.9 Hz), 0.86 (m, 2H), 1.02 (m, 2H), 1.19 (s, 6H), 1.37 (m, 2H), 1.66 (quintet, 2H, 7.3 Hz), 1.75 (quintet, 2H, 7.7 Hz), 1.99 (m, 2H), 2.44 (s, 3H), 2.74 (t, 2H, 7.7 Hz), 2.88 (s, 3H), 2.91 (s, 6H), 3.30 (t, 2H, 7.1 Hz), 6.51 (d, 2H, 8.7 Hz), 6.57 (d, 2H, 8.8 Hz), 6.83 (2d, 4H), 7.12 (m, 2H), 8.24 (d, 2H, 7.4 Hz), 8.54 (2d, 2H); ¹³C NMR (CDCl₃, 125.8 MHz) δ (ppm): 15.14, 18.00, 21.18, 21.45, 26.69, 28.08, 35.42, 37.95, 38.19, 40.66, 47.24, 47.29, 52.78, 110.46, 110.86, 121.26, 122.03, 123.84, 124.65, 130.34, 130.40, 132.19, 132.80, 146.81, 148.01, 148.12, 148.96, 149.07, 152.37, 156.09, 156.24. Also isolated was *meso*-4,5-dimethyl-4,5-di[4-(*N,N*-dimethylamino)phenyl]-octane (18 mg) as a waxy, light yellow solid; ¹H NMR (CDCl₃, 250 MHz) δ (ppm): 0.85 (m, 8H), 1.03 (m, 2H), 1.22 (s, 6H), 1.39 (m, 2H), 2.02 (m, 2H), 2.94 (s, 12H), 6.60 (d,

4H, 9.2 Hz), 6.85 (d, 4H, 8.2 Hz); ^{13}C NMR (CDCl_3 , 62.9 MHz) δ (ppm): 15.03, 17.90, 21.35, 37.80, 40.57, 47.15, 110.73, 130.22, 132.60, 147.86.

4-{4-[2,3-Dimethyl-3-(4-methoxyphenyl)butan-2-yl]phenoxyheptyl}-4'-methyl-2,2'-bipyridine ($\text{C}_7\text{-O-MPB-O}$). A suspension of 2,3-dimethyl-2-(4-hydroxyphenyl)-3-(4-methoxyphenyl)butane (1.0 mmol, 0.29 g), anhydrous potassium carbonate (5.0 mmol, 0.70 g), 18-crown-6 (0.10 mmol, 26 mg), and 4-(7-bromoheptyl)-4'-methyl-2,2'-bipyridine (1.0 mmol, 0.35 g) in acetone (50 mL) was refluxed under nitrogen. After 16 h, TLC analysis (alumina; 9:1 hexanes:EtOAc; iron(III) sulfate dip) indicated that the starting bromide had been consumed. The reaction was cooled and evaporated *in vacuo*, and the white residue was extracted with DCM (3×50 mL) by means of a fine sintered glass funnel. The organic fractions were combined, concentrated *in vacuo* to ca. 5 mL, and purified by SGCC using an eluant of 90:5:5 hexanes:TEA:EtOAc to afford the desired product as a clear, light yellow oil that solidified upon standing (85% yield). ^1H NMR (CDCl_3 , 250 MHz) δ (ppm): 1.26 (s, 12H), 1.42 (m, 6H), 1.75 (m, 4H), 2.44 (s, 3H), 2.70 (t, 2H, 7.93 Hz), 3.78 (s, 3H), 3.92 (t, 2H, 6.40 Hz), 6.70 (m, 4H), 6.94 (m, 4H), 7.13 (d, 2H, 4.9 Hz), 8.23 (s, 2H), 8.55 (2d, 2H). The correct structure of the product was suggested by two-dimensional ^1H -NMR COSY analysis.

6.3.4 Substrate-linked tris(bipyridyl)ruthenium complexes

The preparation of the substrate-linked complexes was similar to that of the unlinked heteroleptic complexes (section 6.2.3). $\text{Ru(dmb)}_2\text{Cl}_2$ or $\text{Ru(bpy)}_2\text{Cl}_2$

(0.010–0.50 mmol) was combined with 1.2 equivalents of the substrate-linked bipyridine in neat methanol (3–50 mL), and the purple mixture was refluxed under argon until it became orange (2–3 h). No acetic acid was used due to the presence of basic amino-substituted substrates. The methanol was removed *in vacuo*, and the dark orange residue was purified either by precipitation (0.1–0.5 mmol) or size-exclusion chromatography (< 0.1 mmol) as per the unlinked complexes. Typical isolated yields of the orange solids were 60–95%. All complexes were isolated as dichloride salts. The structures of the complexes are provided in Scheme 3-3 for DMT and Scheme 4-5 for diphenylalkanes.

Ru(dmb)₂(C₇-NT). Prepared from *Ru(dmb)₂Cl₂* and C₇NT. ¹H NMR (CD₃CN, 250 MHz) δ (ppm): 1.5–1.7 (m, 10H), 2.16 (s, 3H), 2.52 (s, 15H), 2.82 (s + t, 5H), 3.25 (t, 2H, 7.0 Hz), 6.61 (d, 2H, 8.5 Hz), 6.94 (d, 2H, 8.5 Hz), 7.27 (m, 6H), 7.60 (m, 6H), 8.54 (m, 6H). ESI-MS *m/z*: 428.8 (100%) and 856.3 (3%).

Ru(bpy)₂(C₇-NT). Prepared from *Ru(bpy)₂Cl₂* and C₇NT. ¹H NMR (CD₃CN, 250 MHz) δ (ppm): 1.5–1.6 (m, 6H), 1.6–1.7 (m, 4H), 2.17 (s, 3H), 2.56 (s, 3H), 2.80 (s + t, 5H), 3.25 (t, 2H, 7.0 Hz), 6.62 (d, 2H, 8.7 Hz), 6.94 (d, 2H, 8.7 Hz), 7.18 (m, 2H), 7.35 (m, 4H), 7.50 (2d, 2H), 7.71 (m, 4H), 8.02 (t, 4H, 7.9 Hz), 8.42 (2s, 2H), 8.57 (d, 4H, 8.2 Hz). ESI-MS *m/z*: 400.8 (100%) and 800.2 (5%).

Ru(dmb)₂(C₄-NT). Prepared from *Ru(dmb)₂Cl₂* and C₄NT. ¹H NMR (CD₃CN, 250 MHz) δ (ppm): 1.57 (quintet, 2H, 6.7 Hz), 1.70 (quintet, 2H, 6.7 Hz), 2.15 (s, 3H), 2.52 (s,

15H), 2.81 (s + t, 5H), 3.29 (t, 2H, 7.3 Hz), 6.61 (d, 2H, 8.6 Hz), 6.95 (d, 2H, 8.5 Hz), 7.20 (m, 6H), 7.50 (m, 6H), 8.46 (m, 6H). ESI-MS m/z : 407.7 (100%) and 815.1 (6%).

Ru(bpy)₂(C₄-NT). Prepared from Ru(bpy)₂Cl₂ and C₄NT. ¹H NMR (CD₃CN, 250 MHz) δ (ppm): 1.57 (quintet, 2H, 7.0 Hz), 1.70 (quintet, 2H, 7.9 Hz), 2.15 (s, 3H), 2.52 (s, 3H), 2.81 (s + t, 5H), 3.29 (t, 2H, 7.3 Hz), 6.61 (d, 2H, 8.6 Hz), 6.95 (d, 2H, 8.5 Hz), 7.20 (m, 2H), 7.37 (m, 4H), 7.52 (2d, 2H), 7.70 (m, 4H), 8.04 (t, 4H, 7.9 Hz), 8.44 (2s, 2H), 8.55 (d, 4H, 8.2 Hz). ESI-MS m/z : 379.7 (100%) and 758.1 (10%).

Ru(dmb)₂(C₃OC₂-NT). Prepared from Ru(dmb)₂Cl₂ and C₃OC₂NT. ¹H NMR (CD₃OD, 250 MHz) δ (ppm): 1.95 (quintet, 2H, 6.5 Hz), 2.14 (s, 3H), 2.57 (s, 15H), 2.83 (s, 3H), 2.90 (t, 2H, 7.3 Hz), 3.33-3.53 (3t, 6H), 6.57 (d, 2H, 8.6 Hz), 6.89 (d, 2H, 8.6 Hz), 7.27 (m, 6H), 7.59 (m, 6H), 8.55 (m, 6H). ESI-MS m/z : 422.8 (100%) and 879.9 (18%).

Ru(bpy)₂(C₃OC₂-NT). Prepared from Ru(bpy)₂Cl₂ and C₃OC₂NT. ¹H NMR (CD₃OD, 250 MHz) δ (ppm): 1.96 (quintet, 2H, 6.5 Hz), 2.13 (s, 3H), 2.56 (s, 3H), 2.85 (s, 3H), 2.90 (t, 2H, 7.3 Hz), 3.34-3.54 (3t, 6H), 6.57 (d, 2H, 8.6 Hz), 6.90 (d, 2H, 8.6 Hz), 7.30 (d, 2H, 5.2 Hz), 7.48 (m, 4H), 7.58 (d, 2H, 5.8 Hz), 7.80 (m, 4H), 8.09 (t, 4H, 7.8 Hz), 8.58 (s, 2H), 8.69 (d, 4H, 8.3 Hz). ESI-MS m/z : 394.7 (100%) and 823.9 (12%).

Ru(bpy)₂(C₇-N-MPB-N). Prepared from Ru(bpy)₂Cl₂ and C₇N-MPB-N. ¹H NMR (CD₃CN, 400 MHz) δ (ppm): 1.18 (2s, 12H), 1.30-1.37 (m, 6H), 1.51 (quintet, 2H, 7.1

Hz), 1.69 (quintet, 2H, 7.6 Hz), 2.53 (s, 3H), 2.76 (t, 2H, 7.7 Hz), 2.84 (s, 3H), 2.85 (s, 6H), 3.26 (t, 2H, 7.5 Hz), 6.52 (d, 2H, 9.1 Hz), 6.57 (d, 2H, 9.1 Hz), 6.93 (d, 2H, 8.9 Hz), 6.96 (d, 2H, 9.0 Hz), 7.22 (m, 2H), 7.38 (t, 4H, 7.2 Hz), 7.52 (2d, 2H), 7.72 (m, 4H), 8.03 (t, 4H, 7.2 Hz), 8.50 (s, 1H), 8.56 (s, 1H), 8.64 (2d, 4H). ESI-MS m/z : 495.1 (100%).

Ru(bpy)₂(C₄-N-MPB-N). Prepared from Ru(bpy)₂Cl₂ and C₄N-MPB-N. ¹H NMR (CD₃OD, 250 MHz) δ (ppm): 1.20 (2s, 12H), 1.65 (quintet, 2H, 7.5 Hz), 1.73 (quintet, 2H, 8.3 Hz), 2.59 (s, 3H), 2.84 (s, 3H), 2.86 (s, 6H), 2.90 (t, 2H, 7.3 Hz), 3.31 (t under solvent signal, 2H), 6.60 (d, 2H, 9.0 Hz), 6.69 (d, 2H, 8.9 Hz), 6.94 (2d, 4H), 7.30 (2d, 2H), 7.44 (m, 4H), 7.60 (m, 2H), 7.79 (m, 4H), 8.09 (m, 4H), 8.57 (s, 1H), 8.61 (s, 1H), 8.67 (2d, 4H). ESI-MS m/z : 474.2 (100%).

Ru(bpy)₂(C₄-N-MPB-H). Prepared from Ru(bpy)₂Cl₂ and C₄N-MPB-H. ¹H NMR (CD₃OD, 250 MHz) δ (ppm): 1.20-1.24 (2s, 12 H), 1.73 (m, 4H), 2.60 (s, 3H), 2.87 (s, 3H), 2.92 (t, 2H, 7.1 Hz), 3.38 (t, 2H, 7.3 Hz), 6.57 (d, 2H, 8.8 Hz), 6.87 (d, 2H, 9.0 Hz), 7.03-7.10 (m, 5H), 7.29-7.51 (m, 6H), 7.62 (2d, 2H), 7.80 (m, 4H), 8.12 (m, 4H), 8.62 (s, 1H), 8.65 (s, 1H), 8.70 (2d, 4H). ESI-MS m/z : 452.6 (100%), 904.2 (29%), and 939.9 (10%).

Ru(bpy)₂(C₄-O-MPB-N). Prepared from Ru(bpy)₂Cl₂ and C₄O-MPB-N. ¹H NMR (CD₃OD, 250 MHz) δ (ppm): 1.23 (s, 6H), 1.25 (s, 6H), 1.90 (m, 4H), 2.60 (s, 3H), 2.88

(s, 3H), 2.96 (t, 2H, 7.3 Hz), 4.02 (t, 2H, 5.6 Hz), 6.62 (d, 2H, 8.8 Hz), 6.71 (d, 2H, 8.8 Hz), 6.93 (d, 2H, 9.0 Hz), 6.98 (d, 2H, 8.8 Hz), 7.34 (d, 1H, 5.9 Hz), 7.39 (d, 1H, 5.9 Hz), 7.49 (t, 4H, 6.6 Hz), 7.61 (d, 1H, 5.9 Hz), 7.66 (d, 1H, 5.8 Hz), 7.84 (m, 4H), 8.13 (t, 4H, 7.9 Hz), 8.64 (s, 2H), 8.71 (d, 4H, 8.3 Hz). ESI-MS m/z : 467.6 (100%).

Ru(bpy)₂(C₄-N-BZ-N). Prepared from Ru(bpy)₂Cl₂ and C₄N-BZ-N. ¹H NMR (CD₃OD, 250 MHz) δ (ppm): 1.62 (quintet, 2H, 7.6 Hz), 1.76 (quintet, 2H, 8.5 Hz), 2.60 (s, 3H), 2.65 (s, 4H), 2.85 (s, 3H), 2.87 (s, 6H), 2.91 (t, 2H, 7.3 Hz), 3.32 (t under solvent signal, 2H), 6.64 (d, 2H, 8.8 Hz), 6.71 (d, 2H, 8.8 Hz), 6.94 (2d, 4H), 7.32 (2d, 2H), 7.46 (m, 4H), 7.61 (m, 2H), 7.81 (m, 4H), 8.11 (m, 4H), 8.59 (s, 1H), 8.61 (s, 1H), 8.69 (2d, 4H). ESI-MS m/z : 446.3 (100%).

Ru(bpy)₂(C₄-N-MPH-N). Prepared from Ru(bpy)₂Cl₂ and C₄N-MPH-N. ¹H NMR (CD₃OD, 250 MHz) δ (ppm): 0.50 (t, 6H, 7.1 Hz), 1.15 (s, 6H), 1.42 (m, 2H), 1.75 (m, 4H), 2.17 (m, 2H), 2.60 (s, 3H), 2.86 (s, 9H), 2.91 (t, 2H, 7.4 Hz), 3.32 (t under solvent signal, 2H), 6.57 (d, 4H, 8.1 Hz), 6.76 (2d, 4H), 7.30-7.50 (m, 6H), 7.61 (m, 2H), 7.80 (m, 4H), 8.12 (m, 4H), 8.62 (2s, 2H), 8.70 (d, 4H, 8.1 Hz). ESI-MS m/z : 488.1 (100%).

Ru(bpy)₂(C₄-N-MPO-N). Prepared from Ru(bpy)₂Cl₂ and C₄N-MPO-N. ¹H NMR (CD₃CN, 250 MHz) δ (ppm): 0.74 (m, 8H), 0.94 (m, 2H), 1.13 (2s, 6H), 1.32 (m, 2H), 1.55-1.76 (m, 4H), 2.02 (m, 2H), 2.81 (s, 3H), 2.85 (s + t, 8H), 3.30 (t, 2H, 7.6 Hz), 6.55

(2d, 4H), 6.80 (2d, 4H), 7.22 (m, 2H), 7.37 (t, 4H, 6.5 Hz), 7.52 (m, 2H), 7.70 (d, 4H, 5.6 Hz), 8.04 (t, 4H, 7.8 Hz), 8.58 (s, 2H), 8.65 (d, 4H, 8.6 Hz). ESI-MS m/z : 502.1 (100%), 1003.3 (22%).

Ru(bpy)₂(C₇-O-MPB-O). Prepared from *Ru(bpy)₂Cl₂* and C₇O-MPB-O. ¹H NMR (CD₃OD, 250 MHz) δ (ppm): 1.26 (s, 12H), 1.46 (m, 6H), 1.76 (m, 4H), 2.59 (s, 3H), 2.88 (t, 2H, 7.7 Hz), 3.76 (s, 3H), 3.94 (t, 2H, 6.3 Hz), 6.70 (2d, 4H), 6.96 (2d, 4H), 7.35 (t, 2H, 5.7 Hz), 7.49 (t, 4H, 6.4 Hz), 7.63 (m, 2H), 7.83 (m, 4H), 8.13 (m, 4H), 8.62 (s, 1H), 8.64 (s, 1H), 8.72 (d, 4H, 8.3 Hz). ESI-MS m/z : 482.1 (100%).

6.4 Synthesis of other compounds

1-Isopropyl-4-methoxybenzene (4-methoxycumene) was prepared according to published protocols with modifications.¹⁸⁸ 4-Isopropylphenol (0.11 mol, 15 g) was dissolved in 3 M NaOH (50 mL), and the solution was cooled to room temperature. With vigorous stirring, dimethyl sulfate (0.11 mol, 14 g, 10 mL,) was added dropwise over 30 min. The cloudy reaction mixture was then heated to 70-80 °C for one hour to complete the reaction, after which it was supplemented with conc. ammonium hydroxide (5 mL) and stirred for an additional hour to destroy any remaining dimethyl sulfate. The brown reaction mixture was extracted with diethyl ether (3 \times 75 mL), and the organic fractions were pooled, washed with 5% NaOH (2 \times 50 mL) to remove excess starting material followed by brine (2 \times 50 mL), and dried with anhydrous MgSO₄. The ethereal solution was evaporated *in vacuo* to afford a yellow oil, which upon simple distillation afforded

the product as a clear, colourless liquid (bp 206-208 °C; lit.¹⁹¹ 78-79 °C at 9 mm) in 75% yield. ¹H NMR (CDCl₃, 250 MHz) δ (ppm): 1.22 (d, 6H, 7.0 Hz), 2.86 (heptet, 1H, 7.1 Hz), 3.78 (s, 3H), 6.84 (d, 2H, 8.9 Hz), 7.14 (d, 2H, 8.6 Hz). GC-MS *m/z*: 150 (50), 135 (100), 91 (43).

6.5 Laser-flash photolysis

Stock solutions of substrate-linked ruthenium complexes were prepared in high-purity water (Nanopure or EMD Omnisolv), distilled methanol, or acetonitrile (EMD Omnisolv) and stored at -15 °C under argon. When required for use, small portions of the thawed solutions were removed and diluted to the concentrations required, and the remaining stock solutions were purged with argon and returned to cold storage. This procedure most likely minimized their decomposition. No noticeable decomposition of Ru(bpy)₂(C₇N-MPB-N) was observed by ESI-MS after six months of storage. Stock solutions of unlinked ruthenium complexes were prepared in water and stored at -15 °C or at room temperature and were not purged with argon.

6.5.1 Nanosecond laser-flash photolysis

The nanosecond laser-flash photolysis setup for the generation and detection of transients by absorption spectroscopy is of conventional design¹⁹² and is schematically represented in Figure 6-1. The third and second harmonics of a Continuum Nd:YAG NY-61 Q-switched laser (< 8 ns pulse width) at respective wavelengths of 355 nm (≤ 35 mJ/pulse) or 532 nm (≤ 80 mJ/pulse) provides the pulsed light required for excitation.

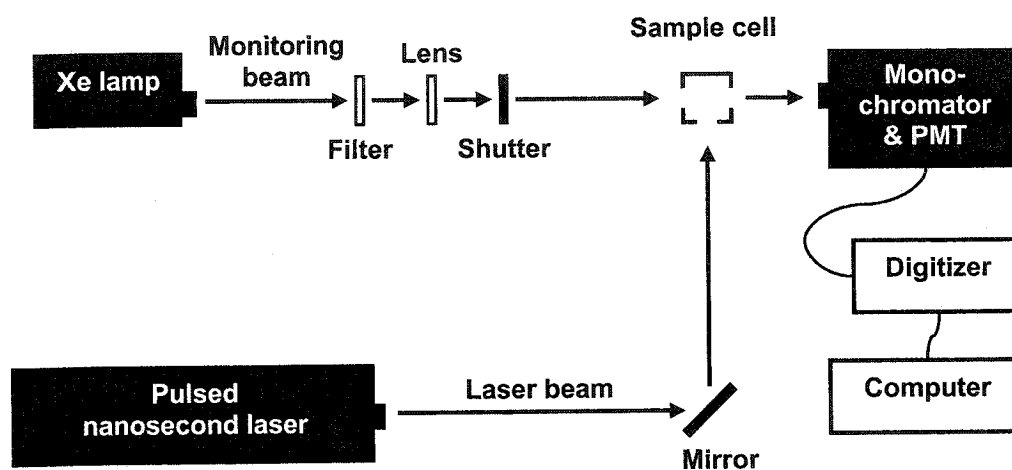


Figure 6-1. Transmission nanosecond laser-flash photolysis schematic for the acquisition of kinetic traces and transient absorption spectra.

The transients produced following excitation are detected by a time-resolved UV-visible spectrophotometer setup arranged perpendicular to the laser excitation beam. A pulsed xenon arc lamp (150 W) provides a monitoring beam that is passed through a wavelength-range filter. The filtered monitoring beam is then focussed on the sample and controlled by means of an electronic shutter. After passing through the sample, the beam is directed into a monochromator-coupled photomultiplier tube. The analog voltage output, which is related to the monitoring beam intensity, is captured as a function of time by a Tektronix 620A digitizing oscilloscope operating at 20 MHz bandwidth (time resolution < 10 ns); changes in the monitoring beam intensity caused by the absorption of light by the generated transients are therefore collected in terms of voltage change versus time. In-house software written in Labview (National Instruments) provides complete

computer-control of the laser-flash photolysis setup, including the selection of monitoring wavelengths and detection timescales, as well as the acquisition of kinetic traces and absorption spectra.

6.5.1.1 Sample preparation

Samples (1-3 mL) for nanosecond laser-flash photolysis were prepared in 7×7 mm² cells made in-house from synthetic quartz tubing (Suprasil). After adjusting the optical density to 0.2–0.4 at the excitation wavelength *via* the addition of sample stock solution or the appropriate diluant (solvent, buffer, or sacrificial electron acceptor solution), samples were capped with rubber septa and gently purged with high-purity nitrogen by means of a long, immersed needle and a short, outlet needle for 15 min in the dark. For Ru(bpy)₃, the extinction coefficient⁷⁴ at 452 nm is 14,600 M⁻¹ cm⁻¹, and as determined from a normalized absorption spectrum, the value at 355 nm is ca. 5,800 M⁻¹ cm⁻¹. Thus, the optical density range measured at 355 nm corresponds to a respective concentration of 50-100 μM, which should also be similar for other complexes.

If the addition of organic substrates was required, freshly prepared acetonitrile solutions of the substrates were injected *via* microsyringe into the sealed sample cell and thoroughly mixed by inversion or vortex. In cases where the sample in the cell were prepared with a solvent other than acetonitrile, the volume of substrate solution added corresponded to no more than 2.5% of the total volume; *e.g.* 50 μL for a 2 mL sample. Any changes to the reaction conditions induced by these small additions are deemed negligible.

Between laser pulses, samples were mixed to ensure that a fresh portion of the sample was exposed to the laser beam. As well, after every 20-25 pulses, samples were replaced with fresh solutions. This was particularly important in experiments where a substrate is rapidly consumed, such as in the carbocation-generation experiments (Chapter 4).

6.5.1.2 Acquisition and processing of absorption kinetic traces

The ability of the laser-flash photolysis system to capture time-resolved voltage changes is fundamental for the generation of kinetic traces, which are typically plots of changes in absorbance as a function of time at a single wavelength of interest. The captured voltage values are related by eq. 6.1 to the absorbance of the sample as well as the light intensity reaching the photomultiplier tube.

$$\begin{aligned} (V_t - V_{ini}) &\propto (I_t - I_{ini}) \\ (A_t - A_{ini}) &= -\log\left(\frac{I_t}{I_{ini}}\right) \end{aligned} \quad (6.1)$$

For simplicity, the initial voltage measured immediately prior to the laser pulse (V_{ini}) is automatically referenced as zero by a baseline correction box, as is the initial absorbance (A_{ini}). The parameter I_{ini} represents the intensity of the light passing through the sample before the pulse, while the parameters A_t , V_t , and I_t respectively correspond to the absorbance, voltage, and intensity of light passing through the sample at time t after the laser pulse. The ratio of I_t to I_{ini} is defined as the transmission of the sample, or the

percentage of light passing through the sample at time t after the laser pulse relative to the intensity before the pulse.

According to the Beer-Lambert law (eq. 6.2), the absorbance of a sample (A) is determined by the concentration of the absorbing transient (c), its extinction coefficient (ϵ), and the path length of the sample cell (l). The cell length and extinction coefficient of a particular transient at a given wavelength are physical properties that remain constant.

$$A = \epsilon cl \quad (6.2)$$

For a transient (T) that decays or grows *via* a first-order or pseudo first-order process, its rate law can be written as shown in eq. 6.3, where $[T]_{\text{ini}}$ is the initial concentration of the transient, $[T]_t$ is the concentration at time t after the laser pulse, and k is the rate constant of decay or growth.

$$[T]_t = [T]_{\text{ini}} e^{-kt} \quad (6.3)$$

While the concentration of a generated transient ($[T]$) cannot be easily measured unless its extinction coefficient is known, the direct relationship between concentration and absorbance allows the simplification of eq. 6.3 to eq. 6.4.

$$A_t = A_{\text{ini}} e^{-kt} \quad (6.4)$$

Equation 6.4 contains the three essential parameters (A_t , A_{ini} , t) collected by the data acquisition system that are required for the determination of the first-order rate constant k . However, stable photoproducts that are generated by laser-flash photolysis can also contribute to the absorbance, and the kinetic trace of a decay may return to a

constant residual value (A_{∞}) as opposed to baseline, represented in Figure 6-2 (a). For the kinetic trace of a growth, A_{∞} represents the final value of the growth. This corrective variable can be incorporated into eq. 6.4 to produce eq. 6.5, which is the basis of virtually all kinetic analyses.

$$A_t = A_{\infty} + A_{\text{ini}} e^{-kt} \quad (6.5)$$

Kinetic traces, each of which are actually 3-5 individual traces collected from multiple laser pulses and automatically averaged into one by the acquisition system, were processed offline with Kaleidagraph (Synergy Software). Over the timescale of the averaged kinetic trace, 250 data points were collected, and 50-55 of these points were at baseline level and situated in the pre-trigger region; *i.e.* the data points prior to the laser pulse, as illustrated in Figure 6-2 (a,c). These points were manually deleted, and the start of the kinetic trace immediately following the laser pulse was reassigned as time zero, as shown in Figure 6-2 (b,d). For the calculation of the rate constant k , estimated values of k , A_{∞} , and A_{ini} were provided to Kaleidagraph, which subsequently calculated a best-fit k value based on the iterative, least-squares Levenberg-Marquardt method.

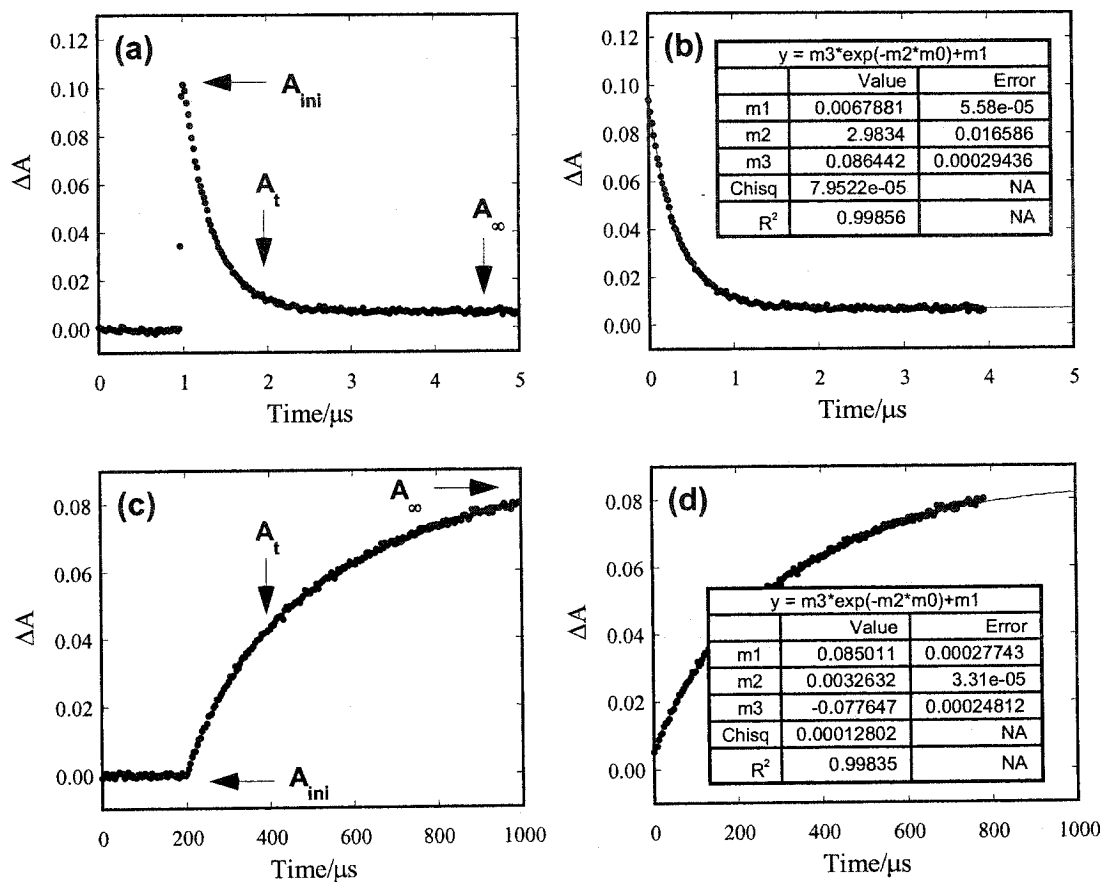


Figure 6-2. Sample time-resolved kinetic traces illustrating (a) a decay along with the pre-trigger region; (b) the same decay without the pre-trigger and analyzed with a monoexponential equation to calculate $k_{\text{decay}} = 3.0 \times 10^6 \text{ s}^{-1}$; (c) a growth including the pre-trigger; and (d) the same growth without the pre-trigger and analyzed with a monoexponential equation to calculate $k_{\text{growth}} = 3.3 \times 10^3 \text{ s}^{-1}$.

6.5.1.3 Acquisition and processing of emission kinetic traces

It is also possible to use the absorption system for the acquisition of emission kinetic traces by a simple modification. Specifically, if the monitoring lamp (Figure 6-1) were either turned off or if the monitoring beam were blocked from reaching the sample by means of a shutter, the setup would be similar to that of a standard fluorimeter, where the detector is arranged perpendicular to the excitation source. In this case, the sample emission intensity (I) is recorded as changes in voltage that are directly proportional to I , as per eq. 6.1. Like absorption, I is directly related to the concentration of an emitting transient. Thus, the first-order rate law shown in eq. 6.5 can be written as per eq. 6.6.

$$I_t = I_\infty + I_{\text{ini}} e^{-kt} \quad (6.6)$$

In this equation, I_t represents the emission intensity at time t after the laser pulse, I_{ini} is the initial intensity of the emitting transient, I_∞ is a final residual value, and k is the first-order decay rate constant. Emission kinetic traces were processed in a manner similar to absorption traces, where the pre-trigger regions were deleted and the time of the kinetic trace start was adjusted.

6.5.1.4 Acquisition of transient absorption spectra

While kinetic traces depict as a function of time at an individual wavelength and permit the determination of rate constants, transient spectra are useful for monitoring absorption changes over a wide range of wavelengths; in this thesis, only absorption spectra were collected, although it is also possible to collect emission spectra. These

time-resolved spectra are practical for the identification of transients that are concomitantly formed, as well as in the determination of absorption maxima. However, unlike a standard photodiode-array UV-visible spectrophotometer that captures spectra spanning the wavelength range of interest all at once and at predefined time intervals, the laser-flash photolysis system compiles transient absorption spectra from individual kinetic traces acquired one wavelength at a time. For instance, the acquisition of spectra spanning 350-550 nm with data points at 10 nm intervals would require the collection of 21 kinetic traces. Typically, each kinetic trace is an average of data from two laser pulses.

Transient absorption spectra at four different time intervals were compiled *via* the selection of four time windows (t_1 - t_4) after the laser pulse from a sample kinetic trace, as represented in Figure 6-3 (a). The average absorbance of the data points in each of the four windows is extracted from the kinetic trace and plotted on the y-axis of the transient absorption spectra, at an x-axis value corresponding to the wavelength at which the kinetic trace was acquired, as shown in Figure 6-3 (b). The acquisition and extraction process is subsequently repeated at other wavelengths, at the same time windows, until the entire desired wavelength range is recorded. Times corresponding to the centre of each time window are also output by the acquisition software.

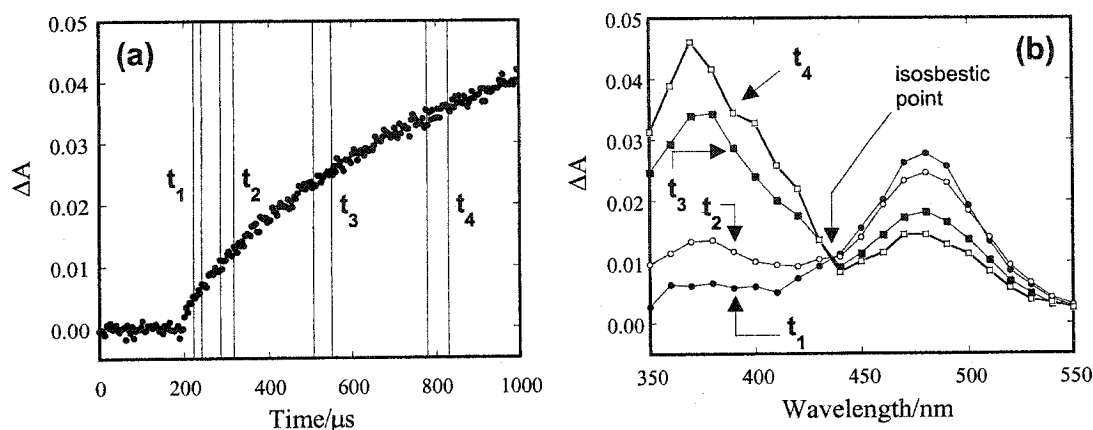


Figure 6-3. (a) Sample kinetic trace illustrating a growth at 390 nm, along with four time windows (t_1 - t_4) used for the construction of transient absorption spectra. (b) Spectra illustrating the increase in absorption at 390 nm at the same time windows selected on the kinetic trace. The concomitant decay and growth, with respective maxima near 480 and 370 nm, also result in an isosbestic point near 435 nm.

6.5.2 Femtosecond laser-flash photolysis (emission)

A highly simplified schematic of the laser-flash setup for the ultrafast detection of emission is provided in Figure 6-4. The pulsed 775 nm output of a solid-state, diode-pumped erbium-fibre Clark-MXR CPA-2001 laser (1 kHz, < 0.8 mJ/pulse, < 150 fs pulse width) is directed into a Clark-MXR STORC-2001 unit, where a portion of the light is frequency-doubled to 388 nm for sample excitation and the remaining light is unchanged and used for streak camera triggering.

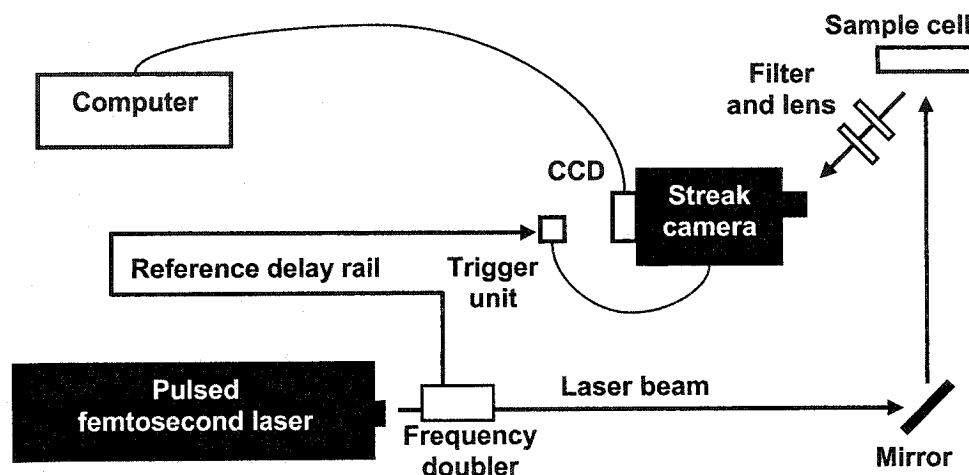


Figure 6-4. Femtosecond laser-flash photolysis schematic for the detection of emission.

Femtosecond systems are more complicated than their nanosecond counterparts in that the speed of light and the distance between various components becomes critical, *i.e.*, the relationship between time and space is fundamental in the design and function of the system. In this setup, the sample is subjected to front-face excitation, and the emission produced by the generated transients is passed through a 500 nm bandpass filter, collimated, and focussed into an Axis Photonique streak camera (< 1 ps time resolution, < 40 μM spatial resolution) equipped with a G2 jitter-free trigger unit and a CCD camera (Sensys). A reference beam synchronizes the streak camera acquisition to the pulsing of the laser. The acquisition also needs to be synchronized with the beginning of the sample emission, and this is done by adjusting the time required for the reference beam to travel from the laser to the trigger unit *via* spatial modification of its path length (delay rail).

Unlike a nanosecond system that uses a photomultiplier tube, the femtosecond system uses a streak camera for the detection of emission; its function is to provide time-resolved emission information in the form of a photographic image (Figure 6-5). Emission from the sample occurs as individual packets of photons, each of which is generated from the excitation of the sample with a single laser pulse. Each photon packet contains temporal information corresponding to the emission intensity (number of photons); in the case of an emission decay, the front of the packet contains more photons than at the rear. As the photon packet enters the streak camera, it is converted to an electron packet by a photocathode. The electron packet, which retains the temporal information and intensity, now in the form of the number of electrons, from the photon packet, is deflected 90° by means of a voltage applied to the deflector plates. The electron packet, which has been converted to a spatial domain, strikes a phosphor screen to produce an image that can be captured by the CCD camera, controlled using Photometrics IPLab software. The intensity of the image (*i.e.* light versus dark) corresponds the number of photons, while the horizontal axis translates to time. These images, which are usually averages of 10-12 min exposures, are then corrected for intrinsic curvature and tilt using in-house software written in Labview 5.1. Vertical summation of the image data allows extraction of kinetic information.

The instrument response function was determined to be 4.0-4.5 ps by measuring the scatter of the incident laser beam on a colloidal suspension of corn starch in water.

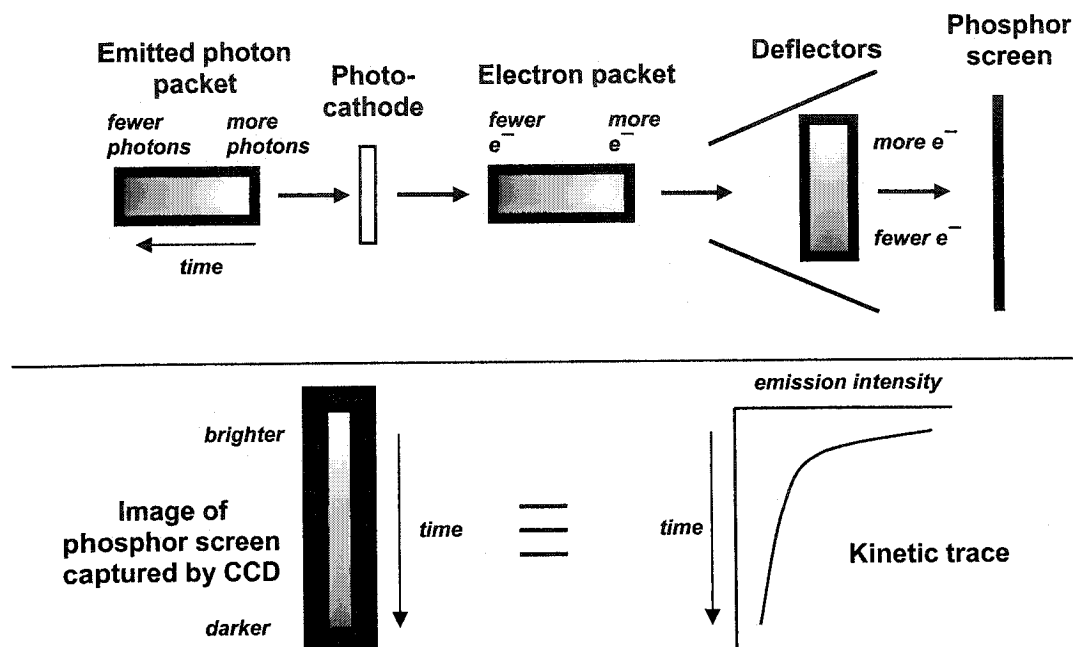


Figure 6-5. Schematic of streak camera operation for the acquisition of emission. The emitted photon packet is converted to an image equivalent to a kinetic trace.

6.5.2.1 Sample preparation

Stock solutions of unlinked ruthenium complexes were prepared in high-purity water (Nanopure or EMD Omnisolv) and stored at $-15\text{ }^{\circ}\text{C}$ or at room temperature. When required for use, the stock solutions were diluted to 2-3 mM and transferred to a Helma $10 \times 1\text{ mm}^2$ quartz cuvette that was previously cleaned with conc. HCl and thoroughly rinsed with high-purity water. Ground state UV-visible absorption spectra of the sample cell were acquired on the spectrophotometer prior to and after laser irradiation to ensure that no noticeable sample degradation occurred during the process.

6.5.2.2 Processing of kinetic traces

Time-resolved emission traces collected on the femtosecond laser system are similar to the traces acquired on the nanosecond system, as described by equation 6.6. However, emission decays can also originate from two transients with different decay rate constants (k_1 , k_2), thus necessitating the expansion of this equation to account for a biexponential kinetic trace, as shown in eq. 6.7.

$$I_t = I_\infty + I_{\text{ini}(1)} e^{-k_1 t} + I_{\text{ini}(2)} e^{-k_2 t} \quad (6.7)$$

Kinetic traces, convoluted with the instrument response function, were analyzed in a manner similar to the nanosecond kinetic traces. Estimates of the rate constants, as well as I_{ini} and I_∞ , were input into in-house software written in Labview 5.1, where the Levenberg-Marquardt algorithm was used for the calculation of rate constants.

6.6 Product studies

A solution of the photolysis mixture (250 mL) was placed in a water-cooled, quartz reaction vessel and purged with nitrogen for 30 minutes prior to photolysis. The magnetically stirred mixture was subsequently irradiated with a Hanovia 450 W mercury lamp equipped with a Pyrex filter (300 nm cutoff). After the desired irradiation time, the reaction mixture was removed from irradiation and extracted with diethyl ether (3×100 mL). The combined ethereal extracts were washed with brine (3×50 mL), dried with anhydrous MgSO_4 , and evaporated under reduced pressure. The residue remaining after evaporation was analyzed by GC-MS and ^1H NMR.

References

1. Wolfenden, R.; Snider, M. J. *Acc. Chem. Res.* **2001**, *34*, 938-945.
2. Garcia-Viloca, M.; Gao, J.; Karplus, M.; Truhlar, D. G. *Science* **2004**, *303*, 186-195.
3. Pauling, L. *Chem. Eng. News* **1946**, *24*, 1375-1377.
4. Wolfenden, R. *Bioorg. Med. Chem.* **1999**, *7*, 647-652.
5. Schramm, V. L. *Annu. Rev. Biochem.* **1998**, 693-720.
6. Markgren, P.-O.; Schaal, W.; Haemaelaenen, M.; Karlen, A.; Hallberg, A.; Samuelsson, B.; Danielson, U. H. *J. Med. Chem.* **2002**, *45*, 5430-5439.
7. Kiso, A.; Hidaka, K.; Kimura, T.; Hayashi, Y.; Nezami, A.; Freire, E.; Kiso, Y. *J. Pept. Sci.* **2003**, *39th*, 297-300.
8. Toraya, T. *Chem. Rec.* **2002**, *2*, 352-366.
9. Stubbe, J.; van der Donk, W. A. *Chem. Rev.* **1998**, *98*, 705-762.
10. Ravn, M. M.; Peters, R. J.; Coates, R. M.; Croteau, R. *J. Am. Chem. Soc.* **2002**, *124*, 6998-7006.
11. Xiong, Q.; Zhu, X.; Wilson, W. K.; Ganesan, A.; Matsuda, S. P. T. *J. Am. Chem. Soc.* **2003**, *125*, 9002-9003.
12. Meyer, M. M.; Segura, M. J. R.; Wilson, W. K.; Matsuda, S. P. T. *Angew. Chem. Int. Ed.* **2000**, *39*, 4090-4092.

13. Herrera, J. B. R.; Wilson, W. K.; Matsuda, S. P. T. *J. Am. Chem. Soc.* **2000**, *122*, 6765-6766.
14. Corey, E. J.; Virgil, S. C.; Cheng, H.; Baker, C. H.; Matsuda, S. P. T.; Singh, V.; Sarshar, S. *J. Am. Chem. Soc.* **1995**, *117*, 11819-11820.
15. Ma, J. C.; Dougherty, D. A. *Chem. Rev.* **1997**, *97*, 1303-1324.
16. Sunner, J.; Nishizawa, K.; Kebarle, P. *J. Phys. Chem.* **1981**, *85*, 1814-1820.
17. Kumpf, R. A.; Dougherty, D. A. *Science* **1993**, *261*, 1708-1710.
18. Deakyne, C. A.; Meot-Ner (Mautner), M. *J. Am. Chem. Soc.* **1985**, *107*, 474-479.
19. Meot-Ner (Mautner), M.; Deakyne, C. A. *J. Am. Chem. Soc.* **1985**, *107*, 469-474.
20. Burley, S. K.; Petsko, G. A. *Science* **1985**, *229*, 23-28.
21. Burley, S. K.; Petsko, G. A. *FEBS Lett.* **1986**, *203*, 139-143.
22. Burley, S. K.; Petsko, G. A. *Adv. Protein. Chem.* **1988**, *39*, 125-189.
23. Mecozi, S.; West, A. P., Jr.; Dougherty, D. A. *J. Am. Chem. Soc.* **1996**, *118*, 2307-2308.
24. Mecozi, S.; West, A. P., Jr.; Dougherty, D. A. *Proc. Natl. Acad. Sci. USA* **1996**, *93*, 10566-10571.
25. Basch, H.; Stevens, W. J. *J. Mol. Struct. (Theochem)* **1995**, *338*, 303-315.
26. Ngola, S. M.; Kearney, P. C.; Mecozi, S.; Russell, K.; Dougherty, D. A. *J. Am. Chem. Soc.* **1999**, *121*, 1192-1201.
27. Shepodd, T. J.; Petti, M. A.; Dougherty, D. A. *J. Am. Chem. Soc.* **1988**, *110*, 1983-1985.

28. Shepodd, T. J.; Petti, M. A.; Dougherty, D. A. *J. Am. Chem. Soc.* **1986**, *108*, 6085-6087.
29. De Wall, S. L.; Meadows, E. S.; Barbour, L. J.; Gokel, G. W. *Proc. Natl. Acad. Sci. USA* **2000**, *97*, 6271-6276.
30. Kearney, P. C.; Mizoue, L. S.; Kumpf, R. A.; Forman, J. E.; McCurdy, A.; Dougherty, D. A. *J. Am. Chem. Soc.* **1993**, *115*, 9907-9919.
31. Stauffer, D. A.; Dougherty, D. A. *Tetrahedron Lett.* **1988**, *29*, 6039-6042.
32. Dougherty, D. A.; Stauffer, D. A. *Science* **1990**, *250*, 1558-1560.
33. Sussman, J. L.; Harel, M.; Frolov, F.; Oefner, C.; Goldman, A.; Toker, L.; Silman, I. *Science* **1991**, *253*, 872-879.
34. Ordentlich, A.; Barak, D.; Kronman, C.; Flashner, Y.; Leitner, M.; Segall, Y.; Ariel, N.; Cohen, S.; Velan, B.; Shafferman, A. *J. Biol. Chem.* **1993**, *268*, 17083-17095.
35. Ariel, N.; Ordentlich, A.; Barak, D.; Bino, T.; Velan, B.; Shafferman, A. *Biochem. J.* **1998**, *335* (Pt 1), 95-102.
36. Loewenthal, R.; Sancho, J.; Fersht, A. R. *J. Mol. Biol.* **1992**, *224*, 759-770.
37. Lund-Katz, S.; Phillips, M. C.; Mishra, V. K.; Segrest, J. P.; Anantharamaiah, G. M. *Biochemistry* **1995**, *34*, 9219-9226.
38. Shoemaker, K. R.; Fairman, R.; Schultz, D. A.; Robertson, A. D.; York, E. J.; Stewart, J. M.; Baldwin, R. L. *Biopolymers* **1990**, *29*, 1-11.
39. Gromiha, M. M. *Biophys. Chem.* **2003**, *103*, 251-258.

40. Pletneva, E. V.; Laederach, A. T.; Fulton, D. B.; Kostic, N. M. *J. Am. Chem. Soc.* **2001**, *123*, 6232-6245.
41. Gallivan, J. P.; Dougherty, D. A. *Proc. Natl. Acad. Sci. USA* **1999**, *96*, 9459-9464.
42. Shi, Z.; Olson, C. A.; Kallenbach, N. R. *J. Am. Chem. Soc.* **2002**, *124*, 3284-3291.
43. Gromiha, M. M.; Santhosh, C.; Ahmad, S. *Int. J. Biol. Macromol.* **2004**, *34*, 203-211.
44. Gromiha, M. M.; Santhosh, C.; Suwa, M. *Polymer* **2004**, *45*, 633-639.
45. Wintjens, R.; Lievin, J.; Rooman, M.; Buisine, E. *J. Mol. Biol.* **2000**, *302*, 395-410.
46. Zaric, S. D.; Popovic, D. M.; Knapp, E. W. *Chemistry* **2000**, *6*, 3935-3942.
47. Nakamura, O. *Kagaku (Kyoto, Japan)* **2003**, *58*, 48-49.
48. Lavieri, S.; Zoltewicz, J. A. *J. Org. Chem.* **2001**, *66*, 7227-7230.
49. Abe, I.; Prestwich, G. D. In *Comprehensive natural products chemistry*; Cane, D. E., Ed.; Elsevier: New York, 1999, pp 267-298.
50. Wendt, K. U.; Schulz, G. E.; Corey, E. J.; Liu, D. R. *Angew. Chem. Int. Ed.* **2000**, *39*, 2812-2833.
51. Johnson, W. S.; Lindell, S. D.; Steele, J. J. *J. Am. Chem. Soc.* **1987**, *109*, 5882-5883.
52. Abe, I.; Prestwich, G. D. *Proc. Natl. Acad. Sci. USA* **1995**, *92*, 9274-9278.
53. Shi, Z.; Buntel, C. J.; Griffin, J. H. *Proc. Natl. Acad. Sci. USA* **1994**, *91*, 7370-7374.

54. Poralla, K.; Hewelt, A.; Prestwich, G. D.; Abe, I.; Reipen, I.; Sprenger, G. *Trends Biochem. Sci.* **1994**, *19*, 157-158.
55. Cattel, L.; Ceruti, M. *Crit. Rev. Biochem. Mol. Biol.* **1998**, *33*, 353-373.
56. Hinshaw, J. C.; Suh, D.-Y.; Garnier, P.; Buckner, F. S.; Eastman, R. T.; Matsuda, S. P. T.; Joubert, B. M.; Coppens, I.; Joiner, K. A.; Merali, S.; Nash, T. E.; Prestwich, G. D. *J. Med. Chem.* **2003**, *46*, 4240-4243.
57. Goldman, R. C.; Zakula, D.; Capobianco, J. O.; Sharpe, B. A.; Griffin, J. H. *Antimicrob. Agents Chemother.* **1996**, *40*, 1044-1047.
58. Buckner, F. S.; Griffin, J. H.; Wilson, A. J.; Van Voorhis, W. C. *Antimicrob. Agents Chemother.* **2001**, *45*, 1210-1215.
59. Joubert, B. M.; Buckner, F. S.; Matsuda, S. P. T. *Org. Lett.* **2001**, *3*, 1957-1960.
60. Kavarnos, G. J.; Turro, N. J. *Chem. Rev.* **1986**, *86*, 401-449.
61. Maslak, P.; Chapman, W. H., Jr. *J. Org. Chem.* **1996**, *61*, 2647-2656.
62. Russo-Caia, C.; Steenken, S. *Physical Chemistry Chemical Physics* **2002**, *4*, 1478-1485.
63. Hara, M.; Tojo, S.; Majima, T. *J. Photochem. Photobiol. A: Chem.* **2004**, *162*, 121-128.
64. Gronheid, R.; Zuilhof, H.; Hellings, M. G.; Cornelisse, J.; Lodder, G. *J. Org. Chem.* **2003**, *68*, 3205-3215.
65. O'Neill, M. A.; Cozens, F. L. *Can. J. Chem.* **2003**, *81*, 647-659.
66. Wetlaufer, D. B. *Adv. Protein Chem.* **1962**, *17*, 303-390.

67. Lew, C. S. Q.; Brisson, J. R.; Johnston, L. J. *J. Org. Chem.* **1997**, *62*, 4047-4056.
68. Hoertz, P. G.; Carlisle, R. A.; Meyer, G. J.; Wang, D.; Piotrowiak, P.; Galoppini, E. *Nano Lett.* **2003**, *3*, 325-330.
69. Piotrowiak, P.; Galoppini, E.; Wei, Q.; Meyer, G. J.; Wiewior, P. *J. Am. Chem. Soc.* **2003**, *125*, 5278-5279.
70. Millett, F.; Durham, B. *Biochemistry* **2002**, *41*, 11315-11324.
71. Engstrom, G.; Rajagukguk, R.; Saunders, A. J.; Patel, C. N.; Rajagukguk, S.; Merbitz-Zahradnik, T.; Xiao, K.; Pielak, G. J.; Trumpower, B.; Yu, C.-A.; Yu, L.; Durham, B.; Millett, F. *Biochemistry* **2003**, *42*, 2816-2824.
72. Yoo, J.; Delaney, S.; Stemp, E. D. A.; Barton, J. K. *J. Am. Chem. Soc.* **2003**, *125*, 6640-6641.
73. Juris, A.; Balzani, V.; Barigelletti, F.; Campagna, S.; Belser, P.; Von Zelewsky, A. *Coord. Chem. Rev.* **1988**, *84*, 85-277.
74. Kalyanasundaram, K. *Coord. Chem. Rev.* **1982**, *46*, 159-244.
75. Braunstein, C. H.; Baker, A. D.; Strekas, T. C.; Gafney, H. D. *Inorg. Chem.* **1984**, *23*, 857-864.
76. Bhasikuttan, A. C.; Suzuki, M.; Nakashima, S.; Okada, T. *J. Am. Chem. Soc.* **2002**, *124*, 8398-8405.
77. Wilker, J. J.; Dmochowski, I. J.; Dawson, J. H.; Winkler, J. R.; Gray, H. B. *Angew. Chem. Int. Ed.* **1999**, *38*, 89-92.
78. Nazeeruddin, M. K.; Zakeeruddin, S. M.; Kalyanasundaram, K. *J. Phys. Chem.* **1993**, *97*, 9607-9612.

79. Kitamura, N.; Rajagopal, S.; Tazuke, S. *J. Phys. Chem.* **1987**, *91*, 3767-3771.
80. Wacholtz, W. F.; Auerbach, R. A.; Schmehl, R. H. *Inorg. Chem.* **1986**, *25*, 227-234.
81. Furue, M.; Maruyama, K.; Oguni, T.; Naiki, M.; Kamachi, M. *Inorg. Chem.* **1992**, *31*, 3792-3795.
82. Lide, D. R., Ed. *CRC Handbook of Chemistry and Physics*; CRC Press: Boca Raton, 1993.
83. Meyer, T. J. *Acc. Chem. Res.* **1989**, *22*, 163-170.
84. Skarda, V.; Cook, M. J.; Lewis, A. P.; McAuliffe, G. S. G.; Thomson, A. J.; Robbins, D. J. *J. Chem. Soc. Perkin Trans. 2* **1984**, 1309-1311.
85. Elliott, C. M.; Hershenhart, E. J. *J. Am. Chem. Soc.* **1982**, *104*, 7519-7526.
86. Slattery, S. J.; Gokaldas, N.; Mick, T.; Goldsby, K. A. *Inorg. Chem.* **1994**, *33*, 3621-3624.
87. Yang, X. J.; Janiak, C.; Heinze, J.; Drepper, F.; Mayer, P.; Piotrowski, H.; Klufers, P. *Inorg. Chim. Acta* **2001**, *318*, 103-116.
88. Slattery, S. J.; Bare, W. D.; Jameson, D. L.; Goldsby, K. A. *J. Chem. Soc. Dalton Trans.* **1999**, 1347-1352.
89. Hathcock, D.; Morris, J.; Madden, J.; Slattery, S. J. *Chemical Educator [Electronic Publication]* **1997**, *2*, No pp.
90. Schepp, N. P.; Johnston, L. J. *J. Am. Chem. Soc.* **1996**, *118*, 2872-2881.
91. Lancelot, S. F.; Cozens, F. L.; Schepp, N. P. *Org. Biomol. Chem.* **2003**, *1*, 1972-1979.

92. Ho, T.-I.; Lin, C.-R.; Pan, K.; Hsu, C.-W. *J. Chin. Chem. Soc.* **2001**, *48*, 983-986.
93. Murphy, R. S.; Bohne, C. *Photochem. and Photobiol.* **2000**, *71*, 35-43.
94. Eberson, L.; Hartshorn, M. P.; Persson, O. *Acta Chem. Scand.* **1998**, *52*, 751-760.
95. Cozens, F. L.; Bogdanova, R.; Regimbald, M.; Garcia, H.; Marti, V.; Scaiano, J. *C. J. Phys. Chem. B* **1997**, *101*, 6921-6928.
96. Schepp, N. P.; Johnston, L. J. *J. Am. Chem. Soc.* **1996**, *118*, 2872-2881.
97. Brede, O.; David, F.; Steenken, S. *J. Chem. Soc. Perkin Trans. 2* **1995**, 23-32.
98. Johnston, L. J.; Schepp, N. P. *Pure App. Chem.* **1995**, *67*, 71-78.
99. Yu, T.; Lin, M. C.; Melius, C. F. *Int. J. Chem. Kinet.* **1994**, *26*, 1095-1104.
100. Johnston, L. J.; Schepp, N. P. *J. Am. Chem. Soc.* **1993**, *115*, 6564-6571.
101. Chen, C.-Y.; Ho, J.-H.; Wang, S.-L.; Ho, T.-I. *Photochem. Photobiol. Sci.* **2003**, *2*, 1232-1236.
102. Lewis, F. D.; Weigel, W. *J. Phys. Chem. A* **2000**, *104*, 8146-8153.
103. Rettig, W.; Strehmel, B.; Majenz, W. *Chemical Physics* **1993**, *173*, 525-537.
104. Roberts, J. C.; Pincock, J. A. *J. Org. Chem.* **2004**, *69*, 4279-4282.
105. Momotake, A.; Arai, T. *J. Photochem. Photobiol. C: Photochem.* **2004**, *5*, 1-25.
106. Seydack, M.; Bendig, J. *J. Fluoresc.* **2000**, *10*, 291-294.
107. Saltiel, J.; Waller, A. S.; Sears, D. F., Jr. *J. Am. Chem. Soc.* **1993**, *115*, 2453-2465.

108. Peters, K. S.; Angel, S. A.; O'Driscoll, E. *Pure App. Chem.* **1989**, *61*, 629-634.
109. Doany, F. E.; Hochstrasser, R. M.; Greene, B. I.; Millard, R. R. *Chem. Phys. Lett.* **1985**, *118*, 1-5.
110. Momicchioli, F.; Corradini, G. R.; Bruni, M. C.; Baraldi, I. *J. Chem. Soc. Faraday Trans. 2* **1975**, *71*, 215-224.
111. Momicchioli, F.; Bruni, M. C.; Baraldi, I.; Corradini, G. R. *J. Chem. Soc. Faraday Trans. 2* **1974**, *70*, 1325-1333.
112. Okamoto, A.; Arnold, D. R. *Can. J. Chem.* **1985**, *63*, 2340-2342.
113. Bock, C. R.; Meyer, T. J.; Whitten, D. G. *J. Am. Chem. Soc.* **1974**, *96*, 4710-4712.
114. Creutz, C.; Sutin, N. *Inorg. Chem.* **1976**, *15*, 496-499.
115. Lin, C.-T.; Sutin, N. *J. Phys. Chem.* **1976**, *80*, 97-105.
116. Navon, G.; Sutin, N. *Inorg. Chem.* **1974**, *13*, 2159-2164.
117. Thanasekaran, P.; Rajendran, T.; Rajagopal, S.; Srinivasan, C.; Ramaraj, R.; Ramamurthy, P.; Venkatachalapathy, B. *J. Phys. Chem. A* **1997**, *101*, 8195-8199.
118. Fukuzumi, S.; Ohkubo, K.; Imahori, H.; Guldi, D. M. *Chem. Eur. J.* **2003**, *9*, 1585-1593.
119. Turro, N. J. *Modern Molecular Photochemistry*; Benjamin: Menlo Park, 1978.
120. Rudenko, A. P.; Zarubin, M. J. *J. Electroanal. Chem.* **1983**, *151*, 89-100.
121. Haga, M.; Dodsworth, E. S.; Eryavec, G.; Seymour, P.; Lever, A. B. P. *Inorg. Chem.* **1985**, *24*, 1901-1906.
122. Kawanishi, Y.; Kitamura, N.; Tazuke, S. *Inorg. Chem.* **1989**, *28*, 2968-2975.

123. Tsuchida, A.; Yamamoto, M.; Nishijima, Y. *J. Phys. Chem.* **1984**, 88.
124. Aufauvre, F.; Dantonnet, M.; Dondon, M. L. *Bull. Soc. Chim. Fr.* **1965**, 3566-3572.
125. Partigianoni, C. M.; Chodorowski-Kimmes, S.; Treadway, J. A.; Striplin, D.; Trammell, S. A.; Meyer, T. J. *Inorg. Chem.* **1999**, 38, 1193-1198.
126. Gray, H. B.; Winkler, J. R. *Q. Rev. Biophys.* **2003**, 36, 341-372.
127. Nunez, M. E.; Barton, J. K. *Curr. Opin. Chem. Biol.* **2000**, 4, 199-203.
128. Johnson, E. T.; Nagarajan, V.; Zazubovich, V.; Riley, K.; Small, G. J.; Parson, W. W. *Biochemistry* **2003**, 42, 13673-13683.
129. Giese, B.; Spichtym, M.; Wessely, G. *Pure App. Chem.* **2001**, 73, 449-543.
130. Giese, B.; Wessely, G.; Spormann, M.; Lindemann, T.; Meggers, E.; Michel-Beyerle, M. E. *Angew. Chem. Int. Ed.* **1999**, 38, 996-998.
131. Nakao, H.; Gad, M.; Sugiyama, S.; Otake, K.; Ohtani, T. *J. Am. Chem. Soc.* **2003**, 125, 7162-7163.
132. Liu, D.; Park, S. H.; Reif, J. H.; LaBean, T. H. *Proc. Nat. Sci. Acad. USA* **2004**, 101, 717-722.
133. Hahm, J.-i.; Lieber, C. M. *Nano Lett.* **2004**, 4, 51-54.
134. Sikes, H. D.; Smalley, J. F.; Dudek, S. P.; Cook, A. R.; Newton, M. D.; Chidsey, C. E. D.; Feldberg, S. W. *Science* **2001**, 291, 1519-1523.
135. Park, J. W.; Lee, B. A.; Lee, S. Y. *J. Phys. Chem. B* **1998**, 102, 8209-8215.

136. Maslak, P.; Chapman, W. H., Jr.; Vallombroso, T. M.; Watson, B. A. *J. Am. Chem. Soc.* **1995**, *117*, 12380-12389.
137. Maslak, P. *Top. Curr. Chem.* **1993**, *1993*, 17-21.
138. Schanze, K. S.; Walters, K. A. In *Molecular and supramolecular photochemistry*; Ramamurthy, V., Schanze, K. S., Eds.; Marcel-Dekker: New York, 1998; Vol. 2, pp 75-127.
139. Sim, B. A.; Milne, P. H.; Griller, D.; Wayner, D. D. M. *J. Am. Chem. Soc.* **1990**, *112*, 6635-6638.
140. Cozens, F. L.; Kanagasabapathy, V. M.; McClelland, R. A.; Steenken, S. *Can. J. Chem.* **1999**, *77*, 2069-2082.
141. Maslak, P.; Asel, S. L. *J. Am. Chem. Soc.* **1988**, *110*, 8260-8261.
142. Arnold, D. R.; Maroulis, A. J. *J. Am. Chem. Soc.* **1976**, *98*, 5931-5937.
143. Maslak, P.; Kula, J.; Chateaufneuf, J. E. *J. Am. Chem. Soc.* **1991**, *113*, 2304-2306.
144. Maslak, P. *Top. Curr. Chem.* **1993**, *168*, 1-46.
145. Maslak, P.; Chapman, W. H., Jr. *Chem. Commun.* **1989**, 1809-1811.
146. Maslak, P.; Chapman, W. H., Jr. *J. Org. Chem.* **1990**, *55*, 6334-6347.
147. Maslak, P.; Chapman, W. H., Jr. *Tetrahedron* **1990**, *46*, 2715-2724.
148. Maslak, P.; Kula, J. *Mol. Cryst. Liq. Cryst.* **1991**, *194*, 293-304.
149. Maslak, P.; Kula, J.; Narvaez, J. N. *J. Org. Chem.* **1990**, *55*, 2277-2279.
150. Maslak, P.; Narvaez, J. N. *Chem. Commun.* **1989**, 138-139.

151. Maslak, P.; Narvaez, J. N. *Angew. Chem.* **1990**, *102*, 302-304.
152. Maslak, P.; Narvaez, J. N.; Kula, J.; Malinski, D. S. *J. Org. Chem.* **1990**, *55*, 4550-4559.
153. Maslak, P.; Narvaez, J. N.; Parvez, M. *J. Org. Chem.* **1991**, *56*, 602-607.
154. Maslak, P.; Narvaez, J. N.; Vallombroso, T. M., Jr. *J. Am. Chem. Soc.* **1995**, *117*, 12373-12379.
155. Maslak, P.; Vallombroso, T. M.; Chapman, W. H., Jr.; Narvaez, J. N. *Angew. Chem.* **1994**, *106*, 110-113.
156. Swain, C. G.; Lupton, E. C., Jr. *J. Am. Chem. Soc.* **1968**, *90*, 4328-4337.
157. Kratt, G.; Beckhaus, H. D.; Lindner, H. J.; Ruechardt, C. *Chem. Ber.* **1983**, *116*, 3235-3263.
158. Kratt, G.; Beckhaus, H. D.; Ruechardt, C. *Chem. Ber.* **1984**, *117*, 1748-1764.
159. Beckhaus, H. D.; Ruechardt, C. *Chem. Ber.* **1977**, *110*, 878-895.
160. Osawa, E.; Ivanov, P.; Jaime, C. *J. Org. Chem.* **1983**, *48*, 3990-3993.
161. Zavitsas, A. A. *J. Phys. Chem. A* **2003**, *107*, 897-898.
162. Hammond, G. S. *J. Am. Chem. Soc.* **1955**, *55*, 334-338.
163. Benko, G.; Kallioinen, J.; Korppi-Tommola, J. E. I.; Yartsev Arkady, P.; Sundstrom, V. *J. Am. Chem. Soc.* **2003**, *124*, 489-493.
164. Bernstein, R. B.; Zewail, A. H. *J. Phys. Chem.* **1986**, *90*, 3467-3469.
165. Damrauer, N. H.; Cerullo, G.; Yeh, A.; Boussie, T. R.; Shank, C. V.; McCusker, J. K. *Science* **1997**, *275*, 54-57.

166. Farrell, I. R.; Matousek, P.; Towrie, M.; Parker, A. W.; Grills, D. C.; George, M. W.; Vlcek, A., Jr. *Inorg. Chem.* **2002**, *41*, 4318-4323.
167. Shiang, J. J.; Walker, L. A., II; Anderson, N. A.; Cole, A. G.; Sension, R. J. *J. Phys. Chem. B* **1999**, *103*, 10532-10539.
168. McCusker, J. K. *Acc. Chem. Res.* **2003**, *36*, 876-887.
169. Browne, W. R.; Coates, C. G.; Brady, C.; Matousek, P.; Towrie, M.; Botchway, S. W.; Parker, A. W.; Vos, J. G.; McGarvey, J. J. *J. Am. Chem. Soc.* **2003**, *125*, 1706-1707.
170. Daul, C.; Baerends, E. J.; Vernooijs, P. *Inorg. Chem.* **1994**, *33*, 3538-3543.
171. Waterland, M. R.; Kelley, D. F. *J. Phys. Chem. A* **2001**, *105*, 4019-4028.
172. Van Houten, J.; Watts, R. J. *J. Am. Chem. Soc.* **1976**, *98*, 4853-4858.
173. Felix, F.; Ferguson, J.; Gudel, H. U.; Ludi, A. *J. Am. Chem. Soc.* **1980**, *102*, 4096-4102.
174. Sprintschnik, G.; Sprintschnik, H. W.; Kirsch, P. P.; Whitten, D. G. *J. Am. Chem. Soc.* **1977**, *99*, 4947-4954.
175. Sullivan, B. P.; Salmon, D. J.; Meyer, T. J. *Inorg. Chem.* **1978**, *17*, 3334-3341.
176. Yang, J.; Seneviratne, D.; Arbatin, G.; Andersson, A. M.; Curtis, J. C. *J. Am. Chem. Soc.* **1997**, *119*, 5329-5336.
177. Hou, Y.-j.; Xie, P.-h.; Zhang, B.-w.; Cao, Y.; Xiao, X.-r.; Wang, W.-b. *Inorg. Chem.* **1999**, *38*, 6320-6322.
178. Hesek, D.; Inoue, Y.; Everitt, S. R. L.; Ishida, H.; Kunieda, M.; Drew, M. G. B. *Inorg. Chem.* **2000**, *39*, 308-316.

179. El Torki, F. M.; Schmehl, R. H.; Reed, W. F. *J. Chem. Soc. Faraday Trans. 1* **1989**, *85*, 349-362.
180. Clay, M. In *Chemistry*; Dalhousie University: Halifax, 2001.
181. McClanahan, S. F.; Dallinger, R. F.; Holler, F. J.; Kincaid, J. R. *J. Am. Chem. Soc.* **1985**, *107*, 4853-4860.
182. Grigg, R.; Holmes, J. M.; Jones, S. K.; Norbert, W. D. *J. A. Chem. Commun.* **1994**, 185-187.
183. Hou, Y.; Xie, P.; Wu, K.; Wang, J.; Zhang, B.; Cao, Y. *Solar Energy Materials and Solar Cells* **2001**, *70*, 131-139.
184. Della Ciana, L.; Hamachi, I.; Meyer, T. J. *J. Org. Chem.* **1989**, *54*, 1731-1735.
185. Gastaminza, A.; Ridd, J. H. *J. Chem. Soc. Perkin Trans. 2* **1972**, 813-815.
186. McMurry, J. E.; Silvestri, M. G.; Fleming, M. P.; Hoz, T.; Grayston, M. W. *J. Org. Chem.* **1978**, *43*, 3249-3255.
187. Nishino, T.; Nishiyama, Y.; Sonoda, N. *Bull. Chem. Soc. Japan* **2003**, *76*, 635-641.
188. Vogel, A. I. *Vogel's Textbook of Practical Organic Chemistry*; 5th ed.; Longman: London; New York, 1989.
189. Pocker, Y.; Beug, M. W. *Biochemistry* **1972**, *11*, 698-707.
190. Hartmann, R. W.; Kranzfelder, G.; Von Angerer, E.; Schoenenberger, H. *J. Med. Chem.* **1980**, *23*, 841-848.
191. Zawadiak, J.; Stec, Z.; Jakubowski, B.; Orlinska, B. *Int. J. Chem. Kinet.* **2003**, *35*, 89-94.

192. Hadel, L. M.; Scaiano, J. C., Ed.; CRC Press: Boca Raton, 1989; Vol. I, pp 279-292.